Finite Element Analysis of Steel-Concrete Composite Floor Systems under Traveling Fires

by

Jason Martinez

A dissertation submitted in partial fulfillment
of the requirements for the degree of
Doctor of Philosophy
(Civil Engineering)
in the University of Michigan
2021

Doctoral Committee:

Associate Professor Ann E. Jeffers, Chair
Professor James R. Barber
Professor Sherif El-Tawil
Associate Professor Jason P. McCormick

Jason Martinez

marjason@umich.edu

ORCID iD: 0000-0003-3737-4762

Dedication

This work is dedicated to my parents, Carmen and Ramon, and my grandmother, Calla. This dissertation would not be possible without their unbelievable sacrifices.

Acknowledgements

I would like to thank my advisor Prof. Ann E. Jeffers for her support and guidance throughout my Ph.D. work. Even though I have learned a great deal from working alongside her, the importance of being kind, supportive, and patient will always resonate with me. I am also grateful for the support and encouragement of my committee members, Prof. Barber, Prof. El-Tawil, and Prof. McCormick. This dissertation would not be realized without their valuable inputs. I have been fortunate to work alongside many members of the Jeffers' research group, including Paul Beata, Ning Liu, Qianru Guo, Ha Nguyen, and Alyssa DeSimone, as well as colleagues from the GGB 1267A office, who made my time at Michigan more enjoyable. To Paul and Ning: the brotherhood that we formed was special, and I am lucky to have shared so many memories together. I would also like to thank several faculty members whose support meant a great deal to me: Prof. Cotel, Prof. Filipov, Prof. Lynch, Prof. Spence, Prof. Wight, and Prof. Yin. Special thanks goes to my first research advisor, Prof. Huabei Liu, who inspired and encouraged me to pursue a doctorate degree. Thank You! I would also like to thank Nathan Fleming for writing the first version of the MATLAB code used in the dissertation for transferring heat transfer data to the structural analysis model. The dissertation would not be possible without the financial support from several sources, including financial support from the Department of Civil and Environmental Engineering, the University of Michigan Rackham Engineering Award, and the National Science Foundation through Grant No. DGE 1256260 and Grant No. CMMI 1253440. This research was also supported in part through computational resources and services provided by the University of

Michigan’s Advanced Research Computing (ARC) Flux HPC cluster. Lastly, the support of my wife Naomi Ramesar has been enormous. I am blessed and lucky to have her in my life.

Table of Contents

List of Tables

List of Figures

Abstract

Traveling fires occur in large open-plan compartment and have been observed in many fire accidents including the First Interstate Bank fire in Los Angeles in 1988, the One Meridian Plaza fire in Philadelphia in 1991, and the World Trade Center Building 7 fire in New York City in 2001. Despite the significant structural damage observed in these incidents, existing fire safety codes do not have regulations dedicated to ensuring the fire safety of large open-plan compartments, nor are traveling fires explicitly considered in the fire design process. To address this deficiency, the dissertation presents a computational study aimed at better understanding the thermal and structural response of steel-concrete composite (SCC) floor systems exposed to traveling fires.

Improvements to the finite element modeling of SCC floor systems were developed as part of the dissertation work. Specifically, a formal macro-modeling approach for SCC floor systems was presented, which addresses a modeling error that has remained largely unreported in the research literature. Using this modeling approach, a numerical analysis of an axially-restrained SCC beam was performed. The results showed that failure of a restrained SCC beam is heavily influenced by its span length: a composite beam with a short span tends to fail in the compressive beam-column stage, while a composite beam with a longer span tends to fail in the tensile catenary stage. Additionally, conditions which are favorable for the mobilization of tensile catenary action were determined, which provides structural engineers with the information required to improve the fire resistance of SCC beams.

A fomulation for an elevated-temperature tension stiffening model for use in the finite element modeling of SCC floor systems was also developed. Surprisingly, no elevated-temperature tension stiffening model existed in the research literature, despite the established role that tension stiffening plays in the modeling of reinforced concrete members at ambient temperature. First, the energy-based stress-strain model of plain concrete developed by Bažant and Oh (1983) was extended to the elevated-temperature domain by developing an analytical formulation for the temperature-dependence of the fracture energy. Then, the elevated-temperature model was developed based on the modification of the proposed elevated-temperature tension softening model. The applicability and validation of the proposed tension stiffening model was then presented through the numerical analysis of several experimental tests of SCC floor systems exposed to fire.

Using a sequentially-coupled *thermal-structural* analysis procedure, the thermal and structural response of two code compliant SCC floor systems were then examined under various fire types, including a family of traveling fires, two post-flashover fires, and a standard fire exposure. The results of the investigation showed that fire insulations derived from prescriptive approaches might not provide adequate safety under traveling fires. Failure times derived using a critical temperature criterion and a critical displacement criterion both showed that SCC floor systems perform poorly under traveling fires, which was not the case under the two post-flashover fires. The findings demonstrate a large vulnerability with prescriptive fire codes, and strengthens the case for the use of performance-based design in engineering practice.

Chapter 1 Introduction

Typically, large open floor spaces are compartmentalized, with partitions aligning with fire protected floor beams. Spreading of fire and smoke from one compartment to another is avoided through a series of containment strategies [1], which allows a reduction of losses resulting from an uncontrolled spreading fire. In a burning compartment, a condition known as flashover, defined as the simultaneous combustion of all combustible materials, can occur. Such a fire is characterized by its uniform burning and homogenous gas temperatures. Current fire safety codes [2,3], design guides [4,5], and standards [6,7], all revolve around ensuring fire safety during a compartment (i.e., post-flashover) fire.

However, structural innovation and evolving architectural trends are resulting in large open spaces becoming a common feature of modern building design, and moreover there are instances where large open spaces are functionally required (e.g., open office space, exhibition halls, library space, etc.). Fire occurring in a large open-plan compartment does not reach flashover, and instead burns locally and travels across the floor plan (i.e., a traveling fire) [8–10]. Traveling fires are characterized by their high flame temperature, rapid heating rate, long burning duration, and spatially non-uniform temperature within a large open floor plan [9,11,12]. These attributes are not present in a conventional post-flashover fire, which occurs in a floor plan that is compartmentalized and is usually characterized by moderate temperature and heating rate, spatially uniform temperature, and short burning duration. Consequently, a traveling fire is considerably different from a post-flashover fire, which casts doubt on the effectiveness of current fire protection strategies to ensure safety in open-plan compartments. Existing fire safety codes

[2,3], design guides [4,5], and standards [6,7] were developed long before the inception of traveling fires as design fires and currently do not consider such fires explicitly.

Traveling fires have been observed in many incidents around the world. Notable fire incidents include the First Interstate Bank fire in Los Angeles in 1988 [13], the One Meridian Plaza fire in Philadelphia in 1991 [14], the World Trade Center (WTC) Building 7 fire in New York City in 2001 [15], the Windsor Tower fire in Madrid in 2005 [16], the Faculty of Architecture Building fire in TU Delft in Netherland in 2008 [17], and the Plasco Building fire in Tehran, Iran, in 2017 [18]. In all these accidents, the floor systems were not compartmentalized, resulting in traveling fires that moved across the floor plans. Significant structural damage was observed in all these incidents, with partial and complete collapse occurring in several cases. In the United States (U.S.), the potential vulnerability of fire codes to safeguard against traveling fires was highlighted in the collapse investigation of the WTC Building 7 by the National Institute of Standards and Technology (NIST), which revealed that a major factor contributing to the collapse of the building was uncontrolled traveling fires [15]. Despite the historically poor performance of structures under traveling fires, an investigation on the adequacy of prescriptive fire codes to safeguard against traveling fires has not yet been carried out.

To address this deficiency, the dissertation presents a computational study aimed at better understanding the thermal and structural response of steel-concrete composite (SCC) floor systems exposed to traveling fires. Using a sequentially-coupled *thermal-structural* analysis procedure, the thermal and structural response of two SCC floor systems are examined under various fire types, including a family of traveling fires, two post-flashover fires, and a standard fire exposure. The two composite buildings examined are code compliant and adhere to U.S. design codes and standards [2,19,20]. The improved Traveling Fires Methodology [12], which is the latest version of the Traveling Fires Methodology [9,11,21], was used to define the spatial and temporal evolution of the traveling fire exposures.

1.1. Overview and Scope of the Dissertation

To enable better numerical evaluations, several deficiencies involved with the finite element modeling of SCC floor systems are addressed as part of the dissertation work. The first advancement includes the development of an elevated-temperature tension stiffening model, defining the average tensile stress-strain response of concrete in cracked reinforced concrete (RC). Although many tension stiffening models exists [22–35], these models were developed exclusively for the ambient-temperature condition. The model presented in this dissertation specifically accounts for degradation of materials with temperature.

The second advancement includes the development of a formal macro-modeling approach for the finite element modeling of SCC floor systems. A review of the research literature reveals that there are many different modeling approaches for SCC floor beams comprised of beam and shell elements (see for e.g., [36–44]). Particularly, the relative location of the reference (i.e., the location of element nodes) of the beam and shell elements are commonly depicted as being arbitrary and differs among researchers. The variability in the modeling approach stems from a modeling error that has remained largely unreported in the research literature, particularly the incorrect classification of a SCC floor system as a classical eccentrically-stiffened plate problem. In this dissertation, the discrepancies between incorrect modeling assumptions are made apparent for restrained beam applications, and a correct approach is proposed that places the reference plane at the geometric centroid of the beam's connection.

After clarifying the modeling assumptions for SCC floor systems in fire, a finite element model is produced to assess the thermal and mechanical response of two code-compliant SCC structures under various fire exposures. A family of traveling fires is considered, along with more traditional compartment fire models, and failure of the floor system is assessed based on the temperature evolution and the transient deformation response of the floor systems.

In summary, the dissertation is comprised of two main goals: (1) enabling better numerical predictions of SCC floor systems exposed to fire, through improvements of known deficiencies; and (2) improving the understanding of the thermal and structural response of SCC floor systems exposed to real fire exposures, including a post-flashover fire and a traveling fire.

1.2. Organization

The organization of this dissertation follows the manuscript format, in which the dissertation chapters are replaced by manuscripts that will be submitted or have already been submitted to peer-reviewed technical journals. The current chapter, Chapter 1, serves as the introduction and has provided an overview of the included material. The remainder of the dissertation consists of the following chapters.

Chapter 2 is a manuscript entitled “Tension Stiffening Model for Composite Floor Systems Exposed to Fire”, which has been submitted to the *Journal of Structural Engineering*. An elevated-temperature tension stiffening model, defining the average tensile stress-strain response of concrete in cracked reinforced concrete, is developed for the finite element analysis of RC and SCC structures exposed to fire.

Chapter 3 is a manuscript entitled “Analysis of Restrained Composite Beams Exposed to Fire”, which has been accepted for publications in *Engineering Structures*. A numerical analysis of an axially-restrained SCC beam was performed to investigate the influence of various parameters, including the fire type, beam slenderness, load factor, restraint stiffness, and the restraint location.

Chapter 4 is a manuscript entitled "Thermal Response of Steel-Concrete Composite Floor Systems under Traveling Fires", which has been submitted to *Fire Safety Journal*. The adequacy of prescriptive codes to safeguard against traveling fires was investigated by analyzing the thermal response of two SCC floor systems exposed to traveling fires.

Chapter 5 is a manuscript entitled "Structural Response of Steel-Concrete Composite Floor Systems under Traveling Fires", which is ready to submit for review. A computational study was carried out to examine the structural response of two SCC floor system exposed to traveling fires.

Chapter 6 summarizes the findings of this research and discusses directions for future work.

Chapter 2 Tension Stiffening Model for Composite Floor Systems Exposed to Fire

In a finite element analysis of reinforced concrete (RC) where a perfect bond exists between the steel reinforcement and concrete, a tension stiffening model is required as input for concrete to account for actions such as bond slip and tension stiffening. However, for the analysis of structures exposed to fire, an established elevated-temperature tension stiffening model does not exist. Thus, a rational approach for developing an elevated-temperature tension stiffening model is presented. The applicability and validation of the proposed tension stiffening model is presented through the numerical analysis of several experimental fire tests on composite floor slabs. The model was shown to be robust in two major ways: (1) accurate predictions of the structural fire response were obtained; and (2) premature divergence of the static analysis due to localized cracking at elevated temperature was avoided. The latter aspect is significant since it allows a static analysis procedure to be utilized in lieu of a more computationally intensive method such as explicit dynamic analysis.

2.1. Introduction

In finite element modeling of reinforced concrete (RC), an accurate solution requires that bond interaction between nodes of finite elements representing the steel rebar and the surrounding concrete be made via dimensionless spring elements. The spring elements define explicitly the local bond force-slip relation between individual nodes of discrete elements representing steel and concrete and allows bond actions between cracked concrete and steel rebar to be directly modeled. These bond actions include: (1) the bond slippage at the concrete-rebar interface; (2) the load transfer between cracked concrete via traversing reinforcing bars; and (3) the stiffening effect of uncracked concrete situated between primary cracks (i.e., tension stiffening).

The direct modeling of bond action in RC members via dimensionless spring elements is known as the *bond-slip approach*, and was pioneered by researchers in the late 1960s [45,46]. However, this approach is often associated with prohibitively large model assembly and simulation time and is often limited to the analysis of small structural components. Computationally efficient elements such as fiber beam elements and multi-layered shell elements are often preferred when the global response of a complete RC structure is required. However, an explicit force-slip relation between components of either a fiber beam or a layered shell element representing the steel and concrete cannot be defined, as these elements are often formulated by assuming full compatibility of strain between the differing fibers or layers [47–50]. Thus, actions such as bond slip and tension stiffening must be implicitly accounted for through the modification of the material model of plain concrete. The indirect modeling of bond action in RC members via the modification of the material model is known as the *tension stiffening approach*, and was pioneered by Scanlon [22] in the early 1970s.

The focus of this paper lies in the tension stiffening approach, which is exclusively used in a finite element analysis of RC where a perfect bond exists between steel and concrete. In this approach, a tension stiffening model representing the average tensile stress carried by the concrete in a cracked RC member is required as input for concrete to implicitly account for actions such as bond slip and tension stiffening. Tension stiffening arises from the bond between steel and concrete, which allows cracked concrete in RC members to carry tensile stress even after severe cracking has occurred. It should be noted that the tension stiffening response of concrete in cracked RC differs significantly from the tension softening response of plain concrete. A *tension* *softening model* represents the tensile stress-strain behavior of plain concrete, which arises from the gradual release of fracture energy as plain concrete undergoes progressive micro-cracking [51], while a *tension stiffening model* represents the average tensile stress-strain of concrete in cracked RC [52]. Both models are used as input for concrete in a finite element analysis, albeit under different circumstances.

Many tension stiffening models have been developed for use in the finite element analysis of RC members [22–35]. These studies demonstrated that the finite element method can be utilized to predict the response of RC members, provided that a tension stiffening model is utilized. Tension stiffening models have also been developed for use in general analysis procedures of RC members [52–55]. These studies demonstrated that an accurate load-deformation response of RC elements can be derived analytically by considering the tension carried by concrete past cracking (i.e., tension stiffening). Although many tension stiffening models currently exists, they were all developed for the ambient-temperature condition. For the analysis of RC structures exposed to fire, an elevated-temperature tension stiffening model does not currently exist. Basic tensile tests of RC specimens that are often used to understand tension stiffening and produce a tension stiffening model [56–60] have yet to be extended to the elevated temperature domain. Additionally, approaches that provide understanding of tension stiffening from experimental tests of flexural or planar RC members [25,52–54,61] have not been extended to the elevated-temperature domain. This deficiency represents a clear knowledge gap. Efforts put forth by the research community during the 1980s and 1990s to better understand tension stiffening have yet to be extended to the elevated temperature domain, despite the established role that tension stiffening plays in the design, analysis, and modeling of RC members at ambient temperature.

The intent of this paper is not to provide a better understanding of tension stiffening at elevated temperature; this can only be achieved through experimental testing, which is outside the scope of this paper. Rather, a rational approach for developing an elevated-temperature tension stiffening model, for use in finite element analysis of composite floor slabs exposed to fire is presented. The proposed model is simple to implement and comprised of parameters that must be calibrated against experimental fire tests. The parameters account for the fact that all the factors which influence tension stiffening are not explicitly accounted for in the model, and knowledge on how these factors influence the tension stiffening response at elevated temperature is not currently available. The applicability and validation of the proposed tension stiffening model is presented through the numerical analysis of several experimental fire test on composite flexural systems, including: (1) Zhou and Wang's fire test on an axially-restrained composite beam (i.e., *Test CB150*) [62,63]; (2) Lim and Wade's fire test on a two-way bending RC slab (i.e., slab *HD12*) [64,65]; (3) the FRACOF fire test on a partially-protected composite floor assembly [66]; and (4) the Cardington Test no. 3 on a corner compartment fire on a partially-protected composite floor system [67,68]. These tests cover a wide range of conditions and present a valid range of test cases for the validation of the proposed tension stiffening model.

The paper is presented in three stages. First, an elevated-temperature tension softening model of plain concrete is developed, based on the extension of the energy-based stress-strain model of concrete developed by Bažant and Oh [51]. The extension revolves around an analytical formulation for the dependence of the fracture energy of concrete with temperature. Next, an elevated-temperature tension stiffening model for RC is developed based on the modification of the proposed elevated-temperature tension softening model. This approach is justified in that the methodology yields a complete representation of the concrete material models required in a finite element analysis. In the absence of tension stiffening, the methodology produces an elevated-temperature tension softening model. Finally, the proposed tension stiffening model is implemented in the finite element software ABAQUS and used to model various experimental fire tests ranging from two-way bending tests of RC slabs exposed to fire, to full-scale test of composite floor systems exposed to fire. In all test cases, a multi-layered shell element is utilized to represent the floor slab, where steel reinforcement is expressed as a uniformly distributed (i.e., smeared) rebar layer. Because ABAQUS assumes full compatibility of strain among the differing layers of their multi-layered shell element, a tension stiffening model is required as input to implicitly account for actions such as bond slip and tension stiffening.

2.2. Background

2.2.1. Tension Softening of Plain Concrete

Bažant and Oh [51] pioneered a methodology to develop an energy-based tensile stress-strain model for concrete. The proposed fracture theory, called the *crack band theory*, revolves around two major assumptions: (1) fracture in a concrete specimen subjected to tension can be described by a band of densely distributed cracks of width w_c, called the crack band region; and (2) the post-cracking response of plain concrete is assumed to be linearly related with increasing strain/displacement as shown in Figure 2-1. The first assumption allows a strain-displacement relation for plain concrete in tension to be made, while the second assumption allows the fracture properties of plain concrete to be characterized by a limited number of parameters. Both assumptions allow the theory to produce a mesh-dependent tensile stress-strain relation of concrete. Since mesh refinement of concrete does not lead to a converged solution [69,70], objectivity of finite element results is achieved by preserving the correct fracture energy released during micro-cracking.

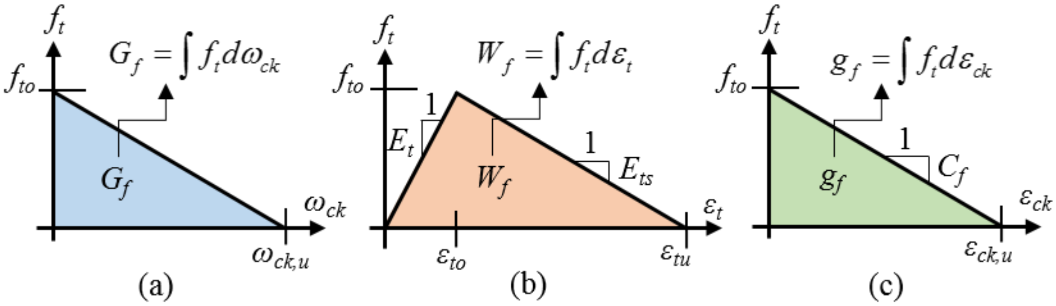

Figure 2-1. Tensile response of plain concrete: (a) stress-cracking strain diagram; (b) stress-cracking strain diagram; and (c) stress-strain diagram.

The crack band theory [51] states that the cracking displacement ω_{ck}, (i.e., the displacement occurring after the tensile strength f_{to} is reached) is related to the cracking strain ε_{ck} (i.e., the additional strain caused by openings of micro-cracks) by the width of the crack band w_c:

$$\varepsilon_{ck} = \frac{\omega_{ck}}{w_c} \tag{2-1}$$

This is justified by the fact that the when the tensile strength f_{to} is reached, the progressive increase of the tensile load causes micro-cracks in the crack band region to open wider, while simultaneously, the portion of the concrete specimen outside of the crack band unloads elastically. Thus, the progressive increase of strain past the cracking strain ε_{to} (i.e., strain at which the tensile strength f_{to} is reached) occurs exclusively in the crack band. Using Equation (2-1), it can be shown that the fracture energy of concrete G_f, which is defined as the area under the post-cracking stress-displacement curve in Figure 2-1(a), is related to the fracture energy density g_f, which is defined as the area under the stress-cracking strain diagram in Figure 2-1(b):

$$G_f = w_c g_f \tag{2-2}$$

Cracking strain ε_{ck} can also be defined as the total tensile strain ε_t minus the elastic strain corresponding to the undamaged material, i.e., $\varepsilon_{ck} = \varepsilon_t - f_t/E_t$. Using this expression, it can be shown that $\varepsilon_{ck,u} = \varepsilon_{tu}$, where $\varepsilon_{ck,u}$ and ε_{tu} are the ultimate tensile strain of the stress-cracking strain in Figure 2-1(b) and stress-strain diagram in Figure 2-1(c), respectively. Since $\varepsilon_{ck,u} = \varepsilon_{tu}$, the area under the total stress-strain diagram in Figure 2-1(c), expressed as W_f, is equivalent to the area under the stress-cracking strain diagram in Figure 2-1(b), expressed as g_f. Using Equation (2-2), G_f can be related to the area under the total stress-strain diagram W_f, by the width of the crack band, i.e., $G_f = w_c W_f$. Using this relationship and assuming a linear post-cracking response, an expression for the ultimate strain ε_{tu} can be derived from known tensile properties G_f and f_{to}, and a complete representation of the stress-strain diagram in Figure 2-1(c) can be constructed.

In the finite element method, the width of the crack band w_c is taken as a characteristic length l_n of the finite element, i.e., $w_c = l_n$. The characteristic length l_n corresponds to a representative dimension of the mesh size h [51,71–75]. The characteristic length depends on many factors, such as the element type, element size, element shape, and the integration scheme. In this study, the characteristic length is taken as $l_n = \alpha_h h$, where α_h is a modification factor equal to $\sqrt{2}$ for linear elements and equal to 1 for quadratic elements [71].

Finally, for concrete with tensile properties G_f and f_{to}, the ultimate strain ε_{tu} can be derived as shown in Equation (2-3). The ultimate strain ε_{tu} is an element-related material parameter, since it is derived from both material properties (i.e., f_{to}, and G_f) and element properties (i.e., h and α_h).

$$\varepsilon_{tu} = \frac{2G_f}{f_{to}\alpha_h h} \tag{2-3}$$

2.2.2. Tension Stiffening of Reinforced Concrete (RC)

Tension stiffening arises from the bond between steel reinforcement and concrete, which allows concrete in cracked RC to carry tension even after severe cracking has occurred. To describe tension stiffening, consider a RC specimen subjected to a tensile force P. The complete tensile response of this RC specimen is shown in Figure 2-2, along with the tensile response of a steel rebar. As the load P is increased, the tensile strength f_{to} is reached within the concrete and the first set of external primary cracks are developed at a tensile load P_o. The location of the primary cracks are dictated by the development length ℓ_d of the member. At this instance, the intact concrete between the primary cracks can still carry tensile stress due to the local bond existing between the concrete and steel. The contribution of tensile stiffness by the uncracked concrete between primary cracks is formally known as tension stiffening.

Under increasing load P, additional primary cracks continue to form at finite spacings based on the length of the remaining intact concrete and the development length ℓ_d. The overall tension carried by the concrete (i.e., tension stiffening) continues to decrease as more primary cracks develop. Once the crack stabilization point has been reached, further increase of the load P causes internal secondary cracks to develop near the reinforcement. The formation of secondary cracks weakens the bond between the concrete and reinforcement, further reducing the tension carried by concrete. The reduction of tension stiffening continues until yielding of the steel occurs. At this point, the response of the RC specimen follows that of the steel rebar, since the reinforcement is not able to transmit a force greater than the yield force across cracks. Similar working principles occur in other RC elements such as RC beams and RC slabs, where severely cracked concrete contributes to the stiffness of the member.

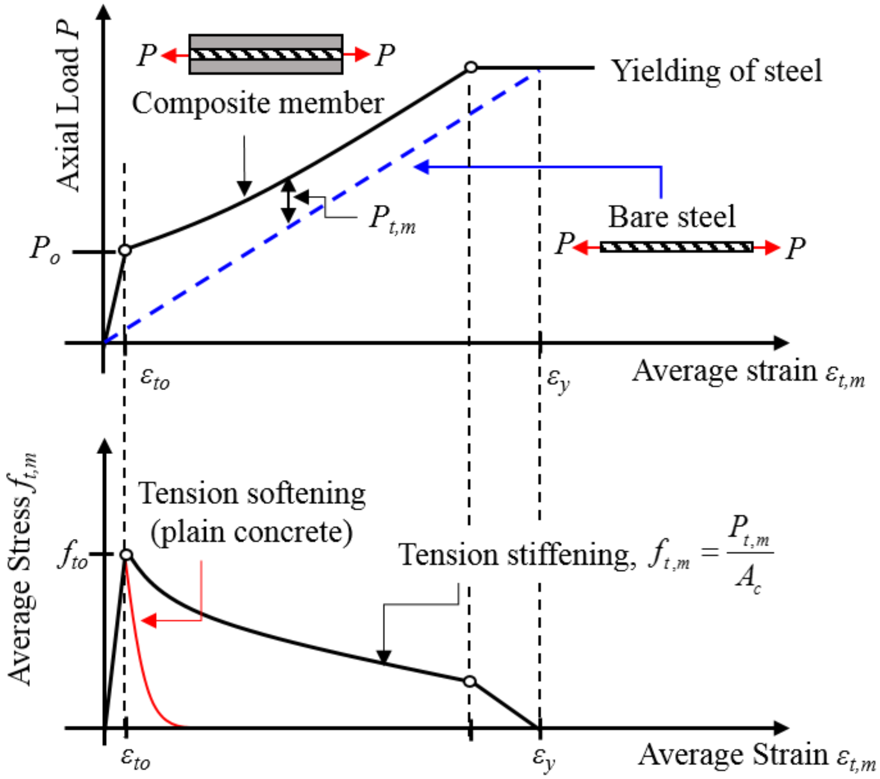

Figure 2-2. Tensile response of RC member and steel rebar (upper image), and the average stress-strain of concrete in RC compared to the stress-strain of plain concrete (lower image).

In a finite element model where a perfect bond exists between steel and concrete, the average tensile stress carried by concrete $f_{t,m}$ as a function of the total strain of the RC member $\varepsilon_{t,m}$, is required as input for concrete to account for actions such as bond slip and tension stiffening. The subscript *m* stands for mean (or average) and is used to distinguish between average stress/strain and conventional stress/strain. Revisiting Figure 2-2, the average tensile stress carried by concrete $f_{t,m}$ can be obtained by dividing the average tensile load carried by the concrete $P_{t,m}$ (see Figure 2-2) by the concrete area in tension A_c [58]. The average stress-strain curve of concrete (i.e., $f_{t,m} - \varepsilon_{t,m}$) defines the tensile stress-strain law of concrete in cracked RC, and differs significantly from that of plain concrete (i.e., $f_t - \varepsilon_t$) as shown in Figure 2-2. Although the post-cracking stage of a tension stiffening curve is described by a softening curve, the term “stiffening” is used to refer to the contribution of tensile stiffness generated by the uncracked concrete between primary cracks.

Although many tension stiffening models exists [22–35], these models were all developed for the ambient-temperature condition. For the analysis of RC structures exposed to fire, an elevated-temperature tension stiffening model does not currently exist. The authors examined well over a hundred research articles and Ph.D. dissertations in which a layered shell element was utilized to model a RC floor slab exposed to fire. Only five articles/dissertations disclosed the tension stiffening model utilized. A review of those articles/dissertations is given below.

Terro [76] investigated the response of RC slabs exposed to fire using the finite element software STRUCT. The tension stiffening curve was expressed using a linear model with an ultimate strain of $\varepsilon_{tu,m}$ = 0.004 (approximately twice the yield strain of steel reinforcement of ε_y = 0.002). No sensitivity analysis was carried out to determine whether a lower $\varepsilon_{tu,m}$ could have been used. Nonetheless, the model provided accurate prediction of the test data examined by Terro.

Huang *et al.* [77] examined the response of RC slabs exposed to fire using the finite element software VULCAN. The ambient-temperature tension stiffening model developed by Vecchio and Collins [53] was utilized. This model is simple and depends only on the tensile strength f_{to}. To include temperature-dependence, the temperature-dependent model of f_{to} from Eurocode 2 Part 1-2 [78] was utilized. Huang *et al.* [77] showed that accurate prediction of test data could be achieved when extending the model by Vecchio and Collins [53] to elevated temperatures.

Deeny [79] examined the response composite floor slabs exposed fire using finite element software ABAQUS. The ambient-temperature tension stiffening model proposed by ABAQUS [80] was utilized. ABAQUS uses a linear tension stiffening model with an ultimate strain $\varepsilon_{tu,m} = \varepsilon_{to} \times TS$, where ε_{to} is the strain corresponding to the tensile strength f_{to} and *TS* is a tension stiffening factor which must be calibrated through a sensitivity analysis. Various values for TS ranging from $TS = 0$ to $TS = 400$ were examined, with a TS factor of 10 chosen for the analyses.

Law [81] examined the response of a complete RC floor exposed to fire using finite element software ABAQUS. Tension stiffening was defined using the fracture energy concept available in ABAQUS. To define the tension stiffening curve, Law [81] used an artificially high value of G_f as input for concrete. Through a sensitivity analysis, a fracture energy of $G_f = 1085$ N/m (approximately 9 times the value of 120 N/m for concrete with a compressive strength of 40 MPa) was deemed to be appropriate.

Florides and Cashell [82] examined the response of composite floor slabs exposed to fire using finite element software ABAQUS. The ambient-temperature tension stiffening model developed by Belarbi and Hsu [52] was utilized. This model is simple and depends only on f_{to}. It is not clear whether temperature-dependence of f_{to} was defined. No validation was presented to show the accuracy of using the model by Belarbi and Hsu [52] outside of ambient-temperature.

2.3. Elevated-Temperature Tension Softening Model

The material model for concrete proposed by Bažant and Oh [51] is extended to the elevated temperature domain by: (1) assuming that temperature does not influence the shape of the model (i.e., a linear post-cracking response is adequate at all temperatures); and (2) using an appropriate temperature-reduction factor to define the peak tensile strength $f_{to,T}$ and the tensile fracture energy $G_{f,T}$ at an arbitrary temperature T. An expression for the ultimate strain $\varepsilon_{tu,T}$ can be derived as shown in Equation (2-4).

$$\varepsilon_{tu,T} = \frac{2G_{f,T}}{f_{to,T}\alpha_h h} \tag{2-4}$$

Here, $f_{to,T} = \beta_{fto} f_{to,20\text{°C}}$ and $G_{f,T} = \beta_{Gf} G_{f,20\text{°C}}$, where β_{fto} and β_{Gf} are the temperature-reduction factor for f_{to} and G_f, respectively. Several temperature-dependent models for β_{fto} can be found in the research literature [78,83]. However, there are limited test data on the temperature effects of the fracture energy G_f. In general, G_f must be determined using a direct tensile test or an indirect three-point bend test on a notched beam [84]. The extension of these tests to the elevated temperature domain has seldom been carried out. To the authors' knowledge, only two tests of a three-point bend test on a notched beam have been performed at elevated temperatures. Bažant and Prat 85] examined the temperature-dependency of G_f for normal strength concrete (NSC) up to a temperature of 200 °C, while Zhang and Bićanić [85] examined the temperature-dependency of G_f for high performance concrete (HPC) up to a temperature of 500 °C. An examination of the test data reveals that a conclusive model for β_{Gf} cannot be generated as shown in Figure 2-3. The discrepancy between the two results shows that additional testing is required to establish the dependency of G_f with temperature.

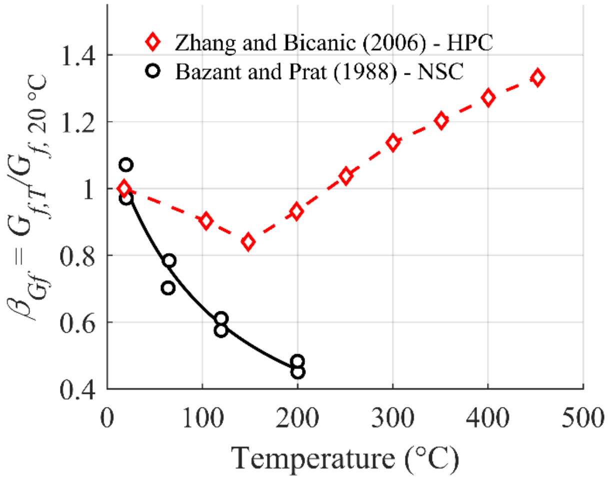

Figure 2-3: Temperature-dependence of the fracture energy G_f of normal strength concrete [86] and high-performance concrete [85].

Using an analytical procedure, a temperature-dependent model for G_f is developed herein. The fracture energy G_f is defined as the area under the stress-cracking displacement curve shown in Figure 2-1(a). Assuming a linear loss of strength after cracking, an expression for G_f at a temperature T can be defined:

$$G_{f,T} = \frac{1}{2} f_{to,T} \omega_{ck,u}^{T} \tag{2-5}$$

where $\omega_{ck,u}$ is the ultimate cracking displacement, where tensile stress can no longer be transferred across the crack band region. Equation (2-5) can be expanded using the temperature-reduction factors for f_{to} and $\omega_{ck,u}$, that is $f_{to,T} = \beta_{fto} f_{to,20°C}$ and $\omega_{ck,u}^{T} = \beta_{\omega ck,u} \omega_{ck,u}^{20°C}$. Rearranging the terms yields:

$$G_{f,T} = \left(\tfrac{1}{2} f_{to,20°C} \omega_{ck,u}^{20°C}\right)\left(\beta_{fto} \beta_{\omega ck,u}\right) \tag{2-6}$$

The expression in the first parentheses is the fracture energy $G_{f,20°C}$, while the expression in the second parentheses is the reduction factor β_{Gf}. Thus, the temperature dependency of the G_f depends on the temperature-dependency of f_{to} and the temperature-dependency of $\omega_{ck,u}$:

$$\beta_{Gf} = \beta_{fto} \beta_{\omega ck,u} \tag{2-7}$$

Because of the limited test data on the tensile response of concrete, a model for the temperature-dependency of $\omega_{ck,u}$ does not exist. However, it is reasonable to assume that $\omega_{ck,u}$ decreases linearly from T = 20 °C up until the temperature at which tensile strength diminishes to zero (i.e., T = 600 °C [78]). An alternative approach is to assume that $\omega_{ck,u}$ is constant from T = 20 °C to T = 100 °C, and then decreases linearly with temperature up to T = 600 °C, which is the temperature-dependent form followed by the peak strength f_{to}. However, the former assumption is more conservative, and is used instead. Using the reduction factor of f_{to} from Eurocode 2 Part 1-2 [78] and the temperature-dependency of $\omega_{ck,u}$ assumed herein, an analytical model for β_{Gf} can be constructed from Equation (2-7) as shown in Table 2-1. Figure 2-4 shows a comparison of the derived β_{Gf} model with the available test data from Bažant and Prat [86] and Zhang and Bićanić [85]. Due to the discrepancy of the two data sets, it is not possible to validate the proposed β_{Gf} model. The validation is left as an endeavor to future researchers as test data becomes available.

Table 2-1. Temperature-dependency of the peak tensile strength f_{to}, ultimate cracking displacement $\omega_{ck,u}$, and fracture energy G_f.

Temperature (° C)	Peak Tensile Strength, β_{fto} [78]	Ultimate Cracking Displacement, $\beta_{\omega ck,u}$	Tensile Fracture Energy, β_{Gf} (Equation (2-7))
20	1.00	1.00	1.00
100	1.00	0.86	0.86
200	0.80	0.69	0.55
300	0.60	0.52	0.31
400	0.40	0.35	0.14
500	0.20	0.17	0.03
600	0.00	0.00	0.00

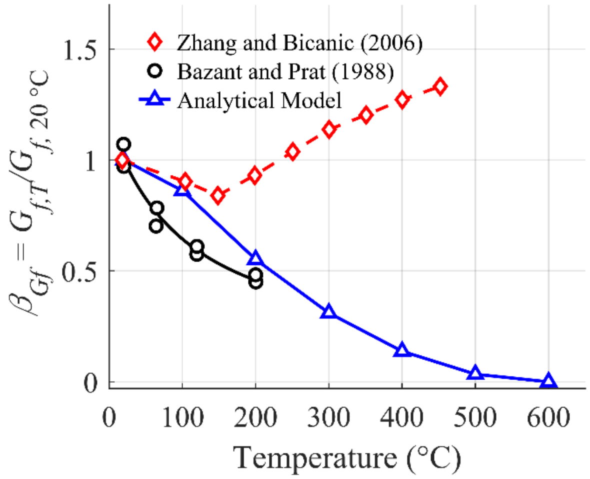

Figure 2-4. Derived analytical model for β_{Gf} compared with available test data from Bažant and Prat [86] and Zhang and Bićanić [85].

2.4. Elevated-Temperature Tension Stiffening Model

A tension stiffening model comprises of two parts: (1) an elastic portion, which mimics the elastic portion of a tension softening curve; and (2) a post-peak portion, which implicitly includes the effects of bond slip and tension stiffening. In the proposed tension stiffening model, the pre-peak response is approximated with a linear ascending branch with slope equal to the elastic modulus E_t up to the tensile strength f_{to} as shown in Figure 2-5. Due to the absence of test data of tension stiffening at elevated temperature, the post-peak response is taken as a modified version of the softening response of the tension softening curve. After f_{to} is reached, stress reduces linearly to an ultimate strain equal to $\varepsilon_{tu,m} = \varepsilon_{tu} \times TS$, where TS is the tension stiffening factor which controls the ductility of the tension stiffening model, relative to the tension softening model. To account for residual tension, a residual strength of $f_{tu,m} = K_{res} f_{to}$ is prescribed, where K_{res} is the residual stiffness factor. The parameters TS and K_{res} controls the extent of tension stiffening included in the model, by modifying the tension softening curve. In the absence of tensile reinforcement (i.e., $TS = 1$ and $K_{res} = 0.01$), the model produces the tension softening model presented in Figure 2-1(a). A complete representation of the proposed tension stiffening model is shown in Figure 2-5. Temperature-dependence is included in the model by utilizing temperature-reduction factors for the elastic modulus β_{Et}, the tensile strength β_{fto}, and the fracture energy β_{Gf}.

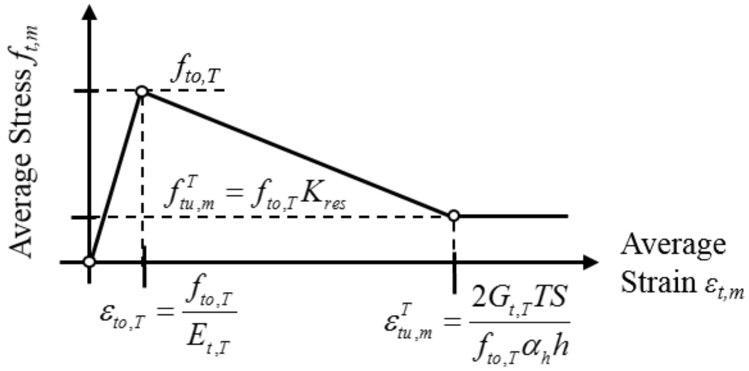

Figure 2-5. Proposed elevated-temperature tension stiffening model.

Central to the proposed model is the need for a sensitivity analysis to determine the appropriate values of TS and K_{res}. These parameters account for the fact that all the factors which influence tension stiffening, such as bond properties, rebar distribution, rebar diameter, etc., are not explicitly accounted for, and knowledge on how these factors influence the tension stiffening response at elevated temperature is not currently available. There may also be additional parameters that influence tension stiffening at elevated temperatures such as the fire heating rate, heating duration, etc., which have yet to be revealed. For simplicity, TS and K_{res} are assumed temperature-independent and are calibrated using test data of structures exposed to fire, which is currently the only form of test data available for the calibration process. The decision to take TS and K_{res} as temperature-independent allows for a relatively straightforward calibration of these parameters to be made, using test data of structures exposed to fire. Additionally the temperature-independent assumption of TS and K_{res} is reasonable for several reasons: (1) temperature independent parameters TS and K_{res} can be used to predict the fire response of composite floor systems with great accuracy as will be shown later in the paper; and (2) direct tension tests of RC specimens at steady-state elevated-temperatures are required to determine the temperature-dependence of TS and K_{res}, however, these tests are not yet available in the research literature. As these tests become available, better representations of the parameter TS and K_{res} can be made.

2.4.1. Mesh Size Restrictions with Temperature

The energy-based material model proposed by Bažant and Oh [51] produces a mesh-dependent tensile stress-strain relation for concrete. Theoretically, a mesh size h can be selected so that the computed ultimate strain ε_{tu} is smaller than the strain at which the tensile strength occurs ε_{to}, i.e., $\varepsilon_{tu} \leq \varepsilon_{to}$. This scenario is called *snap-back* and is a major cause of numerical instability in a static analysis procedures such as the Newton-Raphson solver [69,70]. To avoid snap-back, the following limit is imposed:

$$\varepsilon_{tu} > \varepsilon_{to} \tag{2-8}$$

Using the expression for ε_{tu} in Equation (2-3) and Hooke's law to define ε_{to} (i.e., $\varepsilon_{to} = f_{to}/E_t$), an upper limit on the mesh size h can be derived to prevent snap-back [51]:

$$h < \frac{2G_f E_t}{\left(f_{to}\right)^2 \alpha_h} \tag{2-9}$$

Likewise, snap-back is also an issue in the proposed tension stiffening model since the ultimate strain $\varepsilon_{tu,m}$ is a function of the mesh size h. By imposing $\varepsilon_{tu,m} > \varepsilon_{to}$, an upper limit on the mesh size h is derived to prevent snap-back:

$$h < \frac{2G_{f,T} E_{t,T} TS}{\left(f_{to,T}\right)^2 \alpha_h} \tag{2-10}$$

The right-hand side of Equation (2-10) represents the maximum mesh size $h_{\max}^{T}$ required to prevent snap-back at temperature T. Using the reduction factors β_{Gf}, β_{Et}, and β_{fto}, to define $G_{f,T}$, $E_{t,T}$, and f_{toT}, respectively, a refined expression for $h_{\max}^{T}$ can be produced:

$$h_{\max}^{T} = \left(\frac{2G_{f,20\,^{\circ}C} E_{t,20\,^{\circ}C} TS}{\left(f_{to,20\,^{\circ}C}\right)^2 \alpha_h}\right) \times \left(\frac{\beta_{Gf}\beta_{Et}}{\left(\beta_{fto}\right)^2}\right) \tag{2-11}$$

Equation (2-11) can be furthered simplified as:

$$h_{\max}^{T} = h_{\max}^{20\,^{\circ}C} \times \beta_{h}^{\max} \tag{2-12}$$

where $h_{\max}^{20\,^{\circ}C}$ is the maximum mesh size at ambient-temperature and $\beta_{h}^{\max}$ is the temperature-reduction factor of $h_{\max}^{20\,^{\circ}C}$ to prevent snap-back. The final form of the upper limit on mesh size h to prevent snap-back at all temperatures in the domain of interest Ω_T is shown in Equation (2-13).

$$h < h_{\max}^{T} \qquad \forall\, \boldsymbol{T} \in \boldsymbol{\Omega}_{T} \tag{2-13}$$

When selecting a mesh size, the upper limit in Equation (2-13) must be satisfied at all temperatures in the domain of interest Ω_T. As a demonstration, an example with the following concrete properties is examined: f_{to} = 34.5 MPa, G_f = 138 N/m, and E_t = 20,600 MPa. The temperature-dependence of $E_{t,T}$, and f_{toT}, i.e., β_{Et}, and β_{fto}, are taken from Eurocode 2 Part 1-2 [78], while the temperature-dependence of the fracture energy G_f is taken as $\beta_{Gf} = \beta_{fto}\beta_{\omega ck,u}$. Figure 2-6(a) shows the maximum mesh size $h_{\max}^{T}$ as a function of temperature for a tension stiffening factor of TS = 5. The temperature domain of Ω_T is taken from T = 20 °C up until the temperature at which tensile strength of concrete diminishes to zero, which occurs at T = 600 °C [78]. The critical mesh size h_{max}, defined as the smallest $h_{\max}^{T}$ in the temperature domain Ω_T, corresponds to h_{max} = 180 mm as shown in Figure 2-6(a). Thus, to avoid snap-back response, a mesh size smaller than 180 mm should be selected. To demonstrate snap-back response, the tension stiffening curves corresponding to a mesh size of h = 250 mm are shown in Figure 2-6(b). In the abscissa, average strain is normalized by the yield strain of steel reinforcement at ambient temperature ε_y = 0.002, while in the ordinate, average stress is normalized by the peak tensile strength at ambient temperature f_{to} = 34.5 MPa. A mesh size of 250 mm violates the upper mesh limit for temperature T = 500 ºC, and consequently, snap-back response is observed in the tension stiffening curve corresponding to T = 500 ºC. Finally, Figure 2-6(c) shows h_{max} as a function of TS. As will be shown, the value of TS can vary between TS = 5 and TS = 50, and is a variable that is chosen based on a sensitivity analysis. An increase of TS increases the critical mesh size h_{max} and acts to alleviate the snap-back issue. As a final note, the mesh size selected should also provide a converged solution, which can only be assessed using a mesh sensitivity analysis.

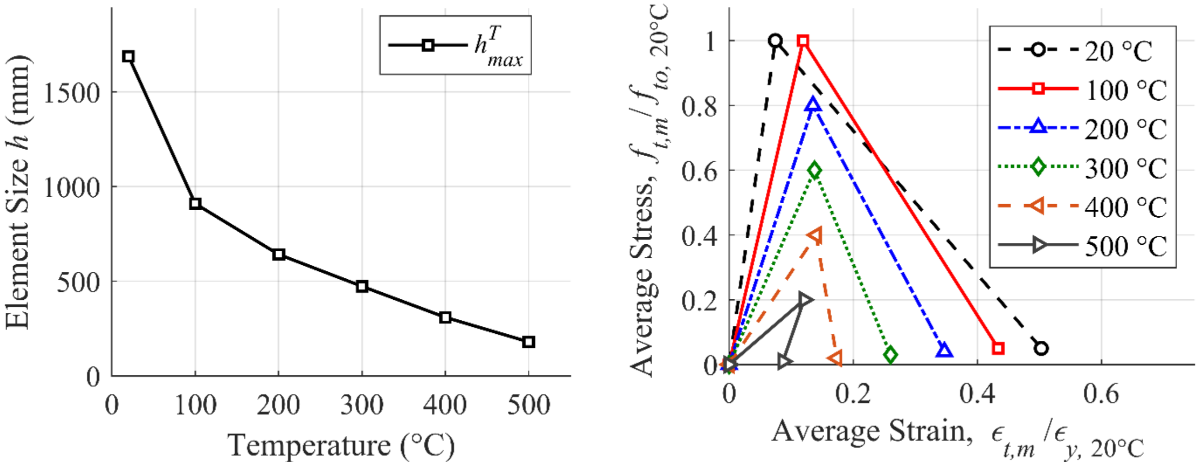

(a) Mesh size restrictions for *TS* = 5

(b) Tension stiffening curves for *h* = 250 mm

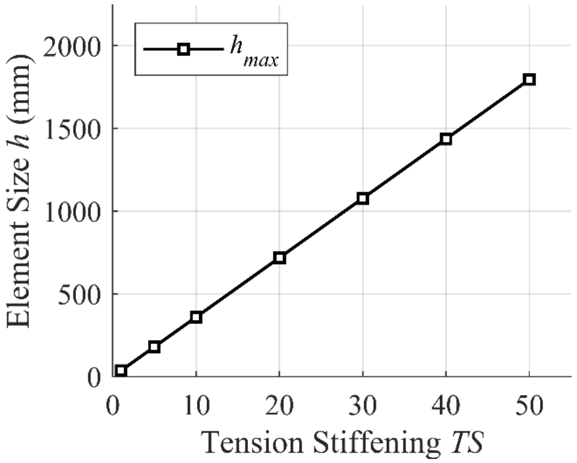

(c) Critical mesh size h_{max} as a function of *TS*

Figure 2-6. Mesh size restrictions: (a) Maximum mesh size $h^T_{\max}$ as a function of temperature for a tension stiffening factor of *TS* = 5; (b) Tension stiffening curves corresponding to a mesh size of *h* = 250 mm showing snap-back response at *T* = 500 ºC; and (c) Critical mesh size h_{max} as a function of the tension stiffening factor *TS*.

2.5. Analysis Overview

A sensitivity analyses is carried out for each test case in order to calibrate the parameters *TS* and K_{res}. The tension stiffening factor *TS* is varied at values of 1, 5, 10, 20, 30, 40, and 50, while the residual stiffness factor K_{res} is varied at values of 0.01, 0.1, and 0.2. Because of the limitations of test data, β_{Gf} is also treated as a variable. Two models are examined, including β_{Gf} = 1 and β_{Gf} =

$\beta_{fto}\beta_{\omega ck,u}$. The final selection of TS, K_{res}, and β_{Gf} for each test case is based on the accuracy of the results and the ability of the static analysis to reach adequate convergence.

2.6. Methodology

Each test case was modeled using an assembly of beam and shell elements using the finite element software ABAQUS [80]. A 4-node quadrilateral shell element *S4R* was used to model the composite slab, while a 2-node Timoshenko beam element *B31* was used to model steel beams and columns. For test cases with floor beams, full composite action was assumed by imposing a rigid coupling constraint between to the aligning nodes of the shell and beam elements.

Both geometric and material nonlinearities were included in the analyses. The metal plasticity model in ABAQUS was used to define the inelastic response of steel, while the damaged plasticity model was used to represent the inelastic response of concrete. Temperature dependence of steel and concrete were defined using the stress-strain-temperature model in Eurocode 3 Part 1-2 [87] and Eurocode 2 Part 1-2 [78], respectively. Finally, thermal expansion was defined using the thermal elongation model of steel and concrete in Eurocode 3 Part 1-2 [87] and Eurocode 2 Part 1-2 [78], respectively

The tensile strength of concrete f_{to} was taken as a tenth of the compressive strength f_{co}, with temperature-dependency defined using the β_{fto} model in Eurocode 2 Part 1-2 [78]. The elastic modulus in tension E_t was taken as the elastic modulus in compression E_c, where E_c was defined as the secant modulus corresponding to $0.33f_{co}$. At ambient-temperature, G_f was defined using the model in the Euro-International Committee for Concrete and International Federation for Prestressing (CEB-FIP) Model Code [88]. For normal weight concrete (NWC), the CEB-FIP Model Code [88] provides an expression for G_f which depends on f_{co} as shown in Equation (2-14).

For light-weight concrete (LWC), the CEB-FIP Model Code [88] provides an expression for G_f which depends on f_{to} as shown in Equation (2-15), where $G_{f,A}$ = 24 N/m for lightweight aggregate with normal weight sand and $G_{f,A}$ = 0 N/m for lightweight aggregate with lightweight sand.

$$G_f = 73\left(f_{co}\right)^{0.18} \tag{2-14}$$

$$G_f = G_{f,A} + 16 f_{to} \tag{2-15}$$

Loads are applied sequentially during each analysis: gravity loads are applied first followed by thermal loads, which are applied as predefined nodal temperature fields. The solution to all analyses were sought using a static solution procedure available in ABAQUS. No viscous damping was introduced in the analysis steps to overcome convergence issues associated with concrete cracking. Also, artificial viscous damping was not utilized, since it did not improve the convergence of the analysis. Instead, tension stiffening was used to overcome convergence issues associated with localized concrete cracking. However, tension stiffening was maintained at a reasonable value as to not artificially increase the stiffness of the structure.

The mesh size selected for each test case was influenced by two factors: (1) accuracy of the solution, which was determined via a mesh sensitivity analysis; and (2) appropriateness of the mesh size to prevent snap-back response, which was prevented by ensuring that the upper limit on the mesh size provided by Equation (2-13) was satisfied in each test case. To eliminate potential bias of concrete cracking due to element shape [51], approximately square shell elements were used to mesh the slab of each test case.

2.7. Results

2.7.1. Zhou and Wang's Composite Beam Test

Li and Wang [89] reported a fire test on an axially-restrained composite beam (i.e., *Test CB150*), which was carried out in a joint effort by Zhou [62] and Wang [63]. The test consists of a composite beam restrained axially by a steel frame as shown in Figure 2-7. The span of the beam between the supports was subjected to heating from a furnace, which closely followed the ISO 834 standard fire as shown in Figure 2-7(b). The floor slab consists of a 74 mm thick C30 NWC with a compressive strength of f_{co} = 43.1 MPa, cast on a 76 mm steel decking. The slab was reinforced with 12 mm bars, with a yield strength of F_y = 270 MPa, spaced at 135 mm in both directions. The floor slab acted compositely with a grade Q235 H200x100x5.5x8 steel beam, having a yield strength of F_y = 271 MPa. Two concentrated loads of magnitude P = 40 kN were applied to the beam as shown in Figure 2-7.

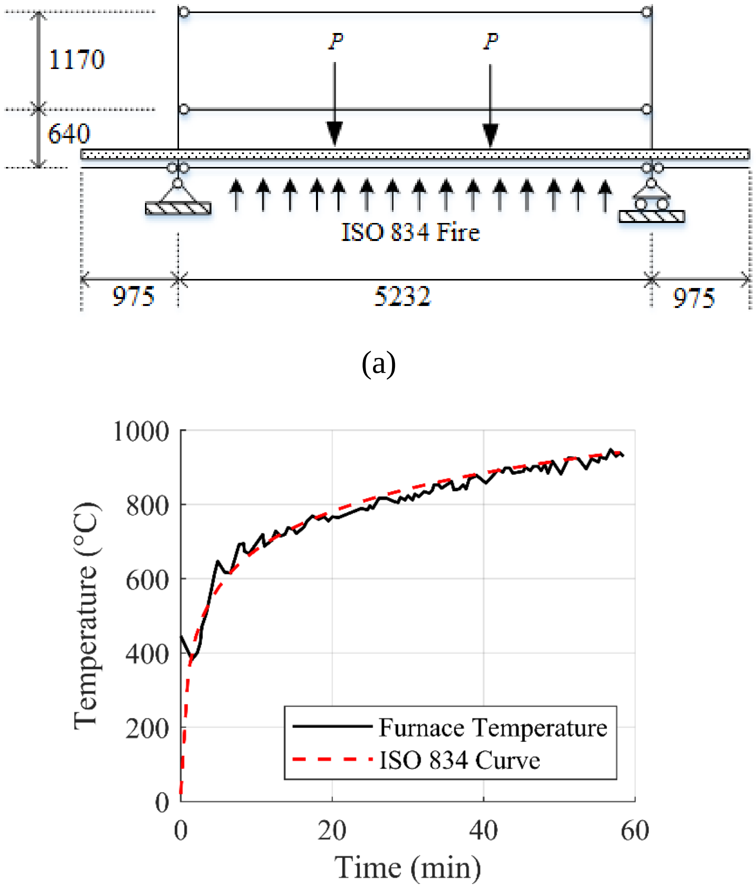

(a)

(b)

Figure 2-7. Test CB150 [62,63]: (a) Test configuration of Test CB150. All dimensions in [mm]; (b) Temperature-time curve of the furnace.

In the structural model, a mesh size of 367 mm x 338 mm was used for shell elements, while a mesh size of 367 mm was used for beam elements. The appropriateness of the mesh size to prevent snap-back response was verified against the upper limit on the mesh size provided by Equation (2-13) and shown in Figure 2-8(a). The appropriateness of the mesh to provide a converged solution was determined via a mesh sensitivity analyses as shown below in Figure 2-8(b). The temperature of the steel beam and slab measured during testing were passed directly to the structural model as predefine temperature fields. For brevity, the predefine temperature fields are not presented in this paper, and can be found in the accompanying reference [62,63,90]. The beam-end connections were idealized as perfectly pinned.

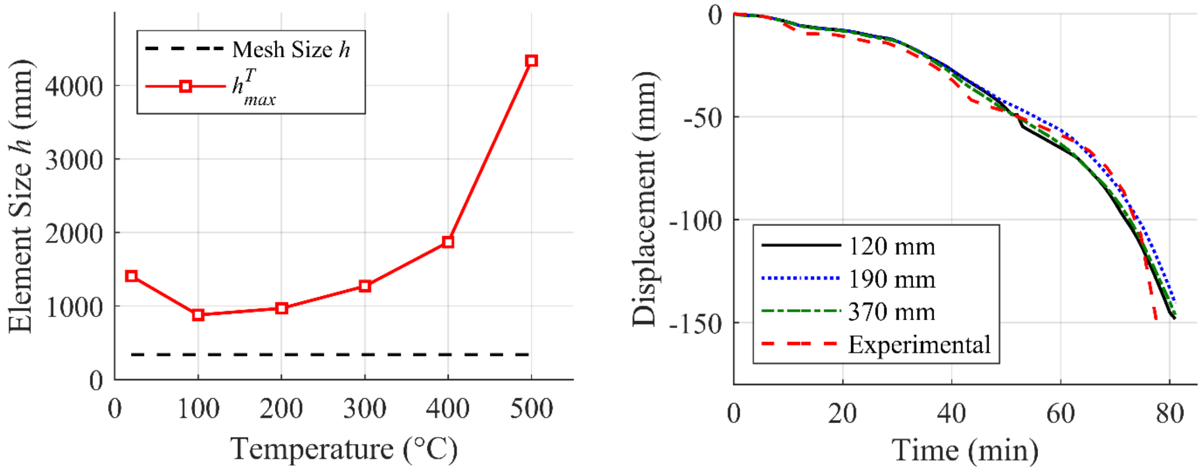

(a) Snap-back response analysis

(b) Mesh sensitivity analysis

Figure 2-8. Mesh size check: (a) Snap-back response analysis; and (b) Mesh sensitivity analysis.

The results of the sensitivity analyses are shown in Figure 2-9 through Figure 2-11: Figure 2-9 shows the influence of β_{Gf}; Figure 2-10 shows the influence of parameter K_{res}; and Figure 2-11 shows the influence of parameter *TS*, each on the predicted response, which is taken as the mid-span displacement of the beam. Only a subset of the results is shown for brevity. Figure 2-9 shows that the displacement-time history is independent of the β_{Gf} model utilized. This objectivity is present for any combination of *TS* and K_{res} used. This aligns with the fact that the tension softening response of plain concrete (or equivalently G_f) has a small influence on the tension stiffening response of cracked RC [59]. Consequently, the temperature-dependence of G_f also has a small influence on the tension stiffening response. Figure 2-10 shows that the structural response is independent of the parameter K_{res}. More specifically, an increase or decrease of K_{res} does not alter the stiffness of the structure. However, for analyses with low *TS* values, where convergence issues were observed, an increase of K_{res} was shown to improve the convergence without altering the response. In Figure 2-10(a), for *TS* = 5 and β_{Gf} = 1, the last converged times of the analysis are observed to increase with increasing values of K_{res}: (1) t_{end} = 56 min for K_{res} = 0.01; (2) t_{end} = 58 min for K_{res} = 0.1; and (2) t_{end} = 82 min for K_{res} = 0.2. Better overall convergence with increasing K_{res} is also observed in Figure 2-11. Figure 2-11 shows the influence of parameter TS on the structural response for various combinations of K_{res} for $\beta_{Gf} = 1$. Except for TS = 1, all the analyses in Figure 2-11(c) run to completion when using K_{res} = 0.2, which shows that a higher K_{res} leads to better convergence of the analysis. The parameter K_{res} acts to improve the convergence of the static analysis, without altering the stiffness of the structure.

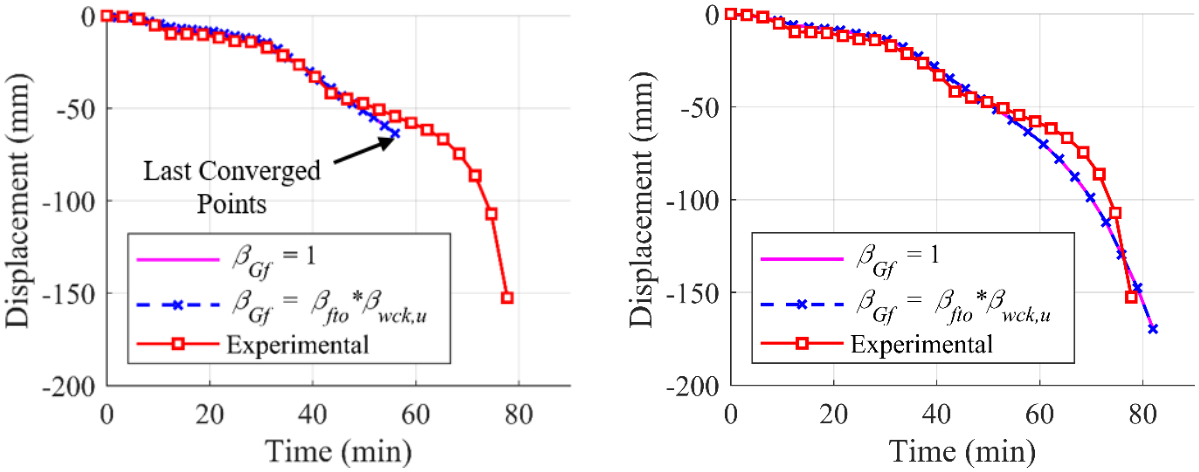

(a) $TS = 5$, $K_{res} = 0.01$ (b) $TS = 30$, $K_{res} = 0.01$

Figure 2-9. Influence of the β_{Gf} model on the mid-span displacement for Test CB150 using: (a) TS = 5, K_{res} = 0.01; and (b) TS = 30, K_{res} = 0.01.

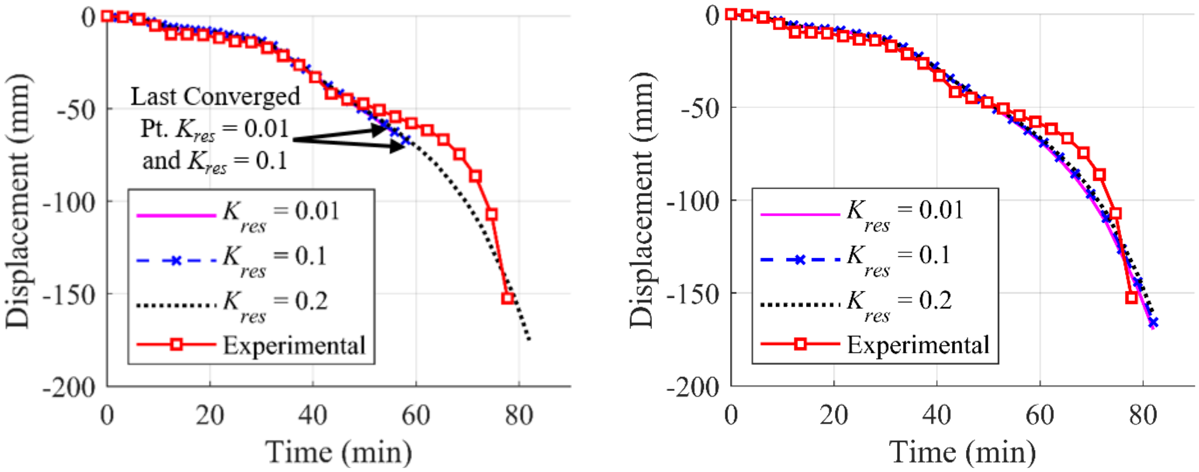

(a) β_{Gf} = 1, *TS* = 5 (b) β_{Gf} = 1, *TS* = 30

Figure 2-10. Influence of K_{res} on the mid-span displacement for Test CB150 using: (a) β_{Gf} = 1, *TS* = 5; and (b) β_{Gf} = 1, *TS* = 30.

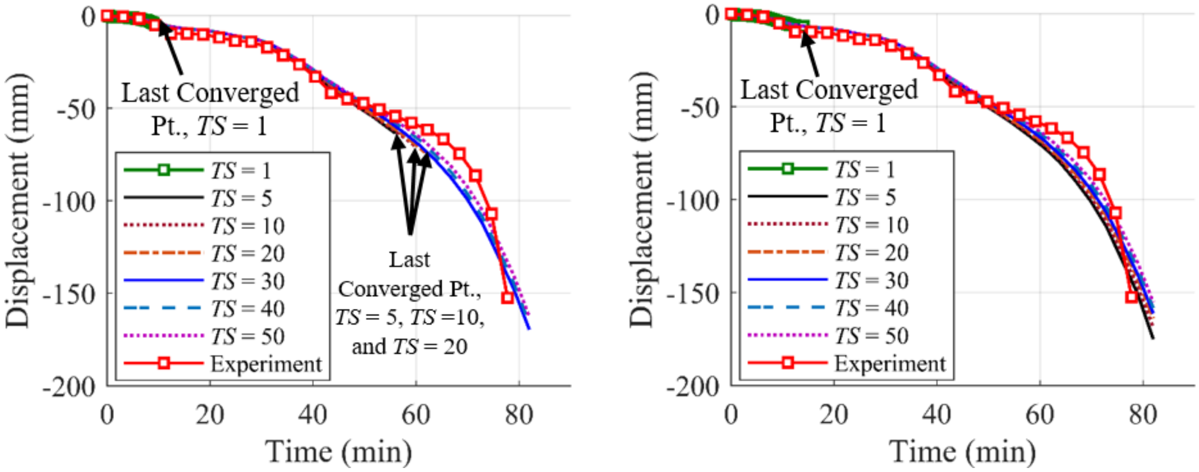

(a) β_{Gf} = 1, K_{res} = 0.01 (b) β_{Gf} = 1, K_{res} = 0.2

Figure 2-11. Influence of *TS* for on the mid-span displacement of Test CB150 using: (a) β_{Gf} = 1, K_{res} = 0.01; and (c) β_{Gf} = 1, K_{res} = 0.2.

Figure 2-11 shows that the response is dependent on *TS*. As *TS* is increased, the displacement-time history is increased. The parameter *TS* acts to increase the overall stiffness of the structure. This aligns with the common knowledge that tension stiffening acts to stiffen the response of a RC member. The parameter *TS* is also observed to influence the convergence of the analysis. Figure 2-11 shows that complete convergence is generally achieved under higher *TS* values (e.g., $TS \geq 30$) compared to lower *TS* values (i.e., $TS = 1$ and $TS = 5$), regardless of the K_{res} value used.

As will be shown, the primary influence of *TS* is to stiffen the response, while the primary influence of K_{res} is to improve the convergence of the analysis. *TS* is also observed to improve the convergence of the analysis. However, this is a secondary influence, since it does so at the cost of increasing the stiffness. The final validation for Test CB150 is shown in Figure 2-12 using $TS = 10$, $K_{res} = 0.2$, and $\beta_{Gf} = 1$. These parameters allowed the best approximation to be made, with the best overall convergence of the analysis.

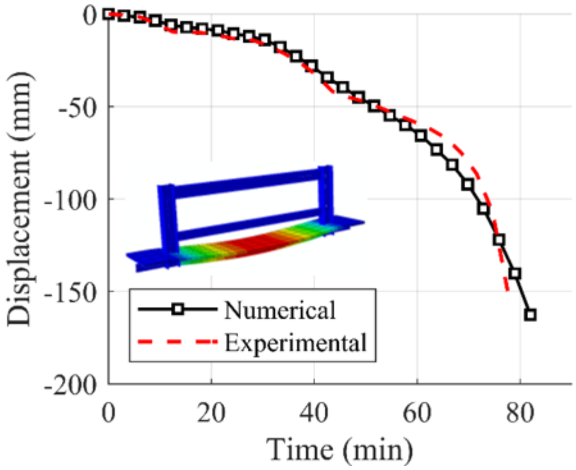

Figure 2-12. Mid-span displacement for Test CB150 using $TS = 10$, $K_{res} = 0.2$, and $\beta_{Gf} = 1$.

2.7.2. Cardington Test no. 3

The Cardington Fire Tests were a series of fire tests carried out on a 8-story steel framed structure with composite floor slabs, conducted between 1995 and 1996 at the British Research Establishment (BRE) Test Facility [67,68]. Test no. 3 consisted of a natural fire applied to a 9.98 m x 7.57 m compartment located at the corner bay of the second floor as shown in Figure 2-13. The floor slab was composed of a 70 mm thick A35 LWC with a compressive strength of f_{co} = 39 MPa, cast on a 60 mm steel deck. The slab was reinforced with A142 reinforcement placed 55 mm from the top of the slab. Two grades of steel were used in the steel frame: (1) S275 Grade 43 with a yield strength of F_y = 308 MPa; and (2) S355 Grade 50 with a yield strength of F_y = 390 MPa. During testing, the slab was loaded with a live load of 5.48 kN/m^2.

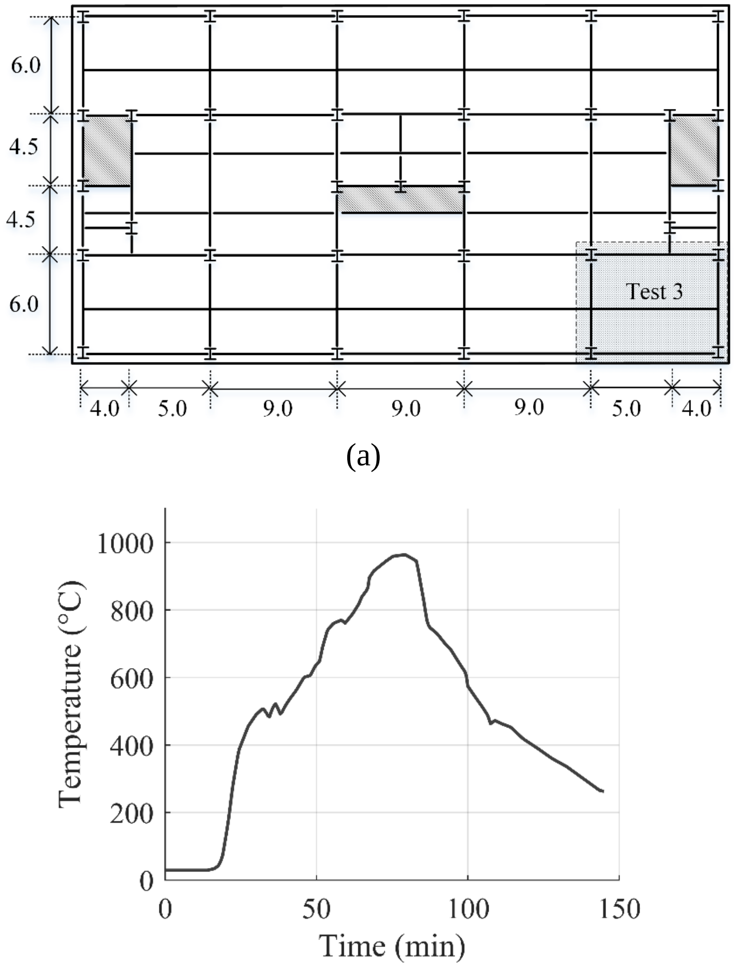
(a)
(b)

Figure 2-13. Cardington Test no. 3[67,68]: (a) Test configuration and floor layout. All dimensions in [m]; (b) Temperature-time curve of fire.

In the structural finite element model, a mesh size of 500 mm x 500 mm was used for shell elements, while a mesh size of 500 mm was used for beam elements. Symmetry was assumed and a quarter of the floor plan was modeled. The temperatures of the beams, girders, columns, and slab measured during testing were passed directly to the structural model as predefine temperature fields. These temperatures are not presented for brevity, and can be found in the accompanying reference [67,68]. Beam-end connections were idealized as perfectly pinned.

The results of the sensitivity analyses are not presented, as similar findings were observed: (1) results were independent of the β_{Gf} model utilized; (2) stiffness was not influenced by K_{res}; (3)

stiffness was influenced by *TS*; and (4) K_{res} acted to improve the convergence of the analysis. For this test case, *TS* was observed to heavily influence the stiffness. Figure 2-14 shows the displacement-time history at the center of the heated slab panel (i.e., location *D11* as shown in the insert of Figure 2-14(a). Figure 2-14(b) shows that for K_{res} = 0.2 and β_{Gf} = 1, peak displacement δ_{max} varied by as much as 100 mm depending on the *TS* value used (δ_{max} = 302 mm for *TS* = 50 while δ_{max} = 412 mm for *TS* = 10). The large variation of displacement shows that tension within the floor slab plays a large role in the response. This is not surprising given that tensile membrane action (TMA) occurred during Test no. 3. TMA is characterized by the balance of membrane (i.e., axial) stresses within the floor slab, which provide a balance between an exterior compression ring and an interior tensile zone. This mechanism differs significantly from the balance of compressive and tensile stresses occurring within the cross-section of the slab during flexure. Parameter *TS* heavily influences the response of floor slabs undergoing membrane action, more so than slabs undergoing flexure.

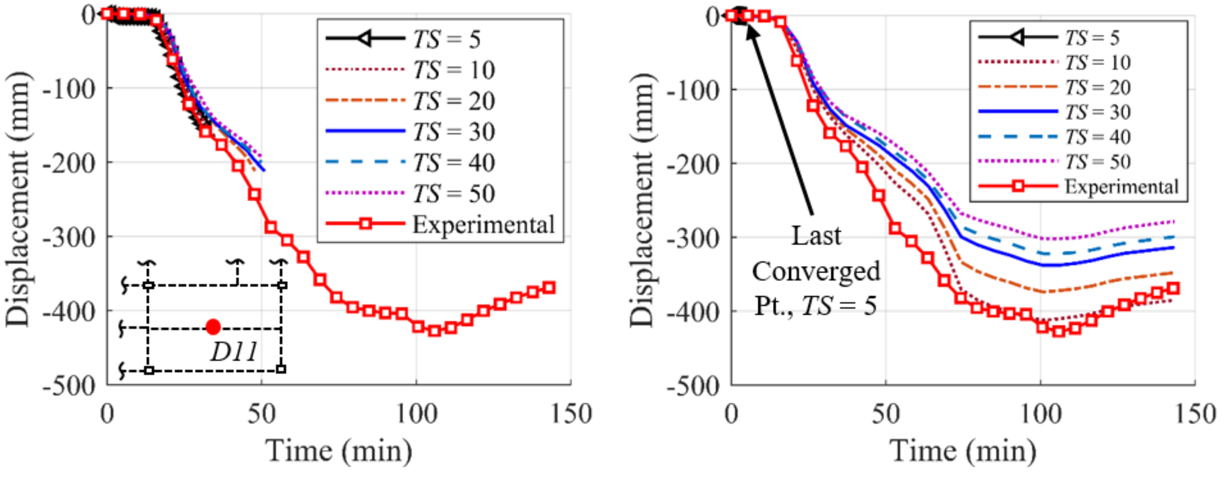

(a) β_{Gf} = 1, K_{res} = 0.01 (b) β_{Gf} = 1, K_{res} = 0.2

Figure 2-14. Influence of *TS* on the displacement at location *D11* for Cardington Test no. 3 using: (a) β_{Gf} = 1, K_{res} = 0.01; and (c) β_{Gf} = 1, K_{res} = 0.2.

The final validation for Test no. 3 is shown in Figure 2-15 using TS = 10, K_{res} = 0.2, and β_{Gf} = 1. These parameters allowed the best approximation to be made, with the best overall convergence of the analysis. Figure 2-15 shows the displacement at two locations within the floor slab, labeled *D11*and *D14*.

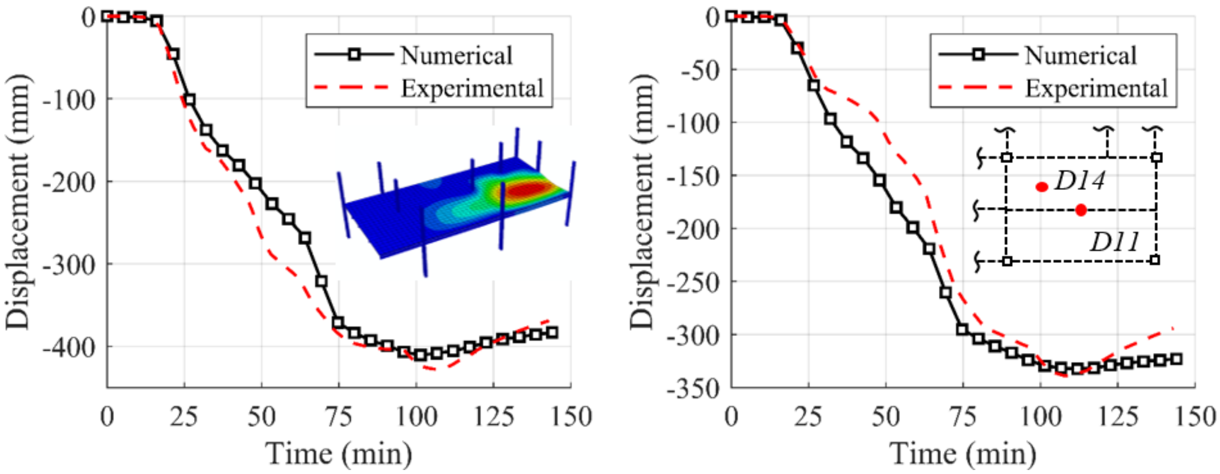

(a) Location *D11*   (b) Location *D14*

Figure 2-15. Displacement for Cardington Test no. 3 using TS = 10, K_{res} = 0.2, and β_{Gf} = 1 at various locations: (a) location *D11*; and (b) location *D14*.

2.7.3. BRANZ Fire Test

The BRANZ fire tests were a series of standard fire tests on simply-supported two-way bending RC slabs, performed in the BRANZ Fire Laboratory in New Zealand in 2002 [64,65]. Each slab had a floor plan of 3.3 m x 4.3 m and was subjected to a 3-hour ISO 834 standard fire exposure. Slab *HD12* was chosen for the validation study. Slab HD12 consisted of 100 mm thick flat RC slab comprised of NWC with a compressive strength of f_{co} = 36.7 MPa, embedded with a 12 mm hot-rolled bars, spaced at 200 mm in both directions. Slab HD12 was loaded with a live load of 3.0 kN/m^2 during testing.

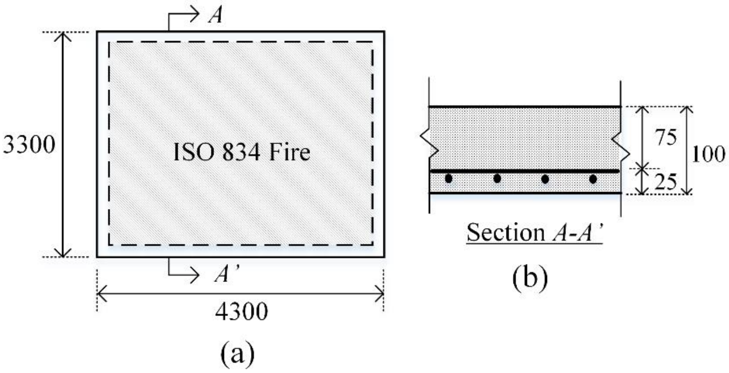

Figure 2-16. Test configuration of BRANZ fire test [64,65]: (a) floor plan dimensions; (b) cross-section. All dimensions in [mm].

The structural model of slab HD12 consisted of shell elements with a mesh size of 200 mm x 200 mm. Due to the symmetry, a quarter of the slab was modeled. The internal temperatures of each slab measured during testing were passed directly to the structural model as predefined temperature fields. These temperatures are not presented for brevity, and can be found in the accompanying reference [64,65]. The final validation for slab HD12 is shown in Figure 2-17. The best approximation, with the best overall convergence of the analysis, was obtained using $TS = 10$, $K_{res} = 0.01$, and $\beta_{Gf} = 1$.

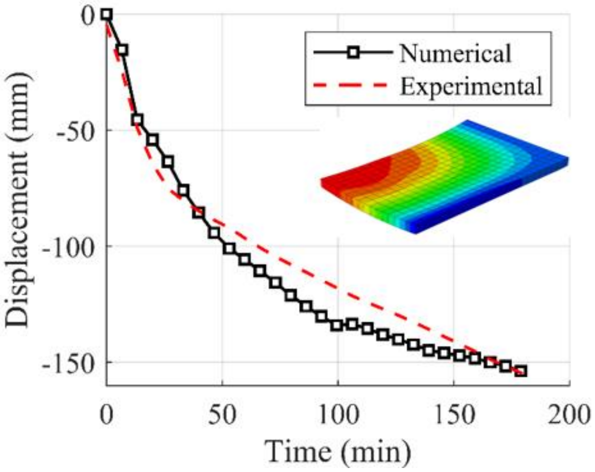

Figure 2-17.Mid-panel displacement of slab HD12 using $TS = 10$, $K_{res} = 0.01$, and $\beta_{Gf} =1$.

2.7.4. FRACOF Fire Test

The FRACOF fire test was a fire test carried out on a partially-protected steel-concrete composite floor assembly, conducted in France in 2008 [66]. The floor assembly was subjected to heating from a furnace, which followed an ISO 834standard fire exposure and then allowed to cool naturally at 2 hours as shown in Figure 2-18. The floor slab was composed of a 97 mm thick C30/37 NWC with a compressive strength of f_{co} = 36.7 MPa, cast on a 58 mm steel decking. The slab was embedded with S500 reinforcement, placed 50 mm from the top of the slab. Floor beams consisted of IPE300 steel sections with a yield strength of F_y = 311 MPa, while girders consisted of IPE400 steel sections with a yield strength of F_y = 423 MPa. To induce TMA, perimeter beams, girders, columns, and connections were all fire protected, while the interior beams were left unprotected. During testing, the floor was loaded with a live load of 3.87 kN/m^2.

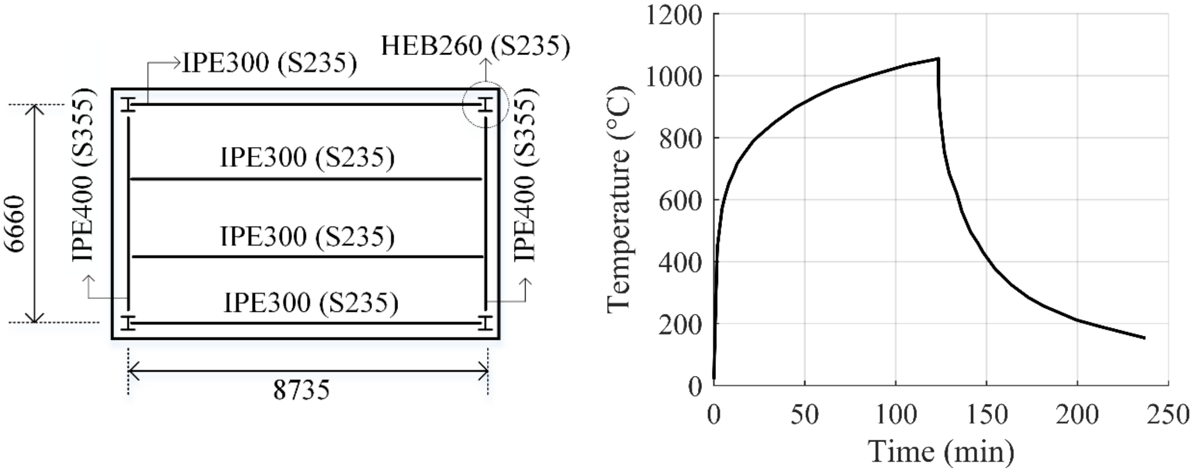

(a) (b)

Figure 2-18. FRACOF fire test [66]: (a) Test configuration. All dimensions in [mm]; and (b) Temperature-time curve of the furnace.

In the structural model, an average mesh size of 200 mm x 200 mm was used for shell elements, while an average mesh size of 200 mm was used for beam elements. The temperatures of the beams, girders, and slab measured during testing were passed to the structural model as predefine temperature fields. These temperatures are not presented for brevity, and can be found in the accompanying reference [66]. Beam-end connections were idealized as perfectly pinned. The final validation of the FRACOF test is shown in Figure 2-19 using $TS = 10$, $K_{res} = 0.2$, and $\beta_{Gf} = 1$. These parameters allowed the best approximation to be made, with the best overall convergence of the analysis. Figure 2-19 shows the displacement at 2 locations within the floor slab, labeled *D1* and *D2*.

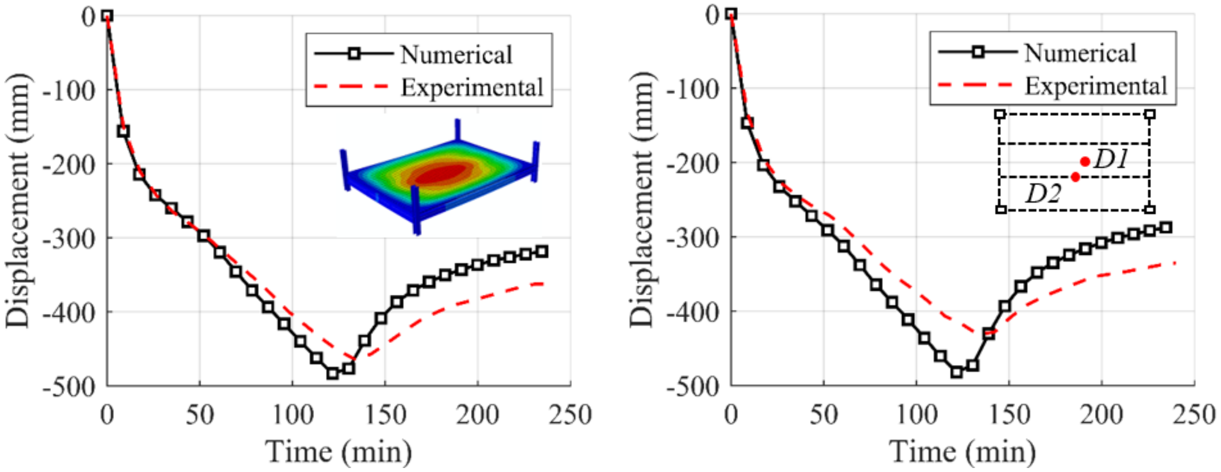

(a) Location *D1* (b) Location *D2*

Figure 2-19. Displacement for the FRACOF fire test using $TS = 10$, $K_{res} = 0.2$, and $\beta_{Gf} = 1$ at various locations: (a) location *D1*; and (b) location *D2*.

2.8. Discussion

The results showed that the proposed tension stiffening model can be used to predict the response of RC and composite floor slabs exposed to fire with great accuracy, provided that the parameters TS and K_{res} are calibrated against the structural response of the structure, which must be known a priori. Parameter TS can be altered to modify the stiffness of the floor slab, while K_{res} can be altered to improve the convergence of the analysis. Additionally, objectivity of the β_{Gf} model was observed, showing that the temperature-dependence of G_f had a small influence on the tension stiffening response. The validation showed that the modeling approach, assumptions, and inputs used in the study are adequate, and could be used to investigate composite floor slabs exposed to fire.

Premature divergence of the analysis was observed under certain combinations of *TS* and K_{res}. Since structural failure was not observed in any of the test cases examined, this divergence is a consequence of one of two factors: (1) localized cracking at elevated temperature, which can influence the material stiffness matrix to become singular, causing the analysis to terminate [80]; and (2) snap-back response, which produces inadmissible tensile stress-strain curves of concrete. While divergence of the static analysis due to inadmissible tensile stress-strain curves (i.e., snap-back response) can be prevented by imposing the upper limit on the mesh size shown in Equation (2-13), divergence due to localized cracking could be bypassed to some degree by utilizing larger values for K_{res}, which was shown to improve the convergence of the static analysis solver in all test cases examined. Thus, the tension stiffening model plays an essential role in both the accuracy of the solution, and on the convergence of the analysis, as was shown in this paper. The significance of this is that a static analysis procedure could be used in lieu of advanced procedures such as explicit dynamic [44] or a fire-dedicated hybrid-static procedure [91].

Finally, a few remarks regarding the proposed tension stiffening model are made. Theoretically, the effects of tension stiffening reduced to zero when all steel rebars have yielded as shown in Figure 2-2. However, a limit of $\varepsilon_{tu,m} \leq \varepsilon_y$ is not imposed in the model for several reasons. Firstly, experimental tests have shown that at strains corresponding to the yielding of reinforcement (0.002), concrete in cracked RC continues to carry tension. Direct tension tests of RC specimens by Williams [56] showed that concrete continues to carry 20 to 55 percent of its tensile strength f_{to} at a strain corresponding to 0.002. Tests of RC panels performed by Belarbi and Hsu [52] showed that concrete can carry ten percent of f_{to} at a strain of 0.002. Vecchio and Collins [53] showed that concrete in cracked RC panels can carry up to fifty percent of f_{to} at a strain of 0.012, which is well above the 0.002 yield strain of steel reinforcement. Secondly, many ambient-temperature tension stiffening models do not impose the limit $\varepsilon_{tu,m} \leq \varepsilon_y$, and analysts are free to violate this limit. Thirdly, for a specific mesh size h, the limit $\varepsilon_{tu,m} \leq \varepsilon_y$ may be violated even when utilizing $TS = 1$ (i.e., no tension stiffening present). Lastly, the results presented demonstrate that $\varepsilon_{tu,m} \leq \varepsilon_y$ may be violated to achieve accurate predictions and allow full convergence of the analysis. To the authors' knowledge only one ambient-temperature tension stiffening model exists which explicitly violates $\varepsilon_{tu,m} \leq \varepsilon_y$ [31]. Even though the model prescribes an ultimate strain of $\varepsilon_{tu,m} = 0.005$ (over twice the yield strain of steel), it was used to win an international RC modeling competition organized in 1981 [92].

Finally, because tension stiffening occurs only in the direction parallel to reinforcement, the proposed model should only be defined for concrete in the material direction parallel to the reinforcement. This is especially important in RC beams, which have reinforcement running in only one direction. In all the test cases examined, the composite slab was bi-axially reinforced through a reinforcement mesh, and thus tension stiffening was defined in the two material directions parallel to the reinforcement axes. Also, the effects of tension stiffening occur only in the concrete neighboring tensile reinforcement. Thus, the proposed model should not be applied to concrete elements remote from tensile reinforcement, including concrete elements near the compressive reinforcement, unless cyclic loading is present and those reinforcement will eventually carry tension. In a deep RC member such as a RC beam, an analysist should consider that the effects of tension stiffening will diminish with distance away from the tensile reinforcement and consider this in the model. As a reference, readers should consult the work of Gilbert and Warner [30], who pioneered an approach for producing a tension stiffening model that depended on the distance of concrete to the tensile reinforcement.

2.9. Conclusion

A methodology for producing an elevated-temperature tension softening and elevated-temperature tension stiffening model was presented. The energy-based stress-strain model of plain concrete developed by Bažant and Oh [51] was extended to the elevated-temperature domain by developing an analytical formulation for the temperature-dependence of the fracture energy G_f. Then, an elevated-temperature tension stiffening model was developed based on the modification of the proposed elevated-temperature tension softening model. The applicability and validation of the proposed tension stiffening model was presented through the numerical analysis of several fire tests on composite floor systems. Based on the results presented, the following conclusions were made:

- The proposed tension stiffening model can be used to predict the response of composite floor slabs exposed to fire with great accuracy, provided that the parameters TS and K_{res} are adequately calibrated.
- The sensitivity analysis revealed that an increase in TS acts to stiffen the response, while an increase in K_{res} acts to improve the convergence of the analysis.
- The temperature-dependence of G_f was shown to have a negligible influence on the structural response, and a temperature-independent β_{Gf} model can be utilized in the proposed tension stiffening model.

- Premature divergence of the analysis due to localized cracking could be bypassed by utilizing larger values of K_{res}, allowing a static analysis procedure to be used, in lieu of advanced procedures such as explicit dynamic.

Finally, a call for experimental testing to the research community is made to address the deficiencies highlighted by the authors. Tests that provide understanding of tension softening of plain concrete and tension stiffening of RC have yet to be extended to the elevated-temperature domain. These tests are required so that formal material models of both plain concrete and RC (i.e., tension softening and tension stiffening models, respectively) can be developed. These tests are also required to validate the models proposed by the authors herein. At a minimum, the following tests are advocated by the authors: (1) direct tension tests of plain concrete specimens subjected to steady-state elevated temperature, measuring the complete stress-displacement curve of each test specimen; (2) three-point bending tests on notched plain concrete beams exposed to steady-state elevated temperature; and (3) direct tension tests of RC specimens subjected to steady-state elevated temperature. These tests should be carried out for a complete range of variables, including an appropriate range of temperatures and material types (e.g., NWC, LWC, etc.) to ensure that a complete scope of the parameters observed in engineering practice are considered.

Chapter 3 Analysis of Restrained Composite Beams Exposed to Fire

The actions of a restrained steel-concrete composite beam exposed to fire are investigated using the finite element software ABAQUS. A parametric study is performed to examine the influence of axial restraint stiffness, beam slenderness, load level, and axial restraint location. The fire scenario is also examined, and two fires are considered including an ASTM E119 standard fire and a design natural fire. Validation of both the heat transfer and structural analyses are presented to establish confidence in the results. The validation sheds new light on the macro-modeling of composite beams comprised of beam and shell elements. Specifically, the reference of the beam elements should be positioned at the geometric centroid of the end-connection when an axial-restraint is present. The study shows that the length of the beam heavily influences the fire response of a restrained composite beam. Composite beams with short spans tend to fail in the compressive beam-column stage, while composite beams with longer spans tend to fail in the tensile catenary stage. Furthermore, conditions that are favorable for inducing catenary action include longer beam spans, increased axial restraint stiffness, increased load level, and positioning of the axial restraint near the top of the beam. Finally, the results show that, for a beam of length L, catenary action is generally developed after the deflection limit of $L/20$ is reached, demonstrating that care should be used when using this deflection limit to evaluate the fire resistance of restrained composite beams.

3.1. Introduction

Due to fire integrity requirements, a fire inside a burning compartment is generally well contained. As a result, expansion during heating and contraction during cooling of fire-exposed floor members are often restrained by the surrounding floor outside the compartment. Significant axial forces are developed in the heated floor beams, and likewise, the adjacent floor experiences an equal and opposite restraint force despite not being exposed to fire. This response differs from floor systems at room temperature, where axial force is negligible, and beams act essentially as independent structural elements.

Initial heating from a fire causes steel floor beams to expand due to thermal expansion. However, restraint from the surrounding structure transforms the beams into beam-columns, as compressive axial forces are generated in the floor beams. The compressive axial force can be significant, often reaching 30% of the axial capacity of the beam at room temperature [93,94] and can even result in local buckling of the bottom flange of the steel beam near the connections [62,63,95,96]. As the temperature of the beam rises and the strength and stiffness of the steel deteriorates, progressive displacement occurs until the beam undergoes tensile catenary action. During this stage, external loads on the beam are carried entirely by axial tension in the beam, which are subsequently carried by the connections and anchored by the surrounding structure. If large tensile forces can be tolerated by the adjacent structure and connections, catenary action can prevent run-away failures at very high temperatures.

The fire response of an axially-restrained beam exposed to a standard fire can be classified into two stages as shown in Figure 3-1. In the first stage, a compressive axial force is developed due to restrained thermal expansion and loads are carried through flexural bending. This stage is known as the beam-column stage since fire-induced compressive forces act to reduce the moment-carrying capacity of the beam. In the second stage, loads are carried entirely by axial tension in the beam. This stage is known as the catenary stage and is typically activated at large beam deflections. The displacement and axial-force response depicted in Figure 3-1 can differ if the beam is laterally unrestrained (i.e., lateral torsional buckling can occur) [93], made of non-compact wide-flanged section (i.e., local buckling occurs prior to yielding) [97], and/or is constructed to act compositely with the resting floor slab [98].

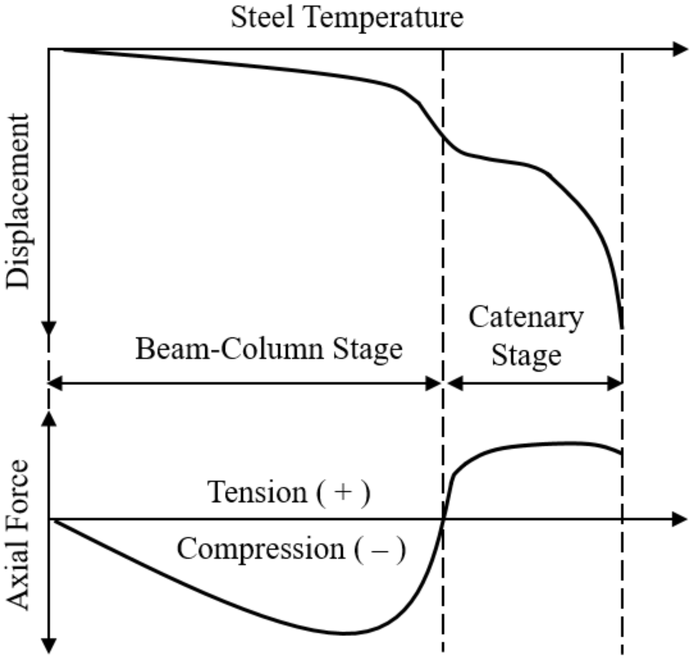

Figure 3-1. Mid-span displacement and axial force response of a restrained steel beam exposed to a standard fire.

There has been considerable effort to experimentally [62,63,95,96] and numerically [93,94,99–102] examine the response of restrained beams exposed to fire. Liu *et al.* [96] carried out experimental tests to study the effects of axial restraint and connection type on a restrained steel beam exposed to fire. The results showed that catenary action was more likely to develop at lower load levels and generally occurred when the beam deflection surpassed a deflection limit of

L/20, where *L* is the span of the beam. Li and Guo [95] examined the behavior of a restrained steel beam under a natural fire exposure. The results showed that restrained thermal expansion led to significant compressive axial forces in the beam, causing local flange buckling of the steel beam. Additionally, catenary action was observed after the beam deflection surpassed the deflection limit of *L*/20. Zhou [62] and Wang [63] examined the fire response of a restrained steel-concrete composite beam (test results are translated to English language by Li and Wang [90]). Local buckling due to restrained thermal expansion was observed to destroy the applied fire insulation on the steel beam. Tensile cracks were also observed in the concrete slab because of tensile catenary action.

Yin and Wang [99] investigated the influence of various parameters on the fire response of an unprotected axially restrained steel beam. Their results showed that the axial restraint stiffness and the load level heavily influenced the response of the beam. An increase in axial restraint stiffness led to lower beam deflections and larger axial forces, while an increase in load level led to larger beam deflections and tensile axial forces; however, the axial restraint stiffness reduced compressive axial force in the beam. Tan and Huang [100] investigated the effect of slenderness ratio, load ratio, thermal gradient, and axial and rotational restraint on the fire response of an unprotected steel beam. Their analyses showed that axial restraint acts to reduce the temperature at which failure of the beam occurs, while rotational restraint acts to increase the failure temperature. Jiang *et al.* [98] examined the influence of boundary condition on the behavior of a steel-concrete composite beam exposed to fire. Axially-restrained support conditions were shown to produce larger mid-span displacement when compared to unrestrained simply-supported conditions. Additionally, no catenary action was observed when rotations of the axially-restrained composite beams were taken as infinitely rigid. Allam *et al.* [102] examined the influence the axial restraint stiffness, load level, thermal gradient, and span-to-depth ratio, on an unprotected steel beam exposed to fire. An increase in the axial restraint stiffness was shown to help activate catenary action, preventing run-away failure.

High-temperature creep has also been shown to have a significant influence on the response of restrained steel beams exposed to fire [93,94,101]. Kodur and Dwaikat [93] examined the restrained response of an unprotected steel beam exposed to fire and showed that the major parameters influencing the response were the fire scenario, load level, axial restraint stiffness, and high-temperature creep. Dwaikat and Kodur [94] carried out a parametric study to examine the influence of key parameters on the restrained response of an unprotected steel beam exposed to fire. The authors showed that better fire performance of steel beams was observed when the axial restraint was positioned near the bottom of the beam. By positioning the beam-end supports near the bottom of the beam, a counter-acting moment at the supports was produced, which reduced beam displacements. The influence of high-temperature creep was also shown to be significant. Kodur and Dwaikat [101] investigated the influence of various parameters on the effects of high-temperature creep in a restrained steel beam exposed to fire, including the load level, heating range, fire scenario, and axial restraint stiffness. The study showed that the axial restraint stiffness heavily influenced the degree to which thermal creep influenced the response of the steel beam.

With the exception of a few studies [62,63,98], previous research has focused primarily on the restrained fire response of bare steel beams. There is limited work on the restrained fire response of composite beams, which is a construction type that is more commonly observed in structures. To address these deficiencies, the actions of restrained steel-concrete composite beams exposed to fire are investigated using the finite element software ABAQUS [80]. The structural modeling approach is validated against test data on restrained steel [95] and restrained composite beams [62,63] exposed to fire. New light is shed on the modeling of composite beams comprised of beam and shell elements. Specifically, the reference of the beam elements should be positioned at the geometric centroid of the end-connection. The validated modeling approach is then used to perform a parametric study to investigate the influence of the beam slenderness, load level, axial restraint stiffness, and the axial restraint location. The effect of fire type is also examined, and two fire types are examined including an American Standard of Testing and Materials (ASTM) E119 standard fire exposure [6] and a design natural fire.

3.2. Parametric Study

A schematic of the restrained composite beam investigated is shown in Figure 3-2. The floor slab consists of a 65 mm thick slab cast on a 75 mm steel decking, which acts compositely with a W18X35 wide-flanged section. The W18X35 steel section is neither slender nor noncompact in flexure, and the plastic moment capacity of the section can be reached without local buckling of the flange or web occurring. The slab contains light-weight concrete with a 28-day compressive strength of f_c' = 34.5 MPa and is reinforced with a 6x 6W1.4/1.4 wire reinforcement placed 25 mm from the top of the slab. The steel beam consists of structural steel ASTM A992 with a yield strength F_y of 345 MPa, while the reinforcement consists of ASTM A185 Grade 65 steel wire with a yield strength of F_y = 450 MPa.

The composite beam is both axially- and rotationally-restrained as shown in Figure 3-2. A set of elastic springs with stiffness $K_a/2$ were used to represent axial restraint, while a set of elastic rotational springs with stiffness K_r were used to represent the rotational restraint at both ends of the beam. In real steel structures, the rotational stiffness of beam-end connections is neither zero (i.e., perfectly pinned) nor infinitely rigid, and depends on the connection type, as well as the effects of composite action offered between the slab and steel beam at the connection. The influence of rotational stiffness was not investigated herein, and a rotational stiffness corresponding to 10% of the rotational stiffness of the steel beam 4*EI*/*L* was arbitrarily chosen.

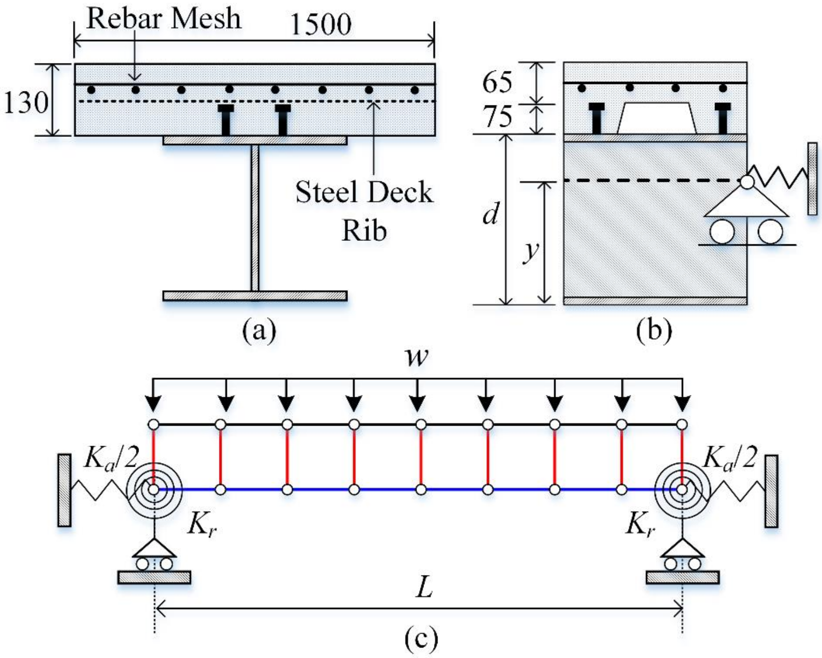

Figure 3-2. Test configuration of the composite beam examined: (a) cross-sectional dimensions; (b) profile view of the beam; (c) span, boundary conditions, and load configuration. All dimensions in [mm].

A fire rating of 1 hour was utilized to define the passive fire protection of the floor beam. CAFCO type 300, a cementitious-based spray-applied fire resistive material (SFRM) from ISOLATEK Int. [103], was chosen arbitrarily for the fire protection design, which was based on the Underwriters Laboratory (UL) Design No. *BXUV.N735* [104]. UL Design No. *BXUV.N735* is applicable for restrained floor beams supporting a ribbed slab and calls for a SFRM thickness of 13 mm to achieve a fire rating of 1 hour.

The axial restraint K_a at the end of the beam is specified as a percentage of the axial stiffness of the steel beam at room temperature and is varied from α = 0, 0.1, 0.5, and 1.0, where α is the axial restraint ratio, defined as:

$$\alpha = \frac{K_a}{E_{s,20\,^\circ C} A_s / L} \tag{3-1}$$

where $E_{s,20\,^\circ C}$ is the Young's modulus of steel at 20 ºC, A_s is the cross-sectional area of the steel beam, and L is the span length of the beam. For $\alpha = 0$, a traditional simply-supported beam is examined, rather than the two roller supports depicted in Figure 3-2.

The slenderness ratio $\lambda = L/r$ is varied from $\lambda = 16.8$ to 67.1, to represent stocky to slender steel beams, where r is the radius of gyration of the steel beam. Since the beam section of W18X35 was kept constant throughout the analyses, the slenderness ratio was varied by adjusting the span from $L = 3$ m to $L = 12$ m. As a result, the influence of the cross-sectional dimensions of the steel beam section was not investigated.

The load factor μ is defined as the ratio of the mid-span bending moment from the applied live load M_L over the nominal bending capacity of the composite beam M_n, i.e., $\mu = M_L/M_n$. Here $M_L = w_L L^2/8$ denotes the mid-span moment for an unrestrained beam and M_n is the nominal moment capacity of the composite beam under positive bending computed using the American Concrete Institute (ACI) [105] and American Institute of Steel Construction (AISC) [19] design specifications. In the parametric study, μ is varied from μ = 0.3, 0.5, and 0.7.

The axial restraint location y is also investigated as shown in Figure 3-2(b). Dwaikat and Kodur [94] demonstrated that the fire response of a restrained steel beam can be significantly influenced by the location of the axial restraint. In real structures, the location of the axial restraint can depend on the connection type and configuration, and even the depth of the steel beam. To reflect the variability, y is varied from $0.25d$, $0.5d$, and $0.75d$, where d is the depth of the beam. The location of the axial restraint is altered in the numerical model by adjusting the position of the reference axis of the beam element in space.

Two fire types are examined, including an ASTM E119 standard fire exposure [6], which is used primarily to determine the fire rating of structural elements, and a design natural fire, which describes a compartment fire that has reached flashover conditions. The design natural fire was defined using the Pettersson *et al.* fire design curves [106]. Using a fire load density of a typical office space and an opening factor of $O = 0.02\ \text{m}^{1/2}$, a short-hot fire is produced as shown in Figure 3-3. The short-hot fire is described by a high peak temperature and a short heating duration, which is followed by a decay phase that allows us to investigate the influence of cooling.

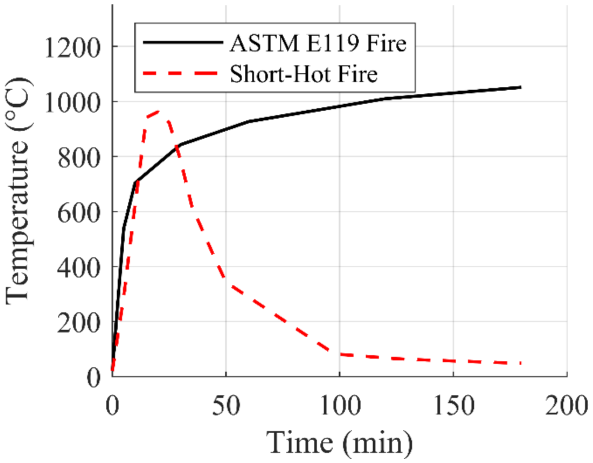

Figure 3-3. Short-hot fire produced from the fire design curves of Pettersson *et al.* [106] and a standard fire exposure taken from ASTM E119 [6].

3.3. Numerical Analysis

A sequentially-coupled thermal-structural analysis procedure is utilized, where numerical heat transfer analysis is carried out to predict member temperatures, and a subsequent structural analysis is ran using the member temperature data. Both analyses are carried out using the finite element software ABAQUS [80]. Details of both the heat transfer model and structural model are presented in the following sections along with numerical validations.

3.3.1. Heat Transfer Analysis

The thermal analyses were carried out using two-dimensional heat transfer models of the composite floor beam and composite slab as shown in Figure 3-4. Each model consisted of 4-node quadrilateral elements *DC2D4*. Since the deck of the slab runs perpendicular to the span (see Figure 3-2), a detailed model of the composite slab was utilized to extract slab temperatures as shown in Figure 3-4(b). The slab in Figure 3-4(a) was included to consider the heat sink effects associated with the slab resting on the steel beam.

Temperature-dependence of the thermal conductivity, specific heat, and mass density of both concrete and steel were defined using the models in Eurocode 2 Part 1-2 [78] and Eurocode 3 Part 1-2 [87], respectively. The temperature-dependent thermal properties of CAFCO 300, measured by Kodur and Shakya [107], were used in the heat transfer analyses. The temperature of the fire was used to define the radiative and convective boundary conditions. An emissivity of $\varepsilon_r = 0.7$ was used to define radiation conditions as prescribed by Eurocode 4 Part 1-2 [108]. To define the convection conditions, Eurocode 1, Part 1-2 [109] prescribes a heat transfer coefficient h_c which depends on the fire type: $h_c = 25$ W/(m^2-K) for a standard fire, and $h_c = 35$ W/(m^2-K) for a natural fire. Following the results of a sensitivity analysis, a mesh size of 3 mm and a time increment of 1 seconds were chosen for the analyses. These analyses are presented in the APPENDIX.

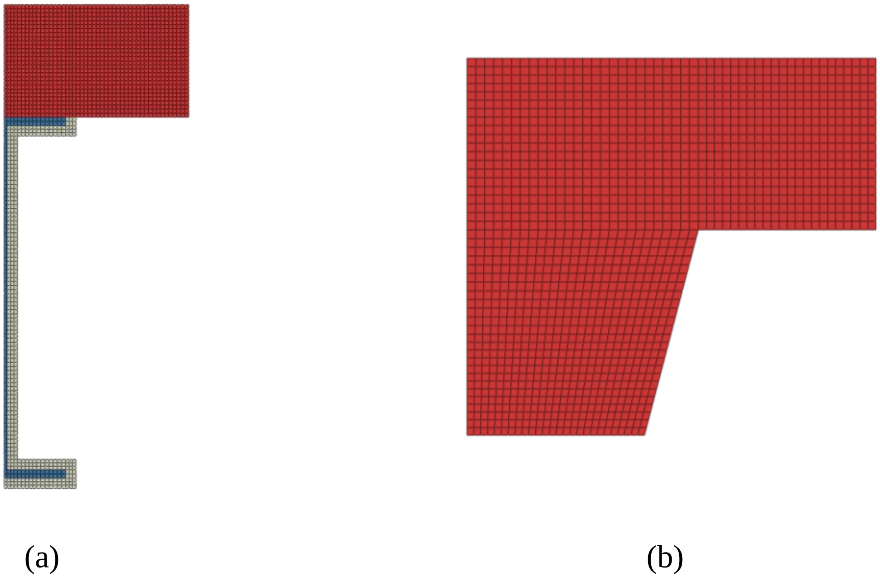

Figure 3-4. Numerical heat transfer model: (a) floor beam; (b) composite slab.

The numerical heat transfer analyses were validated against fire tests on composite slabs performed by Guo and Bailey [110] and Lim and Wade [64,65]. The composite slab tested by Guo and Bailey [110] consisted of a 85 mm thick slab cast on a 60 mm steel deck. Seven composite slabs were examined, each with a floor plan of 1.2 m x 6.45 m. The middle 3 m span of the slab was exposed to a natural fire to examine the slab behavior at both the heating and cooling phase of a fire. The composite slab tested by Lim and Wade, designated as the *HiBond* slab during testing, consisted of a 75 mm thick slab cast on a 55 mm steel deck. The composite slab had a floor plan of 3.3 m x 4.3 m and was exposed to a 3-hour standard fire exposure. Both tests consist of normal weight concrete.

Figure 3-5(a) and Figure 3-5(b) shows the heat transfer results of two composite slabs examined by Guo and Baily (i.e., *Fire 1* and *Fire 2*), while Figure 3-5(c) shows the heat transfer results of the composite slab examined by Lim and Wade. Experimentally recorded temperatures are represented with dashed lines with markers, while numerical results are represented with solid lines. In each test case, 0 mm is taken as the bottom of the slab, which is directly exposed to fire. Close approximation with experimental values were obtained, demonstrating that the modeling approach is sufficiently accurate. The heat transfer of exposed steel members is not as challenging as the heat transfer of concrete slabs, particularly due to the highly isotropic nature of steel and well-defined thermal properties. Thus, validation of heat transfer through steel members is not shown here.

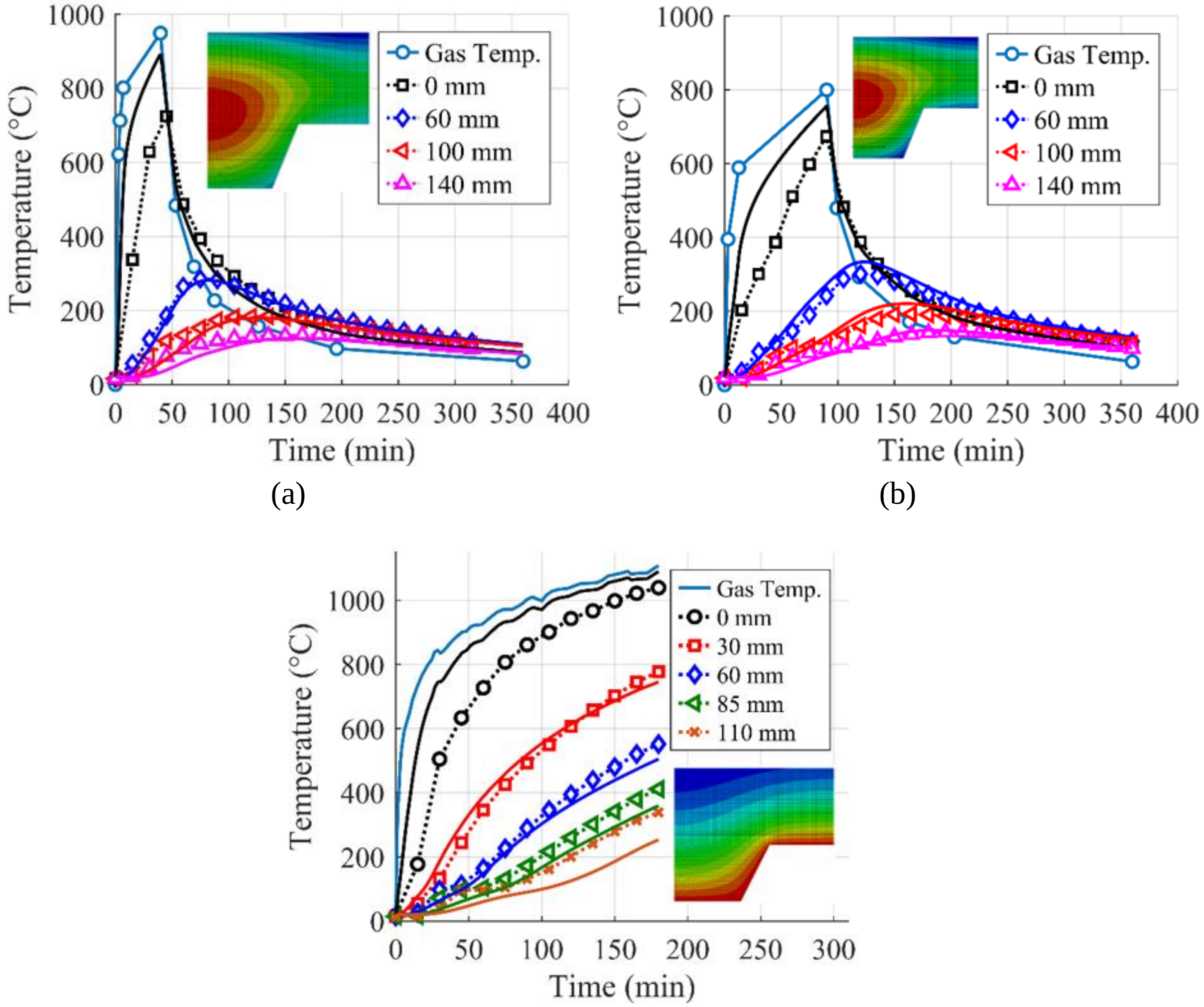

(a) (b)

(c)

Figure 3-5. Numerical heat transfer validation: (a) Guo and Bailey's *Fire 1* test [110]; (b) Guo and Bailey's *Fire 2* test [110]; and (c) Lim and Wade's *BRANZ HiBond* test [64,65]. Solid lines represent numerical results, while dashed lines with grid markers represent experimental data.

3.3.2. Structural Analysis

The composite beam was modeled using an assembly of 2-node Timoshenko beam elements *B31* and 4-node quadrilateral shell elements *S4R*, to represent the steel beam and composite floor slab, respectively. The composite slab was approximated as a flat slab with thickness equal to the thickness of the upper continuous portion of the composite slab plus one-half of the rib depth. To preserve the moment of inertia of the composite section, the offset of the slab from the steel beam was maintained, rather than placing the equivalent slab directly on the steel beam [111]. The reinforcement was modeled as an equivalent smeared steel layer with layer thickness equal to the area of one reinforcing bar divided by its spacing. The steel decking was not considered in the analysis under the assumption that the strength provided by the steel deck is lost during a fire [112]. This is a reasonable assumption given that steel decking is often left unprotected (i.e., without insulation), is relatively thin, and has a high thermal conductivity when compared to concrete. Under a fire exposure, the temperature of the deck rises rapidly and closely follows the gas temperature in the compartment. Finally, full composite action between the composite slab and steel beam was assumed by imposing a rigid constraint between the aligning nodes of the shell and beam elements.

Both geometric and material nonlinearities were included in the analyses. The metal plasticity model in ABAQUS was used to define the inelastic response of steel, while the damaged plasticity model was used to represent the inelastic response of concrete. Temperature dependence of steel and concrete were defined using the stress-strain-temperature model in Eurocode 3 Part 1-2 [87] and Eurocode 2 Part 1-2 [78], respectively. The Eurocode stress-strain models were developed to implicitly include some tolerance for creep since they were derived from transient test results [112]. The tensile response of concrete was defined using the elevated-temperature tension stiffening model proposed by Martinez and Jeffers [113]. Finally, thermal expansion was defined using the thermal elongation model of steel and concrete in Eurocode 3 Part 1-2 [87] and Eurocode 2 Part 1-2 [78], respectively.

Loads were applied sequentially: gravity loads were applied first followed by thermal loads, which were applied as predefined temperature fields. The solution to all analyses were sought using a static solution procedure in ABAQUS/Standard [80]. No viscous damping was introduced in the analysis steps since it did not improve the convergence rate. However, tension stiffening was used to overcome convergence issues associated with initial localized cracking of concrete [113], which allowed a static analysis procedure to be used in lieu of other procedures such as explicit dynamic [44] or a hybrid-static procedure [91].

3.4. Structural Validation

The structural modeling approach was validated against a series of fire test including: (1) Li and Guo's fire test on a restrained steel beam [95]; (2) Wainman and Kirby's standard fire test on a simply-supported steel-concrete composite beam (i.e., *Test 15*) [114]; and (3) Zhou and Wang's standard fire test on a restrained steel-concrete composite beam (i.e., *Test CB150*) [62,63]. The first experimental test examines a bare steel beam, while fire tests by Wainman and Kirby and by Zhou and Wang examined steel-concrete composite beams.

A review of the research literature reveals that there are many modeling approaches when an assembly of beam and shell elements are used to represent a steel-concrete composite beam (see for e.g., [36–44]). These approaches differ in many aspects including: (1) constraint type and constraint condition applied to aligning nodes of the beam and shell elements; (2) element order and type; and (3) relative location of the reference (i.e., the location of element nodes) of the beam and shell elements. Figure 3-6 shows three macro-modeling approaches for composite floor beams, each differing in the reference location of the beam and shell element. A description of each approach is given below:

- Geometric Centroid Approach: The reference of the respective element is positioned at the geometric centroid (or elastic neutral axis) of the respective beam or shell element as shown in Figure 3-6(a). The reference of the beam element is positioned at the geometric centroid of the steel beam, while the reference of the shell elements is positioned at the geometric centroid of the slab. Since it is customary to select the geometric centroid of the member cross-section as the reference location, this approach is labeled the *geometric centroid approach*. This approach is classified as an *offset* approach, since the reference of the beam and shell elements are offset from one another in space.

- Shell-Centered Approach: The reference of the beam element is offset to the geometric centroid of the slab, while the reference of the shell element is positioned at the centroid of the shell as shown in Figure 3-6(b). This approach is used primarily in finite element software *VULCAN* [38,77,115], which is a specialist software developed at the University of Sheffield for the analysis of composite steel-framed buildings exposed to fire. This approach is a *shared-node* approach since the reference of the beam and shell elements are lumped together in space.
- Neutral Axis Approach: The reference of both the beam and shell elements are lumped at the neutral axis of the composite cross-section as shown in Figure 3-6(c). This shared-node approach was developed by Nie *et al.* [37]. For beam spans with both positive and negative bending, the reference of both the beam and shell elements are positioned at the averaged location of both the positive and negative bending sections.

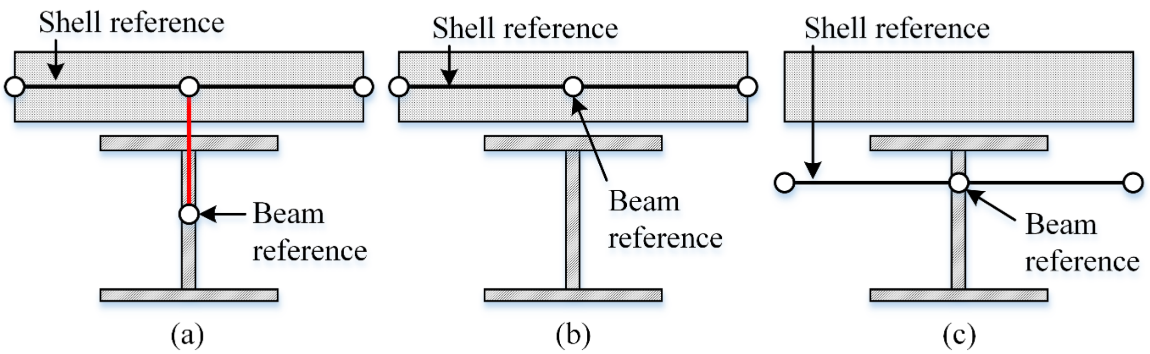

Figure 3-6. Macro-modeling approaches for a composite beam comprised of beam and shell elements: (a) Geometric Centroid Approach; (b) Shell-Centered Approach; and (c) Neutral Axis Approach.

While the primary focus of the validation is to examine whether the response of restrained beams exposed to fire can be accurately captured, a secondary focus was to examine the influence of the modeling approaches in Figure 3-6. It should be noted that ABAQUS allows a user the ability to alter the reference location of both beam and shell elements, without altering the physical position of the member in space, thus preserving the moment of inertia of the composite section.

3.4.1. Li and Guo's Restrained Steel Beam Test

Li and Guo [95] reported a fire test on an axially-restrained steel beam. The test consists of a H250X250X8X12 steel beam restrained axially by a steel frame as shown in Figure 3-7. The steel beam was subjected to a natural fire, with two concentrated loads of P = 130 kN symmetrically placed on the span. The structural model consisted of beam elements with an average mesh size of 188 mm. Experimentally-recorded steel temperatures were passed to the structural model as predefine temperature fields.

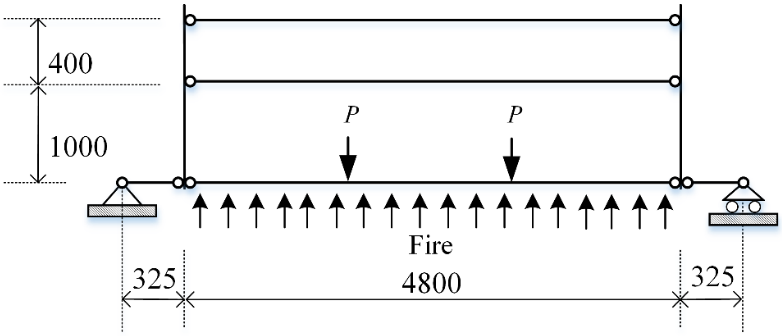

Figure 3-7. Test configuration of Li and Guo's [95] restrained steel beam. All dimensions in [mm].

Figure 3-8(a) shows the mid-span displacement of the beam, while Figure 3-8(b) shows the horizontal displacement of the roller support. Numerical results compare reasonably well with the test data, showing that structural beam elements can be used to capture the fire response of a restrained steel beam. Furthermore, an implicit consideration of thermal creep via the Eurocode stress-strain model of steel could be used to capture the fire response of a restrained steel beam. The Eurocode stress-strain models include an allowance for thermal creep. Although some researchers recommend using an explicit creep model to consider the effects of thermal creep [93,94,101], others, including the authors herein, have shown that an implicit consideration of thermal creep is adequate for modeling restrained steel beams exposed to fire [97,116,117].

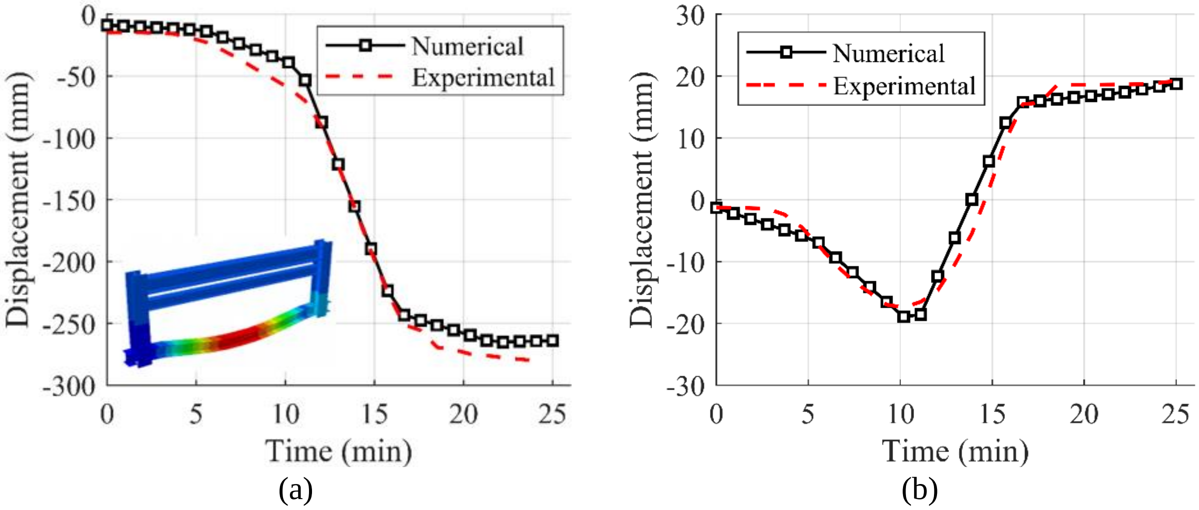

Figure 3-8. Numerically-predicted results for Li and Guo's restrained steel beam test [95]: (a) Mid-span displacement; (b) horizontal displacement at the roller support.

3.4.2. Wainman and Kirby's Composite Beam Test

Wainman and Kirby [114] reported a fire test on a simply-supported composite beam (i.e., *Test 15*). The tests consisted of a 130 mm flat slab resting on a 254x146 mm x 43 kg/m steel beam as shown in shown Figure 3-9. Figure 3-9(a) shows the measured dimensions of the 254x146 mm x 43 kg/m steel beam as presented in the data sheet of Test 15, rather than the nominal dimensions. Composite action between the slab and beam was achieved by 32 shear stud connectors, which were placed evenly along the span. The slab was reinforced with a B503 mesh located 35 mm from the bottom of the slab and A142 mesh positioned 10 mm below the top of the slab.

In the structural model, an average mesh size of 142 mm x 161 mm was used for the plane dimension of shell elements, while an average mesh size of 161 mm was used for beam elements. Steel beam temperature measured during testing were passed to the structural model as predefine temperature fields. Because the through-thickness temperature of the slab was not recorded during testing, a computational heat transfer analysis was carried out to predict the temperature profile of the slab. The results of the heat transfer analysis are presented in Figure 3-9(c).

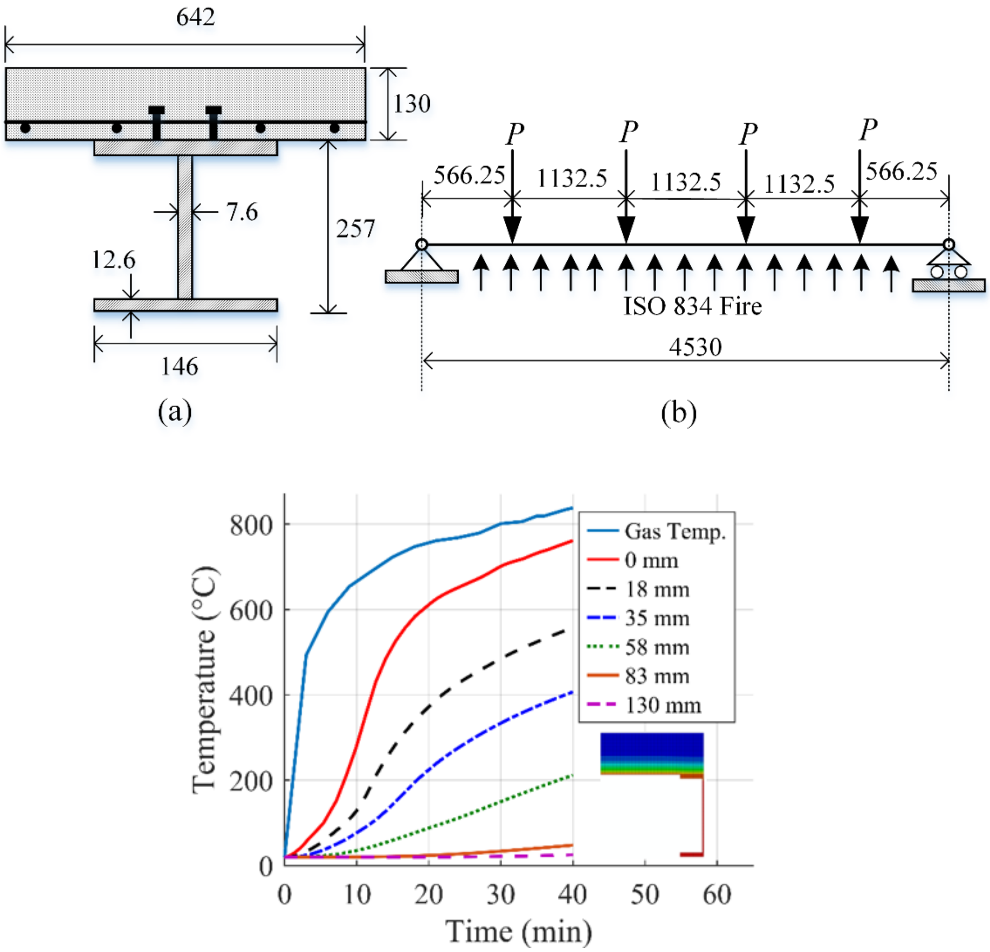

(a)

(b)

(c)

Figure 3-9. Test configuration of Wainman and Kirby's Test 15 [114]: (a) beam cross-section; (b) span and load configuration; (c) heat transfer through slab. All dimensions in [mm].

Figure 3-10(a) shows the mid-span displacement of Test 15 using each modeling approach in Figure 3-6, while Figure 3-10(b) shows a comparison of the mid-span displacement predicted from other researchers [98,118]. Numerical results compare reasonably well with the test data, with the variability arising due to the temperature profile of the slab, which was predicted using heat transfer analysis. Nonetheless, sufficiently accurate results were obtained when compared to the results of other researchers [98,118]. More importantly, Figure 3-10(a) demonstrate that the macro-modeling approach is arbitrary when the structure is axially-unrestrained. This occurs because the net axial force acting on the composite beam is zero, due to the axially-unrestrained support conditions. As will be shown in the following test case, the reference position of the beam element represents the location of the supports. When an axial-restraint is present, different modeling approaches will produce different structural responses.

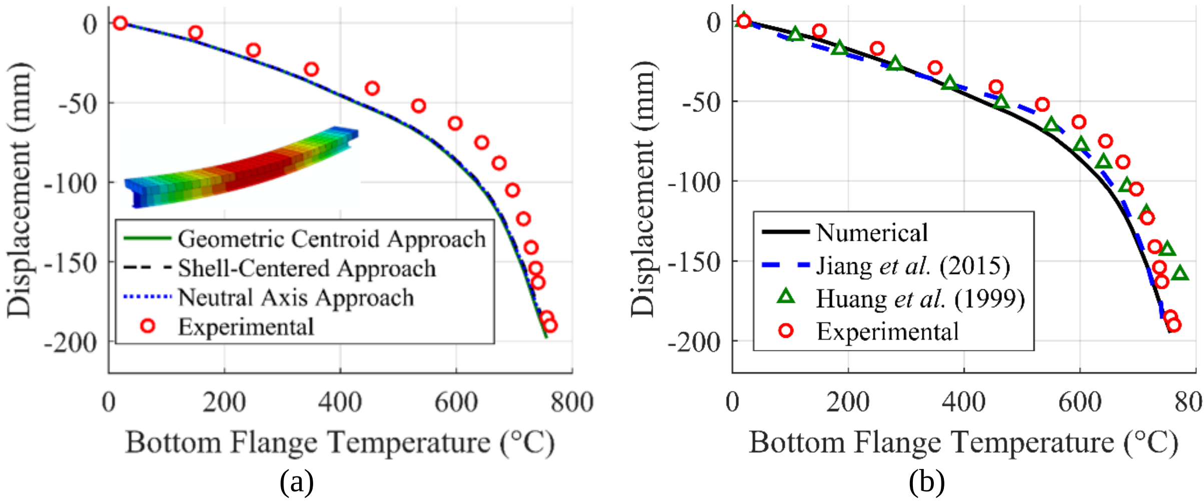

Figure 3-10. Numerically-predicted displacement of Wainman and Kirby's [114] Test 15: (a) influence of the macro-modeling approach; (b) comparison with predictions from other researchers [98,118].

3.4.3. Zhou and Wang's Restrained Composite Beam Test

Li and Wang [90] reported a fire test on an axially-restrained composite beam (i.e., *Test CB150*), which was carried out in a joint effort by Zhou [62] and Wang [63]. The test consists of a composite beam restrained axially by a steel frame as shown in Figure 3-11. The floor slab consists of a 74 mm thick slab cast on a 76 mm steel decking, which acts compositely with an H200x100x5.5x8 steel beam. The slab was reinforced with 12 mm bars, spaced at 135 mm in both directions. Two loads of P = 40 kN were applied to the beam as shown in Figure 3-11. In the structural model, a mesh size of 367 mm x 338 mm was used for shell elements, while a mesh size of 367 mm was used for beam elements. Temperature of the steel beam and slab measured during testing were passed to the structural model as predefine temperature fields.

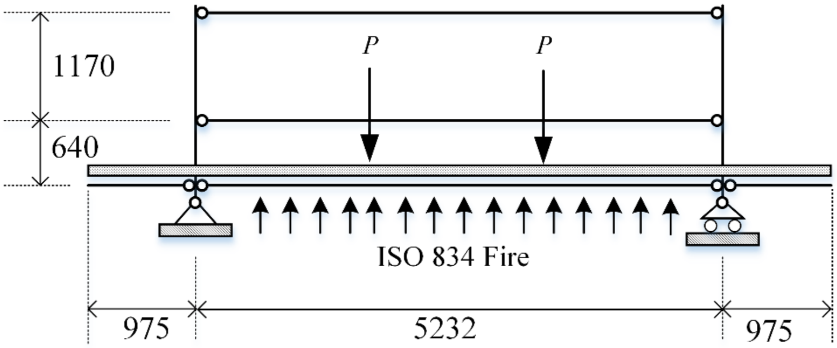

Figure 3-11. Test configuration of Test CB150 [62,63]. All dimensions in [mm].

Figure 3-12(a) shows the mid-span displacement predicted using each modeling approach in Figure 3-6. Each approach produces different structural responses, demonstrating that when an axial restraint is present, the macro-modeling approach is no longer arbitrary. The variability under each approach arises due to the unintentional change of the location of the supports (and hence the eccentricity of the axial force). Because a net axial force is produced, a change in eccentricity leads to a different structural response as shown in Figure 3-12(a). In Test CB150, the centroid of the connection is at the centroid of the steel beam, which explains why the results from the centroid-based approach matched reasonably well with the test data.

Figure 3-12(b) shows the mid-span displacement under three different locations of the shell reference plane (*R.P.*): (1) *R.P.* positioned at the geometric centroid of the shell; (2) *R.P.* positioned at the slab-beam interface; and (3) *R.P.* positioned at the geometric centroid of the beam. In all cases, the reference of the beam element remains at the centroid of the steel. Identical results are obtained under each approach, demonstrating that the reference location of the shell element is arbitrary, regardless of whether an axial restraint is present.

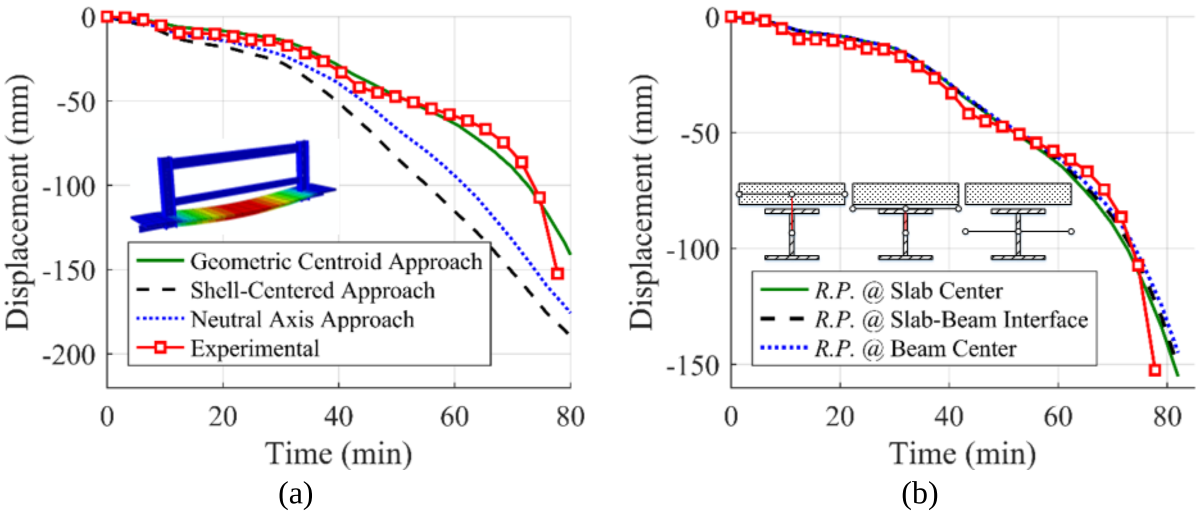

Figure 3-12. Numerically-predicted displacement of Test CB150 [62,63]: (a) influence of the macro-modeling approach; (b) influence of the reference plane (*R.P.*) location of the shell element, with the beam reference maintained at the centroid of the steel beam.

The validation of Test CB150 shows several conclusions: (1) the beam reference should be positioned at the geometric centroid of the connection, while the position of the shell reference is arbitrary; (2) structural elements (i.e., beam and shell elements) can be used to capture the fire response of a restrained composite beam; and (3) an implicit consideration of high-temperature creep via the Eurocode material models of both steel and concrete is adequate to capture the fire response of a restrained composite beam.

3.5. Results

3.5.1. Effect of Axial Restraint Stiffness

The response of the composite beam is heavily influenced by the axial restraint stiffness. Figure 3-13 and Figure 3-14 show the mid-span displacement and axial-force response of the composite beam under the ASTM E119 standard fire and the short-hot fire, respectively, for the parameters L = 10.5 m, y = 0.75d, and μ = 0.7. Relative values of displacements and axial force are shown, with displacements normalized by the deflection limit of $L/20$ and axial forces normalized by the room-temperature axial capacity $P_{y,20°C} = A_sF_{y,20°C}$. In the analyses, negative forces correspond to compressive axial forces, while positive forces correspond to tensile axial forces.

The results show that the deflection rate of the composite beam is influenced by the axial restraint stiffness. Under an ASTM E119 standard fire, larger beam deflections are observed under larger axial restraint stiffness in the early stages of the fire as shown in Figure 3-13(a). The increase of deflection with increasing axial restraint stiffness is caused by restrained thermal expansion early in the fire, which produces a net compressive axial force in the beam as shown in Figure 3-13(b). This stage of the response is referred to as the compressive beam-column stage as shown previously in Figure 3-1. The compressive axial force reduces the moment carrying capacity of the beam, in the same way that an increase in axial force reduces the bending moment capacity of a beam-column. Figure 3-13(b) shows that the peak compressive axial force increases with increasing axial restraint stiffness. As a result, an increase of axial restraint stiffness leads to larger axial compression, which increases the reduction of the moment capacity of the beam, resulting in larger deflections in the early stage of the fire. Due to the absence of a net axial force in the unrestrained case (i.e., α = 0), smaller deflections are observed in the early stage of the fire compared to the restrained cases (i.e., α > 0).

Figure 3-13(a) shows that an increase in axial restraint causes deflections to slow down in the later stage of the fire. The decrease of the deflection with increasing axial restraint is caused by the onset of catenary action. During catenary action, the beam's resistance changes from a flexural (i.e., bending) response to an axial (i.e., tension) response, and loads on the beam are carried directly by the axial spring at the beam-ends. In Figure 3-13(b), the onset of catenary action occurs when the net axial force in the beam changes from compression to tension, which is observed under an axial restraint stiffness of α = 0.5 and α = 1.0. The onset of catenary action is represented by an 'o' marker in Figure 3-13. For these beams, the time occurrence of catenary action is not largely influenced by the restraint stiffness. The level of axial restraint investigated (i.e., α = 0.5 and 1.0) may not have been large enough to significantly influence this time occurrence. In these beams, the rate of deflection slows down in the later stages of the fire, resulting in smaller deflections when compared to the response under the unrestrained case (i.e., α = 0) and α = 0.1. For α = 0 and α = 0.1, the deflection rate continues to increase monotonically until failure occurs. Failure under an axial restraint stiffness of α = 0.1 occurs before tensile catenary action is activated, demonstrating that not all restrained beams undergo catenary action. Failure of the beam is represented by an 'x' marker in Figure 3-13, which represents when numerical instability of the static analysis occurs. Overall, the onset of catenary action occurs much quicker with increased axial restraint stiffness as shown in Figure 3-13(b), which explains why the deflection rate decreases more quickly for α = 1.0 when compared to α = 0.5. Subsequently, larger tensile axial forces are induced with increasing axial restraint stiffness and can reach up to 10% of the axial capacity of the steel beam at room temperature.

Figure 3-13(a) shows that the failure time of the beam, taken as the last converged point of the static analysis, increases with increasing axial restraint stiffness. This demonstrates that the fire resistance rating (FRR) of the composite beam increases with increasing axial restraint stiffness. Additionally, an axially-restrained beam has a larger FRR than an unrestrained beam, since the deflections in an unrestrained beam continues to increase monotonically with time until failure occurs. The improvement in the FRR with increasing axial restraint stiffness is attributed to the onset of tensile catenary action, which was shown to reduce the deflection rate of the beam in the later stages of the fire. It should be noted that although failure is taken as the last converged point of the static analysis, care should be used when using this metric, since instability of the static analysis does not necessarily imply structural failure. A standard method for defining failure of a restrained beam exposed to fire does not currently exists. To this end, the authors viewed the numerical instability of the analysis as a reasonable metric for conservatively defining failure, rather than $L/20$.

The normal stress at both the bottom and top flange of the steel beam, near the supports, are also shown in Figure 3-13(c) and Figure 3-13(d), respectively. In each figure, normal stresses are normalized by the room-temperature yield strength of the beam of $F_{y,20°C}$ = 345 MPa, with the top flange taken as the flange closest to the composite slab. The results show that stresses in the unrestrained case (i.e., $\alpha = 0$) are similar to the restrained case corresponding to $\alpha = 0.1$. This demonstrates an unrestrained beam can have similar stresses as an unrestrained beam with a low axial restraint stiffness despite not having a net axial force. The stresses in an unrestrained beam are purely flexural (i.e., no net axial force), while the stress state in a restrained beam is that of a beam-column (i.e., flexural and axial). At the bottom flange of the beam, an increase of the axial restraint stiffness leads to larger peak tensile stresses but smaller peak compressive stresses as shown in Figure 3-13(c). Alternatively, at the top flange of the beam, an increase of axial restraint stiffness induces compression in the early stages of the fire. This is observed in the restrained case of $\alpha = 0.5$ and $\alpha = 1.0$ in Figure 3-13(d). In these cases, stresses at the end of the analysis surpass the yield strength of the beam.

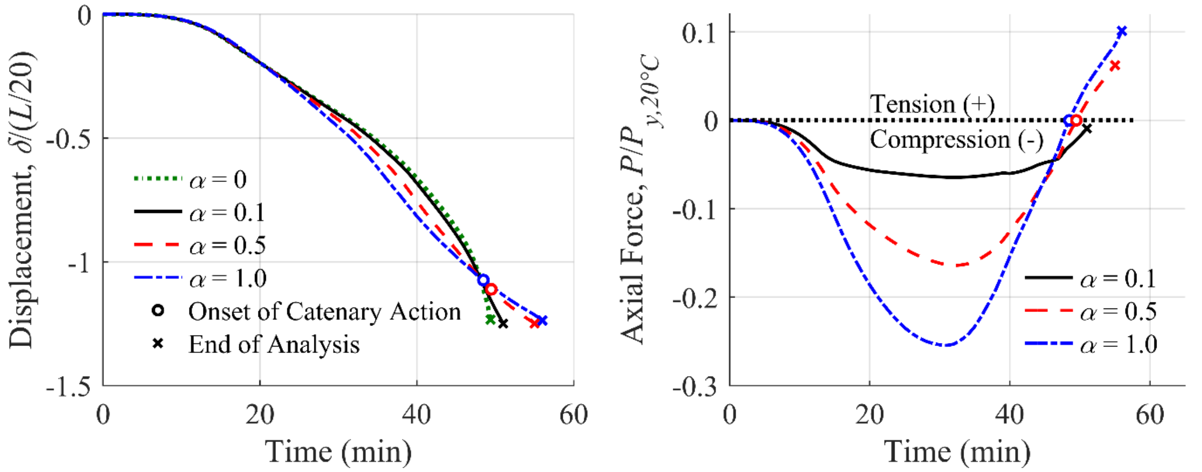

(a) L = 10.5 m, y/d = 0.75, μ = 0.7 (b) L = 10.5 m, y/d = 0.75, μ = 0.7

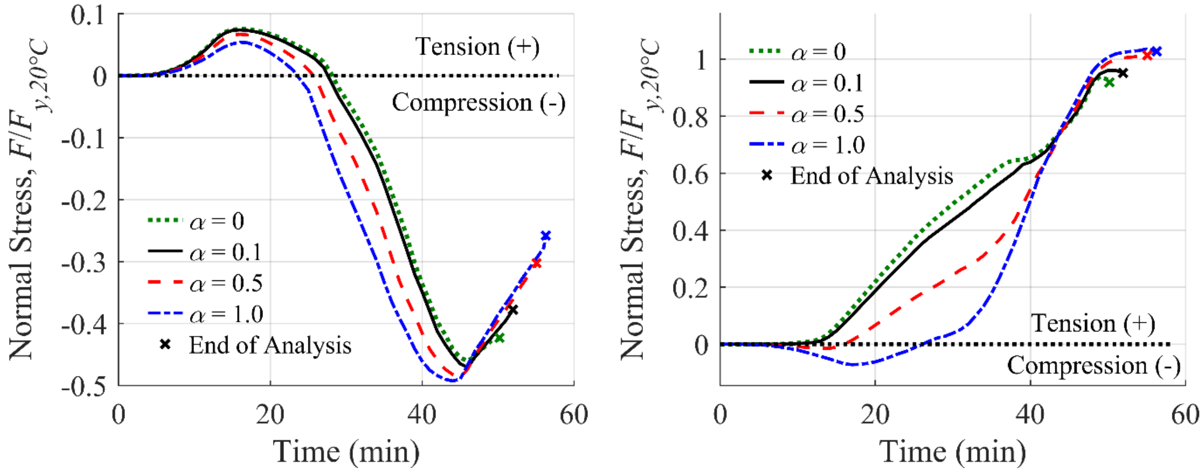

(c) Bottom flange stress (d) Top flange stress

Figure 3-13. Influence of axial restraint stiffness under an ASTM E119 standard fire: (a) mid-span displacement response; (b) axial force response; (c) bottom flange stress; (d) top flange stress.

To investigate the effects of cooling, a generic short-hot natural fire was also examined. The short-hot fire represents a severe fire exposure with a steep growth rate, followed by a sharp decay phase as shown in Figure 3-3. The displacement and axial force response of the restrained composite beam under a short-hot fire are shown in Figure 3-14. While deflections under an ASTM E119 fire continue to increase with time, deflections under a short-hot fire increase with time until material cooling is encountered at about t = 41 min into the fire as shown in Figure 3-14(a). In order to correlate axial force to the temperature of the beam, the axial force response in Figure 3-14(b) is shown in the temperature domain of the bottom flange. During material cooling, steel regains part of its strength and the beam starts to contract. This leads to two observable actions: (1) a decrease in deflection as shown in Figure 3-14(a); and (2) a reduction in the axial compression as shown in Figure 3-14(b). Because of cooling, failure does not occur under a short-hot fire, and the analysis runs to completion.

The reduction of axial compression at the onset of material cooling is produced by restrained thermal contraction. Figure 3-14(b) shows that under the axial restraint stiffness of α = 0.1, a net tensile axial force is produced from restrained thermal contraction. It should be noted that axial tension may have been induced under α = 0.5 and α = 1.0 if the analysis time was extended beyond 3 hours, allowing the beam to cool down to room temperature. However, the analysis time was limited to 3 hours to reduce the computational cost associated with the parametric study. Nonetheless, Figure 3-14(b) shows that the likelihood of developing tension from restrained thermal contraction increases with decreasing axial restraint stiffness, since lower compressive axial forces are developed. Finally, the occurrence of tension from restrained thermal contraction should not be mistaken as tensile catenary action. Catenary action occurs under large displacements, when the beam is still in the heating stage.

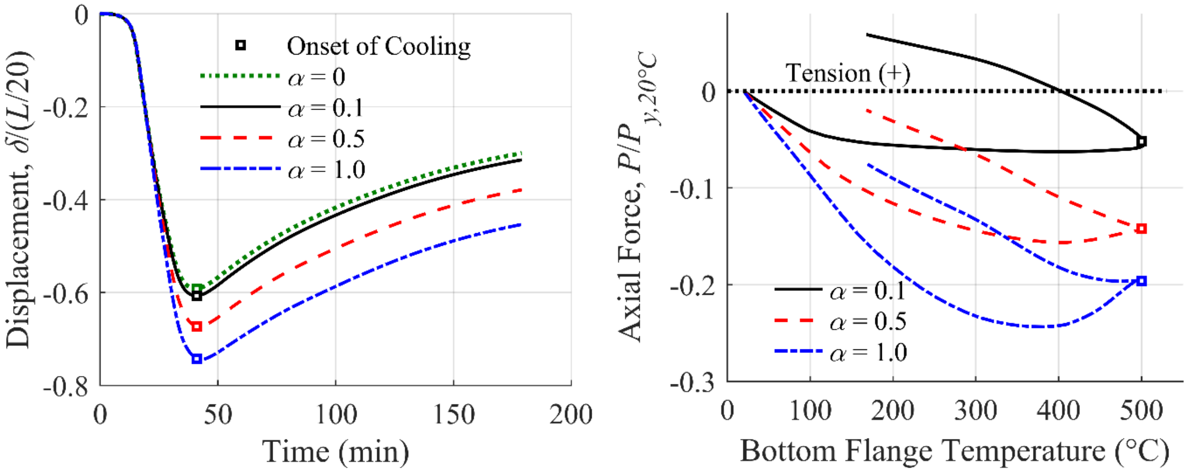

(a) L = 10.5 m, y/d = 0.75 (b) L = 10.5 m, y/d = 0.75

Figure 3-14. Influence of axial restraint stiffness under a short-hot natural fire: (a) mid-span displacement response; (b) axial force response.

3.5.2. Effect of Beam Length

The effect of beam length is shown in Figure 3-15, which shows the mid-span displacement and axial force response of a composite beam with parameters α = 1.0, μ = 0.7, y/d = 0.75 under an ASTM E119 standard fire. Relative values of displacements and axial force are shown, with displacements normalized by $L/20$ and axial forces normalized by $P_{y,20°C}$. The effects of beam length under a short-hot fire are not shown, since similar trends in the displacement response is observed. A discussion on the influence of length on the axial force response under a short-hot fire is reserved for Section 3.5.5.

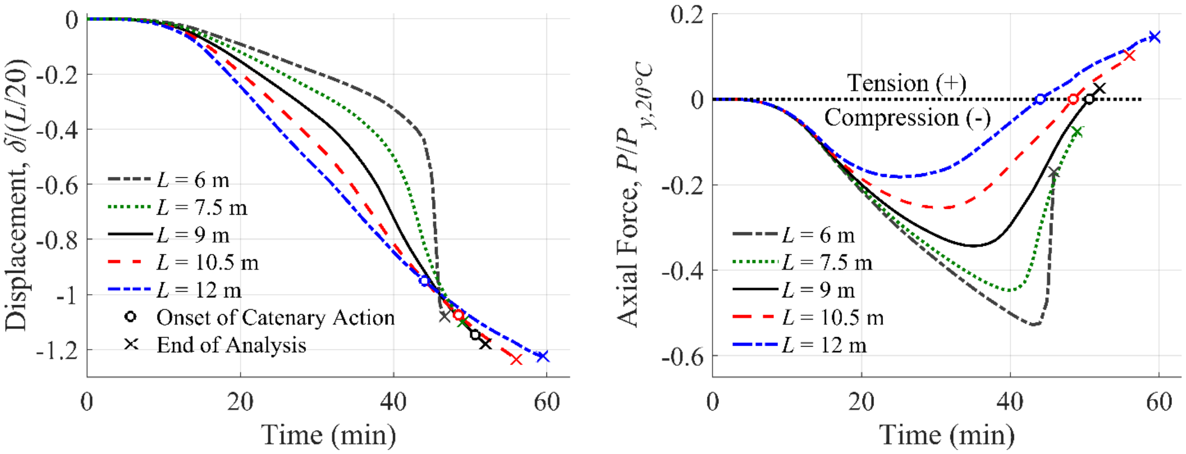

(a) α = 1.0, μ = 0.7, y/d = 0.75 (b) α = 1.0, μ = 0.7, y/d = 0.75

Figure 3-15. Influence of beam length under an ASTM E119 fire: (a) mid-span displacement response; (b) axial force response.

Figure 3-15(a) shows that the rate of deflection in the early stages of the fire is influenced by the length of the beam. Beams with longer spans have a larger initial deflection rate than beams with shorter spans. This is expected since beams with longer spans have smaller bending stiffness (i.e., *EI*/*L*). This explains why the displacement response in Figure 3-15(a) is largely influenced by the length of the beam. Although larger deflections are observed for beams with longer spans in the early stage of the fire, Figure 3-15(a) shows that the deflection rate of longer beams (i.e., *L* = 9 m, 10.5 m, and 12 m) slows down, resulting in smaller displacements in the later stage of the fire. The decrease of the deflection is caused by the onset of tensile catenary action. In Figure 3-15 the onset of catenary action is represented by an ‘o’ marker. Beams with span length *L* = 9 m, 10.5 m, and 12 m undergo catenary action before failure, while beams with span *L* = 6 m and 7.5 m fail in the beam-column stage as shown in Figure 3-15(b). Catenary action generally occurs in beams with longer spans, which explains why the deflection rate of beams with span length *L* = 9 m, 10.5 m, and 12 m reduces in the later stage of the fire. Additionally, the onset of catenary action occurs quicker for beams with longer spans as shown in Figure 3-15(b), which shows that for those beams which undergo tensile catenary action (i.e., L = 12 m, 10.5 m, and 9 m), the onset of catenary action occurs quicker for beams with longer spans. This observation explains why a smaller displacement rate is observed sooner for beams with longer spans, relative to beams with short spans that undergo tensile catenary action. For beams with span L = 6 m and 7.5 m the deflection rate continues to increase monotonically until failure occurs since catenary action is not activated.

Not all beams undergo tensile catenary action before failure. Tan and Huang [100] attributed this to "quasi-buckling", which caused failure of stocky beams (i.e., beams with low slenderness) before the onset of catenary action. The failure is due to sudden buckling of stocky beams, in the same way that a heated column buckles in compression, which results in numerical instability of the static analysis procedure. Quasi-buckling is not a result of local buckling of the web and/or flange. Besides, local buckling is not captured by the beam element representing the wide-flanged steel section. In this investigation, composite beams comprised of stocky steel beams also fail under quasi-buckling, prior to the onset of catenary action. Figure 3-15(b) shows that larger compressive axial forces are produced in stockier shorter beams, which aligns with the quasi-buckling failure explanation. In general, beams with shorter spans fail in the compressive beam-column stage, while beams with longer spans fail in the tensile catenary stage.

Figure 3-15(a) shows that the onset of catenary action generally occurs after the deflection limit of $L/20$ is surpassed, which aligns with observations made from experimental testing of restrained steel beams [95,96]. For the span length of L = 12 m, catenary action is activated prior to the deflection limit of $L/20$, at a normalized deflection of -0.95. However, this is still acceptably close to the deflection limit. This demonstrates that care should be taken when using the deflection limit of *L*/20 to evaluate the FRR of restrained composite beams with long spans. Utilizing this deflection limit may undermine the improved performance associated with tensile catenary action, since it evaluates the performance of the beam while in the compressive beam-column stage. In the beam-column stage, larger displacements are observed at a much quicker rate in beams with longer spans. This translate to smaller FRR for beams with longer spans. However, the results in Figure 3-15(a) demonstrates that beams with longer spans have larger FRR (i.e., a larger failure time, shown in ‘x’) than beams with short spans. The improvement of FRR is associated with the onset of catenary action, which occurs in larger beams prior to failure, and allows the beam to carry loads at much larger displacements.

The direct membrane force per unit width in the longitudinal direction of the composite slab under an ASTM E119 fire are shown in Figure 3-16 for beam span *L* = 6 m, *L* = 9 m, and *L* = 12 m. These membrane forces are taken at the end of the analysis. Membrane forces in shell elements are analogous to axial forces in beam elements, and are used herein to investigate the behavior of the composite slab. Negative forces per unit width correspond to compressive forces, while positive forces per unit width correspond to tensile forces. The results show that there is a compressive region at the mid-span of the slab for each beam, regardless of the span length. This compressive region decreases in both magnitude and size as the length of the beam increases. In particular, the compressive regions at the mid-span of the beams with span *L* = 9 m and *L* = 12 m shows that the entire slab does not have to be in tension for a composite beam to undergo tensile catenary action. In addition, Figure 3-16 shows that each beam has a tensile region at the slab ends. However, it should be noted that the tensile region at the slab ends for the beam with span *L*= 6 m is a result of the rotational spring at the end of the supports (see Figure 3-2), which generates a negative moment during beam deflection. The tensile region is not a result of tensile catenary action, which does not occur as shown previously in Figure 3-15(b). A rotational stiffness corresponding to 10% of the rotational stiffness of the steel beam $4EI/L$ was arbitrarily chosen for the analyses. Shorter beams have a larger rotational spring stiffness compared to longer beams, and thus the rotational spring plays a larger role in generating the tensile region at the end of the slab in shorter beams. The results also show that for beams undergoing tensile catenary action (i.e., L = 9 m and L = 12 m), the tensile region at the end of the beam increases with increasing beam span.

Due to the idealized representation of the composite slab, a complete investigation of localized failures such as concrete crushing and cracking were not investigated herein. These idealizations, including the use of a smeared representation for steel reinforcement, using a tension stiffening model to account for rebar-concrete interaction, and implicitly including the orthotropic effects of the ribs, allowed the global response of the slab to be reasonably captured. However, local responses of the composite slab may not be accurately represented. An investigation of these localized failures are thus left as a future endeavor for researchers who opt to use more sophisticated idealizations which considers the entirety of the composite slab using solid continuum elements.

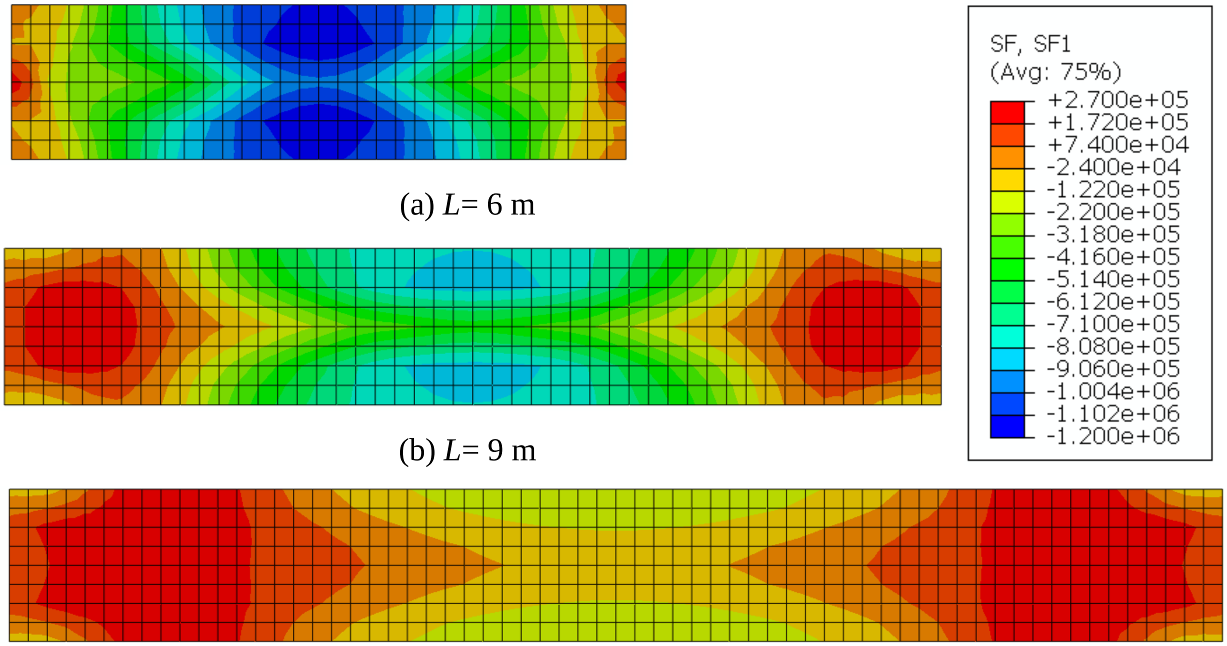

(a) L= 6 m

(b) L= 9 m

(c) L = 12 m

Figure 3-16. Direct membrane force per unit width of the composite slab in the longitudinal direction of the composite beam under an ASTM E119 fire: (a) L = 6 m; (b) L= 9 m; and (c) L = 12 m. Positive magnitude corresponds to tensile forces, while negative magnitude corresponds to positive forces. Membrane forces have units of [N/m].

3.5.3. Effect of Restraint Location

The effects of the axial restraint location are shown in Figure 3-17 for a restrained composite beam with parameters L = 10.5 m, α = 0.5, and μ = 0.7 under an ASTM E119 standard fire. Relative values of displacements and axial force are shown, with displacements normalized by $L/20$ and axial forces normalized by $P_{y,20°C}$. The effects of axial restraint location under a short-hot fire are not shown, since similar trends were observed.

Figure 3-17(a) shows that the deflection rate of the beam is influenced by the location of the axial restraint at the support. Smaller displacements are produced in the early stages of the fire when the axial restraint is positioned near the bottom of the beam (i.e., $y = d/4$). When the axial restraint is positioned at the bottom of the beam, the eccentricity of the fire-induced compression generates a moment at the ends of the beam which counteracts the sagging moment at the mid-span of the beam [94]. This counteracting moment reduces the moment at the mid-span, which reduces the deflection in the early stage of the fire when the beam is in the compressive beam-column stage. However, Figure 3-17(a) shows larger displacements are produced in later stages of the fire when the location of the axial restraint is near the bottom of the beam (i.e., $y = d/4$). The early improvement in deflection from positioning the axial restraint near the bottom of the beam diminishes when the peak compressive axial force is reached. The peak compressive axial force in the beam acts to reduce the moment capacity of the beam, causing the deflection rate to increase. Figure 3-17(b) shows that peak compression is larger when the axial restraint is positioned near the bottom of the beam, which explains why larger displacements are observed under $y = d/4$ at later stage of the fire prior to the onset of catenary action.

Tensile catenary action was induced in the composite beam regardless of the position of the axial restraint as shown in Figure 3-17(b). However, the onset of catenary action occurs quicker when the axial restraint location is positioned at the bottom of the steel beam. This position is associated with a larger peak compression, and subsequently larger displacement rates, which allows the beam to reach catenary action much quicker. An examination of Figure 3-17(b) also shows that peak tensile force increases with increasing axial restraint location. Smaller peak compression generally allows larger tensile forces to be developed in the beam before failure occurs.

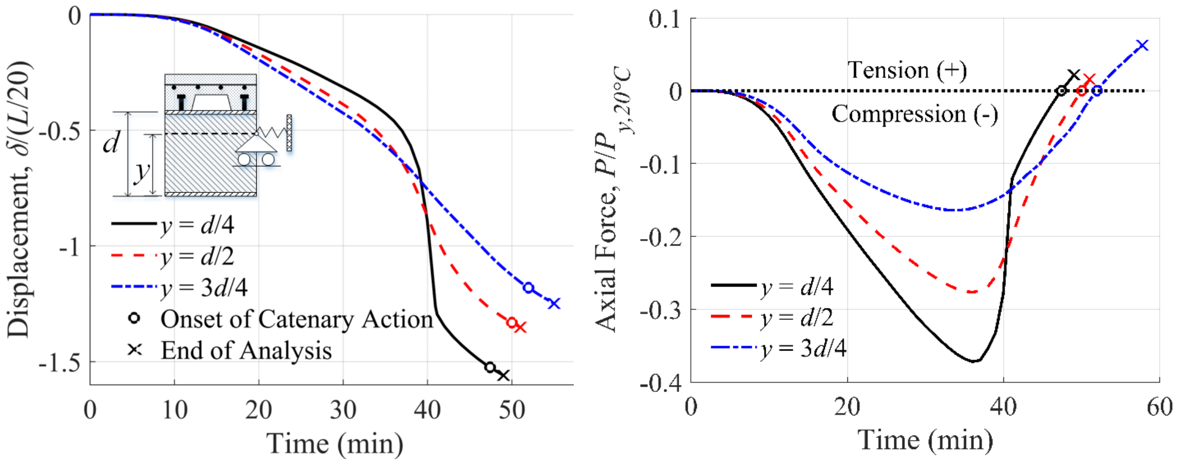

(a) L = 10.5 m, α= 0.5 (b) L = 10.5 m, α= 0.5

Figure 3-17. Influence of axial restraint location under an ASTM E119 standard fire: (a) mid-span displacement response; (b) axial force response.

The influence of the axial restraint location on the peak displacement at failure depends on the length of the beam as shown in Figure 3-18(a). Beams with short spans experience larger peak displacements when the axial restraint is positioned near the top of the beam, while beams with long spans experience larger peak displacements when the axial restraint is positioned near the bottom of the beam. The difference is due to the stage at which failure occurs. Beams with short spans tend to fail in the beam-column stage, where larger displacements are associated with the larger restraint location as shown in Figure 3-17(a). Conversely, beams with long spans tend to fail in the catenary stage, where larger displacements are associated with the smaller restraint location as shown in Figure 3-17(a). This demonstrates that to reduce deflection in short beams, the axial restraint should be positioned near the bottom of the beam, while in long beams, the axial restraint should be positioned near the top of the beam.

Figure 3-18(b) shows the influence of the axial restraint location on the peak compression under an ASTM E119 standard fire. In general, peak compression decreases with increasing axial restraint location. Additionally, Figure 3-18(b) shows that peak compression decreases with increasing beam length. Lastly, Figure 3-18(b) shows that the influence of restraint location on the peak compression increases with increasing beam length. That is, peak axial compression is influenced more heavily by the change in the restraint location in beams with longer spans.

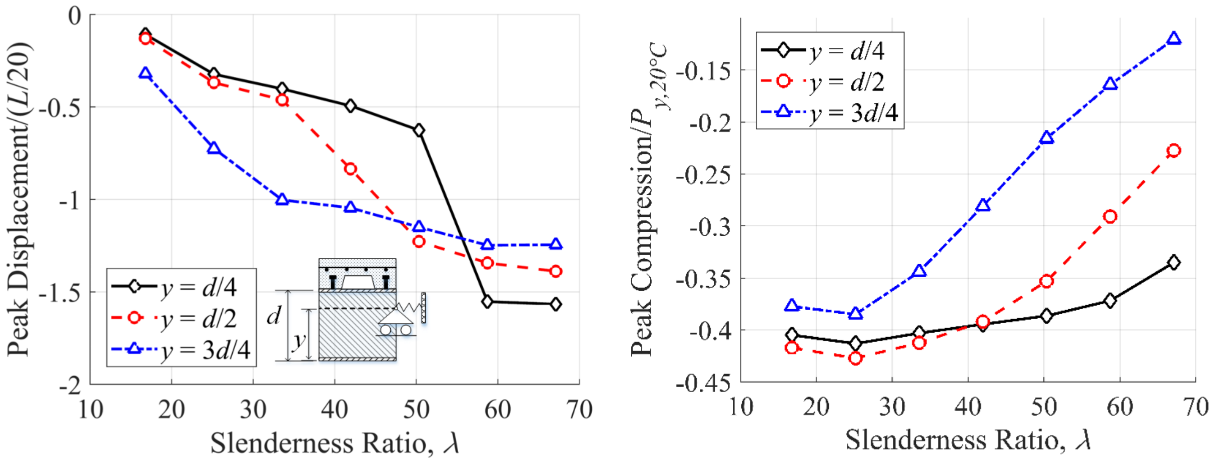

(a) $\alpha = 0.5$, $\mu = 0.7$

(b) $\alpha = 0.5$, $\mu = 0.7$

Figure 3-18. Influence of slenderness and axial restraint location under an ASTM E119 standard fire: (a) peak displacement analysis; (b) peak compression analysis.

3.5.4. Effect of Load Ratio

The influence of load ratio is presented in Figure 3-19, which shows the response of a composite beam with parameters L = 10.5m, y/d = 0.75, and α = 0.5. Figure 3-19(a) shows that the increase of load ratio causes two actions that are favorable for the development of catenary action: (1) increased deflection; and (2) decreased peak compression. In Figure 3-19(b) catenary action is activated under a load ration of μ = 0.7 and occurs after the deflection limit of L/20 is reached. Under a load ratio of μ = 0.5, catenary action is not activated despite the peak displacement surpassing the deflection limit of L/20.

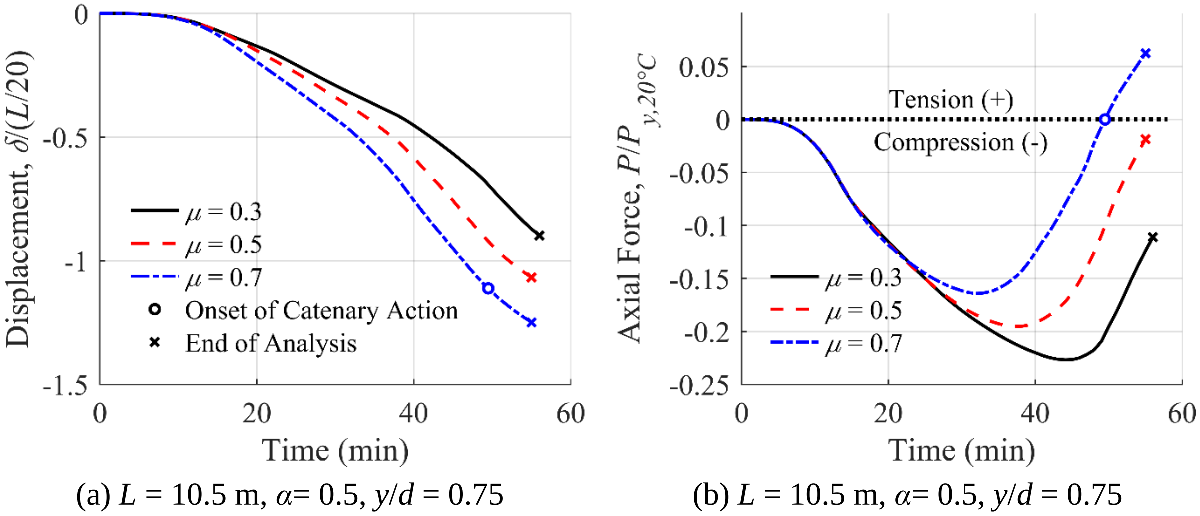

(a) L = 10.5 m, α= 0.5, y/d = 0.75 (b) L = 10.5 m, α= 0.5, y/d = 0.75

Figure 3-19. Influence of load ratio under an ASTM E119 standard fire: (a) mid-span displacement response; (b) axial force response.

A closer investigation of the influence of the load ratio on the peak displacement is presented in Figure 3-20(a), which shows that peak displacement increases with increasing load ratio regardless of the beam length. Alternatively, Figure 3-20(b) shows that the influence of load ratio on the peak compression depends on the length of the beam. Beams with short spans experience a larger peak compression under larger load ratios. However, peak compression decreases with increasing load ratio for beams with long spans. Finally, Figure 3-20(b) shows that the peak compressive axial force can reach up to 40% of the room temperature axial capacity of the steel beam in short composite beams subjected to a large load ratio.

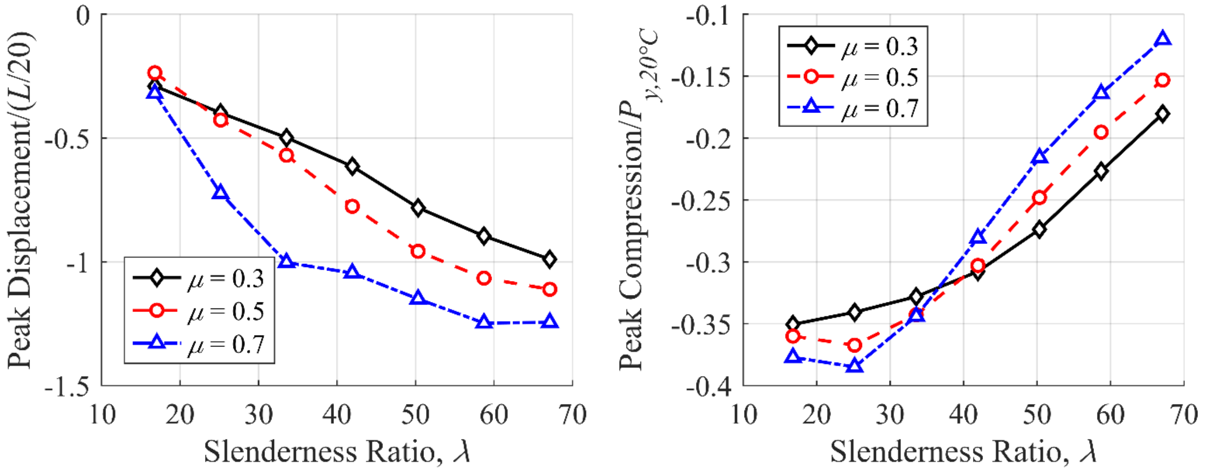

(a) $\alpha = 0.5$, $y/d = 0.75$ (b) $\alpha = 0.5$, $y/d = 0.75$

Figure 3-20. Influence of slenderness and load ratio under an ASTM E119 standard fire: (a) peak displacement analysis; (b) peak compression analysis.

3.5.5. Restrained Thermal Contraction

Figure 3-14(b) demonstrated that cooling from the decay phase of a natural fire activates restrained thermal contraction. Under a low axial restraint stiffness of $\alpha = 0.1$, fire-induced tension was produced in the composite beam. An investigation of the fire-induced tension due to restrained thermal contraction is presented in Figure 3-21. Figure 3-21(a) shows that the peak tension from restrained thermal contraction increases with increasing beam length and can reach up to 6% of the axial capacity of the steel beam at room temperature $P_{y,20°C}$. Figure 3-21(a) also shows that the influence of the restraint location on the peak tension due to restrained thermal contraction depends on the length of the beam. A change in the axial restraint location has a larger influence on the peak tension in beams with large spans, with larger tension developing when the axial restraint is positioned near the top of the beam (i.e., $y = 3d/4$). However, the influence of the axial restraint location on the peak tension is minor. For instance, for $L = 12$ m the peak tension can reach up to 6% of $P_{y,20°C}$ under $y = 3d/4$, while peak tension can reach up to 4.5% of $P_{y,20°C}$ under $y = d/4$.

Figure 3-21(b) shows the influence of load ratio on the peak tension generated from restrained thermal contraction. In general, larger peak tension is produced under a low load ratio. Additionally, the influence of load ratio on peak tension depends on the beam length. Beams with shorter spans experience a larger influence of load ratio on the peak tension compared to beams with longer spans.

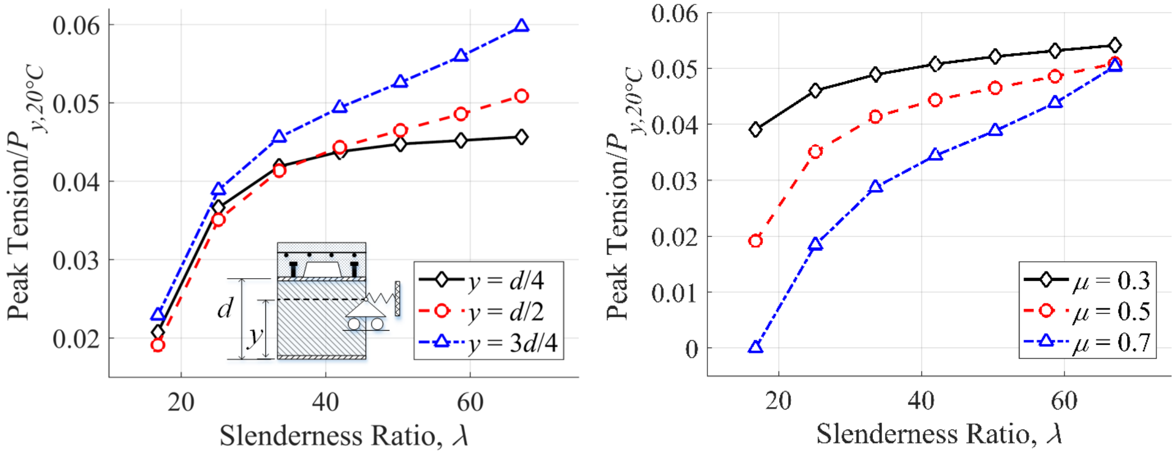

(a) $\alpha = 0.1$, $\mu = 0.5$

(b) $\alpha = 0.1$, $y/d = 0.5$

Figure 3-21. Peak tension produced by restrained thermal contraction during cooling of a short-hot fire: (a) influence of slenderness ratio and axial restraint location; (b) influence of load ratio and span length.

3.6. Discussion

3.6.1. Modeling Approach

When a composite floor system is modeled using an assembly of beam and shell elements, the reference location of the structural elements are commonly depicted in the literature as being arbitrary. While this objectivity holds for axially unrestrained structures, the reference location of the structural elements are no longer arbitrary when axial restraint is present. This modeling issue has remained largely unreported because model validations of composite flexural systems are carried out using fire tests which are predominantly unrestrained.

Previous efforts have been carried out to examine the influence of different modeling approaches when a steel-concrete composite beam consists of beam and shell elements [37,41–43]. However, these investigations were also performed using axially unrestrained structures, which fail to highlight the modeling issue. Rackauskaite *et al.* [44] examined the influence of two different modeling approaches on a case study structure, consisting of a fire-exposed restrained composite beam within a floor slab. A shared-node approach in which the reference of the beam and shell elements were lumped at the slab-beam interface and the traditional approach in Figure 3-6(a) were examined. Although the authors acknowledged the discrepancy of in the displacement and axial force response among each approach, they did not attribute the discrepancy as being associated with the change of the support location with changing position of the beam reference.

The shell-centered approach in Figure 3-6(b) is a popular modeling approach used by researchers when examining steel-concrete composite floor systems exposed to fire. Specifically, it is used in finite element software *VULCAN* [38,77,115], which is a specialist software used for the analysis of composite steel-framed buildings exposed to fire. A possible reason why the approach is used in the software may be attributed to the belief that a composite floor system is an eccentrically-stiffened plate. Eccentrically-stiffened plates can be found in aerospace and naval structures and consist of thin plates that are stiffened by eccentric beams as shown in Figure 3-22. In a stiffened plate problem, supports and loads (both transverse and lateral) act primarily on the plate. Thus, in a macro-model idealization of a stiffened plate, the results are invariant on the location of the beam reference, since the boundary conditions are attached to the plate. The use of the shell-centered approach leads to correct structural predictions in this problem, and the approach has been used heavily in the past, specifically for the analysis of ship structures [119–121]. However, a steel-concrete composite floor system is not strictly an eccentrically-stiffened plate, since the supports are located on the beams, and the modeling approach is invariant on the location of the shell reference. In the presence of an axial-restraint, the shell-centered approach leads to incorrect structural predictions as shown in Figure 3-12(a).

Although most structural engineering problems can be considered axially unrestrained (and the analysis results are invariant on the modeling approach used), the authors hope that the findings presented in this chapter help limit the variability in the modeling approaches observed in future research. This is especially important in the context of structural fire engineering, where restrained structural responses are more common and play an important role in the structural resistance to fire.

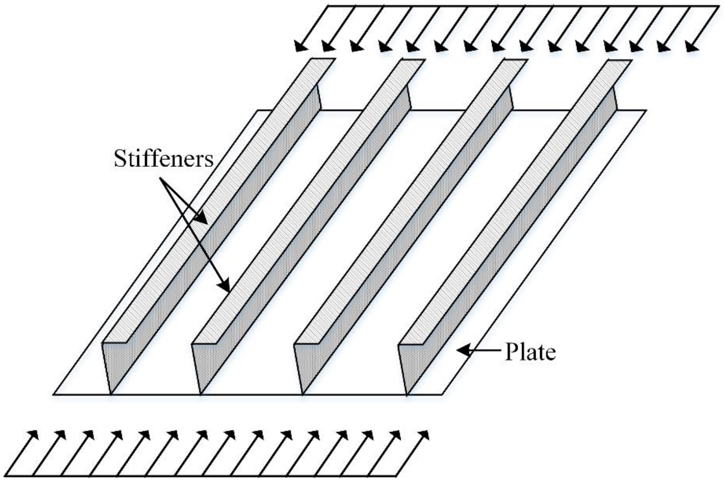

Figure 3-22. Eccentrically-stiffened plate problem with in-plane compressive loads.

3.6.2. Restrained Composite Beams

The results showed that the fire response of a restrained composite beam is heavily influenced by the length of the beam; short beams fail in the compressive beam-column stage, while composite beams with longer spans tend to fail in the tensile catenary stage. Additionally, conditions which are favorable for inducing tensile catenary action were determined, which can be used by engineers to improve the fire resistance of restrained composite beams. These conditions include a longer beam span, an increase of the axial restraint stiffness, an increase of the load level, and the positioning of the axial restraint near the top of the steel beam.

The study also showed that catenary action is generally developed after the deflection limit of $L/20$ is reached. Two major points should be recognized from this observation: (1) utilizing this deflection limit to evaluate the fire resistance of a restrained composite beam may undermine the improved performance associated with tensile catenary action; and (2) very large displacements are required to activate tensile catenary action.

The first point demonstrates a displacement-based failure criterion may not be adequate for analyzing a restrained composite beam. Although the use of a displacement-based failure criterion is common in structural fire engineering, it should only be used for unrestrained structures that experience run-away failure at the onset of failure. In the numerical study, the fire resistance was taken as the last converged point of the static analysis, which presents a better failure metric for restrained beams exposed to fire. However, analysts should be careful with this metric, since instability of the static analysis does not necessarily imply structural failure. Moreover, it is important to note that deflection limits may need to be applied in structural fire experiments for practical reasons since large structural deflections can cause damage to furnaces or other testing equipment.

Designers should consider the effects of large displacements before allowing composite beams to engage in tensile catenary action. Excessive concrete crushing and cracking of the slab occurs at very large displacements. In the parametric study, numerical instability occurred before extensive concrete failure could be reached, and its effect on the restrained composite beam were not strictly investigated. Nonetheless, designers should consider maintaining this level of damage to an acceptable level, as excessive concrete crushing and cracking of the slab may lead to compartment integrity failure. Even if large axial forces can be tolerated by the adjacent structure, excessive concrete crushing and cracking during catenary action may allow flames to spread to neighboring compartments.

Designers should also consider the effects of large tensile forces on the connections of the beam. The connection details at the ends of the beam were not considered in the analysis model, and thus potential failure modes associated with the connections were not considered.

3.7. Conclusion

A numerical analysis of an axially- and rotationally-restrained composite beam was performed to investigate the influence of various parameters, including the fire type, beam slenderness, load factor, restraint stiffness, and the restraint location. Numerical validations for both the heat transfer model and structural model were presented to establish confidence in the results. The following conclusions were made based on the results presented:

- The macro-modeling approach of a composite beam comprised of beam and shell elements is not arbitrary when axial restraint is present. Specifically, the beam reference should be positioned at the geometric centroid of the connection.

- An implicit consideration of high-temperature creep via the Eurocode material models of both steel and concrete was adequate to capture the fire response of a restrained composite beams studied here.
- An increase in the axial restraint stiffness leads to larger displacements in the early stages of a fire. However, in the later stages of a fire, an increase in the axial restraint stiffness leads to smaller displacements. This effect is attributed to tensile catenary action.
- The fire response of a restrained composite beam is heavily influenced by length of the beam. Composite beams with short spans tend to fail in the compressive beam-column stage, while composite beams with longer spans tend to fail in the tensile catenary stage.
- Conditions that are favorable for inducing catenary action in a restrained composite beam include longer beam spans, increased axial restraint stiffness, increased load ratio, and positioning of the axial restraint near the top of the beam.
- Material cooling from the decay phase of a natural fire activates restrained thermal contraction. Under a low axial stiffness, axial tension can be developed, which can reach up to 6% of the axial capacity of the steel beam at room temperature.
- Catenary action is generally developed after the deflection limit of $L/20$, demonstrating that care should be used when using this deflection limit to evaluate the fire resistance of a restrained composite beam. Utilizing this deflection limit may undermine the improved performance associated with catenary action, since it evaluates the performance of the beam while in the compressive beam-column stage.

Experimental tests of restrained composite beams exposed to fire are required to verify the numerical findings presented. Experimental testing can also be used to investigate the influence of the connection behavior, which was not investigated in the paper. Nonetheless, the findings presented herein provide a numerical basis for the preliminary understanding of restrained composite beams exposed to fire.

Chapter 4 Thermal Response of Steel-Concrete Composite Floor Systems under Traveling Fires

The adequacy of prescriptive codes to safeguard against traveling fires was investigated by analyzing the thermal response of two composite floor systems exposed to traveling fires. The composite floor systems were also exposed to a standard fire and two natural fire exposures. The fire rating of each structural member was quantified using the temperature limits available in the ASTM E119 standard. An analysis of peak temperatures is also presented to understand the spatial and temporal evolution of temperature in structural members during a traveling fire. The results show that peak temperature is influenced by the traveling fire size, insulation thickness, and relative position of the member within the floor plan. In addition, fire insulations derived from prescriptive approaches do not provide a consistent level of safety among different member types (i.e., beams, columns, etc.) and different fire types (i.e., standard fire, natural fire, etc.). Furthermore, such insulation designs may not provide adequate protection under traveling fires. The findings demonstrate that fire protection engineers should use an analysis procedure to verify the adequacy of insulation derived from prescriptive approaches, when applied to structural members exposed to traveling fires.

4.1. Introduction

Prescriptive approaches for ensuring fire safety of structures revolve around the standard furnace testing of structural members [6], where often, the condition of acceptance for the test is that the internal temperature of the member stays below a predefined temperature limit for a desired period of time. The standard fire test forms the basis of the regulation of the passive fire protection (i.e., thermal insulation) applied to structural members, primarily under the assumption that equal or greater level of safety is provided during a real fire event. The validity of this assumption rests on the fire scenario used during a fire resistance test, which has little resemblance to a fire exposure occurring inside a burning compartment (i.e., a post-flashover fire). A standard fire is defined as a nominal fire in which the temperature increases monotonically during the entire duration of the test and was constructed to represent a worst-case flashover fire. Due to the absence of cooling, the standard fire has been historically viewed as conservative for most purposes.

However, it is generally believed that a fire occurring in a large open-plan compartment does not reach flashover, and instead burns locally and travels across the floor plan (i.e., a traveling fire) [8–10]. Traveling fires are characterized by their high flame temperature, rapid heating rate, long burning durations, and spatially non-uniform temperatures within a large floor plan [9,11,12]. These attributes are not present in a conventional post-flashover fire, which occurs in a floor plan that is subdivided into compartments and is usually characterized by moderate temperature and heating rate, spatially-uniform temperature, and short burning duration. Consequently, a traveling fire is considerably different from a post-flashover fire, which casts doubt on the effectiveness of current fire protection strategies to ensure safety in open-plan compartments. Furthermore, post-flashover fires and traveling fires are mutually exclusive in that a post-flashover fire will not occur in an open-plan compartment [8–10], which furthers highlights the significance of this investigation.

Currently, traveling fires are not considered in the framework of prescriptive design of structures against fire, since existing fire design guides [4,5] and standards [6,7], were developed long before the inception of traveling fires as design fires (e.g., [81]) and have yet to consider such fires explicitly. Thus, current prescriptive codes may prescribe fire safety solutions that may be unsafe against traveling fires. Specifically, fire insulation design of structural members in open-plan compartments may not provide basic life safety and stability requirements during a traveling fire.

Traveling fires have been observed in many fire accidents worldwide. Notable accidents include the First Interstate Bank fire in Los Angeles in 1988 [13], the One Meridian Plaza fire in Philadelphia in 1991 [14], the World Trade Center (WTC) Building 7 fire in New York City in 2001 [15], the Windsor Tower fire in Madrid in 2005 [16], the Faculty of Architecture Building fire in TU Delft in Netherland in 2008 [17], and the Plasco Building fire in Tehran, Iran, in 2017 [18]. In all these accidents, the floor plans were not compartmentalized, resulting in traveling fires that traveled across the floor plans. Significant fire damage was observed in all these accidents, with partial and complete collapse occurring in several cases. In the United States (U.S.), the potential vulnerability of current U.S. fire codes to safeguard against traveling fires was highlighted in the collapse investigation of the WTC Building 7 by the National Institute of Standards and Technology (NIST), which revealed that a major factor contributing to the collapse of the building was uncontrolled traveling fires [15]. Despite the historically poor performance of structures under traveling fires, an investigation on the adequacy of prescriptive fire codes to safeguard against traveling fires has not yet been carried out.

Previous research on traveling fires has focused on both the analysis of peak temperature and the analysis of failure based on a temperature criterion [11,12,21,122]. Different types of structures have been examined, including a reinforced concrete (RC) floor plan [11,21], a steel-concrete composite floor plan [122], a RC frame [12], and a steel frame [12]. Traveling fires are designated by the percentage of the local burning size A_f relative to the total floor area of the compartment A (e.g., a 10% traveling fire designates a fire in which A_f is 10% of A). This designation is common in the research literature.

Law et al. [21] examined the thermal response of a RC floor plan under various fire types, including a family of traveling fires with sizes ranging from 1% to 100%, two natural fires (i.e., a short-hot and long-cool fire), and a standard fire. The results showed that the largest peak rebar temperature was observed under a 10% and 25% traveling fire. The peak rebar temperature observed under a 10% and 25% traveling fire were also larger than those observed under a long-cool and short-hot fire. To produce a similar peak rebar temperature under a standard fire, a 1 h 37 min and a 1 h 54 min fire exposure was required, respectively. This led the authors to conclude that current design approaches, which only considers post-flashover fires, cannot be assumed to be conservative since larger peak rebar temperatures were observed under a traveling fire.

Stern-Gottfried and Rein [11] examined the thermal response of a RC floor plan under a family of traveling fires with sizes ranging from 1% to 100%. Two natural fires (i.e., a short-hot and a long-cool fire) were also examined. The results showed similar findings as Law et al. [21]: (1) a 10% traveling fire size produced the largest peak rebar temperature in the floor plan; and (2) the peak rebar temperature observed under a 10% traveling fire was larger than those observed under a long-cool and short-hot fire. Failure was also examined using a critical rebar temperature of 400 °C. The quickest failure time was produced under the largest traveling fire size of 100%. In general, the failure time decreased with increasing traveling fire size.

Jiang et al. [122] investigated the thermal response of an unprotected steel-concrete composite floor plan under a family of traveling fires with sizes ranging from 4% to 42%. Using a temperature limit of 550 °C for steel beams, several key findings were observed, including: (1) the quickest failure time was produced under the largest traveling fire size of 42%; (2) the failure time of the steel beams generally increased with distance away from the fire origin; (3) the largest peak temperature in the composite slab was produced under the smallest traveling fire size of 4%; and (4) the peak temperature in the composite floor slab generally increased with distance away from the fire origin. The results demonstrated that peak temperature and failure time in a composite floor plan are uniquely influenced by the traveling fire size.

Rackauskaite et al. [12] investigated the thermal response of a RC and a fire-protected steel frame under a family of traveling fires, with fire size ranging from 0.3% to 55%. The results showed that peak temperature in both frames were influenced by the fire size, and generally occurred away from the fire origin. In the steel frame, the largest peak temperatures in the floor beams were observed under a 10% traveling fire, and not the smallest traveling fire size of 0.3% examined. Similar conclusions were made by Stern-Gottfried and Rein [11] and Law et al. [21], albeit in a RC floor plan.

The adequacy of prescriptive fire codes to safeguard against traveling fires have not been thoroughly studied. Specifically, insulation design of structural members based on prescriptive approaches may be unsafe against traveling fires. To investigate this issue, a series of heat transfer analyses were carried out to determine the thermal response of two steel-concrete composite floor systems exposed to a family of traveling fires. The passive fire protection of the two floor plans were designed using the design listings from the Underwriters Laboratories (UL) [104]. The improved traveling fires methodology [12] was used to define the traveling fire exposures, with the heat transfer analyses carried out using the finite element software ABAQUS [80]. The fire rating of each structural member was quantified using the temperature limits available in the American Society for Testing and Materials (ASTM) E119 [6] standard. For comparative purposes, the composite floor systems were also exposed to an ASTM E119 standard fire and two natural fire, including a short-hot fire and a long-cool fire.

4.2. Case Study Structures

Two case study structures, each steel-framed buildings with composite floor slabs, are examined. Floor plan #1 (based on the designation in Figure 4-1) consists of an interior rigid core, while floor plan #2 utilizes exterior moment resisting frames to resist lateral loads. Both buildings were designed by Agarwal and Varma [123] and adhere to U.S. design codes and standards [2,19,20]. Each building has a rectangular floor plan with 5 bays in the East-West (EW) direction and 3 bays in the North-South (NS) direction, with each bay spanning 7.62 m in length.

The composite floor slab of each building consists of a 65 mm thick light-weight concrete cast on a 75 mm deep ribbed steel deck, reinforced with a 6x 6W1.4/1.4 reinforcement. Interior floor beams in both buildings are W12X19, while girders are W18X35. The perimeter beams in floor plan #1 consists of W12X16 in the NS direction, and W14X22 in the EW direction. The perimeter beams in floor plan #2 consists of W21X93 in the NS direction, and W18X60 in the EW direction. A complete list of column sections for each building are presented in Table 4-1. Only a single-story fire scenario, occurring in the fifth story of the two steel-framed buildings, are examined.

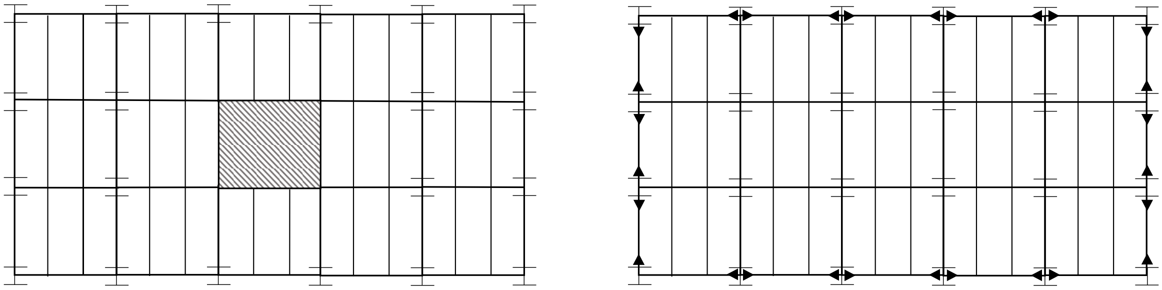
(a) Floor plan #1

(b) Floor plan #2

Figure 4-1. Floor plan of the steel-concrete composite buildings examined: (1) floor plan #1 with an interior rigid core; and (b) floor plan #2 with exterior moment resisting frames.

Table 4-1. Column sections used in floor plan #1 and floor plan #2.

Member Type	Floor Plan #1	Floor Plan #2
Interior Column	W12X58	W12X58
Perimeter NS Column	W10X39	W14X109
Perimeter WE Column	W10X39	W14X99
Corner Column	W8X24	W14X109

4.2.1. Passive Fire Protection Design

Design listings from the Underwriters Laboratories (UL) [104], are chosen for the passive fire protection design of floor plan #1 and floor plan #2. CAFCO 300, a cementitious-based spray-applied fire resistive material (SFRM) from ISOLATEK Int. [103], was chosen for the fire protection design. This product has a thermal conductivity of κ = 0.078 W/m-K, specific heat of c = 1200 J/kg-K, and a density of ρ = 240 kg/m^3 at ambient temperature [103].

Fire ratings of 1 h and 2 h are utilized separately to define the passive fire protection applied to all structural members of each floor plan. The required thickness of SFRM to achieve a fire rating of both 1 h and 2 h in all the steel columns are presented in Table 4-2. The fire protection design of the steel beams are based on UL Design No. *BXUV.N735*, which is applicable for both restrained and unrestrained floor beams supporting a composite floor slab. UL Design No. *BXUV.N735* calls for a SFRM thickness of 13 mm and 24 mm, to achieve a fire rating of 1 h and

2 h, respectively, irrespective of the weight to perimeter ratio (*W*/*D*) of the beam section. The fire proofing of steel columns are based on UL Design No. *BXUV.X790*. The fire proofing of the steel deck of the floor slab is based on UL Design No. *BXUV.D902*. Based on the slab thickness of the two floor plans, no SFRM insulation is required to achieve a fire rating of up to a 2 h. All UL designs selected make use of CAFCO 300, which is consistent with the design.

Table 4-2. Thickness of spray-applied fire resistive material (SFRM) insulation required for all steel columns of floor plan #1 and floor plan #2.

Steel Section	Floor Plan	SFRM Thickness (mm)	
		1 h Rating	2 h Rating
W8X24	Floor plan #1	21	41
W10X39	Floor plan #1	18	35
W12X58	Floor plan #1 and #2	16	30
W14X99	Floor plan #2	13	25
W14X109	Floor plan #2	13	24

4.3. Fire Exposure

The two floor plans are exposed to a variety of fire types, including a family of traveling fires, two natural fires (i.e., post-flashover fires), and a standard fire. Details on each fire type are presented in the following sections.

4.3.1. Traveling Fires

The improved Traveling Fires Methodology (iTFM) [12], which is the latest version of the Traveling Fires Methodology (TFM) [9,11,21], is used to define the spatial and temporal evolution of a one-dimensional (1D) traveling fire. Fundamental to the methodology is the assumption that the burning compartment consists of two distinct regions: (1) the near field region (i.e., the burning region of the fire, where structural members are directly exposed to flames); and (2) the far field region (i.e., the region remote from flames where structural members are exposed to hot gases). The temperature at the near field region is produced using the concept of flame flapping [12], while the temperatures of the far field region are produced using Alpert's ceiling jet correlation [124]. The iTFM defines the temperature-time curves of a traveling fire at discrete locations along the length of the compartment. Furthermore, the iTFM assumes that a 1D traveling fire extends the whole width of the floor plan and travels linearly from one end of the floor plan to the other.

The size of the traveling fire is a variable of the model. To overcome the problem of not knowing the exact size of a traveling fire, a family of traveling fires, ranging from a small traveling fire with a long fire duration to a large traveling fire with a short fire duration, are considered. Since each traveling fire size burns over a specific floor area A_f, traveling fires are designated by the percentage of the burning size relative to the total floor area of the compartment A.

The main input of the iTFM includes the fuel load density q_f, heat release rate per unit area Q'' and the flame flapping angle θ. In this study, these variables are taken as $q_f = 570$ MJ/m^2 (i.e., the 80th percentile design value for an office space [11]), $Q'' = 500$ kW/m^2 (i.e., the typical value for a densely furnished place [11]), and $\theta = 6.5$ ° (i.e., the recommended flapping angle by Quintiere et al. [125]). Here, traveling fire sizes of 5%, 10%, 20%, 30%, 40%, 50%, and a 60% are applied to each floor plan in Figure 4-1. Figure 4-2 shows the relationship between the size of a traveling fire and the fire spread rate and total duration. As the size of the traveling fire decreases, the spread rate decreases, causing the duration time to increase. As a comparison, a 5% traveling fire has a fire duration of 400 min, while a 60% traveling fire has a fire duration of 51 min.

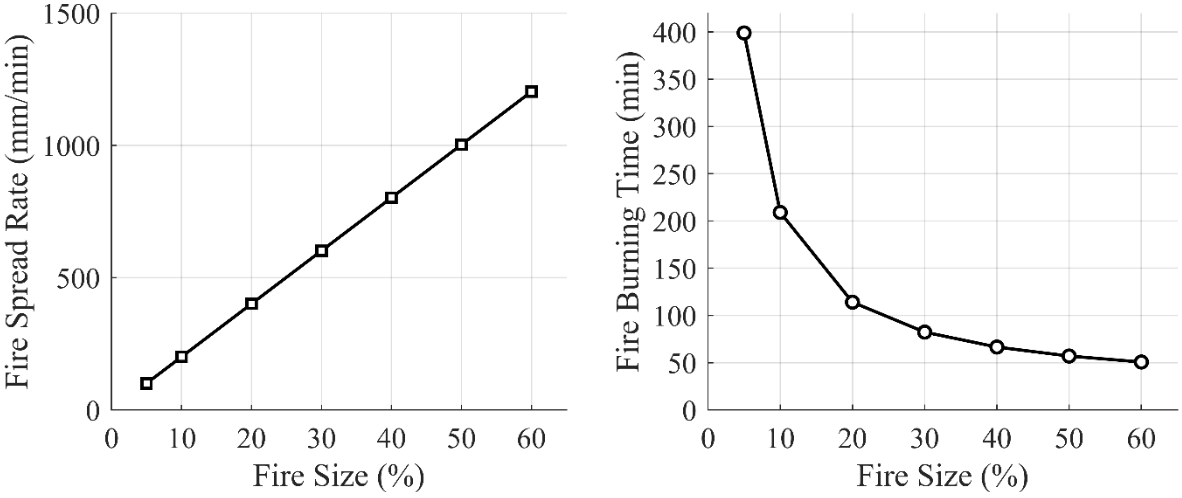

(a)

(b)

Figure 4-2. Properties of traveling fires: (a) spread rate vs. fire size; (b) burning time vs. fire size.

To consider the effects of cooling, a cooling duration of half of the total fire duration is appended to the end of each traveling fire size examined. Figure 4-3 shows the temperature-time curve of each traveling fire size examined at the center of bay 1 and bay 5 of floor plan #1.

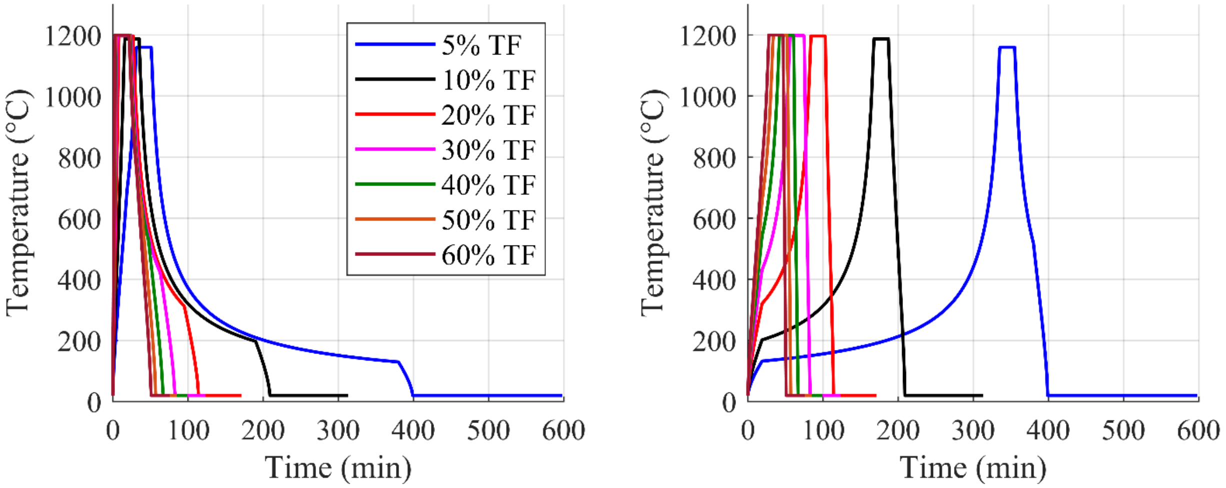

(a) Bay 1

(b) Bay 5

Figure 4-3. Temperature-time curve of each traveling fire size examined in floor plan #1: (a) center of bay 1; and (b) center of bay 5. In the legend, “TF” is an abbreviation for “traveling fire.”

4.3.2. Natural Fires and Standard Fire

Two natural fires, which defines a fire that reaches flashover and includes a cooling phase, and an ASTM E119 standard fire [6], which is used to determine the fire rating of structural members, are also applied to the two floor plans. The natural fires are generated using the fire model by Pettersson et al. [106]. Using two different opening factors of $O = 0.02\ \text{m}^{1/2}$ and $O = 0.08\ \text{m}^{1/2}$, a long-cool and a short-hot fire are produced as shown in Figure 4-4. A high ventilation condition generates a fire with a low peak temperature, but a long fire duration (i.e., a long-cool fire), while a low ventilation condition generates a fire with a high peak temperature, but a short fire duration (i.e., a short-hot fire). The temperature-time curve of these two natural fires, including the ASTM E119 standard fire curve, are compared in Figure 4-4.

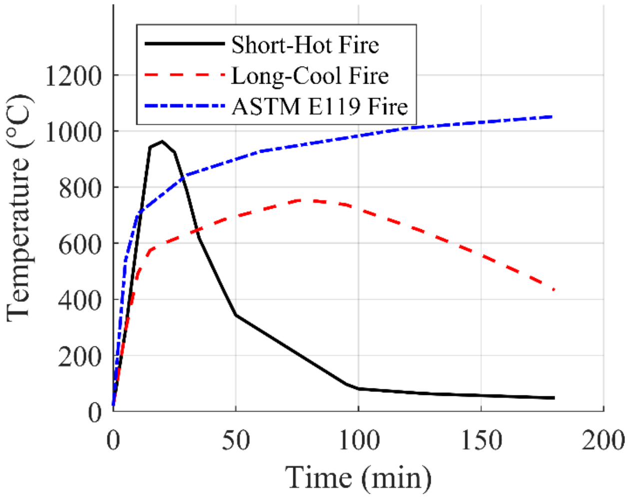

Figure 4-4. Temperature-time curve of a long-cool and short-hot fire produced from the fire model by Pettersson et al. [106] and an ASTM E119 standard fire [6].

4.4. Critical Temperatures

A temperature criterion is used to establish a fire rating of all structural members in each of the two floor plans. The fire rating is based on the comparison of predicted internal temperatures of member with the temperature limits available in the ASTM E119 standard [6]. ASTM E119 gives a temperature criterion in the form of a temperature average across the span/height of the member, or in the form of a single-point maximum as shown in Table 4-3. These temperature limits are independent of the loads applied to structural members and independent of the shape and size of the member. The average temperature limit, in lieu of the maximum single-point limit, is used in the fire rating analysis of steel beams and columns.

Table 4-3. Temperature limit available in the ASTM E119 [6] standard.

Structural Member Type	Limit Type	Temperature Limit (°C)
Steel Columns	Average	538
	Single Point	649
Steel Beams	Average	593
	Single Point	704
Unexposed Side of Floor	Single Point	181
Reinforcing Steel	Single Point	593

4.5. Thermal Analysis

While traveling fires produce spatially non-uniform temperatures within an open-plan compartment, two-dimensional (2D) heat transfer analyses were utilized in lieu of three-dimensional (3D) heat transfer approaches [126–130]. It was assumed that the rate of heat conduction in the longitudinal axis of floor beams and the composite floor slab was gradual in comparison to the spread rate of a traveling fire. This allowed the thermal response of a composite floor slab exposed to a traveling fire to be captured using numerous 2D heat transfer analyses. The iTFM does not currently account for any vertical temperature gradients within a burning compartment, and thus a 2D heat transfer model is adequate for the thermal analysis of heated columns as well.

The thermal analyses were carried out using the finite element software ABAQUS [80]. Four node quadrilateral heat transfer elements *DC2D4* were used to mesh all parts of the analysis models utilized in the study. Figure 4-5 shows the heat transfer model of floor beams (both interior and perimeter beams), columns, and composite floor slab. The model of the interior beam and composite floor slab are reduced using symmetry, with adiabatic boundary conditions assigned to symmetrical edges. Thermal gradients occurring due to partial fire exposure of perimeter beams are accounted for in the analysis model presented in Figure 4-5(b). Thermal gradients occurring in both perimeter and corner columns are accounted for in the analysis model presented in Figure 4-5(c) by adjusting the heated boundary accordingly. The composite slab in the interior and perimeter beam models are included to consider the heat sink effects associated with the slab resting on the steel beam. A detailed model of the composite slab is utilized to extract slab temperatures as shown in Figure 4-5(d), which accurately accounts for the shape of the slab. Following the results of a sensitivity analysis, a mesh size of 3 mm and a time increment of 1 seconds were chosen for the analyses. These analyses are presented in the APPENDIX.

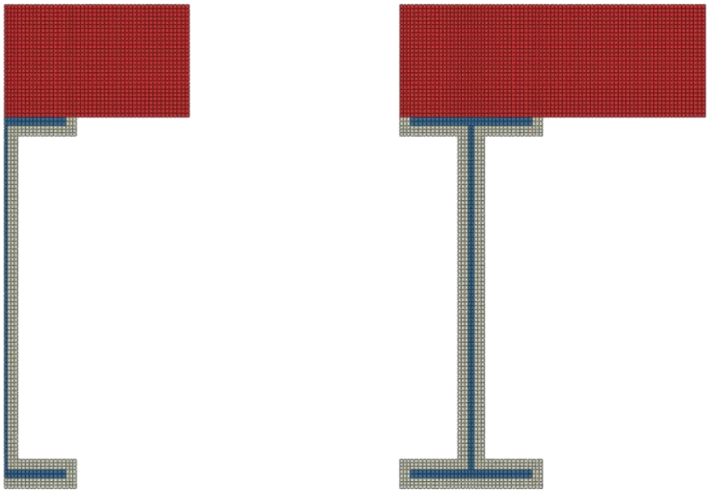

(a) Interior Beam (b) Perimeter Beam

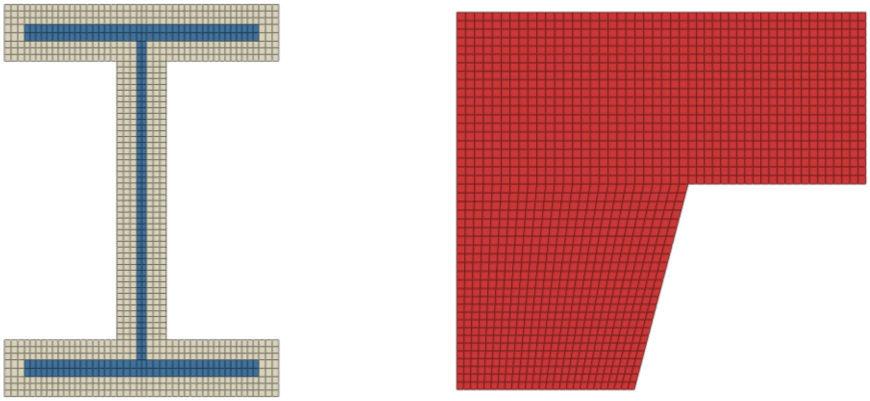

(c) Column (d) Composite Slab

Figure 4-5. Heat transfer model: (a) interior beam; (b) perimeter beam; (c) column; and (d) composite slab.

The temperature-time curve of the fire was used to define the radiative and convective boundary conditions at the fire-exposed surfaces, which is given by:

$$-\kappa \frac{\partial T}{\partial n} = \dot{q}_c'' + \dot{q}_r'' \tag{4-1}$$

where κ is the thermal conductivity of the solid, n is the inward normal to the plane of the surface, $\dot{q}''_r$ is the radiant heat flux, and $\dot{q}''_c$ is the convective heat flux. The radiant heat flux $\dot{q}''_r$ and the convective heat flux $\dot{q}''_c$ are defined by Equation (4-2) and Equation (4-3), respectively.

$$\dot{q}''_r = \Phi \varepsilon_r \sigma_s \left(\overline{T}_g^4 - \overline{T}_s^4 \right) \tag{4-2}$$

$$\dot{q}''_c = h_c \left(T_g - T_s \right) \tag{4-3}$$

In Equation (4-2), Φ is the view factor, which quantifies the geometric relationship between the emitter surface and receiving surface, ε_r is the resultant emissivity, σ_s is the Stephan-Boltzmann constant taken as 5.67 x 10^{-8} W/($m^2 \cdot K^4$), $\overline{T_s}$ is the absolute temperature of the exposed surface (in Kelvin), and $\overline{T_g}$ is the absolute temperature of the hot gas (in Kelvin). To define the radiative boundary conditions, an emissivity of $\varepsilon_r = 0.7$ was used for both steel and concrete as prescribed by Eurocode 4 Part 1-2 [108], while an emissivity of $\varepsilon_r = 0.9$ was used for SFRM insulation [131]. For all surfaces, a view factor of $\Phi = 1$ is conservatively assumed.

In Equation (4-3), T_g is temperature of the hot gas (in Celsius), T_s is the temperature of the fire-exposed surface (in Celsius), and h_c is the heat transfer coefficient of the exposed surface. To define the convective boundary conditions, a heat transfer coefficient of $h_c = 25$ W/(m^2-K) and $h_c = 35$ W/(m^2-K) was used for a standard fire and natural fire respectively as prescribed by Eurocode 1 Part 1-2 [109], while a heat transfer of coefficient of $h_c = 35$ W/(m^2-K) was used for a traveling fire exposure.

Both the radiative and convective boundary conditions of edges not exposed to fire are also defined using Equation (4-2) and Equation (4-3). However, a constant ambient temperature of 20 ºC is prescribed for both T_g and $\overline{T_g}$, and a heat transfer coefficient of h_c = 9 W/(m^2-K) is used as prescribed by Eurocode 1 Part 1-2 [109]. Lastly, symmetrical boundaries are treated as being insulated, that is, the net heat flux through the surface is zero (i.e., $\dot{q}''_c + \dot{q}''_r = 0$ W/m^2).

The main thermal properties required for heat transfer analysis include the thermal conductivity, specific heat, and the mass density. Temperature-dependence of the thermal properties of both concrete and steel were defined using the models in Eurocode 2 Part 1-2 [78] and Eurocode 3 Part 1-2 [87], respectively. Temperature-dependence of the thermal properties of CAFCO 300 insulation are taken from experimental testing by Kodur and Shakya [107]. The complexity of heat transfer of concrete is reduced if the effects of moisture evaporation is considered implicitly in the thermal properties of concrete. The thermal model for specific heat in Eurocode 2 Part 1-2 [78] provides for this implicit consideration by including a spike in specific heat between 100 °C and 115 °C as shown in Figure 4-6(a). Provided that the moisture content of the concrete is not sufficiently high, the effects of moisture evaporation can be adequately considered using the effective specific heat [132]. Eurocode 2 Part 1-2 [78] provides several thermal conductivity models for concrete: (a) an upper bound model for normal weight concrete (NWC); (b) a lower bound model for NWC; and (c) a light-weight concrete (LWC) model. The lower bound model was utilized in the validation cases presented in the following section, which are comprised of NWC, while the LWC model was utilized for the two steel-concrete composite floor systems examined.

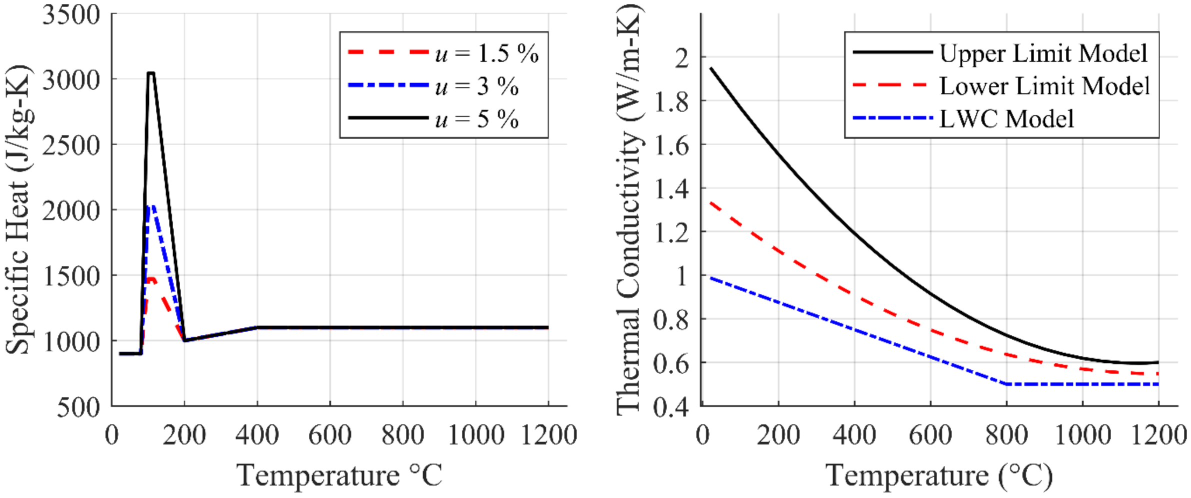

(a) Specific Heat (b) Thermal Conductivity

Figure 4-6. Eurocode 2 Part 1-2 [78] thermal models for concrete: (a) specific heat; and (b) thermal conductivity.

4.5.1. Numerical Validation

Validation of the numerical heat transfer analyses were performed using test data on composite floor slabs exposed to fire including test performed by Guo and Bailey [110], Lim and Wade (i.e., the BRANZ fire tests) [64,65], and Vassart and Zhou (i.e., the COSSFIRE fire test) [66]. The composite slab tested by Guo and Bailey [110] consisted of a 85 mm thick slab cast on a 60 mm steel deck. The composite slab tested by Lim and Wade, identified as the *HiBond* slab, consisted of a 75 mm thick slab cast on a 55 mm steel deck. The composite slab from the COSSFIRE test consisted of a 77 mm thick slab cast on a 58 mm steel deck. Test data on two flat slabs exposed to fire, performed by Lim and Wade [64,65], were also examined to expand the validation study. The two flat slabs, identified as slab *HD12* and slab *D147* [64,65], were both 100 mm thick slabs.

Figure 4-7(a) and Figure 4-7(b) shows the results of the validation study using the two composite floor slabs examined by Guo and Bailey (identified as *Fire 1* and *Fire 2*, respectively), while Figure 4-7(c) and Figure 4-7(d) shows the validation study using the BRANZ *HiBond* composite floor slab and COSSFIRE composite floor slab, respectively. Validation using the test data of the two flat slabs examined by Lim and Wade are shown in Figure 4-8. In both Figure 4-7 and Figure 4-8, experimentally-recorded temperatures are presented with dashed lines with markers, while numerical predictions are presented with solid lines. In each test, “0 mm” is taken as the bottom of the slab, which is directly exposed to fire.

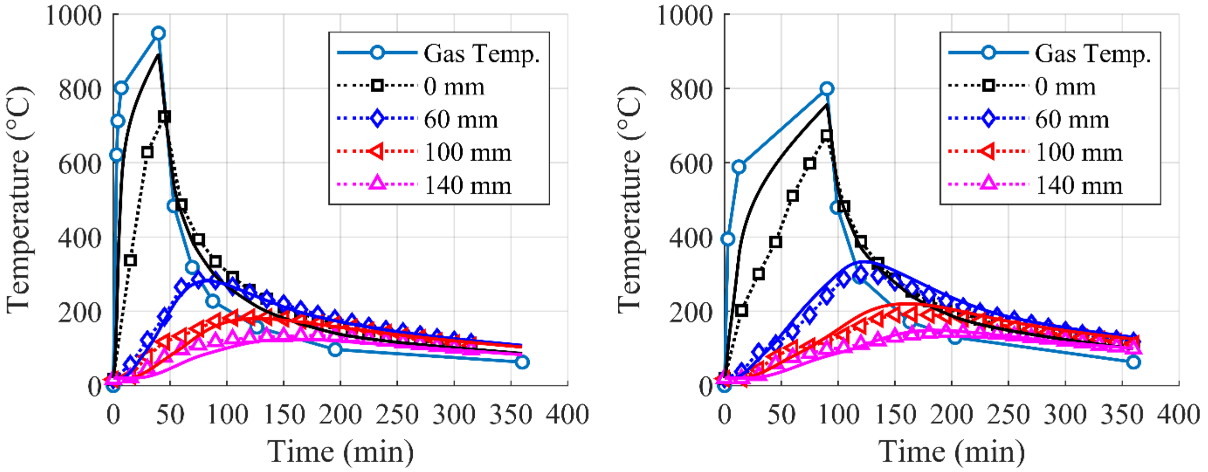

(a) Guo and Bailey's *Fire 1* slab (b) Guo and Bailey's *Fire 2* slab

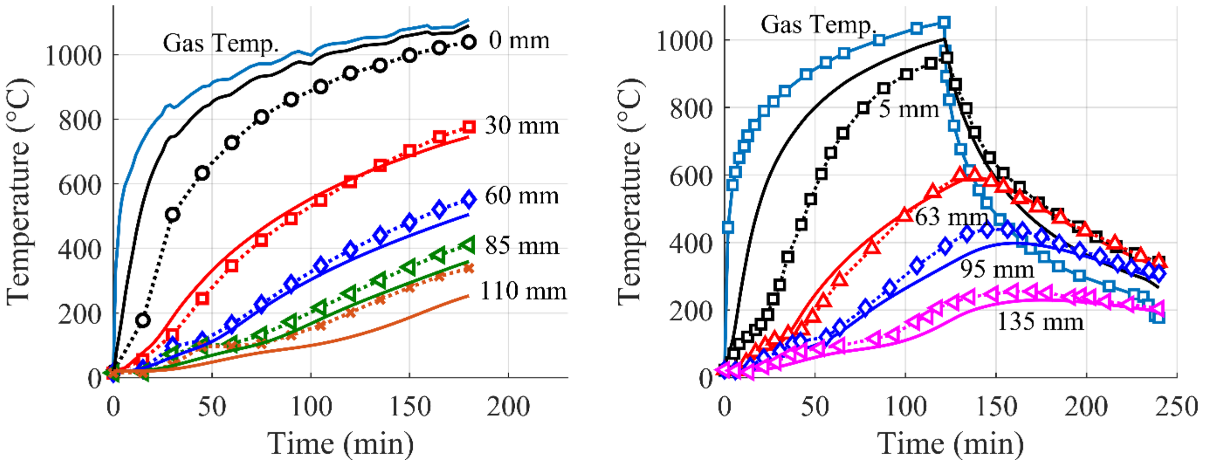

(c) *BRANZ HiBond* slab (d) COSSFIRE slab

Figure 4-7. Numerical validation: (a) Guo and Bailey's *Fire 1* slab [133]; (b) Guo and Bailey's *Fire 2* slab [133]; (c) *BRANZ HiBond* slab [64,65]; (d) COSSFIRE slab [66]. Solid lines represent numerical data, while dashed lines with grid markers represents experimental data.

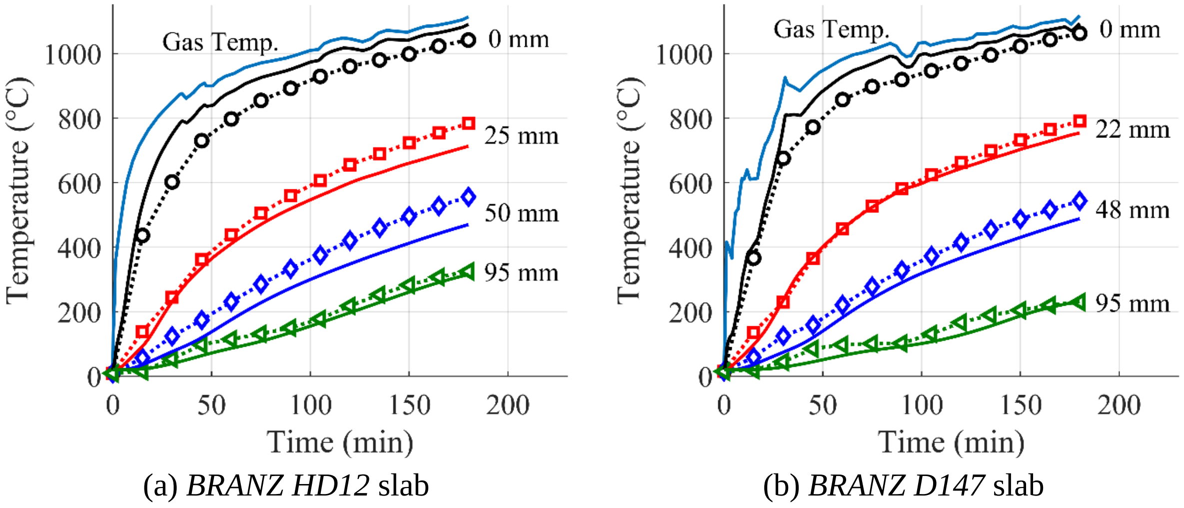

Figure 4-8. Numerical validation: (a) *BRANZ HD12* slab [64,65]; and (b) *BRANZ D147* slab [64,65]. Solid lines represent numerical data, while dashed lines with grid markers represents experimental data.

The modeling approach over predicts the temperature at the bottom of a composite slab (i.e., 0 mm), as shown in all test cases examined in Figure 4-7, with better predictions observed elsewhere within the slab. Poor prediction of temperature at the top of the *BRANZ HiBond* slab in Figure 4-7(c) (i.e., at 85 mm and 110 mm) is acknowledged, but the test may be an outlier given the good predictions in the other test cases. Figure 4-8 demonstrates that the modeling approach is also capable of capturing the thermal response of a heated flat slab, as close approximation between experimental and numerical data are obtained for each of the two flat slabs examined.

It should be noted that the fire rating of the composite floor slab is derived using the temperature of the rebar and the top of the slab as demonstrated in Table 4-3. The results of the validation study demonstrate that sufficiently accurate temperature predictions near the top of the composite floor slab can be achieved, demonstrating that the modeling approach is sufficiently accurate for the intended purpose.

The validation of heat transfer through wide-flanged steel sections was carried out using experimental test data from the Cardington Test no. 3 [67,68]. Test no. 3 consisted of a natural fire applied to a 9.98 m x 7.57 m compartment located at the corner bay of a steel-concrete composite floor system. Specific focus is placed on the interior steel floor beam of Test no. 3, which was left unprotected during testing. Figure 4-9 shows the results of the validation study, which examines the transfer of heat at the bottom flange, web, and top flange of the beam. Close approximation between experimental and numerical data are obtained, demonstrating that the modeling approach is sufficiently accurate. Only one test case was examined, particularly because the heat transfer of fire-exposed steel is not as challenging as the heat transfer of fire-exposed concrete. Kodur et al. [134] also showed that the Eurocode 3 Part 1-2 thermal properties of steel [87] can be used to accurately determine the internal temperatures of an unprotected (i.e., without insulation) heated wide-flanged steel beam.

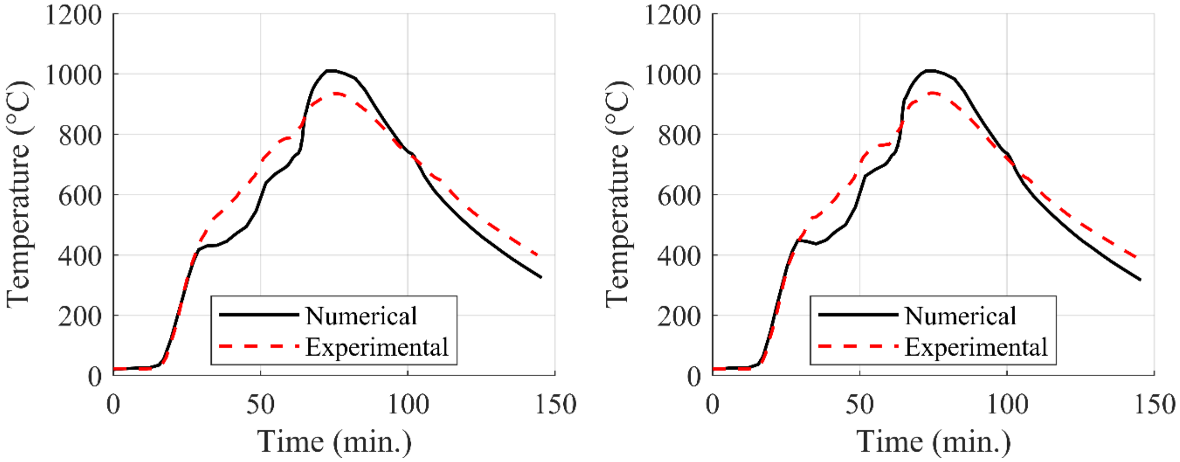

(a) Bottom flange (b) Web

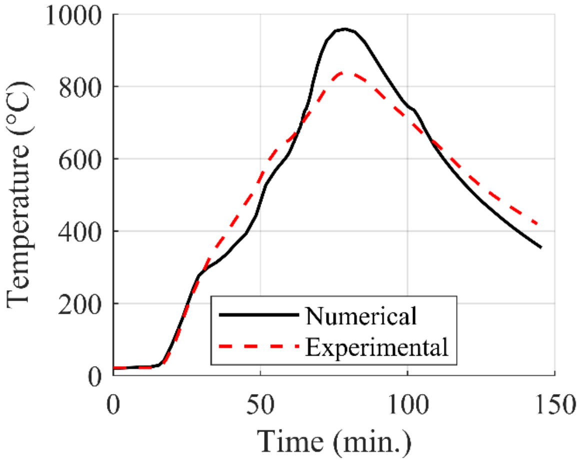

(c) Top flange

Figure 4-9. Numerical validation using temperature data at the mid-span of the interior steel beam from the Cardington Fire Test no. 3 [67,68]: (a) bottom flange; (b) web; and (c) top flange.

4.6. Results

4.6.1. Peak Temperature

An analysis of peak temperature in structural members is presented to understand the spatial and temporal evolution of temperature during a traveling fire. The variation of peak temperature with traveling fire size is presented in Figure 4-10, while the normalized location at which the peak temperatures occurs, relative to the fire origin, is presented in Figure 4-11. In Figure 4-11, $x = 0$

represents the location of the fire origin (at the West end of the floor plan), and $x = 1$ represents the location of the fire extinction (at the East end of the floor plan). For brevity, only the peak temperature analysis of floor plan #2, with a fire rating of 1 h, is presented.

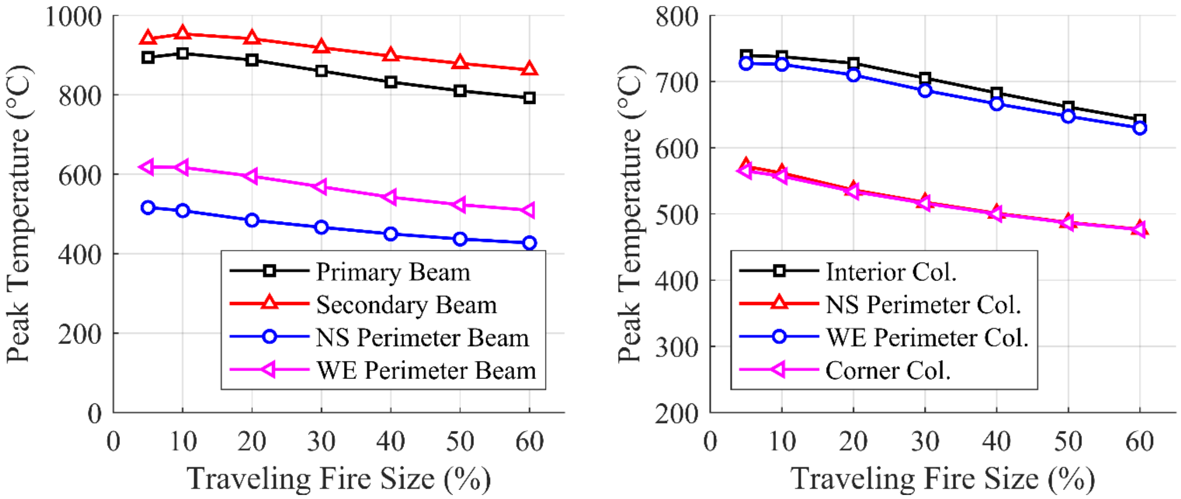

(a) Beams (b) Columns

Figure 4-10. Influence of traveling fire size on the peak temperature of all steel members in floor plan #2, with a fire rating of 1 h: (a) all beam types; (b) all column types.

Figure 4-10(a) and Figure 4-10(b) shows the peak temperature for all beam types (i.e., primary beams, secondary beams, etc.) and for all column types (interior columns, corner columns, etc.), respectively, of floor plan #2. In both beams and columns, peak temperature decreases with increasing traveling fire size, with the largest peak temperature occurring under a 5% and 10% traveling fire. Smaller traveling fires have a smaller fire spread rate and subsequently a larger burning duration as shown previously in Figure 4-2. The long burning duration of a small traveling fire leads to a longer exposure to the near field region (i.e., the local burning region), resulting in larger peak temperatures.

The peak temperatures in interior beams (i.e., primary and secondary beam) are larger than the peak temperatures in perimeter beams (i.e., NS and WE perimeter beams) as shown in Figure 4-10(a). Although primary and secondary beam are fire rated for 1 h, peak temperatures can reach 900°C and 950 °C, respectively, under a 10% traveling fire. Perimeter beams have lower peak temperatures, with peak temperature reaching 620 °C in the WE perimeter beam under a 5% and 10% traveling fire. The lower peak temperature in perimeter beams are attributed to partial heating, where only part of the perimeter beam is exposed to the fire. Conversely, interior beams are fully exposed to fire, leading to larger peak temperatures.

It should be noted that the peak temperature in a steel section also depends on the weight to perimeter ratio W/D. Although the primary and secondary beam are both fully exposed to fire and have the same insulation thickness, peak temperatures for different traveling fire sizes differ by 50 °C. The difference in the peak temperatures is attributed to W/D ratio of each beam section (i.e., $W/D = 0.676$ for the primary beam compared to $W/D = 0.540$ for the secondary beam).

The peak temperatures in interior columns and WE perimeter columns are larger than the peak temperatures in NS perimeter column and corner columns as shown in Figure 4-10(b). Interior columns are fully exposed to fire, leading to larger peak temperatures when compared to other column types, which are partially exposed to fire. WE perimeter columns have larger peak temperatures than NS perimeter columns. This can be attributed to the difference in W/D ratio: NS perimeter column (i.e., W14X109) are comprised of larger wide-flanged sections than WE perimeter column (i.e., W14X99), and the orientation of the two column sections within the floor plan are different, leading to different heating boundary conditions. Although both perimeter columns are insulated with the same thickness of SFRM insulation as shown in Table 4-2, a variation of peak temperatures of about 200 °C is observed under different traveling fires. This demonstrates that the thermal gradient in a perimeter column must be properly accounted for in a heat transfer model.

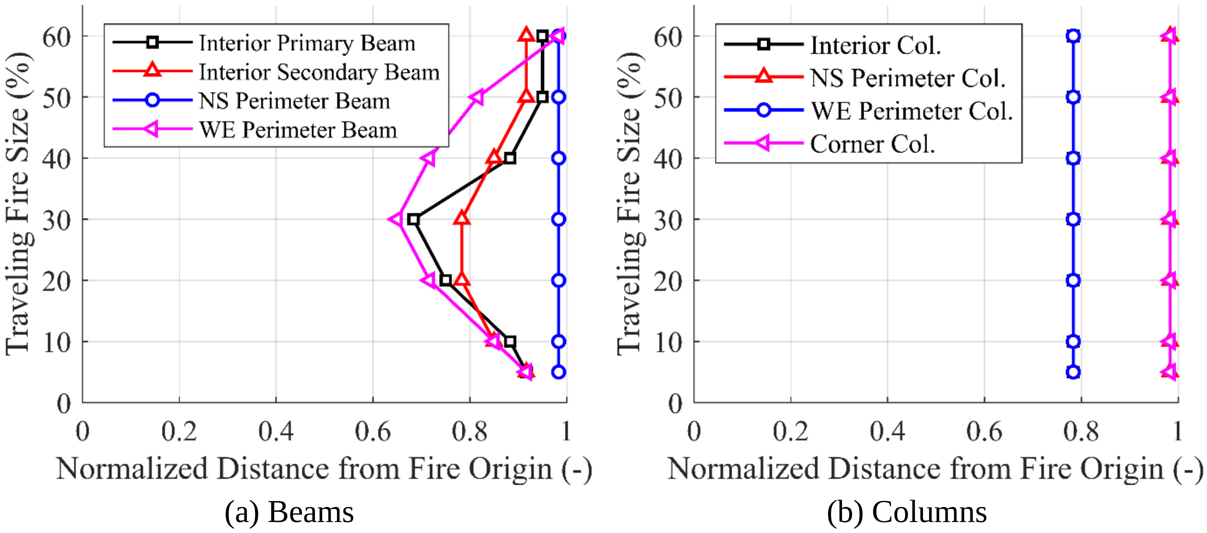

(a) Beams (b) Columns

Figure 4-11. Location of peak temperature for all steel members in floor plan #2, with a fire rating of 1 h: (a) all beam types; (b) all column types.

Figure 4-11(a) and Figure 4-11(b) shows the normalized location at which the peak temperature occurs within the floor plan, for all beam types and column types, respectively, of floor plan #2. Figure 4-11(a) shows that the peak temperatures in the beams generally occur at the end of the fire path, and are confined within the last 60% of the floor plan (i.e., at a normalized distance $x \geq 0.6$). A similar finding was made by Rackauskaite et al. [12], which examined the thermal response of fire-protected steel frames exposed to traveling fires. NS perimeter beams are constrained spatially in a floor plan as shown in Figure 4-1 and thus the location of the peak temperature are limited to occur at either at the fire origin (i.e., $x = 0$) or at the end of the fire path (i.e., $x = 1$). Since larger peak temperatures are generally observed at the end of the fire path (i.e., $x = 1$), peak temperatures in the NS perimeter beam occur at the end of the fire path.

Primary beams and WE perimeter beams are not constrained spatially within a floor plan and span the entire length of the floor plan, in the direction of the traveling fire path. Figure 4-11(a) shows that the location of peak temperature in these beams depends on the traveling fire size. Under a 5% and 60% traveling fire size, peak temperatures occurs at the far end of the structure, away from the fire origin (i.e., $x = 1$). For all other traveling fire sizes, the location of the peak temperature in primary beams and WE perimeter beams occur between the middle and far end of the floor plan at a normalized distance of $0.6 \leq x \leq 0.9$. This demonstrates that an analysis of peak temperature of beams spanning the direction of the traveling fire path is more involved and requires an evaluation of the far end of the structure, away from the fire origin.

The peak temperature in all columns occur at the end of the fire path as shown in Figure 4-11(b), particularly within the last 80% of the floor plan (i.e., at a normalized distance $x \geq 0.8$). It should be noted that the spatial constraint of columns within a floor plan affects both the peak temperature and the location of the peak temperature within the floor plan. For instance, the peak temperatures in interior columns and WE perimeter columns can only be observed at a normalized distance of $x = 0.2$, 0.4, 0.6, and 0.8, which corresponds to the position of these columns within the floor plan. For NS perimeter columns and corner columns, peak temperatures can only be observed at a normalized distance of $x = 0$ and $x = 1$. Thus, an analysis of peak temperature of columns is simpler, since only a few locations within the floor plan, particularly towards the end of the fire path as shown in Figure 4-11(b), must be considered. The spatial positions of NS perimeter columns and corner columns also explains why lower peak temperatures are observed in comparison to WE perimeter columns and interior columns.

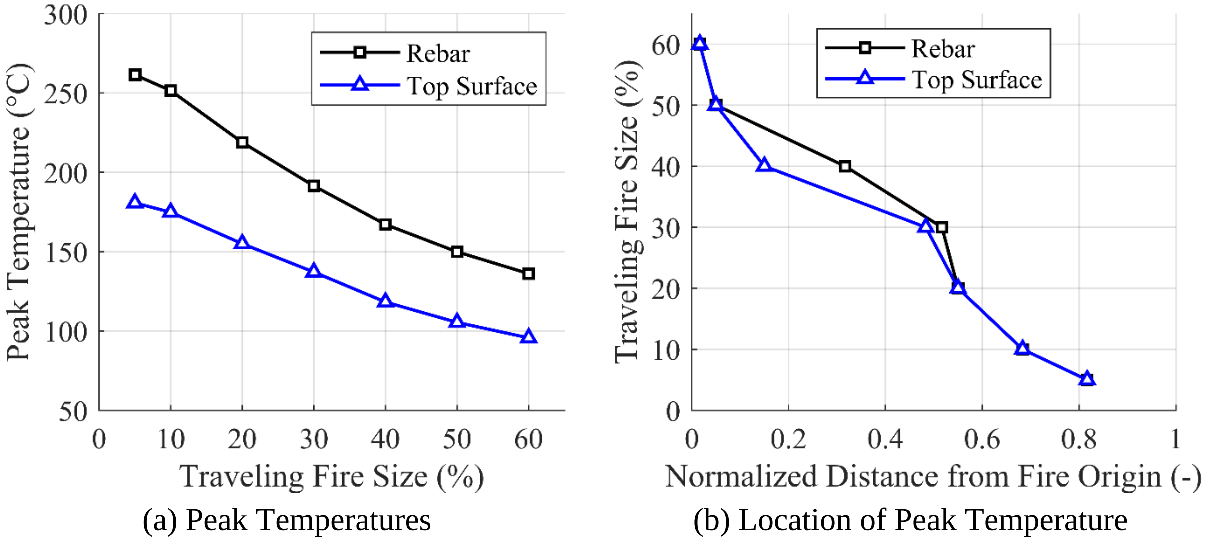

(a) Peak Temperatures (b) Location of Peak Temperature

Figure 4-12. Peak temperature and the location of peak temperature at the rebar and top of the composite floor slab in floor plan #2.

The peak temperature and the location of peak temperature in the rebar and at the top surface of the composite floor slab are shown in Figure 4-12. The largest peak temperature at both locations occurs under the smallest traveling fire sizes of 5% and 10%. Like beams and columns, the peak temperatures in the composite floor slab also decrease with increasing traveling fire size. However, the location of the peak temperature at both the rebar and top surface moves further away from the fire origin with a decrease in the traveling fire size. This differs significantly from beams and columns, where the peak temperatures occur at the last 60% and 80% of the floor plan, respectively, away from the fire origin. Under a 60% traveling fire, peak temperatures in the composite floor slab occurs at the location of the fire origin (i.e., $x = 0$), while under a 5% traveling fire, peak temperatures occur at a normalized distance of about $x = 0.8$.

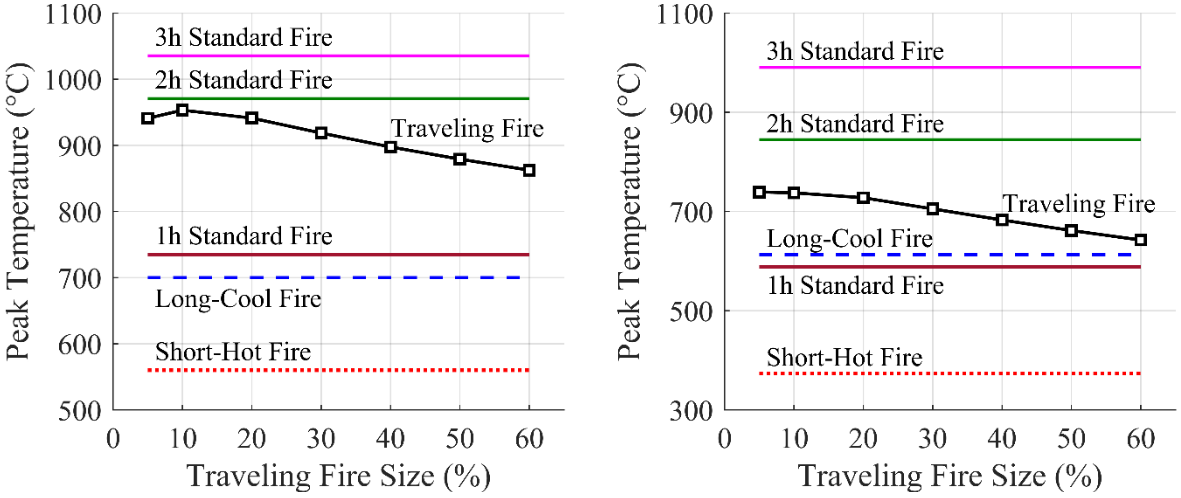

(a) Secondary Beam (b) Interior Column

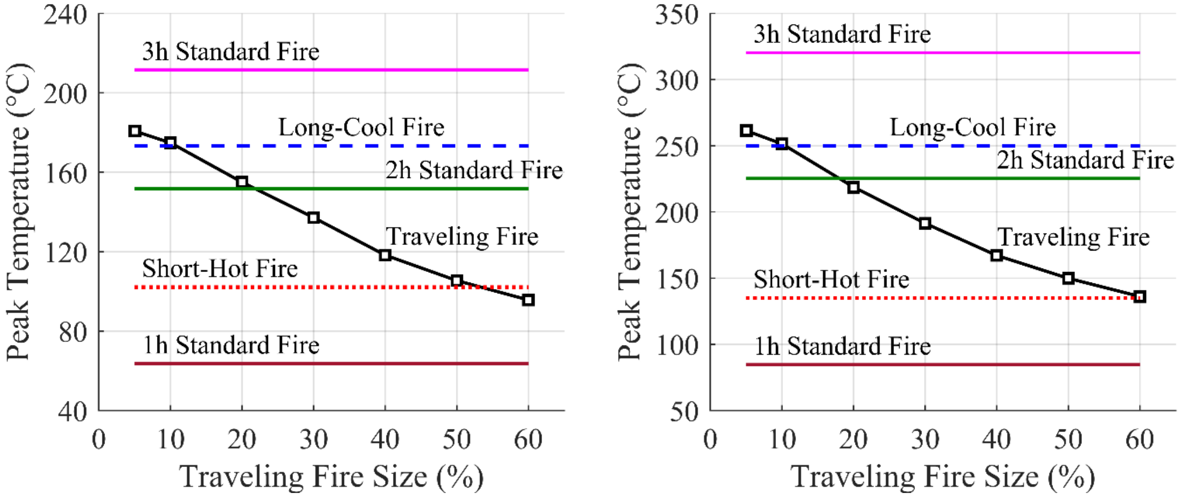

(c) Top Surface of Slab (d) Slab Rebar

Figure 4-13. Influence of fire type on the peak temperature in floor plan #2, with a fire rating of 1 h: (a) secondary beam; (b) interior column; (c) top surface of slab; and (d) slab rebar.

The influence of the fire type (i.e., traveling fire, natural fire, or standard fire) on the peak temperature is shown in Figure 4-13. Only the peak temperature of critical members such as secondary beam, interior column, and the composite floor slab, are examined. These members have larger peak temperatures when compared to similar member types. Similar trends are observed in both the secondary beam and interior column: (1) the peak temperature under traveling fires are larger than those occurring under a 1 h standard fire, a long-cool fire, and a short-hot fire; and (2) the peak temperatures under traveling fires are smaller than those occurring under a 2 h and 3 h standard fire. The smallest peak temperature is observed under a short-hot fire. This is expected given the short-duration of the heating phase in a short-hot fire as shown in Figure 4-4. In the secondary beam, larger peak temperatures are observed during a 1 h standard fire rather than under a long-cool fire, while in the interior column, larger peak temperatures are observed during a long-cool fire rather than under a 1 h standard fire. Generally, peak temperatures from traveling fires are bounded by peak temperatures associated with a 1 h and 2 h standard fire.

Different trends in peak temperatures are observed in the composite floor slab as shown in Figure 4-13(c) and Figure 4-13(d). Peak temperatures under traveling fires are generally larger than those under a short-hot and 1 h standard fire, but are generally not larger than those under a long-cool and 2 h standard fire. In traveling fire sizes larger than 30%, the peak temperature in the rebar and top surface of the slab can be lower than those associated with a long-cool and 2 h standard fire. The peak temperature occurring during a 5% and 10% traveling fire are nearly the same as those occurring under a long-cool fire.

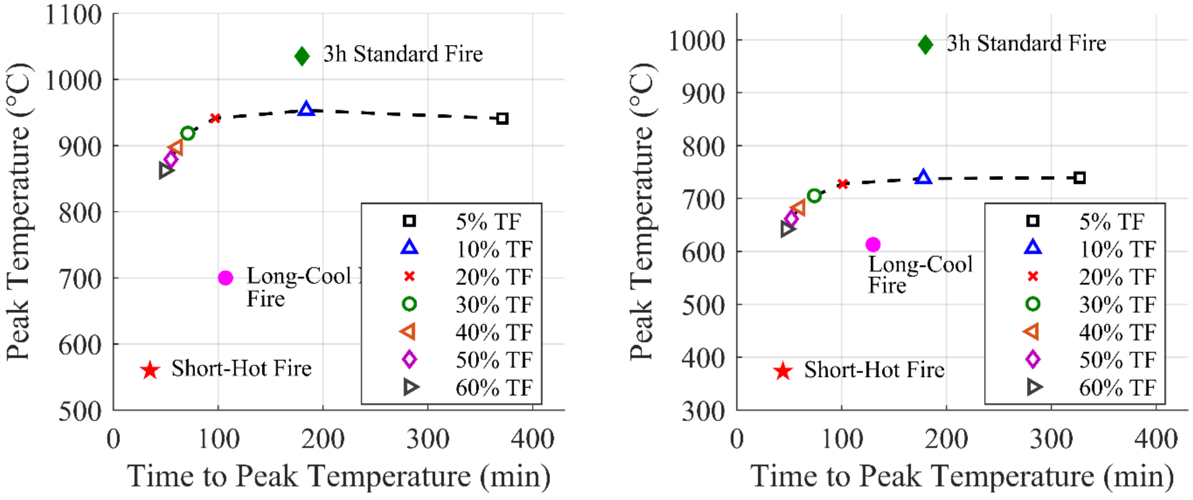

(a) Secondary Beam (b) Interior Column

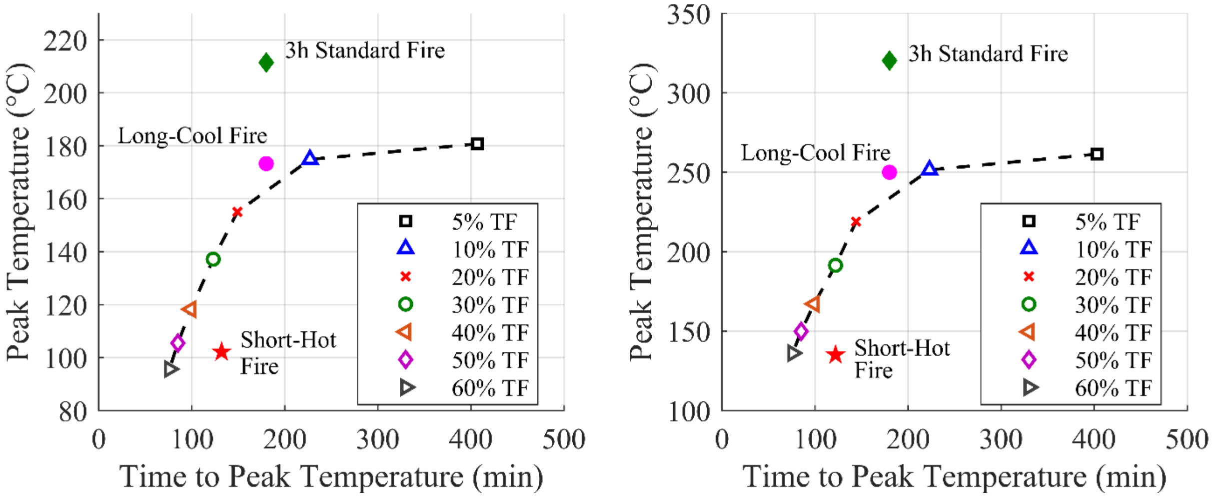

(c) Top Slab (d) Slab Rebar

Figure 4-14. Time to peak temperature in floor plan #2, with a fire rating of 1 h: (a) secondary beam; (b) interior column; (c) top surface of slab; and (d) slab rebar.

The time occurrence of the peak temperature is also examined and is shown in Figure 4-14. Only critical members (i.e., secondary beam, interior column, and the composite slab) are examined. Figure 4-14 shows the peak temperature as a function of the time to peak temperature for each traveling fire size. The peak temperature data from the short-hot fire, long-cool fire, and a 3 h standard fire are also included. In general, the time to peak temperature increases with decreasing traveling fire size in all members. In the secondary beam and interior column, the time occurrence of peak temperature increases drastically for traveling fire size smaller than 20%, with the peak temperature remaining nearly constant. In the secondary beam, a peak temperature of 941 °C occurs at 97 min during a 20% traveling fire, while a peak temperature of 940 °C occurs at 371 min during a 5% traveling fire. The same peak temperature occurs 4 h 34 min apart. The same trend can be seen in the interior column data.

Under larger traveling fires (i.e., ≥ 40% traveling fire), peak temperatures at both the rebar and top surface of the slab can occur much quicker than during a short-hot fire, with the peak temperature under a 60% traveling fire approaching the peak temperatures observed under a short-hot fire. The peak temperature at the rebar and top surface of the slab are very similar under a 5% and 10% traveling fire, however, these peak temperatures occur at significantly different times: 220 min under a 10% traveling fire compared to 400 min under a 5% traveling fire. The peak temperature at the rebar and top surface of the slab under a 5% and 10% traveling fire are very similar to the peak temperatures corresponding to a long-cool fire but occur much later in time.

4.6.2. Fire Resistance Rating

The time to failure of each structural member in floor plan #1 and floor plan #2 are assessed against the ASTM E119 standard fire and are presented in Table 4-4 through Table 4-8. Under an ASTM E119 standard fire, the majority of the computed fire resistance ratings (FRR) surpass the prescribed FRR of either 1 h or 2 h, demonstrating that the insulation design is appropriate under a standard fire. Only the interior column in floor plan #1 and floor plan #2, insulated with a 2 h fire rating, fails to meet the prescribed fire rating as shown in Table 4-6 and Table 4-8. The computed FRR of 110 min for the interior columns is however still within ± 10% of the target fire rating of 2 h. In all cases, the percent relative difference between the computed FRR and prescribed FRR ranged from 3% to 128% under a 1 h fire rating. Under the 2 h fire rating, the percent relative difference between the computed FRR and prescribed FRR ranged from 10% to 43% in members whose internal temperature reached the corresponding ASTM E119 temperature limit. For the composite floor slab, the ASTM E119 temperature limit at the top surface of the slab is reached 125 min into a standard fire, which is above the 2 h limit prescribed by UL Design No. *BXUV.D902*.

The assessment of the FRR reveal that prescriptive design approaches do not provide a consistent level of safety among different structural members. Some members performed significantly better than others under a standard fire despite being insulated under the same fire rating level. This shows that prescriptive codes for fire safety makes it difficult for engineers to quantify the associated level of risk associated with buildings exposed to fire. Under a short-hot and long cool fire, no ASTM E119 temperature limit was reached in any structural member. This demonstrates that the insulation designs chosen are conservative against these two post-flashover fire events. Furthermore, this demonstrates that a larger margin of safety exists during a real post-flashover fire, in comparison to a standard fire.

Table 4-4. FRR of the composite floor slab of floor plan #1 and floor plan #2, under an ASTM E119 standard fire.

Slab Location	Prescribed FRR (min)	FRR Achieved (min)	% Difference
At Rebar	120	Limit Not Reached	N/A
At Top Surface	120	125	4

Table 4-5. FRR of steel members of floor plan #1, with a fire rating of 1 h, under an ASTM E119 standard fire.

Member Type	Section Shape	Prescribed FRR (min)	Achieved FRR (min)	% Difference
Interior Primary Beam	W18X35	60	94	57
Interior Secondary Beam	W12X19	60	78	30
Perimeter NS Beam	W12X16	60	80	33
Perimeter WE Beam	W14X22	60	82	37
Interior Column	W12X58	60	62	3.3
Perimeter NS Column	W10X39	60	89	48
Perimeter WE Column	W10X39	60	72	20
Corner Column	W8X24	60	119	98

Table 4-6. FRR of steel members of floor plan #1, with a fire rating of 2 h, under an ASTM E119 standard fire.

Member Type	Section Shape	Prescribed FRR (min)	Achieved FRR (min)	% Difference
Interior Primary Beam	W18X35	120	163	36
Interior Secondary Beam	W12X19	120	135	13
Perimeter NS Beam	W12X16	120	148	23
Perimeter WE Beam	W14X22	120	151	26
Interior Column	W12X58	120	110	-8.3
Perimeter NS Column	W10X39	120	171	43
Perimeter WE Column	W10X39	120	141	18
Corner Column	W8X24	120	Limit Not Reached	N/A

Table 4-7. FRR of steel members of floor plan #2, with a fire rating of 1 h, under an ASTM E119 standard fire.

Member Type	Section Shape	Prescribed FRR (min)	Achieved FRR (min)	% Difference
Interior Primary Beam	W18X35	60	94	57
Interior Secondary Beam	W12X19	60	78	30
Perimeter NS Beam	W21X93	60	137	128
Perimeter WE Beam	W18X60	60	114	90
Interior Column	W12X58	60	62	3.3
Perimeter NS Column	W14X109	60	95	58
Perimeter WE Column	W14X99	60	72	20
Corner Column	W14X109	60	133	122

Table 4-8. FRR of steel members of floor plan #2, with a fire rating of 2 h, under an ASTM E119 standard fire.

Member Type	Section Shape	Prescribed FRR (min)	Achieved FRR (min)	% Difference
Interior Primary Beam	W18X35	120	163	36
Interior Secondary Beam	W12X19	120	135	13
Perimeter NS Beam	W21X93	120	Limit Not Reached	N/A
Perimeter WE Beam	W18X60	120	Limit Not Reached	N/A
Interior Column	W12X58	120	110	-8.3
Perimeter NS Column	W14X109	120	159	33
Perimeter WE Column	W14X99	120	132	10
Corner Column	W14X109	120	Limit Not Reached	N/A

Under a traveling fire exposure, the ASTM E119 temperature limits were reached in several members of floor plan #1 and floor plan #2. These failures occurred only in structural members insulated with a fire rating of 1 h. No temperature limit was reached in any structural member insulated with a 2 h fire rating, including the composite floor slab. Figure 4-15 shows the computed time to failure under a traveling fire exposure of steel members in floor plan #1 and floor plan #2 that reached the governing ASTM E119 temperature limits. The term “time to failure” is used in the analysis of traveling fires, given that the term “fire resistance rating” is often associated with the standard fire exposure. These failing members include the primary beam, secondary beam, interior column, and WE perimeter column, which coincidentally are also the members with the largest peak temperatures. Figure 4-15 shows that the computed time to failure of each member decreases with increasing traveling fire size and are all generally below the target fire rating limit of 1 h. The smallest time to failure of 20 min was computed for the secondary beam under a 60% traveling fire, which corresponds to a relative difference of -66% when compared to the target fire rating of 1 h. This demonstrates that prescriptive design approaches may prescribe insulation designs that are unsafe against traveling fires.

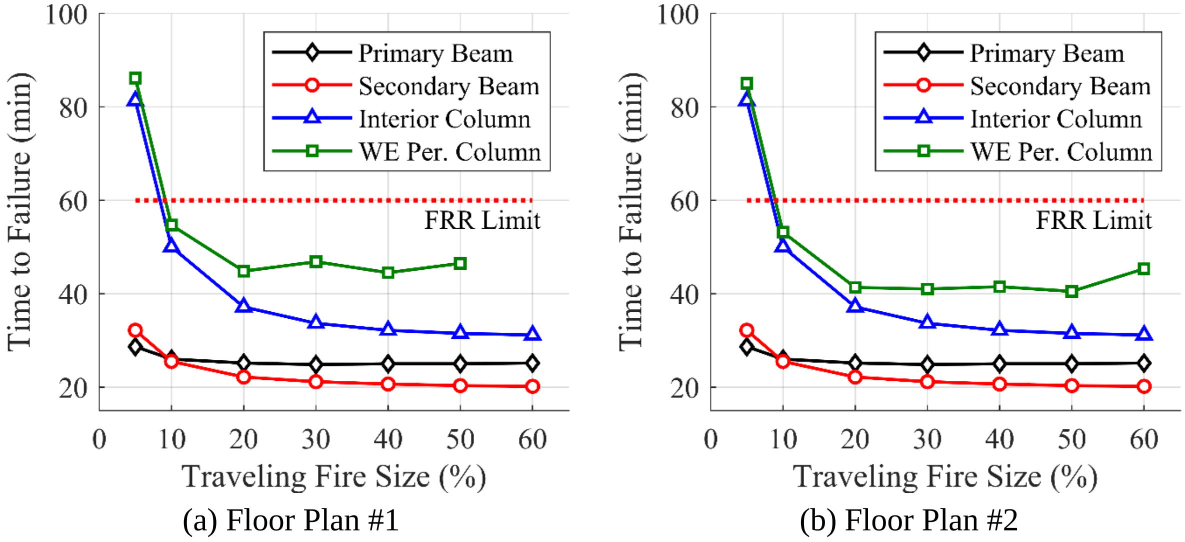

(a) Floor Plan #1

(b) Floor Plan #2

Figure 4-15. Minimum time to failure of steel members with a fire rating of 1 h: (a) floor plan #1; and (b) floor plan #2.

Figure 4-16 shows the influence of the member location on the computed time to failure for each of the failing members of floor plan #1. Normalized distances are used, where $x = 0$ represents the location of the fire origin, and $x = 1$ represents the location of the fire extinction. The analyses reveal that the lowest time to failure are observed at locations closer to the fire origin in all failing members. Additionally, the results show that the computed time to failure decreases with increasing traveling fire size, regardless of the position of the member within the floor plan. This demonstrates that larger traveling fire sizes produce smaller time to failure in structural members that are closer to the fire origin. Similar findings are observed in floor plan #2 with a fire rating of 1 h.

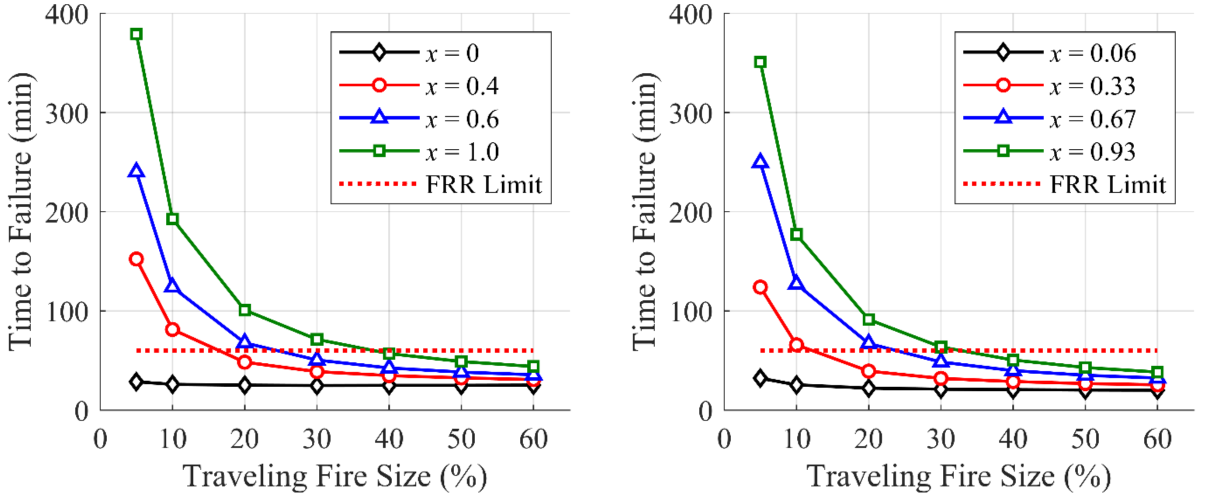

(a) Interior Primary Beam (b) Interior Secondary Beam

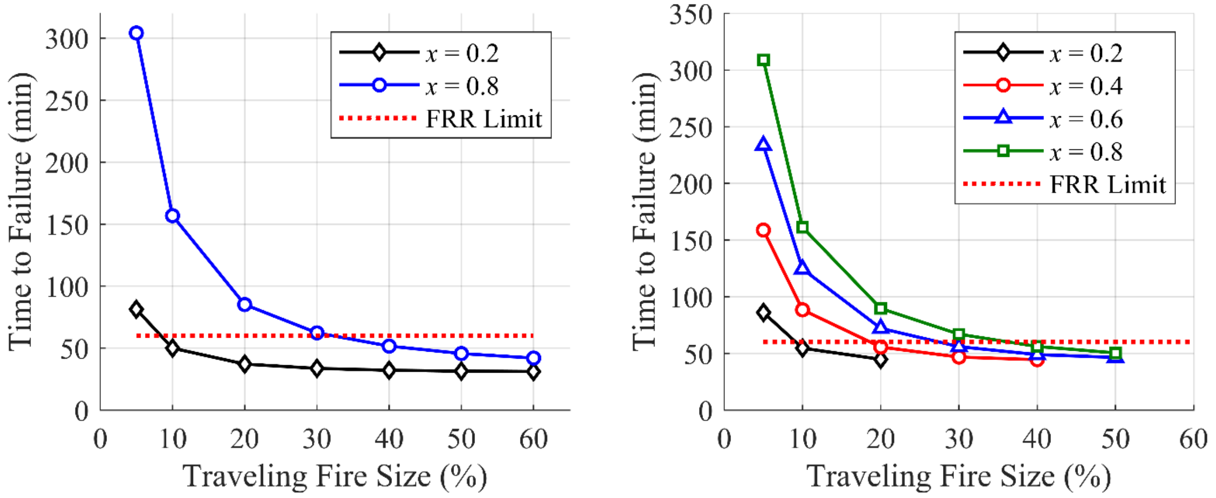

(c) Interior Column (d) Perimeter WE Column

Figure 4-16. Influence of location on the computed time to failure of steel members in floor plan #1 with a fire rating of 1 h.

Even though the insulation design performed well under a standard fire, the same design performed poorly under a traveling fire. Specifically, a low safety margin existed in structural members who were exposed to larger traveling fires and were positioned closer to the fire origin. This demonstrates that fire protection engineers should use caution when designing the passive fire protection of structural members in an open-plan compartment. It is recommend herein that an analysis procedure be used to check the adequacy of insulation design derived from prescriptive approaches when applied to structural members in an open-plan compartment. Such an analysis, utilizing the finite element software ABAQUS and the iTFM, was carried out in this study.

4.7. Conclusion

A series of heat transfer analyses were carried to determine the adequacy of prescriptive codes to safeguard against traveling fires. A family of traveling fires, defined using the improved Traveling Fires Methodology, were applied to two steel-concrete composite floor plans. The fire rating of each structural member was quantified using the temperature limits available in the ASTM E119 standard. An analysis of peak temperature was also carried out to understand the thermal response of composite floor systems under traveling fires. Based on the findings presented, the following conclusions were made:

- Peak temperature in all members generally decreased with increasing traveling fire size.
- Peak temperature in beams occur between the last 60% and 90% of the floor plan (away from the fire origin), while peak temperature in columns occur at the last 80% of the floor plan.
- The location of the peak temperature in a composite floor slab depends on the traveling fire size. Under a 60% traveling fire, peak temperatures occur at the location closest to the fire origin, while under a 5% traveling fire, peak temperatures occur at a location furthest from the fire origin.
- Peak temperatures under a traveling fire are typically larger than peak temperatures under a 1 h standard fire, but smaller than the peak temperatures under a 2 h standard fire.

- Fire insulation derived from prescriptive approaches do not provide a consistent level of safety among different member types (i.e., beams, columns, etc.) and different fire types (i.e., standard fire, natural fire, etc.). Furthermore, such insulation designs may not provide satisfactory protection under traveling fires.
- Under a large traveling fire (i.e., one with a large burning region), steel members which are insulated with a 1 h fire rating can reach the ASTM E119 temperature limit in 20 min (i.e., -66 % relative difference).
- Larger traveling fire sizes will produce a smaller time to failure in structural members that are positioned closest to the fire origin.

Fire protection engineers should utilize a conservative approach when designing the passive fire protection of structural members in an open-plan compartment. Specifically, an analysis procedure should be used to verify the adequacy of insulation design derived from prescriptive approaches. Since only one set of insulation design listings were examined, further research is required to generalize the findings. Nonetheless, the study highlights the need of prescriptive fire codes to be thoroughly investigated against traveling fires.

Chapter 5 Structural Response of Steel-Concrete Composite Floor Systems under Traveling Fires

A computational investigation was carried out to examine the structural response of two steel-concrete composite floor system under traveling fires. The thermal-mechanical analyses were performed using the finite element software ABAQUS, where the traveling fire exposures were defined using the improved Traveling Fires Methodology [12]. Essential factors influencing the fire resistance of the composite floor systems, namely the level of passive fire protection and the passive fire protection scheme were varied in this study. For comparative purposes, the composite floor systems were also exposed to an ASTM E119 standard fire and two natural fire exposures applied to a 4-bay corner compartment. The results of the investigation showed that fire insulations derived from prescriptive approaches might not provide adequate safety under traveling fires. Using a critical displacement criterion, the composite floor systems performed poorly under traveling fires, which was not the case under the two natural fire exposures. Through a performance-based design procedure, it was also shown that improved performance under traveling fires could be achieved through better allocation of the fire protection. Specifically, fire protection from the interior floor beams were removed and applied to the girders and exterior floor beams. This provided an economical fire safety solution when compared to the simultaneous increase of the fire protection to all floor beams and girders, typical of a prescriptive design approach.

5.1. Introduction

Previous research of structures exposed to traveling fires has focused primarily on the response and performance analysis of two-dimensional (2D) steel and concrete frames [21,135–141]. Such an idealization is limited in that it does not capture the full range of load-redistribution occurring in a floor plan. In a steel-concrete composite floor system, loads can be redistributed along both horizontal planes of the floor plan due to the connectivity provided by the composite slab and structural members [142]. Additionally, load-redistribution produced by the composite slab, such as tensile membrane action, are not captured in a 2D idealization that ignores the composite floor slab. Traveling fires are designated by the percentage of the local burning size A_f relative to the total floor area of the compartment A (e.g., a 10% traveling fire designates a fire in which A_f is 10% of A). This designation is common in the research literature.

Law *et al.* [21] examined the structural response of a reinforced concrete (RC) floor plan under various fire types, including a family of traveling fires with sizes ranging from 1% to 100%, two natural fires (i.e., a short-hot and long-cool fire), and a standard fire. Using a critical rebar temperature of 593 °C, a critical deflection limit of $L/20$, and a critical rebar strain of 0.2, a 25% traveling fire was found to produce the highest distress in each failure metric. A 25% traveling fire also produced larger distress in each failure metric compared to the long-cool and short-hot fire exposures. The findings led the authors to conclude that current fire design approaches, which revolves around the standard fire, should not be assumed conservative since larger distress could be achieved under a traveling fire.

Behnam and Rezvani [135] examined the structural response of a seismically-damaged 6-bay 7-story unprotected interior steel frame subjected to a family of traveling fires with fire sizes of 16.7%, 50%, and 100%, and a standard fire. Each fire type was applied to the first story of the frame. To simulate earthquake damage, the structure was pushed to a target displacement corresponding to the life safety level of performance according to the Federal Emergency Management Agency (FEMA) 356 code [143]. Using various failure metrics, including load capacity for columns, and mid-span deflection and rate of deflection for beams, no general trend between failure time and traveling fire size was observed. However, a shorter failure time was observed under a traveling fire compared to the standard fire, leading the authors to conclude that a standard fire is not necessarily the “worst-case” fire exposure.

Rezvani and Ronagh [136] examined the structural response of an unprotected 6-bay 4-story steel moment resisting frame, exposed to a family of traveling fires with fire sizes ranging from 12.5% to 100%, occurring on the first floor of the frame. The stability of the frame was shown to depend on the traveling fire size, with the collapse time decreasing with increasing traveling fire size. The authors generalized that engineers should consider the load-redistributions produced by failing columns when designing steel moment resisting frames against traveling fires.

Behnam [137] examined the structural response of a seismically-damaged 6-bay 3-story RC frame exposed to a family of traveling fires with fire sizes ranging from 1% to 100%, and a standard fire. Each fire was applied to the first story of the frame. To simulate earthquake damage, the structure was pushed to a target level of displacement corresponding to the life safety level of performance according to the FEMA 356 code [143]. Using various failure metrics, including rebar temperature, mid-span deflection, and rate of deflection, the shortest failure time was observed under a traveling fire, rather than a standard fire (i.e., 91 min under a 100% traveling fire compared to 141 min under a standard fire).

Rackauskaite *et al.* [138] examined the structural response of a fire protected 5-bay 10-story steel frame subjected to a series of different fire types, including a family of traveling fires with fire sizes of 2.5%, 10%, 25%, and 48%, two Eurocode parametric fires [109] (i.e., a short-hot and a long-cool fire), a standard fire, and a constant fire curve proposed by the Society of Fire Protection Engineers (SFPE) S.01 standard [144]. Each fire was applied individually to each story level of the steel frame. The study revealed that traveling fires and uniform fires lead to substantially different structural responses. Peak vertical displacement in the floor beams of the frame were found to be dependent on the fire duration, and not the fire type. The results also showed that thermal expansion occurring in fire-affected floor beams are restrained by unburned floor beams of the story above and/or below during a traveling fire. The axial force in the unburned floor beams can reach 60% to 180% of the axial force observed in the fire-affected floor beams.

Rackauskaite *et al.* [139] examined the structural response of a fire-protected 5-bay 10-story interior steel frame subjected to various fire types, including a family of traveling fires with fire sizes ranging from 2.5% to 45%, and a standard fire. Each fire type was applied as a simultaneous multiple-floor fire scenario and as a vertically-spreading fire scenario. The number of multiple floors subjected to a fire were varied between 1 and 10 for each fire type and two inter-floor time delay of 10 min and 25 min were examined for the vertically-spreading fire scenarios. The results showed that a simultaneous multiple-floor fire scenario produced a shorter failure time compared to a vertically-spreading fire scenario involving the same number of floor levels, showing that a simultaneous multiple-floor fire scenario presents a more onerous fire scenario.

Rezvani *et al.* [140] examined the structural response of a fire protected 4-bay 4-story steel frame exposed to a family of traveling fires. The size of the traveling fires ranged from 12.5% to 100% and were applied to the first story of the frame. The results showed that collapse of the steel frame was dependent on the fire size and occurred only under a 25% traveling fire and not the smallest or largest traveling fire examined. The authors concluded that designers should always examine a family of traveling fires with differing fire sizes when designing structures against traveling fires.

Rackauskaite *et al.* [141] investigated the consistency among different failure criteria in predicting the failure time of a fire-protected 5-bay 10-story interior gravity steel frame exposed to both traveling fires and uniform burning fires. Different failure criteria were examined including ultimate strain, utilization, mid-span displacement, and a critical temperature criterion. The results showed that there was no consistency among the different failure criteria examined. Additionally, different fire exposures can produce different failure times, at different locations, and produce different failure mechanism, leading the authors to conclude that no “worst-case” fire scenario can be established.

Although past studies offer valuable insight regarding traveling fires, the structural response of complete building structures under traveling fires have yet to be assessed, which is instrumental in assessing the capability of current fire codes to ensure structural safety during a traveling fire. To address this deficiency, a 3D structural model of a steel-concrete composite building is utilized in this study. Using a sequentially-coupled *thermal-structural* analysis procedure, the structural response of two steel-concrete composite floor systems are examined under various fire types, including a family of traveling fires, two post-flashover fires, and an American Society for Testing and Materials (ASTM) E119 [6] standard fire. The two composite buildings examined are code compliant and adhere to U.S. design codes and standards [2,19,20]. The improved Traveling Fires Methodology [12], which is the latest version of the Traveling Fires Methodology [9,11,21], is used to define the spatial and temporal evolution of the traveling fire exposures.

Essential factors influencing the fire resistance of the composite floor systems, namely the level of passive fire protection and the passive fire protection scheme are also varied in this study. Two protection schemes are examined, including a full protection scheme in which all floor members in the steel-concrete composite floor system are protected with insulation, and a partial protection scheme in which all floor members, with the exception of interior floor beams, are protected with insulation. Several research programs have shown that the fire protection on interior floor beams in a steel-concrete composite floor system may be omitted, owing to the development of tensile membrane action (TMA) [66–68,145–147]. TMA is a self-equilibrating mechanism that occurs in a heated slab panel undergoing large deflections (see Figure 5-1). Provided that the vertical support of the slab panel is maintained, a peripheral compression ring forms at large deflections, which is in equilibrium with a tensile central zone [146]. Gravity load applied to the slab panel are transferred from the central tensile region, to the surrounding peripheral compressive ring, and then to the protected edge beams. This alternative load path allows interior secondary to remain without insulation. However, fire design based on TMA has only been implemented in compartmentalized floor plans [148–150]. It is unclear whether TMA can be used in a large open-plan compartment to design the passive fire protection. Part of the study will investigate whether a partial protection scheme is feasible in a large open-plan compartment.

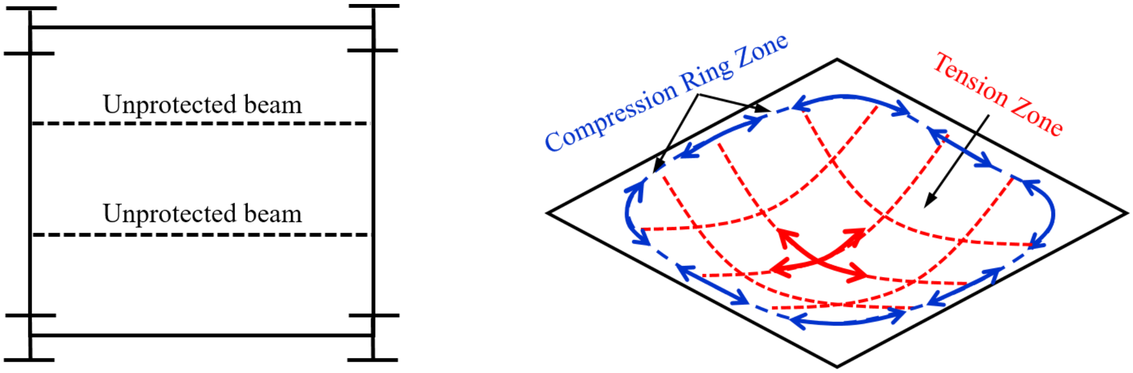

(a) (b)

Figure 5-1. Tensile membrane action (TMA) in a heated steel-concrete composite floor panel: (a) plan view of a partially-protected slab panel; and (b) tension zone and compression ring zone developing under TMA. Figures adapted from [146]

5.2. Study Overview

5.2.1. Case Study Structures

Two case study structures, each 10-story steel-framed buildings with composite floor slabs, are examined. Floor plan #1 (based on the designation in Figure 5-2) consists of interior rigid core walls, while floor plan #2 utilizes exterior moment resisting frames to resist lateral loads. Both buildings were designed by Agarwal and Varma [123] and adhere to U.S. design codes and standards [2,19,20]. Each building has a story height of 3.65 m at each floor level with a rectangular floor plan with 5 bays in the East-West (EW) direction and 3 bays in the North-South (NS) direction, with each bay spanning 7.62 m in length.

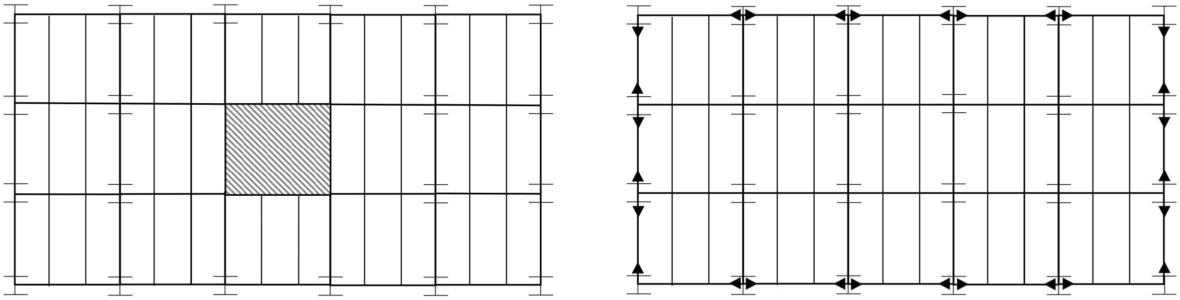
(a) Floor plan #1 (b) Floor plan #2

Figure 5-2. Floor plan of the steel-concrete composite buildings examined: (1) floor plan #1 with an interior rigid core; and (b) floor plan #2 with exterior moment resisting frames. Triangle markers represent rigid beam connections.

The composite floor slab of each building consists of a 65 mm thick light-weight concrete with a compressive strength of f_c' = 34.5 MPa, cast on a 75 mm deep ribbed steel deck. A 6x 6W1.4/1.4 wire reinforcement is placed 25 mm from the top surface of the slab and consists of ASTM A185 Grade 65 steel wire with a yield strength of F_y = 450 MPa. All floor beams were designed to act compositely with the composite floor slab using a design dead and live load of 3.1 kN/m^2 and 2.4 kN/m^2, respectively. In floor plan #1, interior floor beams in all story levels are W12X19, while girders in all floor levels are W18X35. Perimeter beams are also the same in all floor levels and consists of W12X16 in the NS direction, and W14X22 in the EW direction. Column sections vary per floor level as shown in Table 5-1. In floor plan #2, interior floor beams in all story levels are W12X19, while girders in all floor levels are W18X35. Perimeter beams forming the moment resisting frames vary per floor level as shown in Table 5-2. Column sections also vary per floor level and are shown in Table 5-2. In both buildings, structural steel ASTM A992, with a yield strength F_y of 345 MPa, are used for all wide-flanged steel sections. Additional detail regarding the structure can be found in the accompanying reference [123].

Table 5-1. Column section used in floor plan #1

Story	Interior Columns	Corner Columns	Edge Columns
1-2	W14X90	W10X33	W12X53
3-4	W14X74	W8X24	W12X45
5-6	W12X58	W8X24	W10X30
7-8	W8X40	W6X15	W8X24
9-10	W8X24	W6X15	W6X15

Table 5-2. Column and perimeter beam sections used in floor plan #2.

Story	Interior Columns	NS Perimeter and Corner Columns	EW Perimeter Columns	NS Perimeter Beams	EW Perimeter Beam
1-2	W14X90	W14X311	W14X283	W27X217	W21X132
3-4	W14X74	W14X159	W14X145	W21X111	W18X71
5-6	W12X58	W14X109	W14X99	W21X93	W18X60
7-8	W8X40	W14X90	W14X53	W21X83	W18X50
9-10	W8X24	W14X53	W12X45	W18X50	W18X35

5.2.2. Fire Protection Design

Design listings from the Underwriters Laboratories (UL) [104] are chosen for the fire protection design of floor plan #1 and floor plan #2. CAFCO 300, a cementitious-based spray-applied fire resistive material (SFRM) from ISOLATEK Int. [103], was chosen for the fire protection design. This product has a thermal conductivity of κ = 0.078 W/m-K, specific heat of c = 1200 J/kg-K, and a density of ρ = 240 kg/m^3 at ambient temperature [103].

Fire resistance ratings of 1 h and 2 h are utilized separately to define the passive fire protection applied to all structural members of each floor plan. The fire protection design of the steel beams are based on UL Design No. *BXUV.N735*, which is applicable for floor beams supporting a composite floor slab. UL Design No. *BXUV.N735* calls for a SFRM thickness of 13 mm and 24 mm, to achieve a fire rating of 1 h and 2 h, respectively, irrespective of the weight to perimeter ratio (*W*/*D*) of the beam. The fire proofing of steel columns are based on UL Design

No. *BXUV.X790*. The required thickness of SFRM to achieve a fire rating of 2 h in all the steel columns are determined from Equation (5-1), where h is the thickness of SFRM in inches, R is the desired fire rating in minutes, and W/d is the weight to heated perimeter ratio of the column. The fire proofing of the steel deck of the floor slab is based on UL Design No. *BXUV.D902*. Based on the slab thickness of the two floor plans, no SFRM insulation is required to achieve a fire rating of up to a 2 h. All UL designs selected make use of CAFCO 300, which is consistent with the design.

$$h = \frac{R}{75(W/D) + 32} \qquad (5\text{-}1)$$

Several passive fire protection schemes are investigated. These include:

- All floor beams and girders are fire protected with a 1 h fire rating (Figure 5-3(a));
- All floor beams and girders are fire protected with a 2 h fire rating (Figure 5-3(a));
- Interior floor beams are left unprotected (i.e., without insulation), while all other floor beams and girders are fire protected with a 2 h fire rating (Figure 5-3(b)).

In all protection schemes, columns were fire protected using a 2 h fire rating to prohibit column buckling as a governing failure mode. Fischer *et al.* [151] showed that gravity columns of these two composite buildings were susceptible to inelastic buckling when fire protected using a 1 h fire rating and exposed to a compartment fire. The third fire protection scheme exemplifies a partial protection scheme in which the fire protection from the interior floor beams (i.e. those beams spanning between girders) are removed, and essentially moved to the girders and exterior floor beams (i.e., those beams spanning between columns).

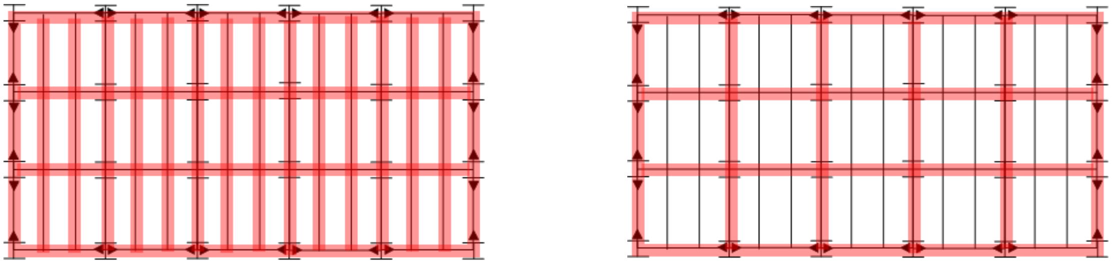

(a) Full protection scheme

(b) Partial protection scheme

Figure 5-3. Passive fire protection schemes investigated: (a) full protection scheme; and (b) partial protection scheme. Red highlights represents beams with fire insulation.

5.2.3. Mechanical Loading

Gravity loads acting on the composite floor system follow the load combination recommended by the American Society of Engineers (ASCE) and Structural Engineering Institute (SEI) *ASCE/SEI 07-16* standard [152], i.e.,

$$U = 1.2DL + 0.5LL + T \tag{5-2}$$

Here U is the overall factored gravity load; DL is the gravity dead load; T is the load resulting from the fire scenario, and LL is the gravity occupancy live load. Uniform live loads for typical office buildings are taken from ASCE/SEI 07-16 as 2.4 kN/m^2, while gravity dead load is computed from the density of steel and concrete as 3.1 kN/m^2.

5.3. Fire Exposure

The two floor plans are exposed to a variety of fire types, including a family of traveling fires, two post-flashover fires, and a standard fire. Traveling fires are applied to the entire floor plan of the two composite floor systems, while the uniform burning fires (i.e., post-flashover fires and standard fire) are applied to a 4-bay compartment, placed in the Southeast corner of the buildings. Each fire is applied to the fifth story of each building. Details of each fire type are presented in the following sections.

5.3.1. Traveling Fires

The improved Traveling Fires Methodology (iTFM) [12] is used to define the spatial and temporal evolution of a 1D traveling fire. Fundamental to the methodology is the assumption that the burning compartment consists of two distinct regions: (1) the near field region (i.e., the burning region of the fire, where structural members are directly exposed to flames); and (2) the far field region (i.e., the region remote from flames where structural members are exposed to hot gases). The temperature at the near field region is produced using the concept of flame flapping [12], while the temperatures of the far field region are produced using Alpert's ceiling jet correlation [124]. The iTFM defines the temperature-time curves of a traveling fire at discrete locations along the length of the compartment. Furthermore, the iTFM assumes that a 1D traveling fire extends the whole width of the floor plan and travels linearly from one end of the floor plan to the other.

The size of the traveling fire is a variable of the model. To overcome the problem of not knowing the exact size of a traveling fire, a family of traveling fires, ranging from a small traveling fire with a long fire duration to a large traveling fire with a short fire duration, are considered. Since each traveling fire size burns over a specific floor area A_f, traveling fires are designated by the percentage of the burning size relative to the total floor area of the compartment A.

The main input of the iTFM includes the fuel load density q_f, heat release rate per unit area Q'', and the flame flapping angle θ. In this study, these variables are taken as $q_f = 570$ MJ/m^2 (i.e., the 80th percentile design value for an office space [11]), $Q'' = 500$ kW/m^2 (i.e., the typical value for a densely furnished places [11]), and θ = 6.5° (i.e., the recommended flapping angle by Quintiere et al. [125]). Here, traveling fire sizes of 5%, 10%, 20%, 30%, 40%, 50%, and a 60% are applied to each floor plan in Figure 5-2. Figure 5-4 shows the relationship between the size of a traveling fire and the fire spread rate and total duration. As the size of the traveling fire decreases, the fire spread rate decreases, causing the fire duration time to increase. As a comparison, a 5% traveling fire has a total fire duration of 400 min, while a 60% traveling fire has a total fire duration of 51 min.

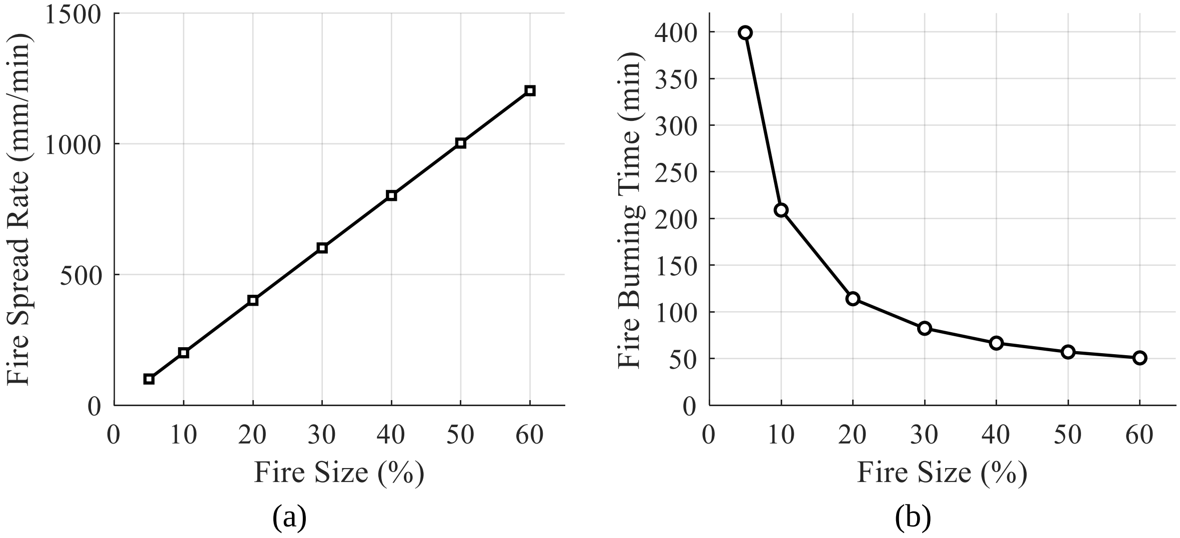

Figure 5-4. Properties of traveling fires: (a) spread rate vs. fire size; (b) burning time vs. fire size.

To consider the effects of cooling, a cooling duration of half of the total fire duration is appended to the end of each traveling fire size examined. Figure 5-5 shows the temperature-time curve of each traveling fire size examined at the center of bay 1 and bay 5 of floor plan #1.

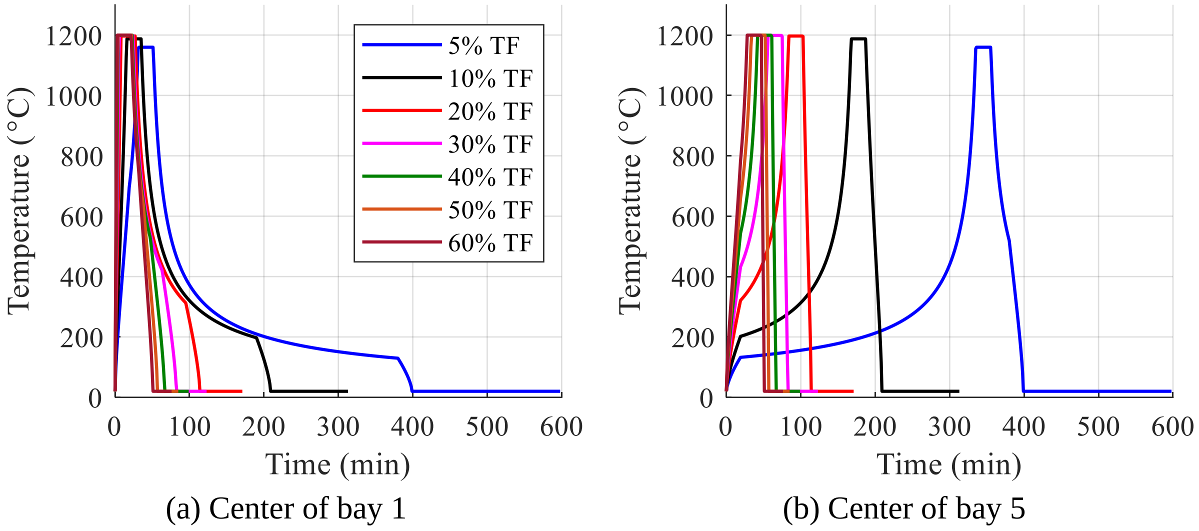

(a) Center of bay 1 (b) Center of bay 5

Figure 5-5. Temperature-time curve of each traveling fire size examined in floor plan #1: (a) center of bay 1; and (b) center of bay 5. In the legend, "TF" is an abbreviation for "traveling fire."

5.3.2. Natural Fires and Standard Fire

Two natural fires, which defines a fire that reaches flashover and includes a cooling phase, and an ASTM E119 standard fire [6], which is used to determine the fire rating of structural members, are also applied to the two floor plans. These fires are applied to a 4-bay compartment, placed in the Southeast corner of the building as shown in Figure 5-6(a) and Figure 5-6(b). The natural fires are generated using the fire model by Pettersson et al. [106]. Using two different opening factors of $O = 0.02\ \mathrm{m}^{1/2}$ and $O = 0.08\ \mathrm{m}^{1/2}$, a long-cool and a short-hot fire are produced as shown in Figure 5-6(c). A high ventilation condition generates a fire with a low peak temperature but a long fire duration (i.e., a long-cool fire), while a low ventilation condition generates a fire with a high peak temperature but a short fire duration (i.e., a short-hot fire). The temperature-time curve of these two natural fires, including the ASTM E119 standard fire curve, are compared in Figure 5-6(c).

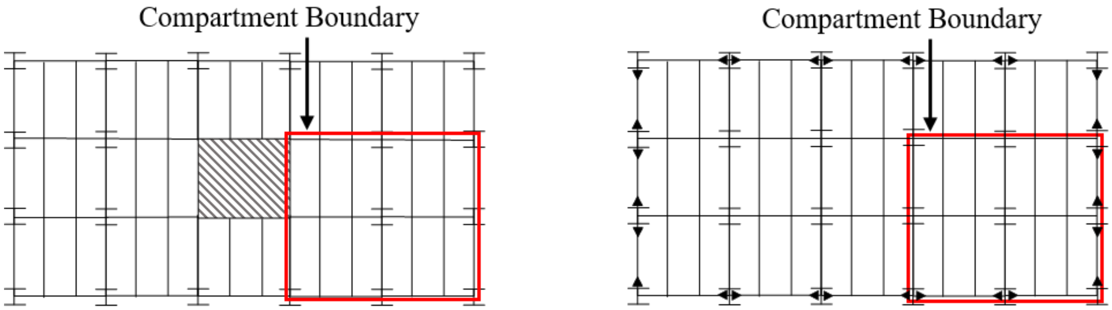

(a) Floor plan #1 (b) Floor plan #2

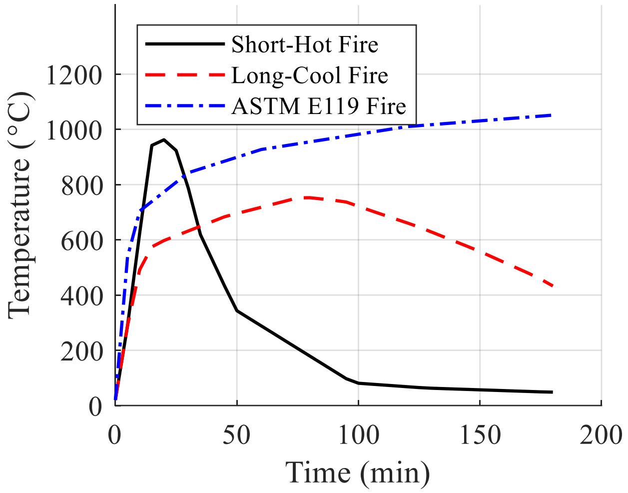

(c) Uniform burning fires examined

Figure 5-6. A 4-bay compartment placed in the Southeast corner of each floor plan examined. The compartment fires examined include a long-cool and short-hot fire produced from the design curves by Pettersson et al. [106] and an ASTM E119 standard fire [6].

5.4. Methodology

A sequentially-coupled fire-thermal-structural analysis procedure is utilized as shown in Figure 5-7. The iTFM [12] is used to define the evolution of a 1D traveling fire exposure in the form of gas temperature-time curve at discrete locations along the length of the compartment (Figure 5-7(a)). A numerical heat transfer analysis is then used to predict the internal temperatures of all fire exposed members (Figure 5-7 (b)). The temperature-time curves predicted by the iTFM are used to define the radiative and convective boundary conditions of the heat transfer analyses.

Finally, a structural analysis is ran using the member temperature data (Figure 5-7(c)). Both the thermal and mechanical simulations are ran using the finite element software ABAQUS [80] and described in the following sections.

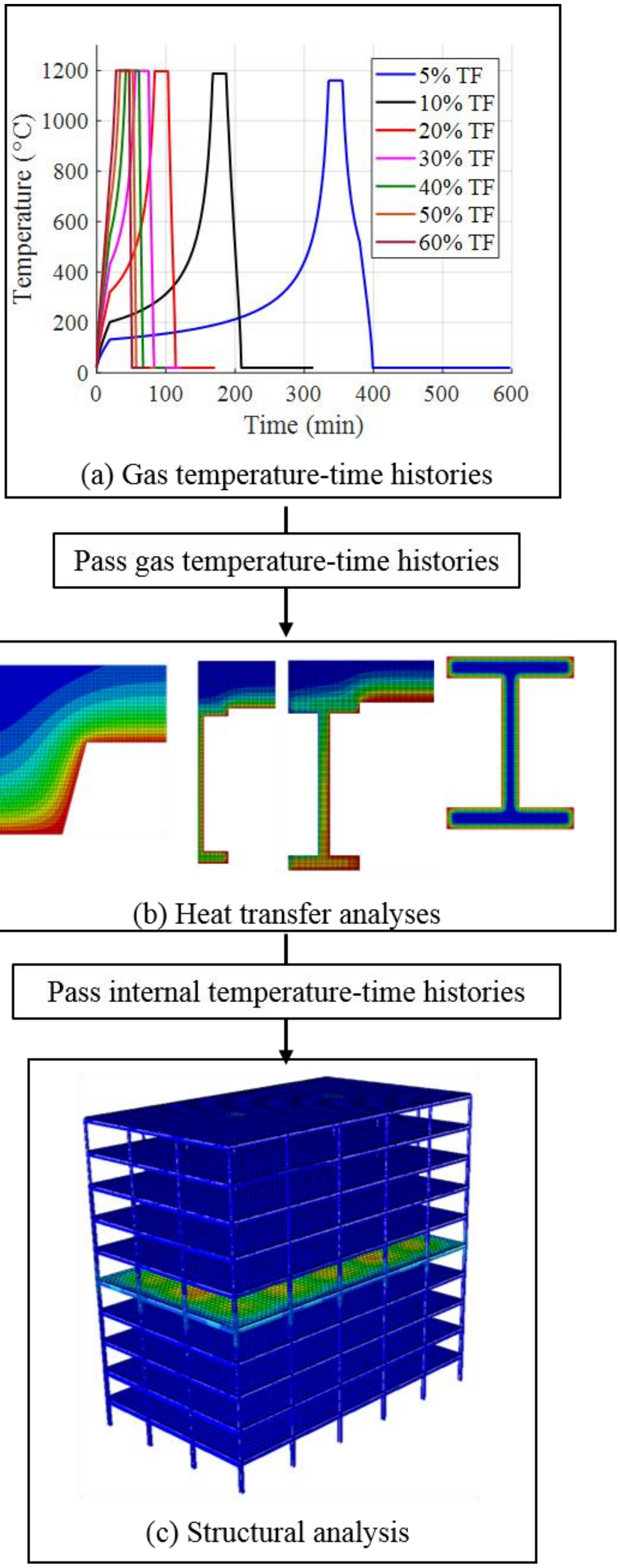

Figure 5-7. Sequentially-coupled fire-thermal-mechanical simulation overview.

5.5. Heat Transfer Analysis

While traveling fires produce spatially non-uniform temperatures within an open-plan compartment, 2D heat transfer analyses were utilized in lieu of 3D heat transfer approaches [126–130]. It was assumed that the rate of heat conduction in the longitudinal axis of floor beams and the composite floor slab was gradual in comparison to the spread rate of a traveling fire. This allowed the thermal response of a composite floor slab exposed to a traveling fire to be captured using numerous 2D heat transfer analyses. The iTFM does not currently account for any vertical temperature gradients within a burning open-plan compartment, and thus a 2D heat transfer model is adequate for the thermal analysis of heated columns as well.

The thermal analyses were carried out using the finite element software ABAQUS [80]. Four node quadrilateral heat transfer elements *DC2D4* were used to mesh all parts of the analysis models utilized in the study. Figure 5-8 shows the heat transfer model of floor beams (both interior and perimeter beams), columns, and composite floor slab. The model of the interior beam and composite floor slab are reduced using symmetry, with adiabatic boundary conditions assigned to symmetrical edges. Thermal gradients occurring due to partial fire exposure of perimeter beams are accounted for in the analysis model presented in Figure 5-8(b). Thermal gradients occurring in both perimeter and corner columns are accounted for in the analysis model presented in Figure 5-8(c) by adjusting the heated boundary accordingly. The composite slab in the interior and perimeter beam models are included to consider the heat sink effects associated with the slab resting on the steel beam. A detailed model of the composite slab is utilized to extract slab temperatures as shown in Figure 5-8(d), which accurately accounts for the shape of the slab. Following the results of a sensitivity analysis, a mesh size of 3 mm and a time increment of 1 seconds were chosen for the analyses. These analyses are presented in the APPENDIX.

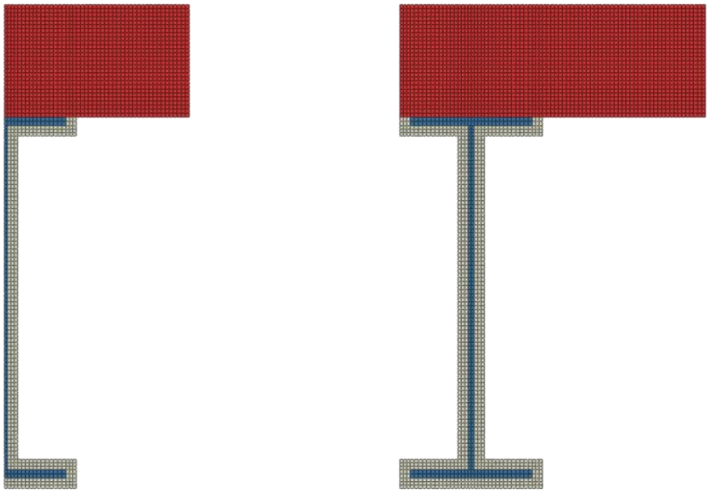

(a) Interior beam (b) Perimeter beam

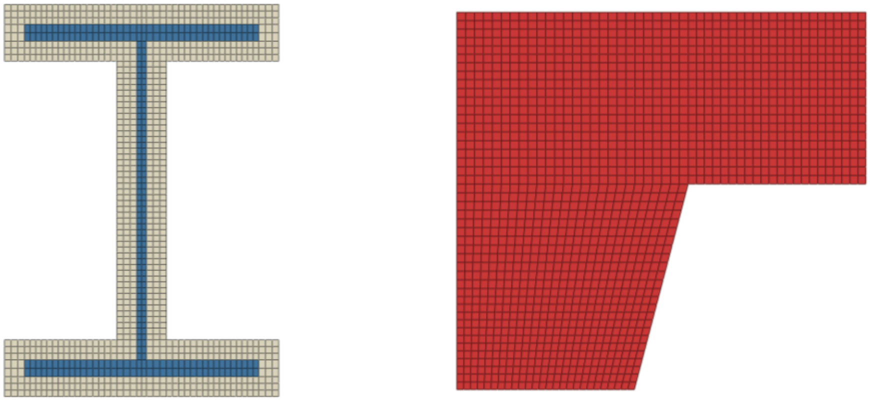

(c) Column (d) Composite slab

Figure 5-8. Heat transfer model: (a) interior beam; (b) perimeter beam; (c) column; and (d) composite slab.

Temperature-dependence of the thermal conductivity, specific heat, and mass density of both concrete and steel were defined using the models in Eurocode 2 Part 1-2 [78] and Eurocode 3 Part 1-2 [87], respectively. Temperature-dependence of the thermal conductivity, specific heat, and mass density of CAFCO 300 insulation are taken from experimental testing by Kodur and Shakya [107]. The temperature-time curve of the fire was used to define the radiative and convective boundary conditions of the heat transfer analyses. To define the radiative boundary conditions, an emissivity of $\varepsilon_r = 0.7$ was used for both steel and concrete as prescribed by Eurocode

4 Part 1-2 [108], while an emissivity of ε_r = 0.9 was used for SFRM insulation [131]. To define the convective boundary conditions, a heat transfer coefficient of h_c = 25 W/(m^2-K) and h_c = 35 W/(m^2-K) was used for a standard fire and natural fire respectively as prescribed by Eurocode 1 Part 1-2 [109], while a heat transfer of coefficient of h_c = 35 W/(m^2-K) was used for a traveling fire exposure.

5.5.1. Numerical Validation

Validation of the numerical heat transfer analyses were performed using test data on composite floor slabs exposed to fire including test performed by Guo and Bailey [110], Lim and Wade (i.e., the BRANZ fire tests) [64,65], and Vassart and Zhou (i.e., the COSSFIRE fire test) [66]. The composite slab tested by Guo and Bailey [110] consisted of a 85 mm thick slab cast on a 60 mm steel deck. The composite slab tested by Lim and Wade, identified as the *HiBond* slab, consisted of a 75 mm thick slab cast on a 55 mm steel deck. The composite slab from the COSSFIRE test consisted of a 77 mm thick slab cast on a 58 mm steel deck. For brevity, additional data regarding each test case is not presented and can be found in the accompanying references.

Figure 5-9(a) and Figure 5-9(b) show the results of the validation study using the two composite floor slabs examined by Guo and Bailey (identified as *Fire 1* and *Fire 2*), while Figure 5-9(c) and Figure 5-9(d) shows the validation study using the BRANZ *HiBond* composite floor slab and COSSFIRE composite floor slab, respectively. In Figure 5-9, experimentally-recorded temperatures are presented with dashed lines with markers, while numerical predictions are presented with solid lines. In each test, “0 mm” is taken as the bottom of the slab, which is directly exposed to fire.

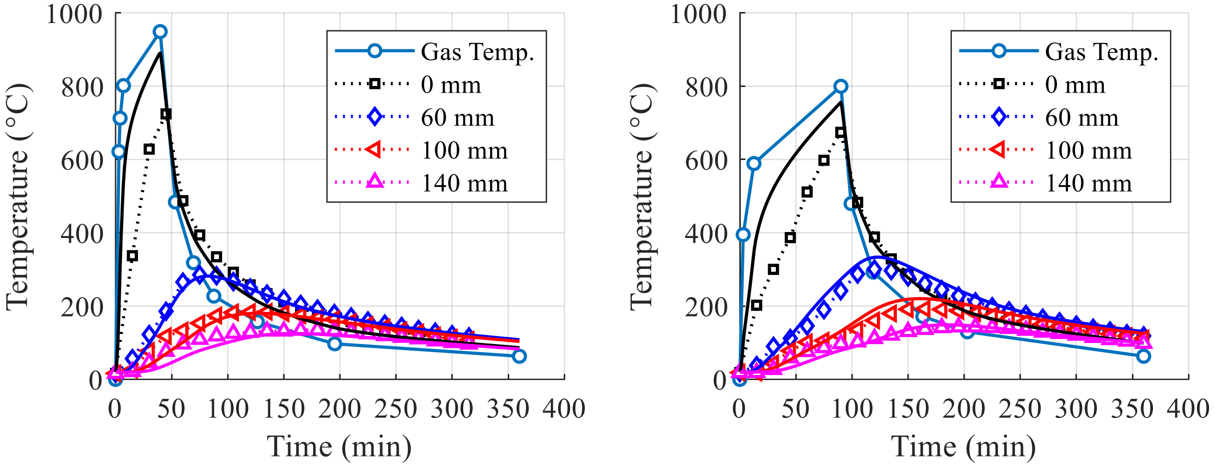

(a) Guo and Bailey's *Fire 1* slab (b) Guo and Bailey's *Fire 2* slab

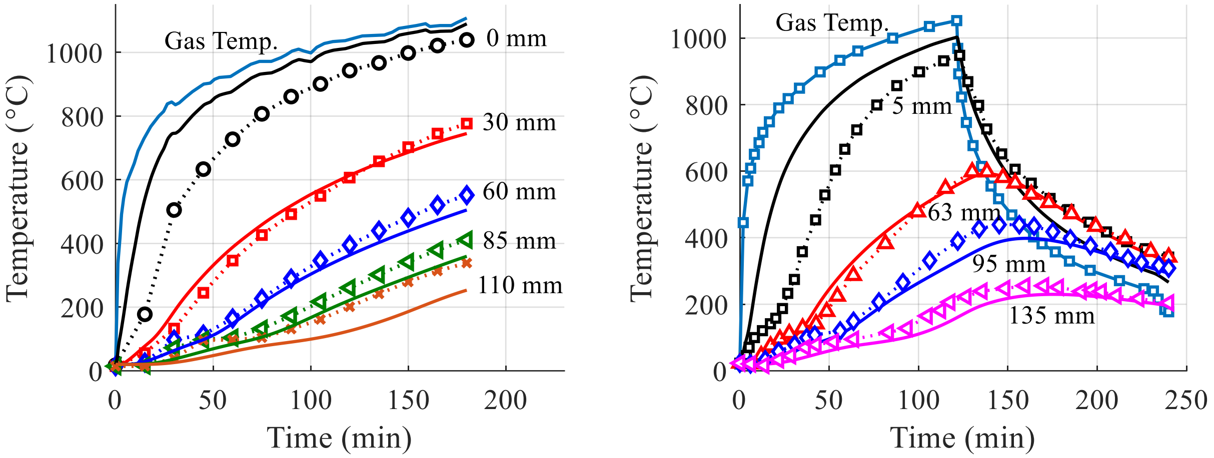

(c) *BRANZ HiBond* slab (d) COSSFIRE slab

Figure 5-9. Numerical validation: (a) Guo and Bailey's *Fire 1* slab [133]; (b) Guo and Bailey's *Fire 2* slab [133]; (c) *BRANZ HiBond* slab [64,65]; (d) COSSFIRE slab [66]. Solid lines represent numerical data, while dashed lines with grid markers represents experimental data.

The modeling approach over predicts the temperature at the bottom of a composite slab (i.e., 0 mm), as shown in all test cases examined in Figure 5-9, with better predictions observed elsewhere within the slab. Poor prediction of temperature at the top of the *BRANZ HiBond* slab in Figure 5-9(c) (i.e., at 85 mm and 110 mm) is acknowledged, but the test may be an outlier given the good predictions in the other test cases. Overall, close approximation with experimental values were obtained, demonstrating that the modeling approach is adequate.

The validation of heat transfer through wide-flanged steel sections was carried out using experimental test data from the Cardington Test no. 3 [67,68]. Test no. 3 consisted of a natural fire applied to a 9.98 m x 7.57 m compartment located at the corner bay of a steel-concrete composite floor system. Specific focus is placed on the interior steel floor beam of Test no. 3, which was left unprotected during testing. Figure 5-10 shows the results of the validation study, which examines the transfer of heat at the bottom flange, web, and top flange of the beam. Close approximation between experimental and numerical data are obtained, demonstrating that the modeling approach is sufficiently accurate. Only one test case was examined, particularly because the heat transfer of fire-exposed steel is not as challenging as the heat transfer of fire-exposed concrete. Kodur et al. [134] also showed that the Eurocode 3 Part 1-2 thermal properties of steel [87] can be used to accurately determine the internal temperatures of an unprotected (i.e., without insulation) heated wide-flanged steel beam.

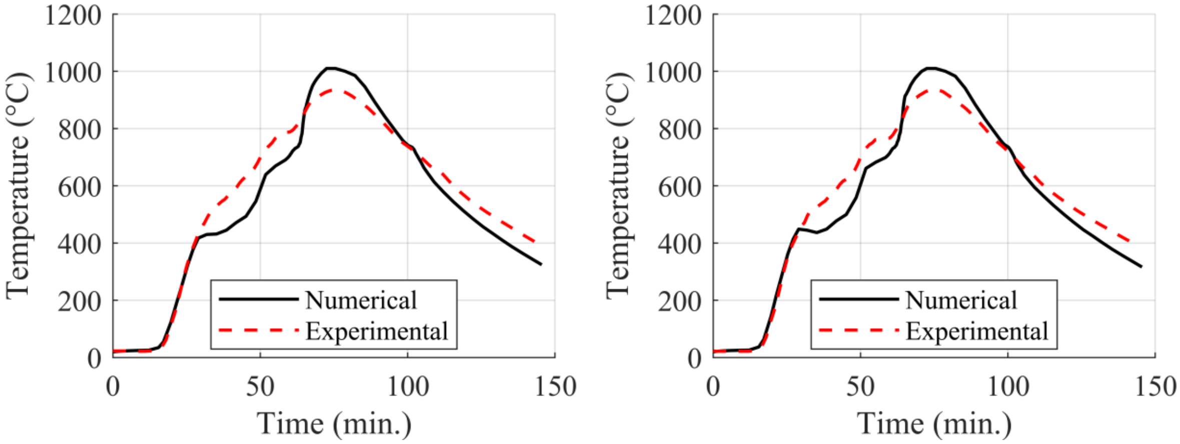

(a) Bottom flange (b) Web

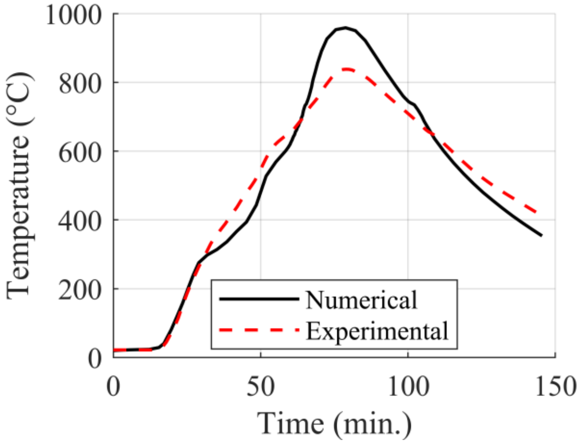

(c) Top flange

Figure 5-10. Numerical validation using temperature data at the mid-span of the interior steel beam from the Cardington Fire Test no. 3 [67,68]: (a) bottom flange; (b) web; and (c) top flange.

5.6. Structural Analysis

The structural analyses were also carried out using the finite element software ABAQUS [80]. The two composite buildings were modeled using an assembly of beam and shell elements as shown in Figure 5-11. A 4-node quadrilateral shell element *S4R* was used to model the composite floor slab, while a 2-node Timoshenko beam element *B31* was used to model steel beams and columns. The anisotropic behavior of the ribbed slab was considered implicitly by using an average depth. Full composite action was assumed by imposing a rigid constraint between the aligning nodes of the shell and beam elements. A mesh size of 635 mm x 635 mm was used for shell elements, while an average mesh size of 635 mm was used for beam elements. The mesh sizes selected were based on the results of a mesh sensitivity analysis. In both floor plans, shear tab connections are idealized as perfect pins, while moment connections in floor plan #2 are treated as fixed connections. In floor plan #1, the influence of the interior rigid core is included implicitly through idealized support conditions at each floor level (i.e., pinned support at the edges of the slab at the core). This simplification is justified since lateral loads are not applied to the building during the fire event.

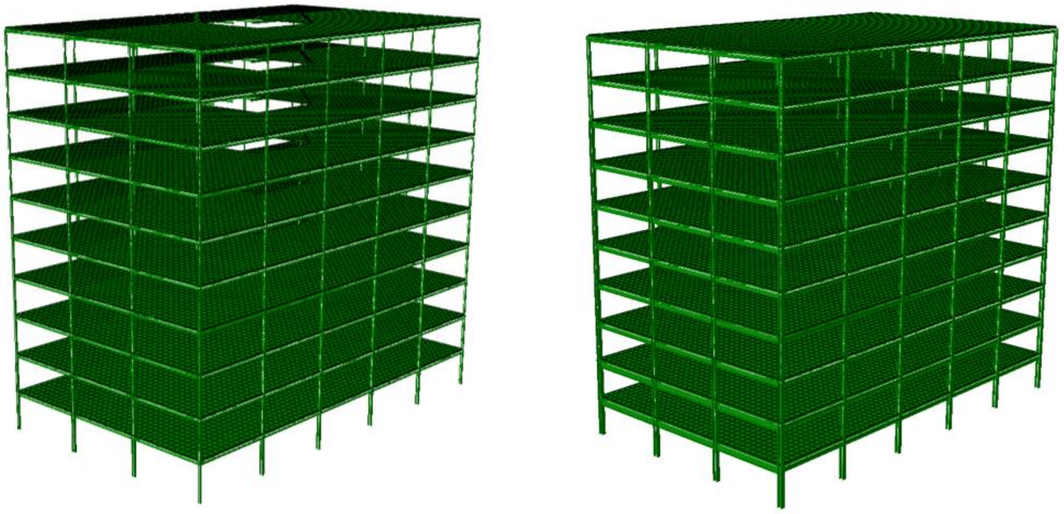

(a) Floor plan #1

(b) Floor plan #2

Figure 5-11. Isometric view of the structural analysis models with rendering of beam and shell elements: (a) floor plan #1; and (b) floor plan #2.

Both geometric and material nonlinearities were included in the analyses. The metal plasticity model in ABAQUS was used to define the inelastic response of steel. As input, the engineering stress-strain curves (f *vs.* ε) converted to true stress-true plastic strain curves (f_{true} *vs.* ε_{true}^{pl}) using Equation (5-3) and Equation (5-4) respectively, where E_s is the elastic modulus of steel.

$$f_{true}=f(1+\varepsilon) \tag{5-3}$$

$$\varepsilon_{true}^{pl}=\ln(1+\varepsilon)-\frac{f_{true}}{E_s} \tag{5-4}$$

Temperature dependence of structural steel was defined using the stress-strain-temperature model in Eurocode 3 Part 1-2 [87]. Poisson's ratio for steel was taken as $v = 0.3$. Thermal expansion was included in the analyses by utilizing the thermal elongation model ($\Delta l/l_o$ *vs.* T) in Eurocode 3 Part 1-2 [87]. ABAQUS requires the secant coefficient of expansion α_{sec} as input to define the thermal expansion strain ε_{th} at an arbitrary temperature T, relative to a reference temperature T_o. Thus, the thermal elongation model $\Delta l/l_o$ *vs.* T is converted to a coefficient of expansion model (α_{sec} *vs.* T) using Equation (5-5).

$$\alpha_{sec}=\frac{\varepsilon_{th}}{T-T_o} \tag{5-5}$$

The damaged plasticity model in ABAQUS was used to represent the inelastic response of concrete. Temperature dependence of concrete was defined using the compressive stress-strain-temperature model in Eurocode 2 Part 1-2 [78]. Poisson's ratio for concrete was taken as $v = 0.19$. The temperature-dependent thermal elongation model ($\Delta l/l_o$ *vs.* T) of concrete in Eurocode 2 Part 1-2 [78] was converted to a coefficient of expansion model (α_{sec} *vs.* T) using Equation (5-5). The tensile response of concrete was defined using the elevated-temperature tension stiffening model proposed by Martinez and Jeffers [113].

Loads were applied sequentially: gravity loads were applied first followed by thermal loads, which were applied as predefined temperature fields. The solution to all analyses were obtained using a static solution procedure in ABAQUS/Standard [80] with tension stiffening used to overcome convergence issues associated with localized concrete cracking in the early stages of the fire. Since columns were fire protected to a 2 h fire rating to prohibit column buckling, use of an explicit dynamic procedure was not required.

5.6.1. Numerical Validation

Validation of the structural analyses were performed using test data on composite floor slabs exposed to fire including the FRACOF fire test [66] and the Cardington Test no. 3 [67,68].

5.6.1.1. FRACOF Fire Test

The FRACOF fire test was a fire test carried out on a partially-protected steel-concrete composite floor assembly, conducted in France in 2008 [66]. The floor assembly had a plan dimension of 6.66 m x 8.7 m and was subjected to a 2 h standard fire exposure. The floor slab was composed of a 97 mm thick C30/37 normal weight concrete with a compressive strength of $f_{c'}$ = 36.7 MPa, cast on a 58 mm steel decking. The slab was embedded with S500 reinforcement, placed 50 mm from the top of the slab. Floor beams consisted of IPE300 steel sections with a yield strength of F_y = 311 MPa, while girders consisted of IPE400 steel sections with a yield strength of F_y = 423 MPa. During testing, the floor was loaded with a live load of 3.87 kN/m^2.

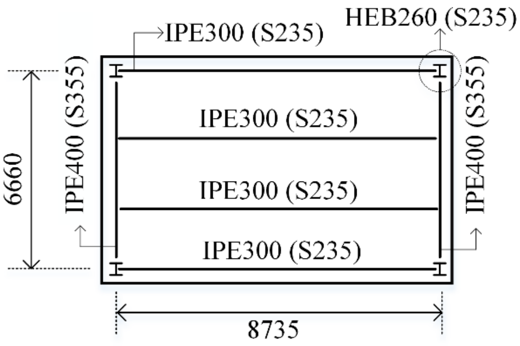

Figure 5-12. Test configuration of FRACOF fire test [66]. All dimensions in [mm].

In the structural model, an average mesh size of 200 mm x 200 mm was used for shell elements, while an average mesh size of 200 mm was used for beam elements. The temperatures of the beams, girders, and slab measured during testing were passed to the structural model as predefined temperature fields. Beam-end connections were idealized as perfectly pinned. The final validation of the FRACOF test is shown in Figure 5-13. Figure 5-13 shows the displacement at 2 locations within the floor slab, labeled *D1* and *D2*. Close approximation with experimental values were obtained, demonstrating that the modeling approach is sufficiently accurate.

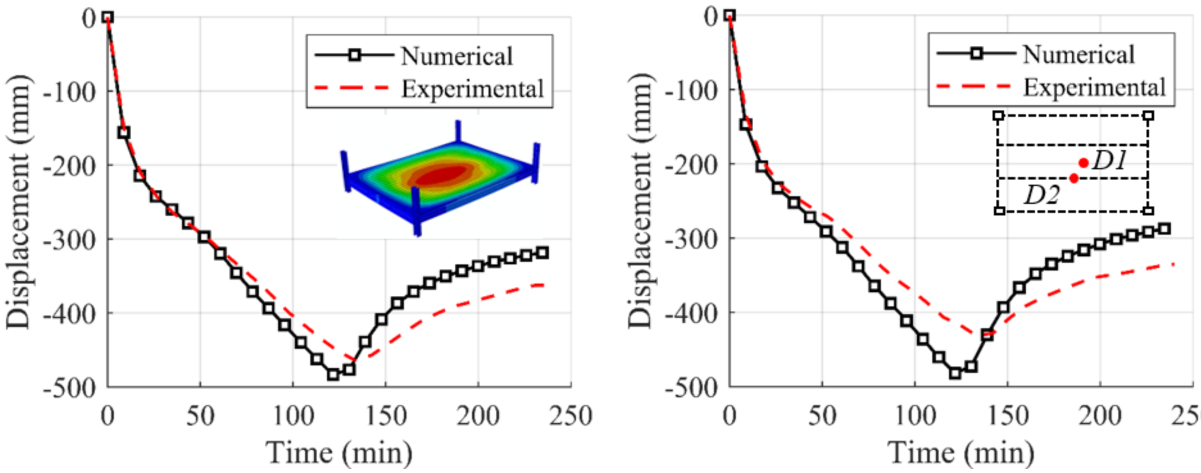

(a) At Location *D1* (b) At Location *D2*

Figure 5-13. Displacement of the FRACOF fire test: (a) location *D1*; and (b) location *D2*.

5.6.1.2. Cardington Test no. 3

The Cardington Fire Tests were a series of fire tests carried out on a 8-story steel framed structure with composite floor slabs, conducted between 1995 and 1996 at the British Research Establishment (BRE) Test Facility [67,68]. Test no. 3 consisted of a natural fire applied to a 9.98 m x 7.57 m compartment located at the corner bay of the second floor. The floor slab was composed of a 70 mm thick A35 light-weight concrete with a compressive strength of $f_{c'}$ = 39 MPa, cast on a 60 mm steel deck. The slab was reinforced with A142 reinforcement placed 55 mm from the top of the slab. Two grades of steel were used in the steel frame: (1) S275 Grade 43 with a yield strength of F_y = 308 MPa; and (2) S355 Grade 50 with a yield strength of F_y = 390 MPa. During testing, the slab was loaded with a live load of 5.48 kN/m^2.

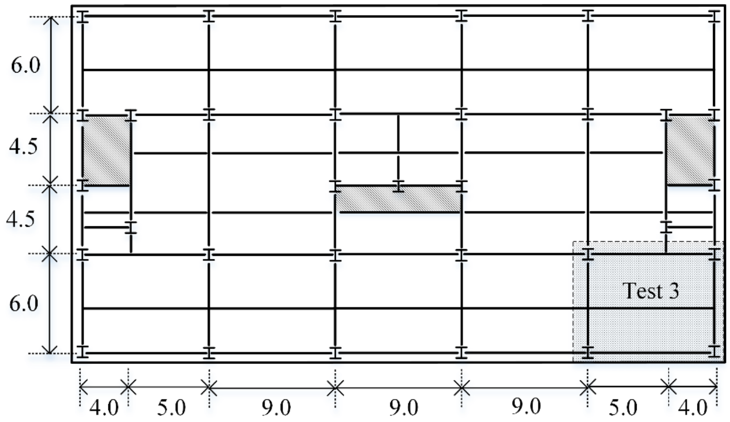

Figure 5-14. Test configuration of Cardington floor test [67,68]. All dimensions in [m].

In the structural finite element model, an average mesh size of 500 mm x 500 mm was used for shell elements, while an average mesh size of 500 mm was used for beam elements. Symmetry was assumed and a quarter of the floor plan was modeled. The temperatures of the beams, girders, columns and slab measured during testing were passed directly to the structural model as predefined temperature fields. Beam-end connections were idealized as perfectly pinned. The final validation for Test no. 3 is shown in Figure 5-15. Figure 5-15 shows the displacement at two locations within the floor slab, labeled *D11*and *D14*. Close approximation with experimental values were obtained, demonstrating that the modeling approach is sufficiently accurate.

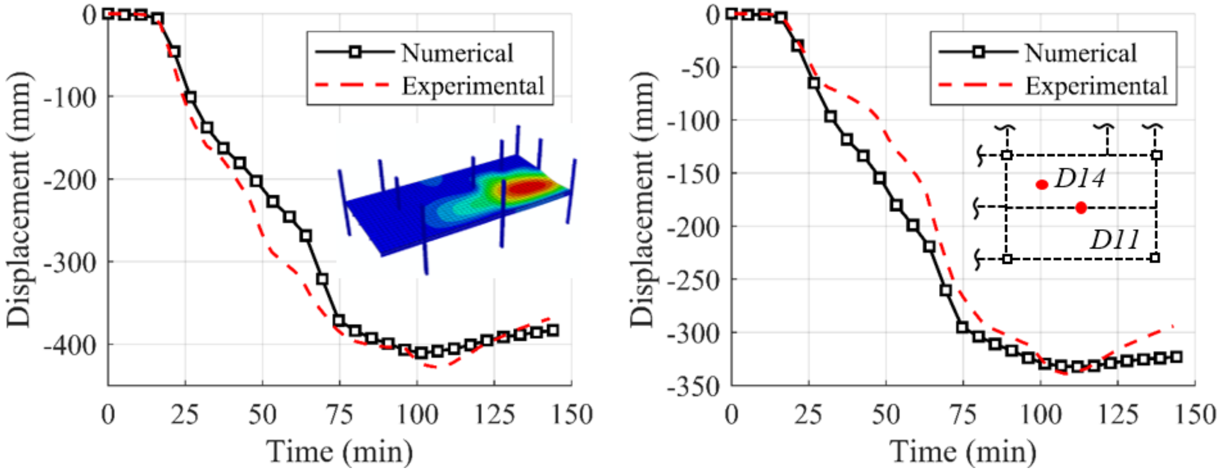

(a) At Location *D11*

(b) At Location *D14*

Figure 5-15. Displacement for Cardington Test no. 3 at various locations: (a) location *D11*; and (b) location *D14*.

5.7. Results

5.7.1. General Response

The fire response of the composite floor plan is largely influenced by the traveling fire size. Figure 5-16 shows the vertical slab displacement at the center of the bay closest to the fire ignition (i.e., location *S1*), and the bay furthest from the fire ignition (i.e., location *S5*). Similar behaviors were observed in both floor plans and with various levels of fire protection, and for brevity, only displacements of floor plan #2 with a full protection scheme and a 1 h fire rating are shown. In all figures, displacements are normalized by the displacement limit of $L/20$, where L is the span of the bay.

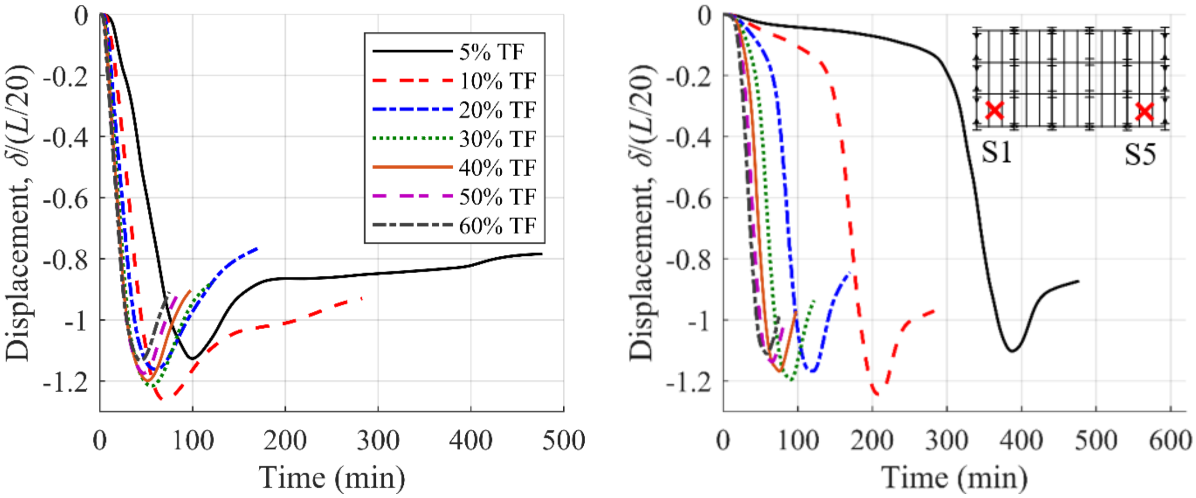

(a) Center of bay 1 (i.e., *S1*) (b) Center of bay 5 (i.e., *S5*)

Figure 5-16. Vertical slab displacement of floor plan #2 with a full protection scheme and a 1 h fire rating: (a) Center of bay 1 (i.e., location *S1*); (b) Center of bay 5 (i.e., location *S5*). In the legend, "TF" is an abbreviation for "traveling fire."

At location *S1*, the rate of displacement is nearly independent of the burning size of the traveling fire as shown in Figure 5-16(a). Since this bay is at the fire ignition point, the center of the bay experiences the near field region of a traveling fire at nearly the same time, regardless of the fire size. The displacement at this bay increases monotonically for each traveling fire until the peak displacement is reached. The peak displacement at this bay is dependent on the relationship between the burning size and travel speed of the traveling fire, which was shown previously in Figure 5-4(a). Although a larger traveling fire may engulf the first bay entirely, it does so for a short period. Conversely, a smaller traveling fire may engulf the first bay partially, but it does so for a longer period. The burning size and travel speed properties of a 10% traveling fire size results in the worst traveling fire scenario at bay 1 in terms of peak displacement, rather than the traveling fire with the largest burning area (i.e., 60% traveling fire), or the traveling fire with the longest fire duration (i.e., a 5% traveling fire).

At location *S5*, the initial rate of displacement is dependent on the burning size of the traveling fire as shown in Figure 5-16(b). Since this bay is at the far end of the floor plan, and far away from the fire ignition point, it experiences the burning region of a traveling fire at different times, depending on the travel speed of the fire. In general, the displacement at this bay is initially caused by heating from the smoke region of a traveling fire. When the burning region of the fire reaches this bay, the displacement rate increases due to the rise of temperature. Consequently, the rate of displacement prior to the arrival of the burning region is smaller than the rate of displacement at the arrival of the burning region. This is observable in the displacement response associated with a 5%, 10%, and 20% traveling fire as shown in Figure 5-16(b), without the need to scale the abscissa of the figure. Additionally, the time occurrence of the peak displacement at *S5* differs per traveling fire, primarily due to the different travel speed of each traveling fire size. Under a 5% traveling fire the peak displacement occurs at 390 min into the fire, while under a 60% traveling fire the peak displacement occurs at 60 min into the fire.

Similar trends are observed for floor plan #1 with a full protection scheme and a 1 h fire rating as shown in Figure 5-17, that is: (1) at location *S1*, the rate of displacement is nearly independent of the burning size of the traveling fire; and (2) at location *S5*, the rate of displacement is dependent on the burning size of the traveling fire (or the travel speed). These trends are independent of the fire rating of the floor beams and can be seen in each floor plan with a full protection scheme and a 2 h fire rating. It should be noted under a 1 h fire rating, slab displacements in both floor plan surpass the displacement limit of *L*/20 in all traveling fires, demonstrating that traveling fires produce displacements of the floor slab that are structurally significant.

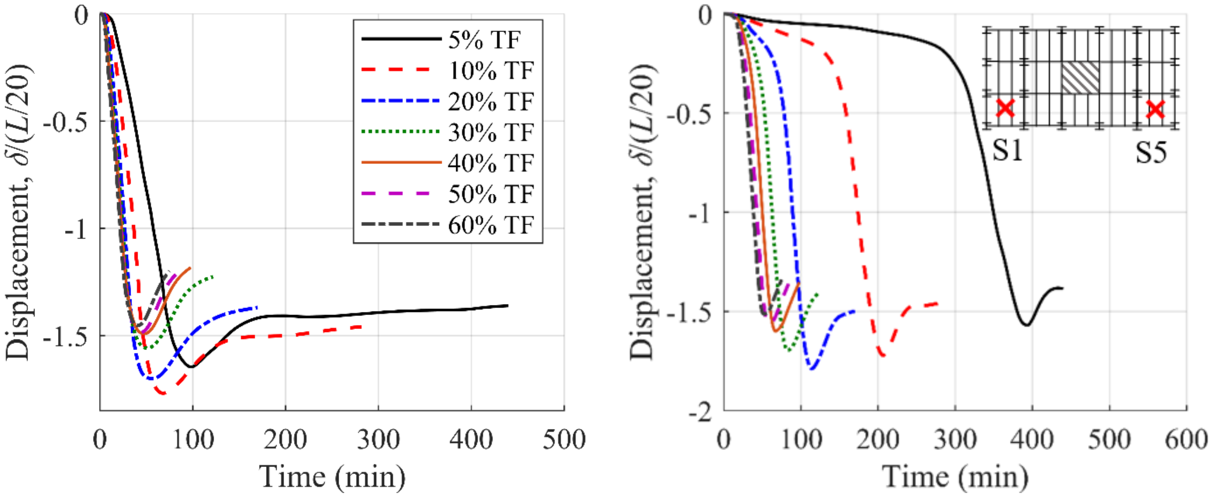

(a) Center of bay 1 (i.e., *S1*)

(b) Center of bay 5 (i.e., *S5*)

Figure 5-17. Vertical slab displacement of floor plan #1 with a full protection scheme and a 1 h fire rating: (a) Center of bay 1 (i.e., location *S1*); (b) Center of bay 5 (i.e., location *S5*).

The displacement response under a short-hot, long-cool, and ASTM E119 standard fire, are shown in Figure 5-18. For brevity, only displacements of floor plan #2 with a full protection scheme and a 1 h fire rating are shown. Displacements are shown at the center of each bay exposed to fire (i.e., locations *U1*, *U2*, *U3*, and *U4*, as shown in Figure 5-18(d)). In all figures, displacements are normalized by the displacement limit of *L*/20.

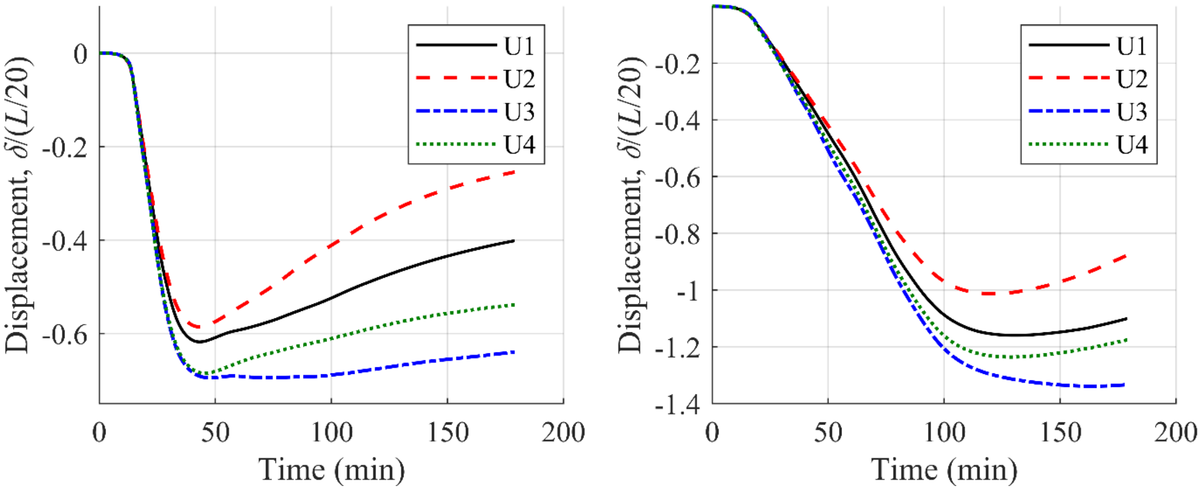

(a) Short-Hot Fire

(b) Long-Cool Fire

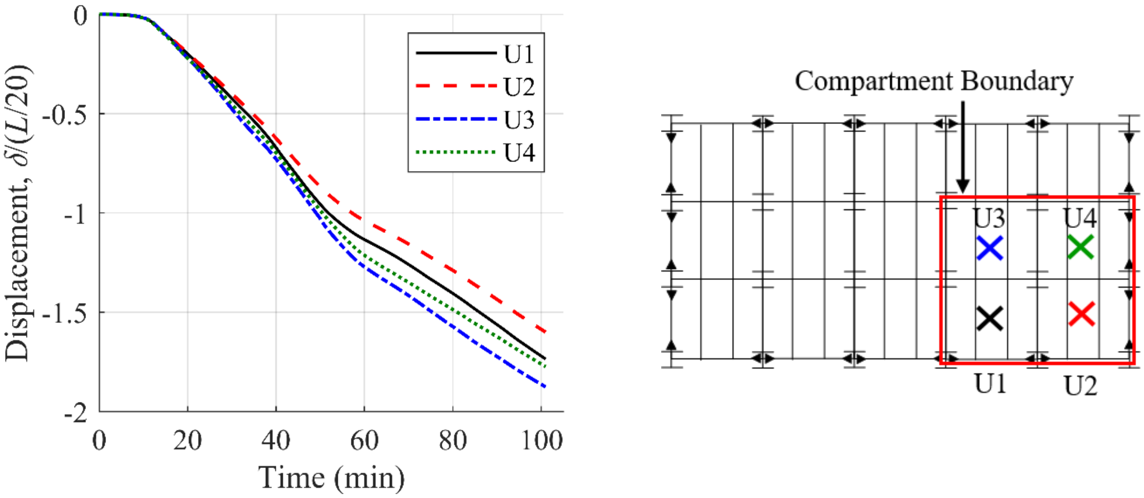

(c) ASTM E119 Fire

(d) Floor plan #2

Figure 5-18. Slab displacement of floor plan #2 with a full protection scheme and 1 h fire rating: (a) short-hot fire; (b) long-cool fire; (c) ASTM E119 standard fire; and (d) floor plan #2 with displacement labels *U1* through *U4*.

The short-hot fire represents a fire exposure with a steep growth rate, followed by a sharp decay phase, all occurring in a short period as shown previously in Figure 5-6(c). Due to the steep growth rate of a short-hot fire, the displacement rate of the composite slab are also steep. However, due to the short burning duration, displacements are maintained below the displacement limit of *L*/20, with the largest normalized peak displacement of 0.75 occurring at location *U3*. In general, displacement at each bay increase with time up until material cooling of the slab is encountered at about t = 48 min. During cooling, heated members regain part of their strength, resulting in a reduction of displacements over time.

Similar trends are observed during a long-cool fire, which represents a moderate fire exposure with a slow growth rate but a longer burning duration (see Figure 5-6(c)). Due to the moderate growth rate of a long-cool fire, the displacement rate of the composite slab is smaller in comparison to those under a short-hot fire. However, larger displacements are observed due to the longer burning duration, with peak displacement at each bay surpassing the displacement limit of $L/20$. The largest normalized peak displacement is 1.4, and occurs at location *U3*. Displacement at each bay also increases with time up until cooling of the slab is encountered. During cooling, heated members regain part of their strength, resulting in a reduction of displacements over time.

Displacements under an ASTM E119 standard fire increase monotonically with time as shown in Figure 5-18(c). Peak displacements at each bays are above the displacement limit $L/20$, with the largest normalized peak displacement of 1.8 occurring at location *U3*. It should be noted that in all uniform burning fires, larger peak displacements are observed at location *U3*. This is attributed to the axial-restraint provided on all edges of the interior slab panel.

5.7.2. Peak Displacement

An analysis of peak displacement is presented in Figure 5-19, which shows the relationship between the traveling fire size and peak slab displacement for both floor plans, each with a full protection scheme. Peak displacements are examined at three locations along the floor plan. Location *S1* represents the first bay closest to the fire ignition point, while location *S3* and *S5* represents the bay at the center of the floor plan, and the bay furthest from the fire ignition point, respectively. In all figures, peak displacements are normalized by the displacement limit of *L*/20.

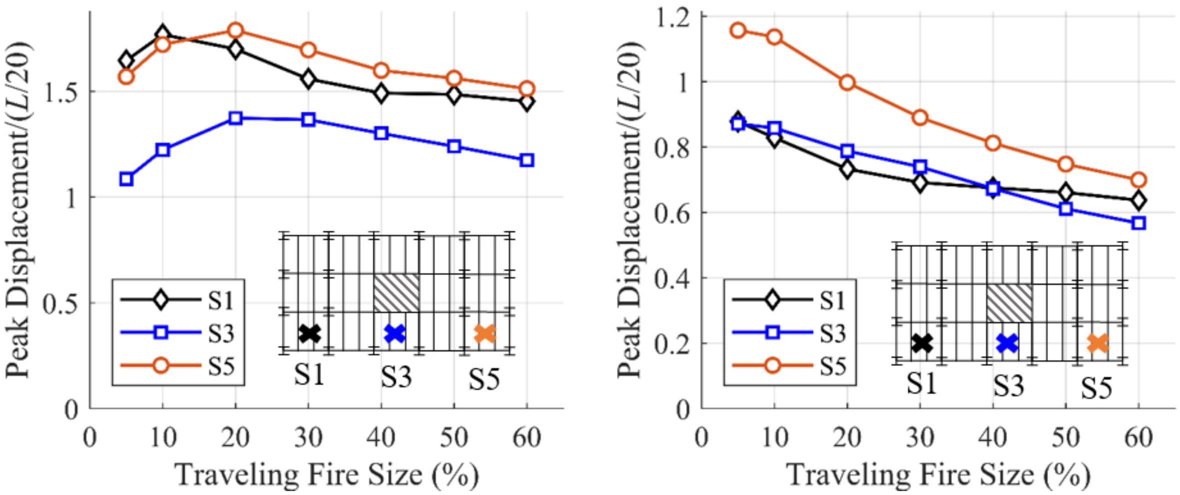

(a) Floor Plan #1, 1 h fire rating

(b) Floor Plan #1, 2 h fire Rating

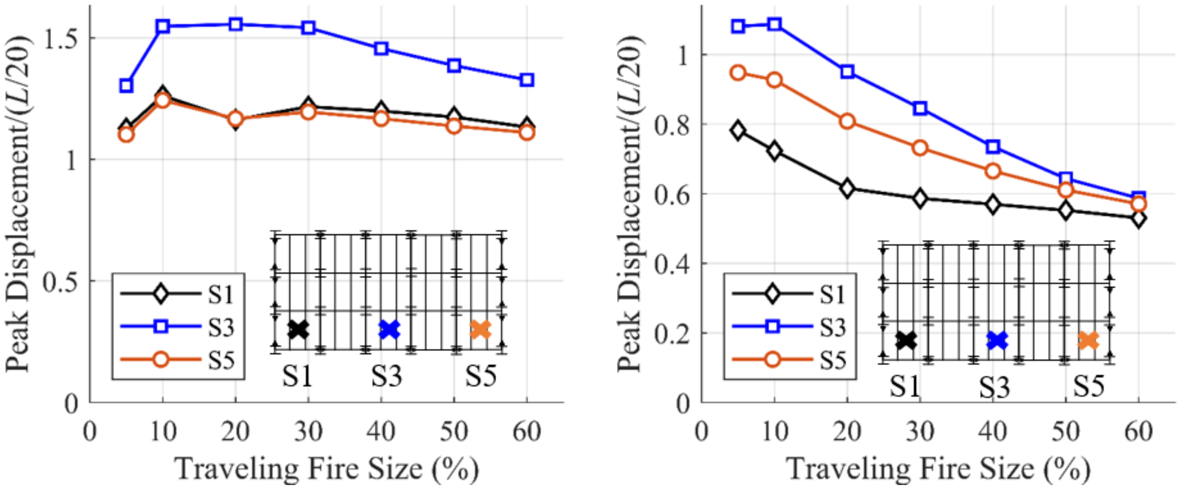

(c) Floor plan #2, 1 h fire rating

(d) Floor Plan #2, 2 h fire rating

Figure 5-19. Influence of traveling fire size on peak slab displacement: (a) floor plan #1 with a 1 h fire rating; (b) floor plan #1 with a 2 h fire rating; (c) floor plan #2 with a 1 h fire rating; and (d) floor plan #2 with a 2 h fire rating.

Figure 5-19 demonstrates that the fire rating of the floor plan influences the relationship between the traveling fire size and the peak slab displacement. Under a 2 h fire rating, the relationship between peak displacement and traveling fire size is nearly linear, with larger peak displacements corresponding to the 5% traveling fire. Under a 1 h fire rating, the relationship between peak displacement and traveling fire size is nonlinear, with peak displacements occurring under a 10% or 20% traveling fire, depending on the location being analyzed. The above findings demonstrates that the critical traveling fire size, in terms of peak displacement, is dependent on the fire rating of the composite floor plan. Moreover, the determination of the critical traveling fire size requires a family of traveling fires to be examined.

Figure 5-19 also reveals information regarding the critical location at which the peak displacement occurs. In floor plan #1, larger peak displacements generally occur at the bay furthest from the fire ignition point (i.e., location *S5*). In floor plan #2, larger peak displacements generally occur at the center of the entire floor plan (i.e., location *S3*). These observations are generally maintained for each traveling fire and are independent of the fire rating of the floor plan. Thus, the critical location corresponding to the largest peak displacement is dependent on the characteristics of the floor plan, and not the traveling fire size nor the fire rating of the floor plan. This observation corrects the long standing notion that the critical location corresponding to the largest peak displacements occurs at the bay furthest from the fire ignition point [138].

Figure 5-20 shows the relationship between peak displacement and time to peak displacement for different fire types. Both floor plans are examined, each with a full protection scheme. In Figure 5-20, peak displacements associated with uniform burning fires (i.e., short-hot, long-cool, and ASTM E119 standard fire) are represented with solid colored markers, while peak displacements associated with traveling fires are represented with white-filled markers, all connected with a dash line. Lastly, the peak displacements in Figure 5-20 are all taken from the critical location of each floor plan, that is location *S5* for floor plan #1 under a traveling fire, location *S3* for floor plan #2 under a traveling fire, and location *U3* for both floor plans under a uniform burning fire.

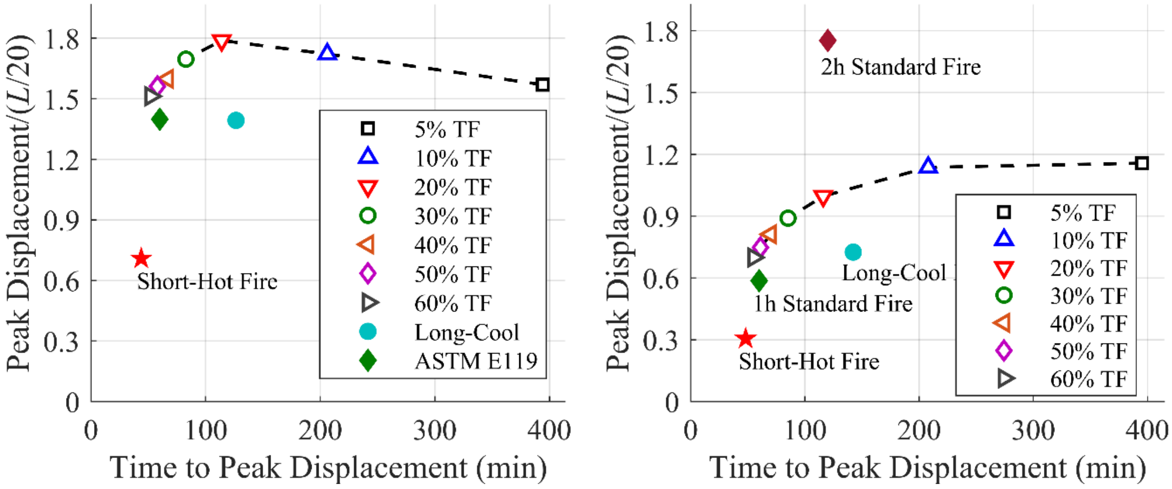

(a) Floor plan #1, 1 h fire rating (b) Floor plan #1, 2 h fire rating

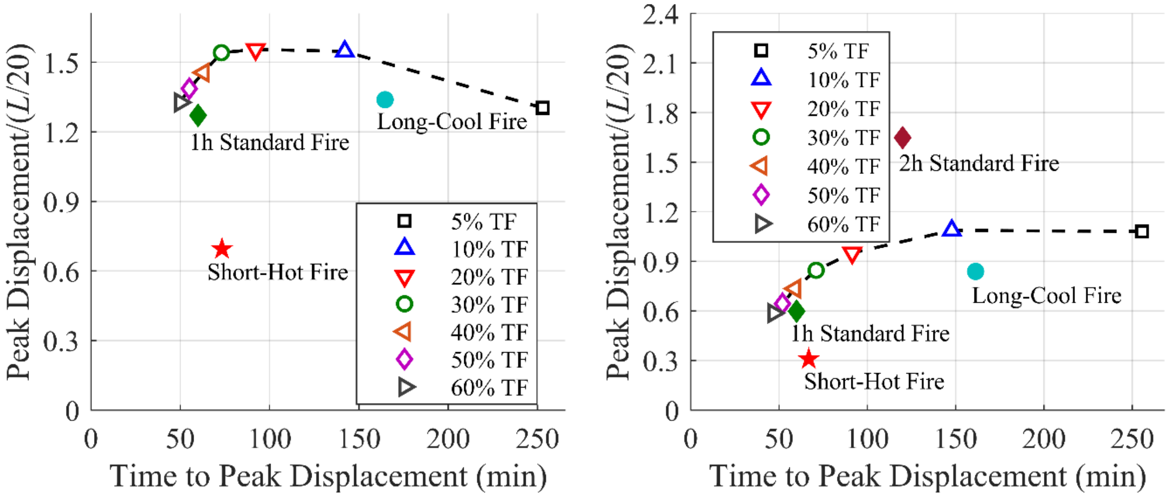

(c) Floor plan #2, 1 h fire rating (d) Floor plan #2, 2 h fire rating

Figure 5-20. Relationship between peak displacement and time to peak displacement for each fire type examined: (a) floor plan #1 with a 1 h fire rating; (b) floor plan #1 with a 2 h fire rating; (c) floor plan #2 with a 1 h fire rating; (d) floor plan #2 with a 2 h fire rating.

Several trends are observed, including:

- Time to peak displacement decreases with increasing traveling fire size, irrespective of the floor plan and fire rating;
- In both floor plans, each with a 1 h fire rating, peak displacements from traveling fires are all above the displacement limit of *L*/20;
- In both floor plans, each with a 1 h fire rating, peak displacements from traveling fires are all larger than peak displacements from a short-hot fire, long-cool fire, and 1 h standard fire exposure;
- In both floor plans, each with a 1 h fire rating, peak displacements from a 1 h standard fire exposure and a long-cool fire are nearly identical, and each surpass the displacement limit of *L*/20;
- In both floor plans, each with a 2 h fire rating, only peak displacements from 5% and 10% traveling fires surpass the displacement limit of *L*/20;
- In both floor plans, each with a 2 h fire rating, peak displacements from traveling fires are all larger than peak displacements from 1 h standard fire exposure, but smaller than peak displacement from a 2 h standard fire exposure;
- In both floor plans, each with a 2 h fire rating, peak displacements from a long-cool fire are larger than peak displacements from a 1 h standard fire exposure.

5.7.3. Displacement-Based Performance Analysis

In this study, the time to reach the displacement limit *L*/20, where *L* is the span of the bay, was quantified for each of the two floor plans. As mentioned previously, buckling of columns was prevented in the analyses by applying a 2 h fire rating, which allowed emphasis of the composite floor plan to be made. To this end, the displacement limit *L*/20 was used as a conservative metric of performance for the two composite floor system, and not a metric of failure.

The time to *L*/20 of each floor plan is presented in Figure 5-21, which shows the relationship between the traveling fire size and the time to *L*/20 of each floor plan, each with a full protection scheme and a 1 h fire rating. For brevity, time to *L*/20 was computed at floor locations *S1*, *S3*, and *S5*, which were previously described in section 5.7.2. The results show that time to *L*/20 decreases with increasing traveling fie size, as well as decreases with distance closer to the fire ignition point. Thus, the smallest time to *L*/20 of 22 min occurs at location *S1* under a 60% traveling fire for floor plan #1. Similarly, the smallest time to *L*/20 of 29 min occurs at location *S1* under a 60% traveling fire for floor plan #2. These time to *L*/20 are significantly under the 1 h fire rating limit of each floor plan (i.e., – 63% and – 52%, for floor plan #1 and floor plan #2, respectively), and demonstrate that each floor plan performs poorly under a traveling fire.

Under a 2 h fire rating, each floor plan performs satisfactorily under traveling fires, and thus the results are not shown for brevity. In both floor plans, the displacement limit *L*/20 is reached in only a 5% and 10% traveling fire. In floor plan #1, the limit is reached at 374 min under a 5% traveling fire, and at 195 min under a 10% traveling fire, each at location *S5*. In floor plan #2, the limit is reached at 235 min under a 5% traveling fire, and at 131 min under a 10% traveling fire, each at location *S3*. These times are well above the 2 h fire rating limit and demonstrate adequate performance under traveling fires.

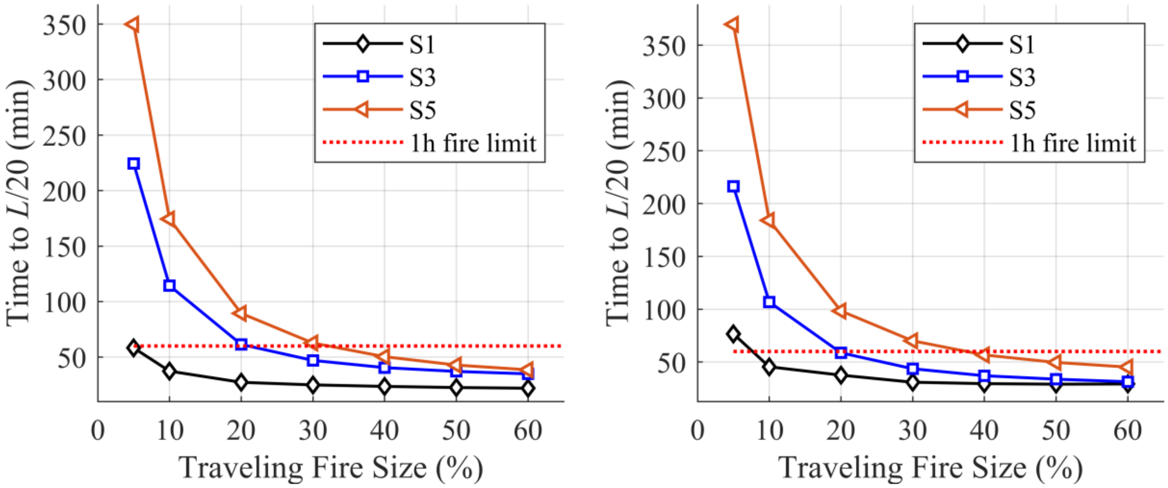

(a) Floor plan #1, 1 h fire rating (b) Floor plan #2, 1 h fire rating

Figure 5-21. Influence of the traveling fire size on the time to *L*/20: (a) floor plan #1 with a 1 h fire rating; and (b) floor plan #2 with a 1 h fire rating.

A comparison of the time to *L*/20 under different fire types are also shown in Figure 5-22, which shows time to *L*/20 as a function of location along the floor plan. Normalized locations with respect to the fire ignition point are presented in Figure 5-22, where $x = 0$ represents the location of the fire ignition point and $x = 1$ represents the location of the fire extinction. For brevity, only time to *L*/20 associated with a 60% traveling fire size are shown, since this fire size produces the smallest time to *L*/20 as shown previously in Figure 5-21.

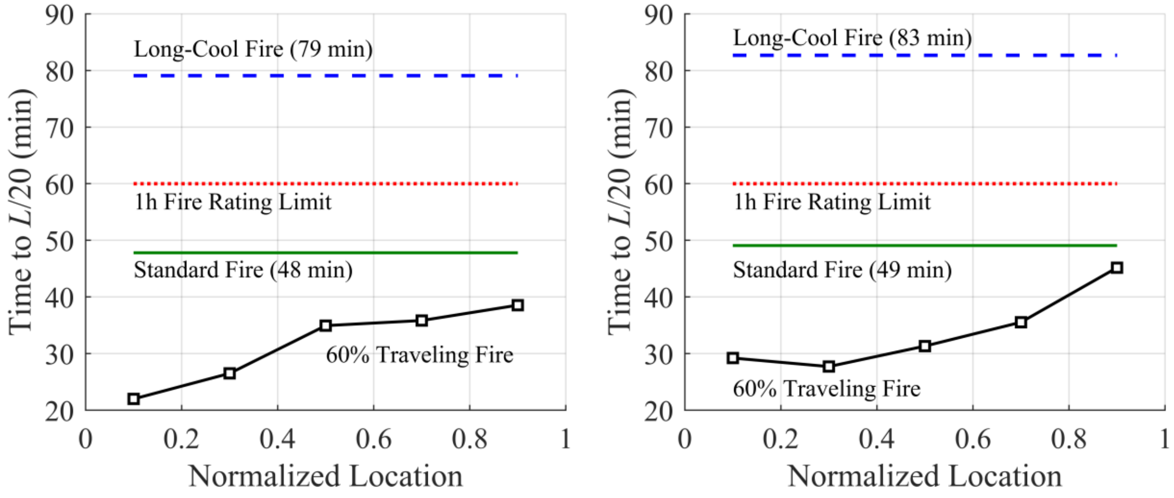

(a) Floor plan #1, 1 h fire rating (b) Floor plan #2, 1 h fire rating

Figure 5-22. Comparison of the time to *L*/20 under different fire types: (a) floor plan #1 with a 1 h fire rating; and (b) floor plan #2 with a 1 h fire rating. *L*/20 not reached under a short-hot fire exposure.

The results show that time to *L*/20 under traveling fires are well below those associated with a short-hot fire, long-cool fire, and standard fire. The time to *L*/20 under a long-cool fire and standard fire are very similar for each floor plan, and occur at about 80 min and 48 min, respectively. Under a short-hot fire, the displacement limit of *L*/20 was not reached in either floor plan. These findings demonstrates that insulation design via a prescriptive approach are conservative under real fire exposures, particularly under a short-hot and long-cool fire. Furthermore, a standard fire was shown to be conservative, when compared to either a short-hot and long-cool fire. In general, a larger margin of safety exists under a uniform burning fire than a traveling fire.

5.7.4. Fire Protection Scheme

As was previously shown, the two composite floor systems exhibited poor performance under traveling fire exposures, particularly when floor beams and girders where fire protected with a 1 h fire rating (see Figure 5-22). Thus, this section presents a design example within the framework of performance-based design, in which improved performance of the two composite floor systems under traveling fires is achieved through a modified protection scheme. Rather than simultaneously increasing the fire protection applied to all floor beams and girders, fire protection of the interior floor beams are removed, and essentially applied to the girders and exterior floor beams to increase the fire resistance of those members. While the former represents a design approach common in a prescriptive fire design framework, the latter represents an unconventional design approach, which is only allowed in a performance-based design framework. Specifically, the girders and the exterior floor beams of each floor plan are fire protected with a 2 h rating, while interior floor beams are left unprotected (see Figure 5-3(b)).

The displacement response of both floor plans under a 60% traveling fire are shown in Figure 5-23. Three different fire protection schemes are examined, including a full protection scheme with a 1 h fire rating, a full protection scheme with a 2 h fire rating, and the partial protection scheme described previously. For brevity, only displacements at the critical location of each floor plan, that is location *S5* for floor plan #1, and location *S3* for floor plan #2, are examined. The results show that use of a partial protection scheme leads to improved performance under a traveling fire when compared to the response of each floor plan with a full protection scheme and a 1 h fire rating. Under the partial protection scheme, the displacement rate is larger than the displacement rate from a full protection scheme with a 1 h fire rating. A change of the displacement rate occurs during the onset of tensile catenary action (TMA), which is illustrated with a square marker in Figure 5-23. The peak displacement under a partial protection scheme are smaller than those from a full protection scheme with a 1 h fire rating, but larger than peak displacements from a full protection scheme with a 2 h fire rating. More importantly, peak displacements from a partial protection scheme are well below the displacement limit of *L*/20, demonstrating an improved performance relative to the peak displacements from a full protection scheme with a 1 h fire rating, which are well above the displacement limit of *L*/20.

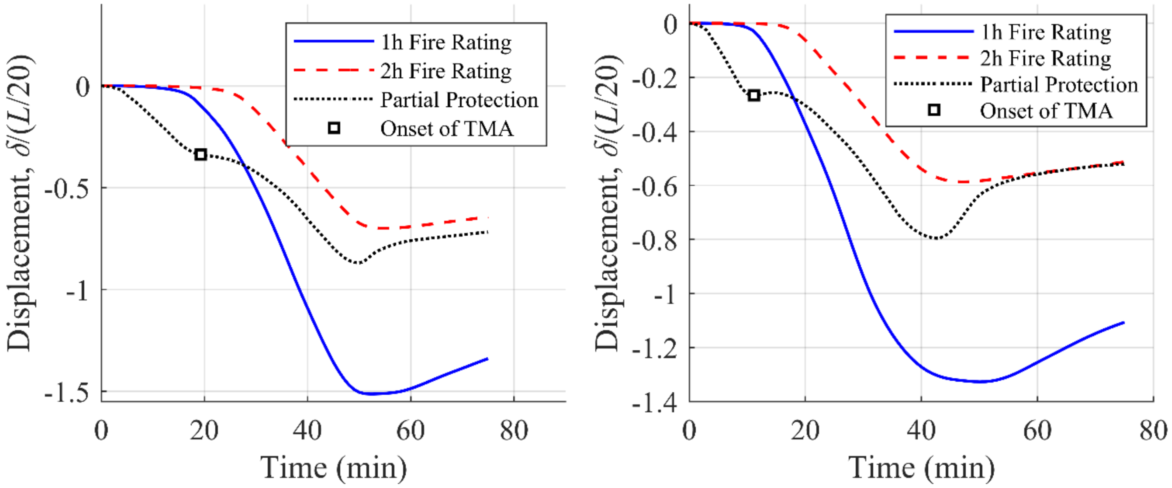

(a) Floor plan #1, location *S5* (b) Floor plan #2, location *S3*

Figure 5-23. Influence of the fire protection scheme on the displacement response of each floor plan under a 60% traveling fire (a) Floor plan #1, location *S5;* (b) Floor plan #2, location *S3*.

In general, peak displacements from using a partial protection are smaller than those occurring from a full protection scheme with a 1 h fire rating for all the traveling fire sizes examined. Figure 5-24 shows a comparison of peak displacement for the two fire protection schemes for each traveling fire size. Comparisons are made at the critical location of each floor plan (i.e., location *S5* for floor plan #1 and location *S3* for floor plan #2). Only a few traveling fire sizes produce a peak displacement above the *L*/20 displacement limit under the partial protection scheme, but are all below a normalized displacement of 1.08. An analysis of the time to *L*/20 for those traveling fire sizes with peak displacements above *L*/20 reveals adequate performance under the partial protection scheme. In floor plan #1, the smallest time to *L*/20 occurs at 107 min under a 20% traveling fire, while in floor plan #2, the smallest time to *L*/20 occurs at 70 min under a 30% traveling fire. Both time to *L*/20 are above 1 h, demonstrating the adequacy of the proposed partial protection scheme against traveling fires.

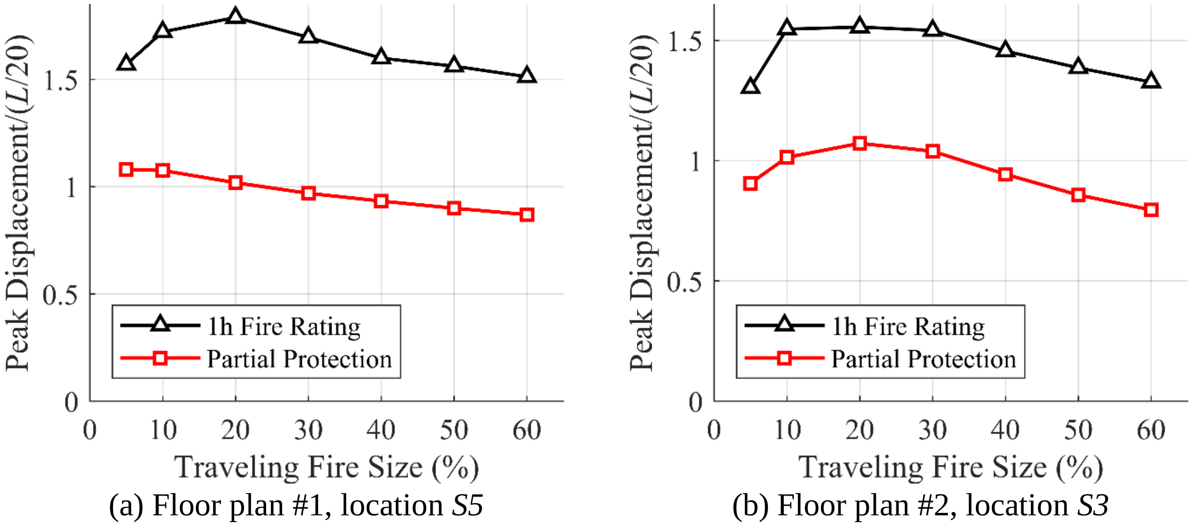

(a) Floor plan #1, location *S5* (b) Floor plan #2, location *S3*

Figure 5-24. Influence of the fire protection scheme on peak displacements observed during a traveling fire: (a) floor plan #1, location *S5*; (b) Floor plan #2, location *S3*.

The beam-end axial forces of floor plan #2 under a 60% traveling fire are shown in Figure 5-25. Three different fire protection schemes are examined, including a full protection scheme with a 1 h fire rating, a full protection scheme with a 2 h fire rating, and the partial protection scheme described previously. For brevity, axial forces are examined at three locations, labeled *B1*, *B2*, and *B3*, as shown in Figure 5-25(d), which represent end connections of girders. Normalized values of axial force are shown, with axial forces normalized by the room-temperature axial capacity $P_{y,20°C} = A_sF_{y,20°C}$. In the analyses, negative forces correspond to compressive axial forces, while positive forces correspond to tensile axial forces.

The results show similar axial-force responses for the full protection schemes, irrespective of the location examined. Restrained thermal expansion from initial heating induces compression in the girder. The compressive axial force can reach up to 38% of the axial capacity of the girder at room temperature. As the temperature of the girder rises and the strength and stiffness of the steel deteriorates, progressive displacement occurs until the girder undergoes tensile catenary action. The onset of catenary action is represented by an 'o' marker in Figure 5-25. During this stage, external loads on the girder are carried entirely by axial tension in the girder, which are subsequently carried by the connections. The onset of catenary action occurs quicker under a 1 h fire protection scheme when compared to a 2 h fire protection scheme at every location. This occurs because progressive displacement occurs quicker under a 1 h fire protection scheme when compared to a 2 h fire protection scheme owing to less fire protection. Finally, peak axial tension is larger under a 1 h fire protection scheme at all locations owing to the larger displacements occurring due to less fire protection.

The axial-force response of the girders under a partial protection scheme are cyclic in nature, and shift from tension to compression, and back to tension as shown in Figure 5-25 . Large displacements of the unprotected floor beams during the early stage of a traveling fire induces tension in the girders, as the girders support the unprotected floor beams. Since girders are fire protected with a 2 h fire rating, compression induced from restrained thermal expansion is delayed owing to the delay in heating of the girders. Tension in the first tension phase can reach 20% of the axial capacity of the girder at room temperature as shown in Figure 5-25. As the temperature of the girders rises, restrained thermal expansion from initial heating induces compression in the girder. Similar values of peak axial compression are observed in both the partial protection scheme and the full protection scheme with a 2 h fire rating at all locations examined. As the temperature of the girder rises and the strength and stiffness of the steel deteriorates, progressive displacement occurs until the girder undergoes tensile catenary action. The onset of catenary action under a partial protection scheme occurs sooner when compared to a full protection scheme with a 2 h fire rating, with larger peak tension values. When compared to the full protection scheme with a 1 h fire rating, the partial protection scheme decreases the peak axial compression force, delays the onset of catenary action, and reduces the peak axial tension force. These improvements demonstrate the adequacy of the proposed partial protection scheme against traveling fires.

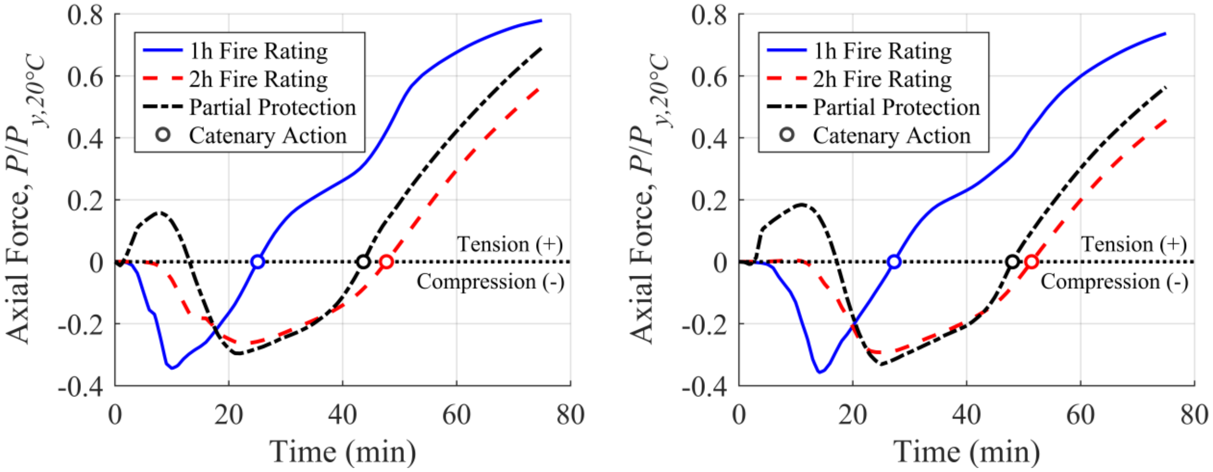

(a) Beam end *B1*

(b) Beam end *B2*

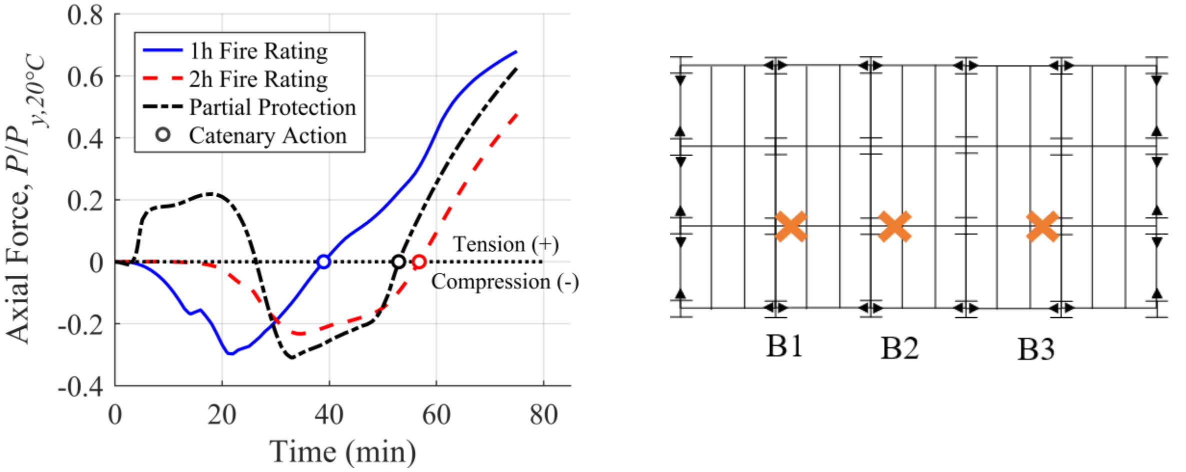

(c) Beam end *B3*

(d) Floor plan #2

Figure 5-25. Influence of the fire protection scheme on the beam-end axial force of floor plan #2 under a 60% traveling fire: (a) location *B1;* (b) location *B2*; (c) location *B3*, and (d) floor plan #2 with labels *B1* through *B3*.

The findings are not exclusive to traveling fires and are observed under the three uniform burning fires examined. Figure 5-26 shows the displacement response of floor plan #2 under a short-hot, long-cool, and ASTM E119 standard fire, all at location *U1*. In all three uniform burning fires, the initial rate of displacement is reduced after the onset of TMA. Additionally, peak displacements corresponding to the partial protection scheme are well below those corresponding to a full protection scheme with a 1 h fire rating. Under a long-cool fire, peak displacement is below the displacement limit of *L*/20. Under an ASTM E119 standard fire, time to *L*/20 occurs at 65 min under a partial protection scheme, compared to 49 min with a full protection scheme with a 1 h fire rating.

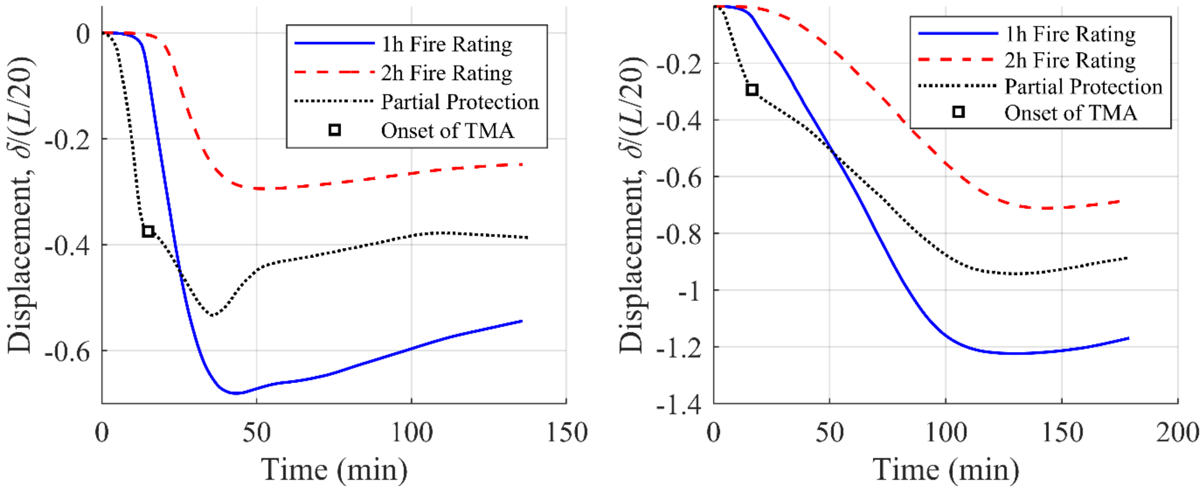

(a) Short-hot fire

(b) Long-cool fire

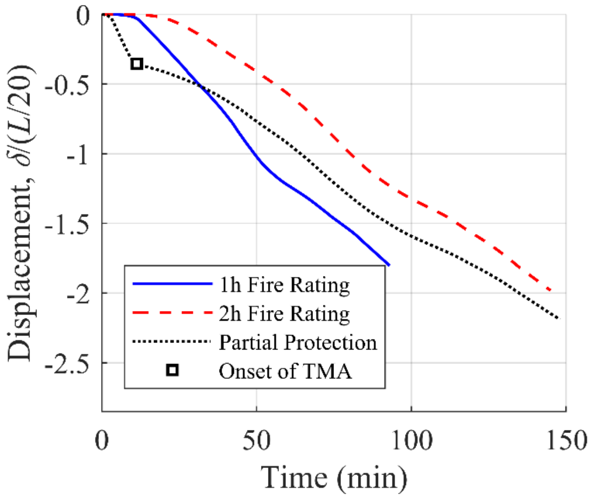

(c) ASTM E119 standard fire

Figure 5-26. Influence of the fire protection scheme on the displacement response of floor plan #2 exposed to a uniform burning fire: (a) short-hot fire; (b) long-cool fire; and (c) ASTM E119 standard fire. Displacements are shown at location *U1*.

It should be noted that the total thickness of fire insulation applied to the floor members in the partial protection scheme described above differs by +3% when compared to the total thickness of fire insulation applied to the floor members in the full protection scheme with a 1 h fire rating. Compared to the full protection scheme with a 2 h fire rating, the total thickness of fire insulation from the partial protection scheme differs by -44%. The findings demonstrates that through better allocation of the fire protection, improved performance can be achieved. The improved performance is attributed to TMA and show that TMA could be used in large open-plan compartments to provide economical fire safety solutions. Lastly, fire protection engineers should note that an increase of fire protection of girders and exterior floor beams will reduce useable height space of a floor plan.

5.8. Conclusion

A computational investigation was carried out to understand the structural response and performance of two steel-concrete composite floor system under traveling fires. A sequentially-coupled fire-thermal-structural analysis procedure was utilized, where the improved Traveling Fires Methodology was used to define the traveling fire exposure. Based on the results presented, the following conclusions were made:

- The initial rate of displacement is influenced by the size of the traveling fire for locations of the floor plan away from the fire ignition point.
- The fire rating of the floor plan influences the relationship between the traveling fire size and the peak slab displacement. Thus, the critical traveling fire size, in terms of peak displacement, is dependent on the fire rating of the composite floor plan.
- The critical location corresponding to the largest peak displacement is dependent on the characteristics of the floor plan, and not the traveling fire size nor the fire rating of the floor plan.

- Time to *L*/20 decreases with increasing traveling fie size, as well as decreases with distance closer to the fire ignition point.
- Under traveling fires, time to *L*/20 of each floor plan were significantly lower than the fire rating of the floor plan, demonstrating that prescriptive approaches can prescribe insulation designs that are unsafe against traveling fires.
- Tensile membrane action could be utilized in large open-plan compartments to provide economical fire safety solutions under traveling fire exposures.

Chapter 6 Summary, Conclusion, and Future Work

6.1. Summary

Existing fire safety codes do not have regulations for ensuring the fire safety of large open-plan compartments. This is concerning given the historically poor performance of structures in traveling fire accidents [13–18]. To address this deficiency, a numerical investigation was carried out to understand the thermal and structural response of two steel-concrete composite (SCC) floor systems exposed to traveling fires. The adequacy of prescriptive fire codes to safeguard against traveling fires was examined by comparing heat transfer and structural analysis data of the SCC floor systems exposed to both traveling fires and post-flashover fires. Additionally, improvements to the finite element modeling of SCC floor systems were developed, which enabled better numerical evaluations to be made.

An elevated-temperature tension-stiffening model for use in finite element modeling of both reinforced concrete (RC) slabs and SCC floor systems was developed in CHAPTER 2. The energy-based stress-strain model of plain concrete developed by Bažant and Oh [51] was extended to the elevated-temperature domain by developing an analytical formulation for the temperature-dependence of the fracture energy G_f. Then, an elevated-temperature tension-stiffening model was developed based on the modification of the proposed elevated-temperature tension-softening model. The applicability and validation of the proposed tension-stiffening model was presented through the numerical analysis of several fire tests on composite floor systems, including the FRACOF fire test [66] and Cardington Test no. 3 [67,68].

In CHAPTER 3, a formal macro-modeling approach for the finite element modeling of SCC floor systems was presented. Using this modeling approach, a numerical analysis of an axially restrained SCC beam was performed to investigate the influence of various parameters, including the fire type, beam slenderness, load factor, restraint stiffness, and the restraint location. In addition, validation of both the thermal and structural models were presented to establish confidence in the results.

In CHAPTER 4, a series of heat transfer analyses were carried to determine the adequacy of prescriptive codes to safeguard against traveling fires. A family of traveling fires, defined using the improved Traveling Fires Methodology (iTFM) [12], were applied to two SCC floor systems. Two post-flashover fires and a standard fire exposure were also examined. The fire rating of each structural member was quantified using the temperature limits available in the American Society for Testing and Materials (ASTM) E119 [6] standard. An analysis of peak temperature was also carried out to understand the thermal response of composite floor systems under traveling fires.

In CHAPTER 5, a computational investigation was carried out to understand the structural response of two SCC floor system exposed to traveling fires. In addition, the two SCC floor systems were examined under two post-flashover fires and a standard fire exposure. A sequentially-coupled thermal-structural analysis procedure was utilized, where the thermal and structural analysis were carried out using the finite element software ABAQUS [80], and the iTFM [12] was used to define the spatial and temporal evolution of the traveling fire exposures. In addition, validation of both the thermal and structural models were presented to establish confidence in the results.

6.2. Conclusion

A summary of key findings in each of the previous chapter are presented below:

CHAPTER 2:

- The proposed tension stiffening model can be used to predict the response of composite floor slabs exposed to fire with great accuracy, provided that the parameters TS and K_{res} are adequately calibrated.
- The sensitivity analysis revealed that an increase in TS acts to stiffen the response, while an increase in K_{res} acts to improve the convergence of the analysis.
- The temperature-dependence of G_f was shown to have a negligible influence on the structural response, and a temperature-independent β_{Gf} model can be utilized in the proposed tension stiffening model.

CHAPTER 3:

- The macro-modeling approach of a composite beam comprised of beam and shell elements is not arbitrary when axial restraint is present. Specifically, the beam reference should be positioned at the geometric centroid of the connection.
- An implicit consideration of high-temperature creep via the Eurocode material models of both steel and concrete was adequate to capture the fire response of the restrained composite beams studied here.
- An increase in the axial restraint stiffness leads to larger displacements in the early stages of a fire. However, in the later stages of a fire, an increase in the axial restraint stiffness leads to smaller displacements. This effect is attributed to tensile catenary action.

- The fire response of a restrained composite beam is heavily influenced by length of the beam. Composite beams with short spans tend to fail in the compressive beam-column stage, while composite beams with longer spans tend to fail in the tensile catenary stage.
- Conditions that are favorable for inducing catenary action in a restrained composite beam include longer beam spans, increased axial restraint stiffness, increased load ratio, and positioning of the axial restraint near the top of the beam.
- Material cooling from the decay phase of a natural fire activates restrained thermal contraction. Under a low axial stiffness, axial tension can be developed, which can reach up to 6% of the axial capacity of the steel beam at room temperature.
- Catenary action is generally developed after the deflection limit of $L/20$, demonstrating that care should be used when using this deflection limit to evaluate the fire resistance of a restrained composite beam. Utilizing this deflection limit may undermine the improved performance associated with catenary action, since it evaluates the performance of the beam while in the compressive beam-column stage.
- Premature divergence of the analysis due to localized cracking could be bypassed by utilizing larger values of K_{res}, allowing a static analysis procedure to be used, in lieu of advanced procedures such as explicit dynamic.

CHAPTER 4:

- Peak temperature in all members generally decreased with increasing traveling fire size.
- Peak temperature in beams occur between the last 60% and 90% of the floor plan (away from the fire origin), while peak temperature in columns occur at the last 80% of the floor plan.

- The location of the peak temperature in a composite floor slab depends on the traveling fire size. Under a 60% traveling fire, peak temperatures occur at the location closest to the fire origin, while under a 5% traveling fire, peak temperatures occur at a location furthest from the fire origin.
- Peak temperatures under a traveling fire are typically larger than peak temperatures under a 1 h standard fire, but smaller than the peak temperatures under a 2 h standard fire.
- Fire insulation derived from prescriptive approaches do not provide a consistent level of safety among different member types (i.e., beams, columns, etc.) and different fire types (i.e., standard fire, natural fire, etc.). Furthermore, such insulation designs may not provide satisfactory protection under traveling fires.
- Under a large traveling fire (i.e., one with a large burning region), steel members which are insulated with a 1 h fire rating can reach the ASTM E119 temperature limit in 20 min (i.e., -66 % relative difference).
- Larger traveling fire sizes will produce a smaller time to failure in structural members that are positioned closest to the fire origin.

CHAPTER 5

- The initial rate of displacement is influenced by the size of the traveling fire for locations of the floor plan away from the fire ignition point.
- The fire rating of the floor plan influences the relationship between the traveling fire size and the peak slab displacement. Thus, the critical traveling fire size, in terms of peak displacement, is dependent on the fire rating of the composite floor plan.

- The critical location corresponding to the largest peak displacement is dependent on the characteristics of the floor plan, and not the traveling fire size nor the fire rating of the floor plan.
- Time to *L*/20 decreases with increasing traveling fie size, as well as decreases with distance closer to the fire ignition point.
- Under traveling fires, time to *L*/20 of each floor plan were significantly lower than the fire rating of the floor plan, demonstrating that prescriptive approaches can prescribe insulation designs that are unsafe against traveling fires.
- Tensile membrane action could be utilized in large open-plan compartments to provide economical fire safety solutions under traveling fire exposures.

6.3. Recommendation for Future Works

6.3.1. Testing of Concrete and RC in Tension

Experimental tests that provide understanding of tension softening of plain concrete and tension stiffening of RC have yet to be extended to the elevated-temperature domain. These tests are required so that formal material models of both plain concrete and RC (i.e., tension softening and tension stiffening models, respectively) can be developed. These tests are also required to validate the models proposed in CHAPTER 2. At a minimum, the following tests are recommended as part of future research:

- Direct tension tests of plain concrete specimens subjected to steady-state elevated temperature, measuring the complete stress-displacement curve of each test specimen.

- Three-point bending tests on notched plain concrete beams exposed to steady-state elevated temperature.
- Direct tension tests of RC specimens subjected to steady-state elevated temperature.

These tests should be carried out for a complete range of variables, including an appropriate range of temperatures and material types (e.g., normal weight concrete, light-weight concrete, etc.) to ensure that a complete scope of the parameters observed in engineering practice are considered.

6.3.2. Structural Model

The resilience of SCC floor systems under traveling fires are largely dependent on the buckling response of fire-exposed columns, and to some extent the fracture of beam-end connections of critical floor members such as girders. These two failure mechanisms were not considered in the structural models, and were beyond the current scope of the dissertation.

To prevent buckling of columns, columns in the numerical models were fire protected using a 2 h fire rating. This assumption allowed a static analysis solver to be utilized, and focus to be placed on the fire response of the SCC floor system (i.e., floor beams, girders and composite slab). For SCC floor systems with columns fire protected using a 1 h fire rating, buckling failure may be a governing failure mode, which demands an explicit dynamic analysis to be used. Specifically, Fischer *et al.* [151] showed that gravity columns of the two SCC buildings examined in the dissertation were susceptible to inelastic buckling when fire protected using a 1 h fire rating and exposed to a compartment post-flashover fire. It can be assumed within reason, that similar inelastic buckling can occur under traveling fire exposures.

The resilience of SCC floor systems are largely dependent on the beam-end connections, since failure of girder-to-beam connections could lead to partial collapse of the floor system. One potential direction of future research is to use macro-based connectors with temperature-dependent properties, to represent shear tab connections more accurately (see for e.g., [153]). The structural model utilized simplified joint assumption for beam-end connections, such as a perfect pin or a perfect fixed connection. This idealization prohibits localized failure and subsequent redistribution of forces to be considered in the analysis model. For this reason, future studies involving SCC floor systems should consider beam-connection behavior via macro-based connectors representing beam-end connections.

All experimental test cases examined in the validation study were composite floor plans designed with full composite action between the steel beam and composite slab. The validation study demonstrated that assuming a rigid constraint between the aligning nodes of the shell and beam elements representing the composite slab and steel beam, respectively, was an adequate assumption. However, the degree of composite action may be important in composite floor plans designed with partial composite action between the steel beam and composite slab and may require a correct representation of the bond slippage between the beam and slab during flexure. Future studies should examine SCC floor systems which were designed with a partial composite action and account for beam-slab bond behavior and failure using connectors representing shear studs.

Finally, instrumentation of structural fire tests are insufficient to enable a high level of validation of structural models. Currently, displacement is predominantly used to validate structural models, which can be considered a low level of validation. Better instrumentation should be utilized to provide better data for use in model validation such as member axial forces and rebar strain.

6.3.3. Traveling Fires Model

Currently, two theoretical representations of traveling fire models can be found in the research literature: (1) the Traveling Fire Methodology (TFM), originally developed by researchers Stern-

Gottfried, Rein, and Law [9,11,21], and later improved by Rackauskaite *et al*. [12]; and (2) the Extended Traveling Fire Method (ETFM), developed by Dai *et al*. [154,155]. The improved Traveling Fire Methodology (iTFM) [12], which is the latest version of the TFM, was used in this study to define the traveling fire exposure. Compared to the ETFM, the iTFM is more established and has been used extensively in the past [11,21,122,135–141]. The iTFM is also relatively easier to implement, as it can be easily programmed, which is in contrast to the ETFM, which requires the FIRM zone model [156] to be utilized. One main limitation to the iTFM, for example, is that it assumes one-dimensional fire spread, whereas realistic fires spread in two directions. The influence of 2D fire spread on the 3D structural response of SCC systems has yet to be determined. It should be stated that although the iTFM and ETFM represents the state of the art of the field, both models have not yet been validated due to the lack of experimental data regarding fires in large open-plan compartments [10].

For this reason, experimental data on traveling fires is critical for the future advancement of research on structures exposed to traveling fires. Such test would allow improvements to the available traveling fire design models to be made, which will lead to better understanding of how structures respond under traveling fires. Although very costly, the scientific fire community should embrace this initiative and challenge with open arms.

Appendix A

Appendix A includes a summary of a mesh sensitivity study for both the heat transfer and structural analysis models.

A.1. Heat Transfer Analyses

A sensitivity analysis of both the mesh size Δx and time step increment of the analysis Δt are shown below for a heat transfer model of both a composite slab and a steel column exposed to an ASTM E119 standard fire. Figure A-1 show the pair of mesh size and time step increment combinations examined for the composite slab model. The result of the sensitivity analysis are presented in Figure A-2 and shows that the variation of mesh size and time step increment has a negligible effect. Thus, the combination of Δx = 3 mm, Δt = 1 s are selected for the heat transfer analysis of composite slabs exposed to fire.

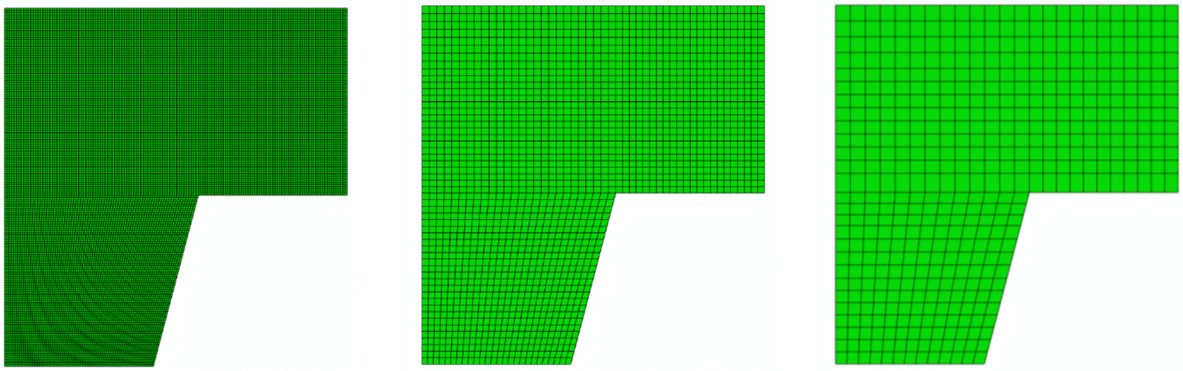

(a) Δx = 1 mm, Δt = 0.1 s (b) Δx = 3 mm, Δt = 1 s (c) Δx = 6 mm, Δt = 15 s

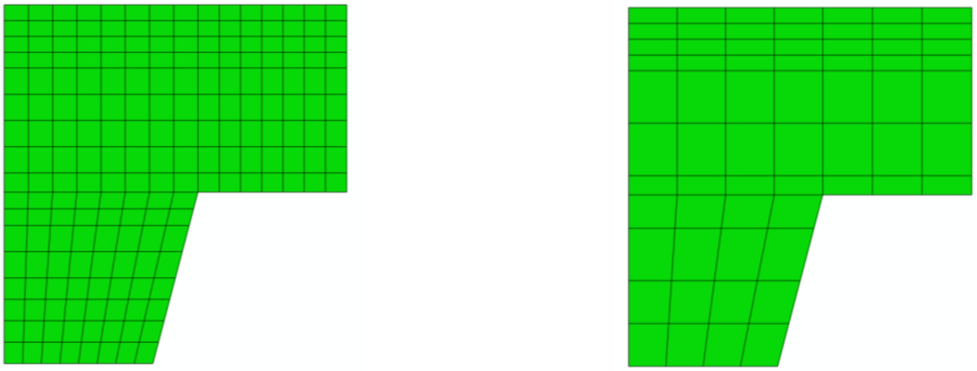

(d) Δx = 10 mm, Δt = 30 s (e) Δx = 20 mm, Δt = 60 s

Figure A-1. Mesh and time step increment analyzed for the composite slab heat transfer model.

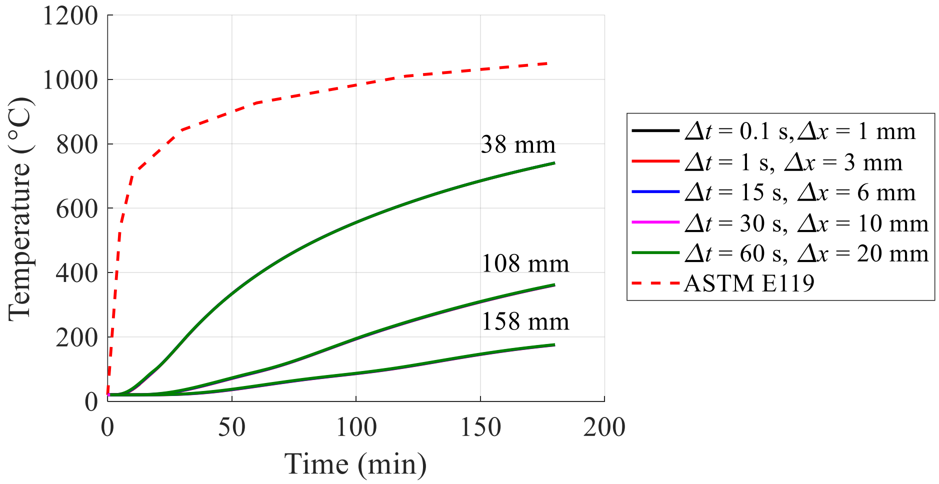

Figure A-2. Results of a mesh and time step increment sensitivity analysis of the composite slab heat transfer model.

Figure A-3 show the pair of mesh size and time step increment combinations examined for the steel column model. The result of the sensitivity analysis are shown in Figure A-4 and shows that the variation of mesh size and time step increment is significant in the early stages of the fire. The combination of Δx = 3 mm, Δt = 1 s are selected for the heat transfer analysis of steel sections exposed to fire.

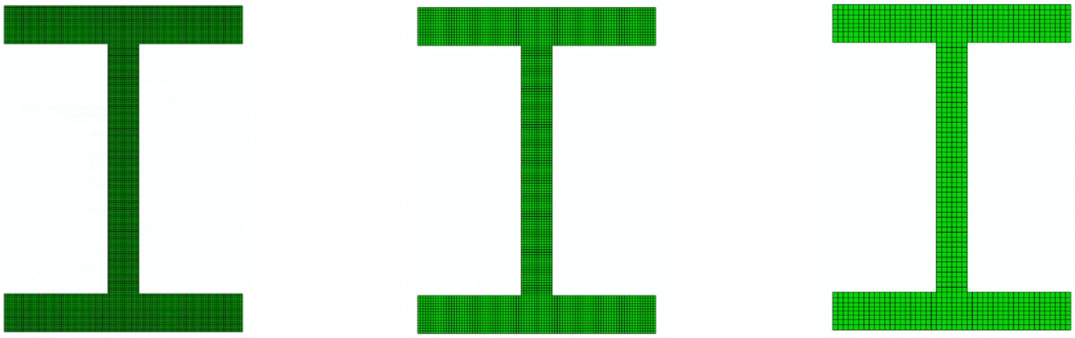

(a) Δx = 1 mm, Δt = 0.1 s (b) Δx = 3 mm, Δt = 1 s (c) Δx = 6 mm, Δt = 15 s

(d) Δx = 10 mm, Δt = 30 s (e) Δx = 20 mm, Δt = 60 s

Figure A-3. Mesh and time step increment analyzed for the steel column heat transfer model.

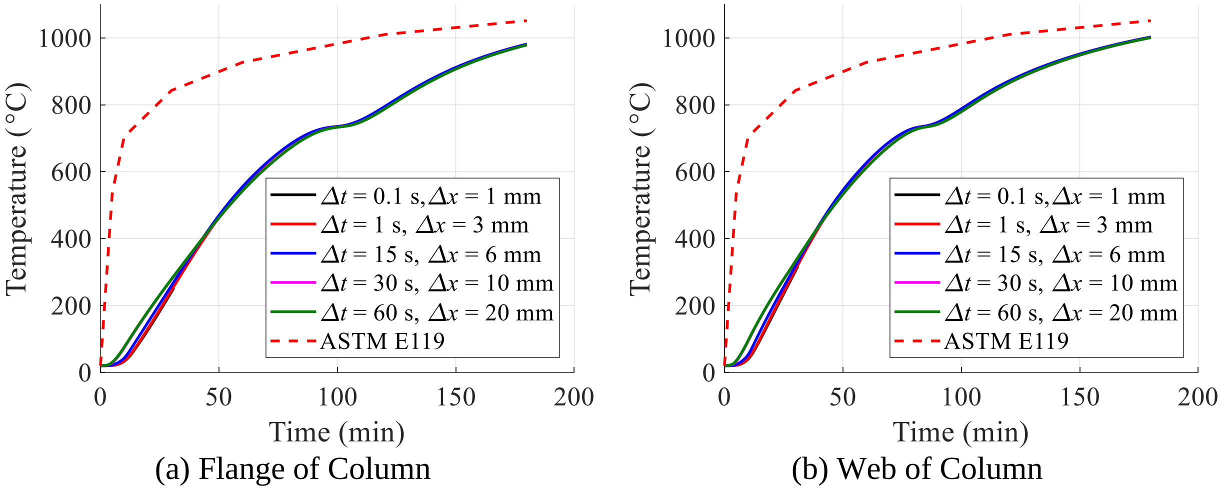

(a) Flange of Column

(b) Web of Column

Figure A-4. Results of a mesh and time step increment analysis of the steel column heat transfer model. Two locations are examined: (a) temperature at the flange; and (b) temperature at the web.

A.2. Structural Analyses

A sensitivity analysis of the mesh size used in the structural analysis is presented below. The floor plan in Figure A-5 is exposed to a short-hot fire occurring in a 4-bay corner compartment. Four mesh sizes were examined, including 159 mm, 318 mm, 635 mm, and 1,270 mm. Displacement at location "x", as indicated in Figure A-5(a), is presented in Figure A-5(b) for each mesh size. The results show that displacement converges with decreasing mesh size. Displacement from a mesh size of 635 mm compare reasonably well with the converged displacement obtained using a mesh size of 159 mm. A mesh size of 635 mm was chosen for the analysis.

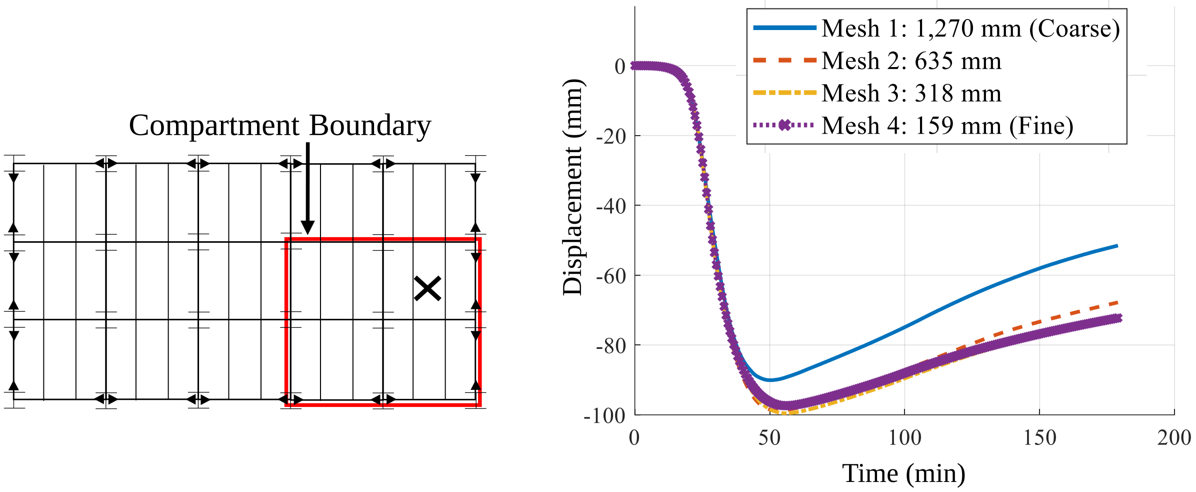

(a) Floor plan (b) Displacement

Figure A-5. Mesh sensitivity analysis of structural analysis model.

A sensitivity analysis of the mesh size used in the structural models of several experimental test cases are presented below. These test cases include: (1) Zhou and Wang's fire test on an axially-restrained composite beam (i.e., *Test CB150*) [62,63]; (2) Lim and Wade's fire test on a two-way bending RC slabs (i.e., slab *HD12*) [64,65]; (3) the FRACOF fire test on a partially-protected composite floor assembly [66]; and (4) the Cardington Test no. 3 on a corner compartment fire on a partially-protected composite floor system [67,68].

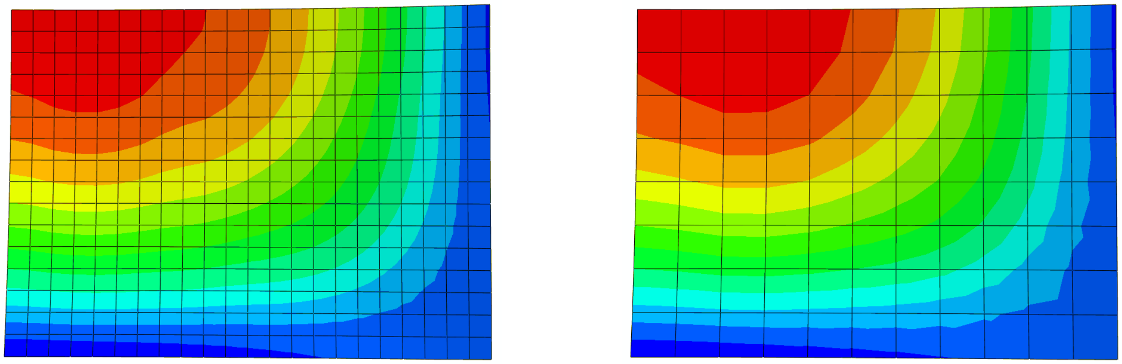

(a) 100 mm (a) 200 mm

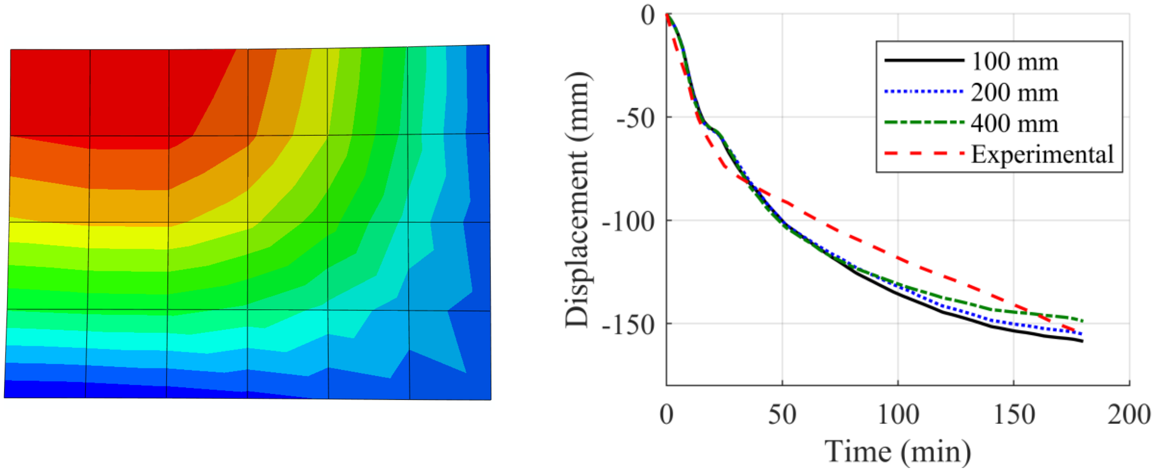

(c) 400 mm (d) Displacement

Figure A-6. Mesh sensitivity analysis of structural analysis model for Lim and Wade's *HD12* test [64,65].

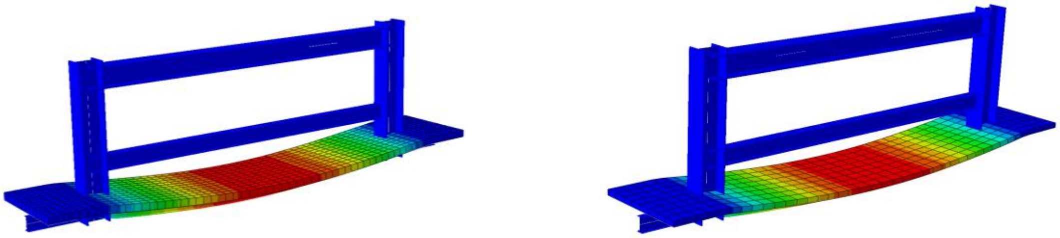

(a) 120 mm

(a) 190 mm

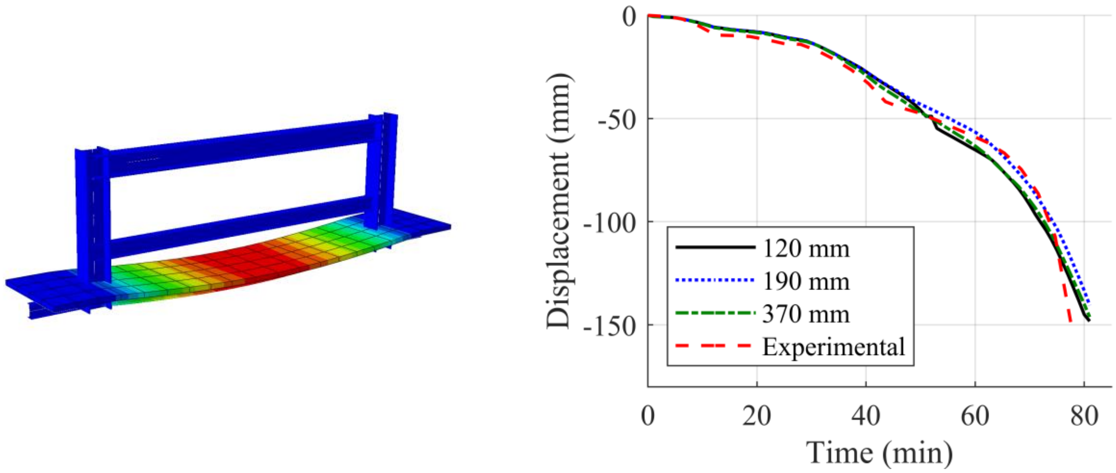

(c) 370 mm

(d) Displacement

Figure A-7. Mesh sensitivity analysis of structural analysis model for Zhou and Wang’s *Test CB150* [62,63].

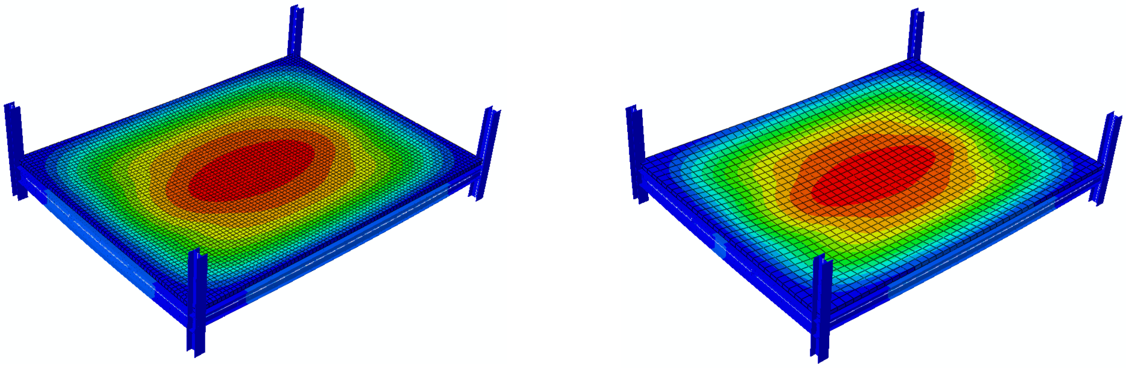

(a) 100 mm (a) 200 mm

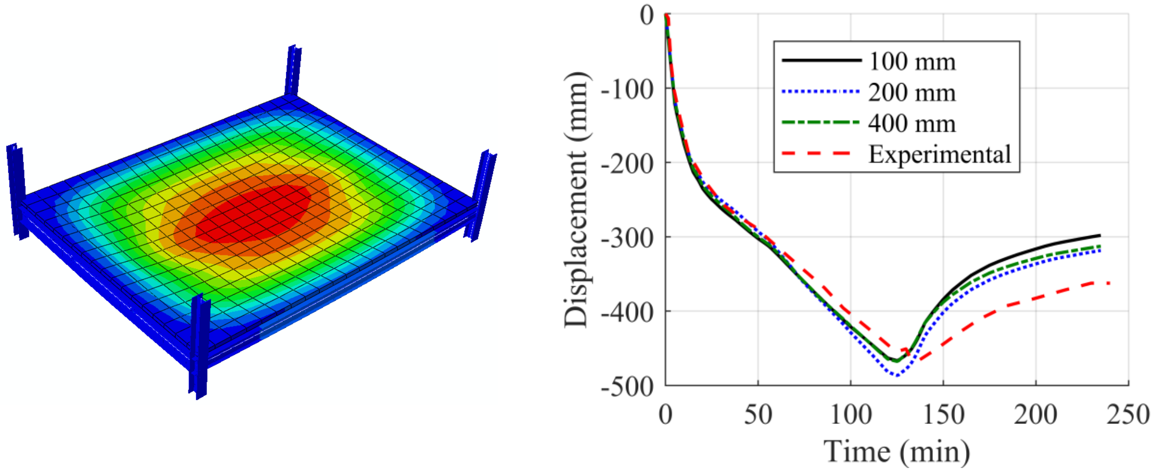

(c) 400 mm (d) Displacement

Figure A-8. Mesh sensitivity analysis of structural analysis model for the FRACOF fire test [66].

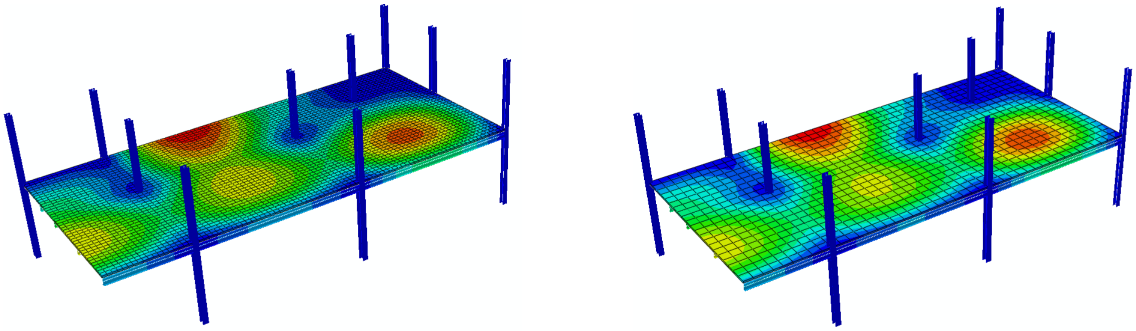

(a) 100 mm (a) 200 mm

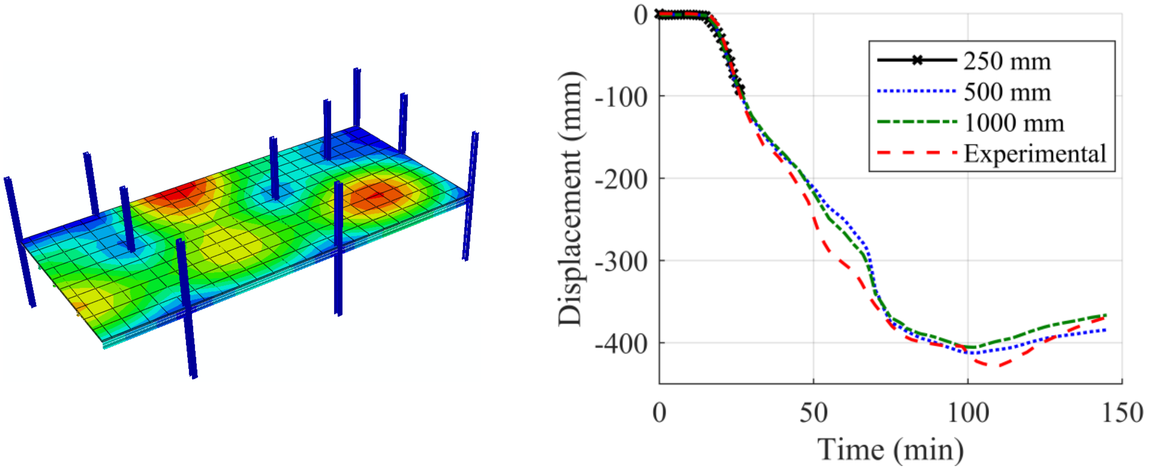

(c) 400 mm (d) Displacement

Figure A-9. Mesh sensitivity analysis of structural analysis model for Cardington Test no. 3 [67,68].

Bibliography

[1] Buchanan AH. Structural Design for Fire Safety. 1st ed. Chichester: John Wiley & Sons, Ltd.; 2002.

[2] International Code Council (ICC). International Buidling Code. Country Club Hills, IL.: International Code Council, Inc.; 2003.

[3] National Fire Protection Association (NFPA). NFPA 500: Building Construction and Safety Code 2018.

[4] Rudy JL, Marlo JP, Loannides SA, Alfawakhiri F. Steel Design Guide 19: Fire Resistance of Structural Steel Framing 2003.

[5] American Concrete Institutie (ACI) Committee 216. Code Requirements for Determining Fire Resistance of Concrete and Masonry Construction Assemblies 2014.

[6] ASTM E119-14. Standard test methods for fire tests of building construction and materials 2014:1–35. https://doi.org/10.1520/E0119-14.

[7] International Orginization for Standardization (ISO). Fire-resistance tests-elements of building construction, Part 1: General requirements 1999.

[8] Stern-Gottfried J, Rein G, Bisby L a., Torero JL. Experimental review of the homogeneous temperature assumption in post-flashover compartment fires. Fire Saf J 2010;45:249–61. https://doi.org/10.1016/j.firesaf.2010.03.007.

[9] Stern-Gottfried J, Rein G. Travelling fires for structural design-Part I: Literature review. Fire Saf J 2012;54:74–85. https://doi.org/10.1016/j.firesaf.2012.06.003.

[10] Dai X, Welch S, Usmani A. A critical review of "travelling fire" scenarios for performance-based structural engineering. Fire Saf J 2017;91:568–78. https://doi.org/10.1016/j.firesaf.2017.04.001.

[11] Stern-Gottfried J, Rein G. Travelling fires for structural design-Part II: Design methodology. Fire Saf J 2012;54:96–112. https://doi.org/10.1016/j.firesaf.2012.06.011.

[12] Rackauskaite E, Hamel C, Law A, Rein G. Improved Formulation of Travelling Fires and Application to Concrete and Steel Structures. Structures 2015;3:250–60. https://doi.org/10.1016/j.istruc.2015.06.001.

[13] Routley JG. Interstate Bank Building Fire, Los Angeles, California (USFA-TR-022) 1988.

[14] Routley JG, Jennings C, Chubb M. Highrise Office Building Fire One Meridian Plaza, Philadelphia, Pennsylvania (USFA-TR-049) 1991.

[15] McAllister TP, Gann RG, Averill JD, Gross JL, Grosshandler WL, R. LJ, et al. Federal Building and Fire Safety Investigation of the World Trade Center Disaster: Structural Fire Response and Probable Collapse Sequence of World Trade Center Building 7 (NIST NCSTAR 1-9) 2008.

[16] Fletcher I, Borg A, Hitchen N, Welch S. Performance of Concrete in Fire: A Review of the State of the Art, with a Case Study of the Windsor Tower Fire. Proc. 4th Internatioanl Work. Struct. Fire, Aveiro, Portugal: 2006, p. 779–90.

[17] Zannoni M, Bos JGH, Engel KE, Rosenthal U. Fire at the Faculty of Architecture 2008.

[18] Behnam B. Fire Structural Response of the Plasco Building: A Preliminary Investigation Report. Int J Civ Eng 2019;17:563–80. https://doi.org/10.1007/s40999-018-0332-x.

[19] American Institute of Steel Construction (AISC). Specification for Structural Steel Buildings 2010.

[20] American Society of Civil Engineers (ASCE). Minimum Design Loads for Buildings and Other Structures 2010.

[21] Law A, Stern-Gottfried J, Gillie M, Rein G. The influence of travelling fires on a concrete frame. Eng Struct 2011;33:1635–42. https://doi.org/10.1016/j.engstruct.2011.01.034.

[22] Scanlon A. Time Dependent Deflections of Reinforced Concrete Slabs (Ph.D. Thesis). University of Alberta, Edmonton, Canada, 1971.

[23] Scanlon A, Murray DW. Time-Dependent Reinforced Concrete Slab Deflections. J Struct Div 1974;100:1911–24.

[24] Stevens NJ, Uzumeri SM, Collins MP, Will GT. Constitutive Model for Reinforced Concrete Finite Element Analysis. ACI Struct J 1991;88:49–59. https://doi.org/10.14359/3105.

[25] Marzouk H, Chen ZW. Nonlinear analysis of normal- and high-strength concrete slabs. Can J Civ Eng 1993;20:696–707. https://doi.org/10.1139/l93-086.

[26] Choi C-K, Cheung S-H. Tension stiffening model for planar reinforced concrete members. Comput Struct 1996;59:179–90. https://doi.org/10.1016/0045-7949(95)00146-8.

[27] Stramandinoli RSB, La Rovere HL. An efficient tension-stiffening model for nonlinear analysis of reinforced concrete members. Eng Struct 2008;30:2069–80. https://doi.org/10.1016/j.engstruct.2007.12.022.

[28] Lin CS, Scordelis AC. Nonlinear analysis of RC shells of general form. J Struct Div 1975;101:523–38.

[29] Vebo A, Ghali A. Moment-Curvature Relation of Reinforced Concrete Slabs. J Struct Div 1977;103:515–31.

[30] Gilbert RI, Warner RF. Tension Stiffening in Reinforced Concrete Slabs. J Struct Div 1978;104:1885–900.

[31] Červenka V. Constitutive Model for Cracked Reinforced Concrete. ACI J Proc 1985;82:877–82. https://doi.org/10.14359/10409.

[32] Balakrishnan S, Elwi AE, Murray DW. Effect of Modeling on NLFE Analysis of Concrete Structures. J Struct Eng 1988;114:1467–87. https://doi.org/10.1061/(ASCE)0733-9445(1988)114:7(1467).

[33] Link RA, Elwi AE, Scanlon A. Biaxial Tension Stiffening due to Generally Oriented Reinforcing Layers. J Eng Mech 1989;115:1647–62. https://doi.org/10.1061/(ASCE)0733-9399(1989)115:8(1647).

[34] Vecchio FJ. Nonlinear Finite Element Analysis of Reinforced Concrete Membranes. ACI Struct J 1989;86:26–35. https://doi.org/10.14359/2620.

[35] Massicotte B, Elwi AE, MacGregor JG. Tension-Stiffening Model for Planar Reinforced Concrete Members. J Struct Eng 1990;116:3039–58. https://doi.org/10.1061/(ASCE)0733-9445(1990)116:11(3039).

[36] Memari AM, West HH. Computation of bridge design forces from influence surfaces. Comput Struct 1991;38:547–56. https://doi.org/10.1016/0045-7949(91)90006-8.

[37] Nie J, Tao M, Cai CS, Chen G. Modeling and investigation of elasto-plastic behavior of steel–concrete composite frame systems. J Constr Steel Res 2011;67:1973–84. https://doi.org/10.1016/j.jcsr.2011.06.016.

[38] Huang Z, Burgess IW, Plank RJ. Three-Dimensional Analysis of Composite Steel-Framed Buildings in Fire. J Struct Eng 2000;126:389–97. https://doi.org/10.1061/(ASCE)0733-9445(2000)126:3(389).

[39] Gupta AK, Ma PS. Error in eccentric beam formulation. Int J Numer Methods Eng 1977;11:1473–7. https://doi.org/10.1002/nme.1620110910.

[40] Chen Y. Distribution of vehicular loads on bridge girders by the FEA using ADINA: modeling, simulation, and comparison. Comput Struct 1999;72:127–39. https://doi.org/10.1016/S0045-7949(99)00032-2.

[41] Chan THT, Chan JHF. The use of eccentric beam elements in the analysis of slab-on-girder bridges. Struct Eng Mech 1999;8:85–102. https://doi.org/10.12989/sem.1999.8.1.085.

[42] Chung W, Sotelino ED. Three-dimensional finite element modeling of composite girder bridges. Eng Struct 2006;28:63–71. https://doi.org/10.1016/j.engstruct.2005.05.019.

[43] Stadler M. Design of Composite Slab Systems in Case of Fire Using Simplified Finite Element Analyses (Ph.D. Thesis). Stahlbau 2013;82:632–3. https://doi.org/10.1002/stab.201390134.

[44] Rackauskaite E, Kotsovinos P, Rein G. Model parameter sensitivity and benchmarking of the explicit dynamic solver of LS-DYNA for structural analysis in case of fire. Fire Saf J 2017;90:123–38. https://doi.org/10.1016/j.firesaf.2017.03.002.

[45] Ngo D, Scordelis AC. Finite Element Analysis of Reinforced Concrete Beams. ACI J Proc 1967;64:152–63. https://doi.org/10.14359/7551.

[46] Nilson AH. Nonlinear Analysis of Reinforced Concrete by the Finite Element Method. ACI J Proc 1968;65:757–66. https://doi.org/10.14359/7510.

[47] Beata PA. Computational Approaches to Fire-Structure Interaction and Real-Time Fire Monitoring (Ph.D. Thesis). University of Michigan, 2017.

[48] Jeffers AE, Sotelino ED. An efficient fiber element approach for the thermo-structural simulation of non-uniformly heated frames. Fire Saf J 2012;51:18–26. https://doi.org/10.1016/j.firesaf.2012.02.002.

[49] Jeffers A, Sotelino E. Analysis of Steel Structures in Fire with Force-Based Frame Elements. J Struct Fire Eng 2012;3:287–300. https://doi.org/10.1260/2040-2317.3.4.287.

[50] Liu N, Jeffers AE. Adaptive isogeometric analysis in structural frames using a layer-based discretization to model spread of plasticity. Comput Struct 2018;196:1–11. https://doi.org/10.1016/j.compstruc.2017.10.016.

[51] Bažant ZP, Oh BH. Crack band theory for fracture of concrete. Matériaux Constr 1983;16:155–77. https://doi.org/10.1007/BF02486267.

[52] Belarbi A, Hsu TTC. Constitutive Laws of Concrete in Tension and Reinforcing Bars Stiffened By Concrete. ACI Struct J 1994;91:465–74. https://doi.org/10.14359/4154.

[53] Vecchio FJ, Collins MP. The Modified Compression-Field Theory for Reinforced Concrete Elements Subjected to Shear. ACI J Proc 1986;83:219–23. https://doi.org/10.14359/10416.

[54] Prakhya GKV, Morley CT. Tension-Stiffening and Moment-Curvature Relations of Reinforced Concrete Elements. ACI Struct J 1990;87:597–605. https://doi.org/10.14359/2680.

[55] Gupta AK, Maestrini SR. Tension-Stiffness Model for Reinforced Concrete Bars. J Struct Eng 1990;116:769–90. https://doi.org/10.1061/(ASCE)0733-9445(1990)116:3(769).

[56] Williams A. Tests on large reinforced concrete elements subjected to direct tension - Tech. Rep. No. 42.562. London: Cement and Concrete Association; 1986.

[57] Carreira DJ, Chu KH. Stress-Strain Relationship for Reinforced Concrete in Tension. ACI

J Proc 1986;83:21–9. https://doi.org/10.14359/1756.
[58] Bischoff PH. Effects of shrinkage on tension stiffening and cracking in reinforced concrete. Can J Civ Eng 2001;28:363–74. https://doi.org/10.1139/l00-117.
[59] Fields K, Bischoff PH. Tension Stiffening and Cracking of High-Strength Reinforced Concrete Tension Members. ACI Struct J 2004;101:447–56. https://doi.org/10.14359/13330.
[60] Bischoff PH, Paixao R. Tension stiffening and cracking of concrete reinforced with glass fiber reinforced polymer (GFRP) bars. Can J Civ Eng 2004;31:579–88. https://doi.org/10.1139/l04-025.
[61] Kaklauskas G, Ghaboussi J. Stress-Strain Relations for Cracked Tensile Concrete from RC Beam Tests. J Struct Eng 2001;127:64–73. https://doi.org/10.1061/(ASCE)0733-9445(2001)127:1(64).
[62] Zhou HY. Theoretical and Experimental Research on Fire Resistance of Steel-Concrete Composite Beams (Ph.D. Thesis). Tongji University, 2004.
[63] Wang YZ. Behavior and Design of Composite Beam in Fire with Considering Global Structure Effect (Ph.D. Thesis). Tongji University, 2006.
[64] Lim LCS. Membrane Action in Fire Exposed Concrete Floor Systems (Ph.D. Thesis). University of Canterbury, 2003.
[65] Lim LCS, Wade C. Experimental Fire Tests of Two-Way Concrete Slabs. Fire Engineering Research Report 02/12 2002:1–108.
[66] Vassart O, Zhao B. FRACOF Engineering Background. Report developed for the Leonardo Da Vinci Programme: Fire Resistance Assessment of Partially Protected Composite Floors (FRACOF). 2011:1–132.
[67] British Steel. The behaviour of a multi-storey steel framed building subjected to fire attack: Experimental Data 1998.
[68] British Steel. The Behaviour of Multi-Storey Steel Framed Buildings in Fire. 1999.
[69] Crisfield MA. Snap-through and snap-back response in concrete structures and the dangers of under-integration. Int J Numer Methods Eng 1986;22:751–67. https://doi.org/10.1002/nme.1620220314.
[70] de Borst R. Computation of post-bifurcation and post-failure behavior of strain-softening solids. Comput Struct 1987;25:211–24. https://doi.org/10.1016/0045-7949(87)90144-1.
[71] Rots JG. Computational Modeling of Concrete Fracture (Ph.D. Thesis). Delft University of Technology, Delft, The Netherlands, 1988.
[72] Hofstetter G, Mang HA. Computational plasticity of reinforced and prestressed concrete structures. Comput Mech 1996;17:242–54. https://doi.org/10.1007/BF00364827.
[73] Feenstra PH, de Borst R. Constitutive Model for Reinforced Concrete. J Eng Mech 1995;121:587–95. https://doi.org/10.1061/(ASCE)0733-9399(1995)121:5(587).
[74] Leibengood LD, Darwin D, Dodds RH. Parameters Affecting FE Analysis of Concrete Structures. J Struct Eng 1986;112:326–41. https://doi.org/10.1061/(ASCE)0733-9445(1986)112:2(326).
[75] Oliver J. A consistent characteristic length for smeared cracking models. Int J Numer Methods Eng 1989;28:461–74. https://doi.org/10.1002/nme.1620280214.
[76] Terro MJ. Numerical Modeling of the Behavior of Concrete Structures in Fire. ACI Struct J 1998;95:183–92. https://doi.org/10.14359/538.
[77] Huang Z, Burgess IW, Plank RJ. Nonlinear Analysis of Reinforced Concrete Slabs Subjected to Fire. ACI Struct J 1999;96:127–35. https://doi.org/10.14359/604.

[78] European Committee for Standardization (CEN). Eurocode 2: Design of Concrete Structures – part 1-2: General rules – Structural fire design 2002.
[79] Deeny S. The Implications of Compartment Fire Non-Uniformity for the Membrane Action of Reinforced Concrete Slabs (Ph.D. Thesis). The University of Edinburgh, 2010.
[80] Dassault Systémes Simulia Corp. (DSS). ABAQUS 6.14 Online Documentation 2014.
[81] Law A. The Assessment and Response of Concrete Structures Subjected to Fire (Ph.D. Thesis). The University of Edinburgh, 2010.
[82] Florides MM, Cashell KA. Numerical Modelling of Composite Floor Slabs Subject to Large Deflections. Structures 2017;9:112–22. https://doi.org/10.1016/j.istruc.2016.10.003.
[83] Lam ES, Fang S. Direct Tensile Behavior of Normal-Strength Concrete at Elevated Temperatures. ACI Mater J 2014;111:641–50. https://doi.org/10.14359/51686915.
[84] Hillerborg A. The theoretical basis of a method to determine the fracture energy Gf of concrete. Mater Struct 1985;18:291–6. https://doi.org/10.1007/BF02472919.
[85] Zhang B, Bićanić N. Fracture energy of high-performance concrete at high temperatures up to 450°C: the effects of heating temperatures and testing conditions (hot and cold). Mag Concr Res 2006;58:277–88. https://doi.org/10.1680/macr.2006.58.5.277.
[86] Bažant ZP, Prat PC. Effect of Temperature and Humidity on Fracture Energy of Concrete. ACI Mater J 1988;85:262–71. https://doi.org/10.14359/2127.
[87] European Committee for Standardization (CEN). Eurocode 3: Design of steel structures – Part 1-2: General rules – Structural fire design 2005.
[88] International Federation for Structural Concrete (fib). fib Model Code for Concrete Structures 2010. Weinheim, Germany: Wiley-VCH Verlag GmbH & Co. KGaA; 2013. https://doi.org/10.1002/9783433604090.
[89] Li G, Wang P. Advanced Analysis and Design for Fire Safety of Steel Structures. Berlin, Heidelberg: Springer Berlin Heidelberg; 2013. https://doi.org/10.1007/978-3-642-34393-3.
[90] Li G-Q, Wang P. Advanced Analysis and Design for Fire Safety of Steel Structures. Berlin, Heidelberg: Springer Berlin Heidelberg; 2013. https://doi.org/10.1007/978-3-642-34393-3.
[91] Liu N, Plucinsky P, Jeffers AE. Combining Load-Controlled and Displacement-Controlled Algorithms to Model Thermal-Mechanical Snap-Through Instabilities in Structures. J Eng Mech 2017;143:04017051. https://doi.org/10.1061/(ASCE)EM.1943-7889.0001263.
[92] Collins MP, Vecchio FJ, Mehlhorn G. An international competition to predict the response of reinforced concrete panels. Can J Civ Eng 1985;12:624–44. https://doi.org/10.1139/l85-070.
[93] Kodur VKR, Dwaikat MMS. Response of steel beam–columns exposed to fire. Eng Struct 2009;31:369–79. https://doi.org/10.1016/j.engstruct.2008.08.020.
[94] Dwaikat M, Kodur V. Effect of Location of Restraint on Fire Response of Steel Beams. Fire Technol 2010;46:109–28. https://doi.org/10.1007/s10694-009-0085-9.
[95] Li G-Q, Guo S-X. Experiment on restrained steel beams subjected to heating and cooling. J Constr Steel Res 2008;64:268–74. https://doi.org/10.1016/j.jcsr.2007.07.007.
[96] Liu TC., Fahad M., Davies J. Experimental investigation of behaviour of axially restrained steel beams in fire. J Constr Steel Res 2002;58:1211–30. https://doi.org/10.1016/S0143-974X(01)00062-1.
[97] Dwaikat M, Kodur V. Engineering Approach for Predicting Fire Response of Restrained Steel Beams. J Eng Mech 2011;137:447–61. https://doi.org/10.1061/(ASCE)EM.1943-7889.0000244.
[98] Jiang J, Li G-Q, Usmani A. Analysis of Composite Steel-concrete Beams Exposed to Fire

using OpenSees. J Struct Fire Eng 2015;6:1–20. https://doi.org/10.1260/2040-2317.6.1.1.

[99] Yin Y., Wang Y. A numerical study of large deflection behaviour of restrained steel beams at elevated temperatures. J Constr Steel Res 2004;60:1029–47. https://doi.org/10.1016/j.jcsr.2003.09.005.

[100] Tan K-H, Huang Z-F. Structural Responses of Axially Restrained Steel Beams with Semirigid Moment Connection in Fire. J Struct Eng 2005;131:541–51. https://doi.org/10.1061/(ASCE)0733-9445(2005)131:4(541).

[101] Kodur VKR, Dwaikat MMS. Effect of high temperature creep on the fire response of restrained steel beams. Mater Struct 2010;43:1327–41. https://doi.org/10.1617/s11527-010-9583-y.

[102] Allam A, Nassif A, Nadjai A. Behaviour of restrained steel beam at elevated temperature – parametric studies. J Struct Fire Eng 2019;10:324–39. https://doi.org/10.1108/JSFE-11-2018-0036.

[103] ISOLATEK. CAFCO User’s Manual 2008.

[104] Underwriters Laboratories (UL). UL Databases and Directories 2017.

[105] American Concrete Institutie (ACI). Building Code Requirements for Structural Concrete and Commentary 2014.

[106] Petterson O, Magnusson SE, Thor J. Fire engineering design of steel structures 1976.

[107] Kodur VKR, Shakya AM. Effect of temperature on thermal properties of spray applied fire resistive materials. Fire Saf J 2013;61:314–23. https://doi.org/10.1016/j.firesaf.2013.09.011.

[108] European Committee for Standardization (CEN). Eurocode 4: Design of composite steel and concrete structures - Part 1-2: General rules - Structural fire design 2005.

[109] European Committee for Standardization (CEN). Eurocode 1: Actions on structures – Part 1-2: General actions – Actions on structures exposed to fire 2002.

[110] Guo S, Bailey CG. Experimental behaviour of composite slabs during the heating and cooling fire stages. Eng Struct 2011;33:563–71. https://doi.org/10.1016/j.engstruct.2010.11.014.

[111] Buchanan AH, Abu AK. Structural Design for Fire Safety. Second Edi. Chichester, UK: John Wiley & Sons, Ltd; 2017. https://doi.org/10.1002/9781118700402.

[112] Wang Y, Burgess I, Wald F, Gillie W. Performance-Based Fire Engineering of Structures. Boca Raton, FL.: CRC Press; 2012.

[113] Martinez J, Jeffers AE. Elevated-Temperature Tension Stiffening Model for Reinforced Concrete Structures under Fire. In: Nadjai A, Ali F, Franssen J-M, Vassart O, editors. 10th Int. Conf. Struct. Fire SIF’18, Belfast, UK: Ulster University; 2018, p. 463–70.

[114] Wainman DE, Kirby BR. Compendium of UK Standard Fire Test Data: Unprotected Structural Steel - 1. Ref. No. RS/RSC/S10328/1/87/B. 1988:1–26.

[115] Bailey CG, Burgess IW, Plank RJ. Computer simulation of a full-scale structural fire test. Struct Eng 1996;74:93–100.

[116] Dwaikat MMS, Kodur VKR. A performance based methodology for fire design of restrained steel beams. J Constr Steel Res 2011;67:510–24. https://doi.org/10.1016/j.jcsr.2010.09.004.

[117] Zhang C, Li GQ, Usmani A. Simulating the behavior of restrained steel beams to flame impingement from localized-fires. J Constr Steel Res 2013;83:156–65. https://doi.org/10.1016/j.jcsr.2013.02.001.

[118] Huang Z, Burgess IW, Plank RJ. The influence of shear connectors on the behaviour of

composite steel-framed buildings in fire. J Constr Steel Res 1999;51:219–37. https://doi.org/10.1016/S0143-974X(99)00028-0.

[119] Deb A, Booton M. Finite element models for stiffened plates under transverse loading. Comput Struct 1988;28:361–72. https://doi.org/10.1016/0045-7949(88)90076-4.

[120] Mukhopadhyay M. Stiffened plate plane stress elements for the analysis of ships' structures. Comput Struct 1981;13:563–73. https://doi.org/10.1016/0045-7949(81)90052-3.

[121] Davies JM, Hughes OF, Mistree F. Finite elements in the design of optimum ship structures 1976.

[122] Jiang Y, Kotsovinos P, Usmani A, Rein G, Stern-Gottfried J. Numerical Investigation of Thermal Responses of a Composite Structure in Horizontally Travelling fires Using OpenSees. Procedia Eng 2013;62:736–44. https://doi.org/10.1016/j.proeng.2013.08.120.

[123] Agarwal A, Varma AH. Fire induced progressive collapse of steel building structures: The role of interior gravity columns. Eng Struct 2014;58:129–40. https://doi.org/10.1016/j.engstruct.2013.09.020.

[124] Alpert RL. Calculation of response time of ceiling-mounted fire detectors. Fire Technol 1972;8:181–95.

[125] Quintiere JG, Rinkinen WJ, Jones WW. The Effect of Room Openings on Fire Plume Entrainment. Combust Sci Technol 1981;26:193–201. https://doi.org/10.1080/00102208108946960.

[126] Jeffers AE, Sotelino ED. Fiber Heat Transfer Element for Modeling the Thermal Response of Structures in Fire. J Struct Eng 2009;135:1191–200. https://doi.org/10.1061/(ASCE)ST.1943-541X.0000043.

[127] Jeffers AE. Triangular Shell Heat Transfer Element for the Thermal Analysis of Nonuniformly Heated Structures. J Struct Eng 2016;142:04015084. https://doi.org/10.1061/(ASCE)ST.1943-541X.0001335.

[128] Jeffers AE. Heat transfer element for modeling the thermal response of non-uniformly heated plates. Finite Elem Anal Des 2013;63:62–8. https://doi.org/10.1016/j.finel.2012.08.009.

[129] Jeffers AE, Beata PA. Generalized shell heat transfer element for modeling the thermal response of non-uniformly heated structures. Finite Elem Anal Des 2014;83:58–67. https://doi.org/10.1016/j.finel.2014.01.003.

[130] Liu N, Beata PA, Jeffers AE. A mixed isogeometric analysis and control volume approach for heat transfer analysis of nonuniformly heated plates. Numer Heat Transf Part B Fundam 2019;75:347–62. https://doi.org/10.1080/10407790.2019.1627801.

[131] LaMalva KJ, editor. Structural Fire Engineering. Reston, VA: American Society of Civil Engineers (ASCE); 2018. https://doi.org/10.1061/9780784415047.

[132] Lamont S, Usmani A., Drysdale D. Heat transfer analysis of the composite slab in the Cardington frame fire tests. Fire Saf J 2001;36:815–39. https://doi.org/10.1016/S0379-7112(01)00041-8.

[133] Hamerlinck R, Twilt L, Stark JWB. A Numerical Model for Fire-exposed Composite Steel/ concrete Slabs. 10th Int. Spec. Conf. Cold-Formed Steel Struct., St. Louis, Missouri: University of Missouri-Rolla; 1990, p. 115–30.

[134] Kodur V, Dwaikat M, Fike R. High-Temperature Properties of Steel for Fire Resistance Modeling of Structures. J Mater Civ Eng 2010;22:423–34. https://doi.org/10.1061/(ASCE)MT.1943-5533.0000041.

[135] Behnam B, Rezvani FH. Structural Evaluation of Tall Steel Moment-Resisting Structures

in Simulated Horizontally Traveling Postearthquake Fire. J Perform Constr Facil 2014:1–12. https://doi.org/10.1061/(ASCE)CF.1943-5509.0000696.

[136] Rezvani FH, Ronagh HR. Structural response of a MRF exposed to travelling fire. Proc Inst Civ Eng - Struct Build 2015;168:619–35. https://doi.org/10.1680/jstbu.14.00046.

[137] Behnam B. On the Effect of Travelling Fire on the Stability of Seismic-Damaged Large Reinforced Concrete Structures. Int J Civ Eng 2016;14:535–45. https://doi.org/10.1007/s40999-016-0023-4.

[138] Rackauskaite E, Kotsovinos P, Jeffers A, Rein G. Structural analysis of multi-storey steel frames exposed to travelling fires and traditional design fires. Eng Struct 2017;150:271–87. https://doi.org/10.1016/j.engstruct.2017.06.055.

[139] Rackauskaite E, Kotsovinos P, Rein G. Structural response of a steel-frame building to horizontal and vertical travelling fires in multiple floors. Fire Saf J 2017. https://doi.org/10.1016/j.firesaf.2017.04.018.

[140] Rezvani FH, Behnam B, Ronagh HR, Jeffers AE. Robustness assessment of a generic steel fire-protected moment-resisting frame under travelling fire. Eur J Environ Civ Eng 2018;22:64–81. https://doi.org/10.1080/19648189.2016.1179679.

[141] Rackauskaite E, Kotsovinos P, Jeffers A, Rein G. Computational analysis of thermal and structural failure criteria of a multi-storey steel frame exposed to fire. Eng Struct 2019;180:524–43. https://doi.org/10.1016/j.engstruct.2018.11.026.

[142] Suwondo R, Cunningham L, Gillie M, Bailey C. Progressive collapse analysis of composite steel frames subject to fire following earthquake. Fire Saf J 2019;103:49–58. https://doi.org/10.1016/j.firesaf.2018.12.007.

[143] Federal Emergency Management Agency (FEMA356). Prestandard and Commentary for the Seismic Rehabilitation of Buildings: Rehabilitation Requirements 2000.

[144] Society of Fire Protection Engineers (SFPE) S.01. SFPE Engineering Standard on Calculating Fire Exposures to Structures. 2012.

[145] Bailey CG, White D., Moore D. The tensile membrane action of unrestrained composite slabs simulated under fire conditions. Eng Struct 2000;22:1583–95. https://doi.org/10.1016/S0141-0296(99)00110-8.

[146] Bailey CG. Membrane action of slab/beam composite floor systems in fire. Eng Struct 2004;26:1691–703. https://doi.org/10.1016/j.engstruct.2004.06.006.

[147] Gillie M, Usmani a. S, Rotter JM. A structural analysis of the Cardington British Steel Corner Test. J Constr Steel Res 2002;58:427–42. https://doi.org/10.1016/S0143-974X(01)00004-9.

[148] Plank RJ. Performance Based Fire Engineering in the UK. Int J High-Rise Build 2013;2:1–9.

[149] Lelli L, Loutan J. Advanced analyses of the membrane action of composite slabs under natural fire scenarios. J Struct Fire Eng 2018;9:77–90. https://doi.org/10.1108/JSFE-12-2016-0020.

[150] Elhami Khorasani N, Gernay T, Fang C. Parametric Study for Performance-Based Fire Design of US Prototype Composite Floor Systems. J Struct Eng 2019;145:04019030. https://doi.org/10.1061/(ASCE)ST.1943-541X.0002315.

[151] Fischer EC, Varma AH, Agarwal A. Performance-Based Structural Fire Engineering of Steel Building Structures: Design-Basis Compartment Fires. J Struct Eng 2019;145:04019090. https://doi.org/10.1061/(ASCE)ST.1943-541X.0002370.

[152] American Society of Civil Engineers (ASCE). Minimum Design Loads and Associated

Criteria for Buildings and Other Structures (ASCE/SEI 7-16) 2017. https://doi.org/10.1061/9780784414248.

[153] Nguyen H, Jeffers AE, Kodur V. Computational simulation of steel moment frame to resist progressive collapse in fire. J Struct Fire Eng 2016;7:286–305. https://doi.org/10.1108/JSFE-12-2016-020.

[154] Dai X, Jiang L, Maclean J, Welch S, Usmani A. A conceptual framework for a design travelling fire for large compartments with fire resistant islands. 14th Int. Conf. Exhib. Fire Sci. Eng. (Interflam 2016), Royal Holloway College, Nr Windsor, UK: 2016, p. 1039–50.

[155] Dai X, Jiang L, Maclean J, Welch S, Usmani AS. Implementation of a New Design Travelling Fire Model for Global Structural Analysis. Proc. 9th Int. Conf. Struct. Fire, 2016, p. 959–66.

[156] Janssens ML. An Introduction to Mathematical Fire Modeling. 2nd ed. CRC Press; 2000.